学位論文

Wavenumber Measurement of the Lower Hybrid Wave by an Electrostatic Probe with an Embedded High Impedance Resistor in the TST-2 Spherical Tokamak

（TST-2 球状トカマクにおける
高抵抗素子内蔵型静電プローブを用いた
低域混成波の波数計測）

平成 25 年 12 月　博士（理学）申請
東京大学大学院理学系研究科
物理学専攻
角田　英俊

Wavenumber Measurement of the Lower Hybrid Wave by an Electrostatic Probe with an Embedded High Impedance Resistor in the TST-2 Spherical Tokamak

Hidetoshi Kakuda

Department of Physics
Graduate School of Science, The University of Tokyo
December 2013

Abstract

Nuclear fusion is expected to become one of the main energy sources in the future society. The tokamak, which confines the plasma in the shape of a "doughnut" by magnetic fields, is regarded as the leading candidate for magnetic fusion power plant. There is a special class of tokamak, called the spherical tokamak (ST), which confines the plasma in the shape closer to a sphere rather than a doughnut. The ST has two advantages over the conventional tokamak: being more compact and having better stability at high β (β is the ratio of the plasma pressure to the magnetic pressure), leading to the possibility of realizing a more economical fusion power plant.

In order to realize the ST fusion power plant, the elimination of (or at least reduction of the size of) the ohmic heating (OH) solenoid is necessary. The OH solenoid is the coil located on the inboard side of the torus which is normally used to drive the plasma current (necessary to confine the tokamak plasma) inductively. However, there are two fatal disadvantages: inductive current drive cannot be used to drive the plasma current in steady state, and it occupies the precious space on the inboard side of the torus. A new method of non-inductive plasma current drive, capable of steady state operation, is needed. Radio frequency (RF) waves offer a possibility to drive the plasma current in steady state by giving their momentum to the plasma continuously. Among RF waves, the lower hybrid wave (LHW) is promising due to its high current drive efficiency during the initial phase of tokamak (including ST) plasmas. Although many successful demonstrations of non-inductive plasma current drive using the LHW have been reported, the development of efficient plasma current drive by the LHW in ST devices has just begun.

In the Tokyo Spherical Tokamak-2 (TST-2) device, located on Kashiwa Campus of the University of Tokyo, non-inductive plasma current drive experiments using the LHW at a frequency of 200 MHz are being conducted. Although nearly 20 kA of plasma current has been achieved already, the current drive efficiency is still low, and needs to be improved. In order to accomplish this, it is necessary to understand the physics of current drive in the initial ST plasma driven by the LHW, and to use this knowledge to improve the efficiency and reach higher levels of plasma current. Direct measurements of the LHW amplitude and wave number in ST devices can provide important information because the wavenumber determines wave propagation and absorption in the plasma.

A new method for measuring the wavenumber of the LHW using an electrostatic probe with an embedded high impedance ($100\,\mathrm{k\Omega}$) non-magnetic resistor is suggested and used for LHW wavenumber measurement at 200 MHz in TST-2. The LHW is the slow wave and is an electrostatic wave, which is characterized by the oscillation of the electrostatic potential ϕ_p. The electrostatic probe is used with an expectation to measure the temporal variation of ϕ_p associated with the LHW directly because the electrostatic probe can measure the electrostatic potential directly. The reason for using a high impedance resistor is to reduce the current drawn from the plasma to suppress the perturbation caused by the probe. Also, ϕ_p is linearly related to the floating potential V_f, which is measured by the electrostatic probe with high impedance. By measuring the phase difference between signals detected by such high-impedance-embedded electrostatic probes (high impedance Langmuir probes), the wavenumber of the LHW can be measured.

A probe assembly consisting of three high impedance Langmuir probes, a single magnetic loop, and a single plain electrostatic probe (plain Langmuir probe) is used to measure the LHW wavenumber at 200 MHz in RF start-up plasmas with the plasma current of up to 2 kA, electron density of $4 \times 10^{16}\,\mathrm{m^{-3}}$, and electron temperature of up to 50 eV in TST-2. The LHW is launched from the dielectric-loaded waveguide array antenna (grill antenna) and the wavenumber parallel to the toroidal magnetic field ($k_\parallel$) of the main lobe of the launched wave is $40\,\mathrm{m^{-1}}$.

The waves which can exist in the RF start-up plasma are limited to three types: the fast wave, the slow wave (LHW) and the electromagnetic wave. Based on the calibrated sensitivity of the probe assembly to the electromagnetic wave using a coaxial calibrator, the ratio of signal amplitudes measured by the high impedance Langmuir probes ($\sim 4\,\mathrm{mV}$) to that measured by the magnetic probe ($\sim 6\,\mathrm{mV}$)

cannot be explained by the fast wave nor the electromagnetic wave. Therefore, it can be concluded that the LHW makes the dominant contribution to the measured signal. It is also shown that the component of current at $200\,\mathrm{MHz}$ drawn from the high impedance Langmuir probe is estimated to be less than $0.64\,\mathrm{mA}$, at least by $40\,\%$ smaller than that drawn by the plain Langmuir probe of $1.1\,\mathrm{mA}$, signifying the effectiveness of using a high impedance resistor to measure the signal closer to the floating potential at $200\,\mathrm{MHz}$, and therefore closer to that originating from the LHW.

Measurements of the identical wave using different pairs of the high impedance Langmuir probes by rotating the probe assembly gave the same phase difference, confirming the validity of wavenumber measurement. The direction of the measured wavenumber was nearly along the toroidal direction and counter-clockwise viewed from the top, consistent with the direction of the main component of the $k_\parallel$ spectrum of the launched wave. Meanwhile the measured absolute value of the toroidal wavenumber was $k_\parallel = 19.6 \pm 11.0\,\mathrm{m}^{-1}$, smaller by a factor of two compared to the main wavenumber component of the wave launched by the grill antenna, $k_\parallel = 40\,\mathrm{m}^{-1}$. This difference cannot be explained by a spatially uniform cold plasma model with Maxwellian electron velocity distribution function, even with the inclusion of $k_\parallel$ upshift/downshift and the presence of two different wavenumbers.

A possible scenario to explain the measured toroidal wavenumber of $k_\parallel = 19.6 \pm 11.0\,\mathrm{m}^{-1}$ was given by a non-Maxwellian electron velocity distribution function with a larger population of fast electrons moving in the direction of the main lobe of the launched wave compared to the Maxwellian distribution, indicating that the contribution of fast electrons to wave damping is important. This scenario suggests that the main component of the launched wavenumber around $k_\parallel = 40\,\mathrm{m}^{-1}$ is absorbed by such fast electrons before reaching the probe assembly, and the wavenumber components not absorbed by the plasma reached the probe assembly, and were detected as $k_\parallel = 19.6 \pm 11.0\,\mathrm{m}^{-1}$. From the Landau damping condition, the measured value of $k_\parallel = 19.6 \pm 11.0\,\mathrm{m}^{-1}$ requires fast electrons with energies in the range $2.8\,\mathrm{keV}$ (for $k_\parallel = 40\,\mathrm{m}^{-1}$) to $11.2\,\mathrm{keV}$ (for $k_\parallel = 20\,\mathrm{m}^{-1}$) during the initial phase of RF start-up plasmas in TST-2.

Contents

List of Figures

5

List of Tables

Chapter 1

Introduction

1.1   Nuclear Fusion

Nuclear fusion is expected to be one of the main energy sources in the future. One of its advantages is the high energy conversion efficiency based on the equation derived by Albert Einstein,

$$E = mc^2, \tag{1.1}$$

where E, m, and c are energy, mass, and the speed of light, respectively. This equation indicates that the mass multiplied by the square of the speed of light is equivalent to the energy, and implies that the mass change of Δm can be converted to the energy of Δmc^2. This relationship is realized in reactions of atomic nuclei such as nuclear fission or nuclear fusion. The physical origin of this energy is the difference in nuclear binding energies depending on the atomic species as shown in Fig. 1.1. Since the binding energy is defined as the energy necessary for splitting nuclei into individual pieces, nuclei with higher binding energy per nucleon are in lower energy states. Therefore, energy is gained by fusion or fission of nuclei in the positive or negative gradient region of Fig. 1.1, and the amount of energy gained per change of mass number becomes larger as the absolute value of the gradient increases.

There are many kinds of fusion reactions. Some of them are listed below [2]:

$$\begin{align} D + T &\rightarrow \alpha + n + 17.6 \, \text{MeV}, \tag{1.2}\\ D + D &\rightarrow \text{He}^3 + n + 3.27 \, \text{MeV}, \tag{1.3}\\ D + D &\rightarrow T + p + 4.03 \, \text{MeV}, \tag{1.4}\\ D + \text{He}^3 &\rightarrow \alpha + p + 18.3 \, \text{MeV}, \tag{1.5} \end{align}$$
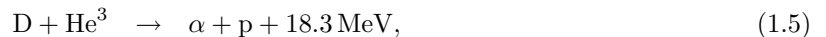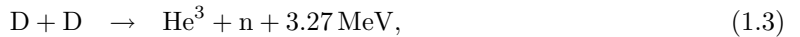
where symbols used in Eqs. (1.2)–(1.5) represent

$$\begin{align} \text{n} &: \quad \text{neutron, } {}_0\text{n}^1, \\ \text{p} &: \quad \text{hydrogen nucleus (proton), } {}_1\text{H}^1, \\ \text{D} &: \quad \text{deuterium nucleus (deuteron), } {}_1\text{H}^2, \\ \text{T} &: \quad \text{tritium nucleus (triton), } {}_1\text{H}^3, \\ \alpha &: \quad \text{helium nucleus (alpha), } {}_2\text{He}^4, \\ \text{He}^3 &: \quad \text{helium-3 nucleus, } {}_2\text{He}^3. \end{align}$$

The D-T fusion reaction Eq. (1.2) has the highest fusion cross section up to a deuteron energy of $300 \, \text{keV}$ as shown in Fig. 1.2 and is the prime candidate reaction for a fusion power plant. In the D-T reaction, deuterium (D) and tritium (T) fuse to produce energetic neutron and alpha particle (helium nucleus). The alpha particles heat the plasma to maintain the pressure necessary for further fusion
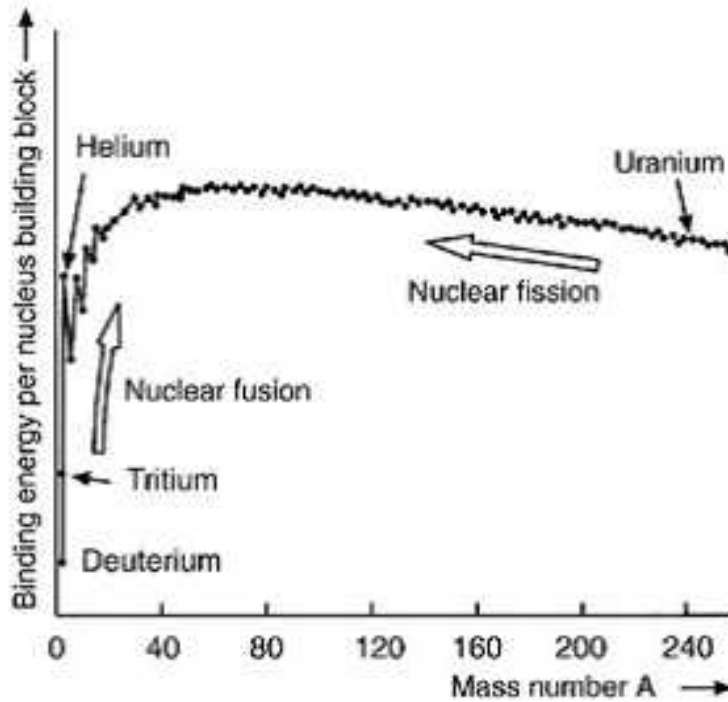
Figure 1.1: Binding energy per nucleon [1].

reactions. A criterion for a power producing thermonuclear reactor was considered by Lawson, and is known as the Lawson criterion [3]. Using this criterion, the condition for D-T reactions to continue without external power is known as the ignition condition [4]

$$nT\tau_{\mathrm{E}} > 3 \times 10^{21} \ \mathrm{m}^{-3} \, \mathrm{keV} \, \mathrm{s}, \qquad (1.6)$$

where n and T are the plasma density and temperature, and τ_{E} is the energy confinement time defined as the e-folding decay time of the plasma energy due to the heat conduction loss. A set of parameters satisfying this condition is, for example, $n = 2 \times 10^{20} \, \mathrm{m}^{-3}$, $T = 10 \, \mathrm{keV}$, and $\tau_{\mathrm{E}} = 3 \, \mathrm{s}$.

1.2 Plasma

At high temperatures necessary for nuclear fusion, virtually all atoms are ionized and they behave as an ionized gas. This state of matter is called the plasma, in which free ions and free electrons interact with each other through the electromagnetic force. In this section, two fundamental parameters for describing the plasma, temperature and density, are defined under near-equilibrium state using statistical mechanics, and then pressure is introduced. Also, characteristic quantities of the plasma such as plasma frequency, Debye length, Coulomb collision frequency, and plasma resistivity are described [5].

1.2.1 Temperature and Density

In a near-equilibrium state, in which the particles collide with each other more often than energy and particle replacement, it is reasonable to use equilibrium statistical mechanics to give a good approximation to the temperature. In statistical mechanics, based on the principle of equal a priori

11
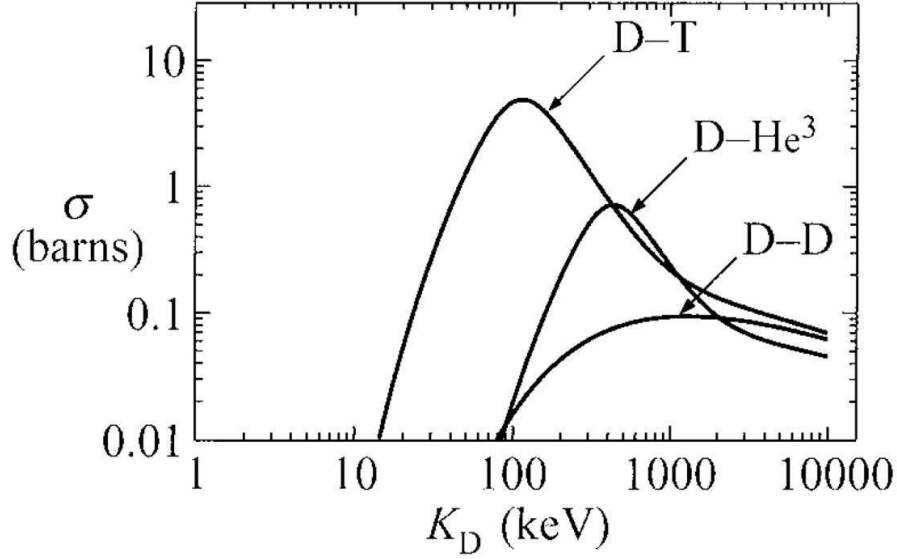
Figure 1.2: Experimentally measured cross sections for the D-T, D-He^3, and D-D fusion reactions. $1\,\text{barn} = 10^{-28}\,\text{m}^2$ and K_D represents a deuteron kinetic energy [2].

probabilities, one thinks of the number of microstates Ω of a system where a specific particle has an energy E in the plasma whose total energy is $E_\text{tot}\,(\gg E)$ including this single particle. Here, the plasma, with the specific single particle removed, is regarded as a thermal bath of energy $E_\text{tot} - E$ and the number of microstates Ω can be regarded as a function of the energy of the bath as

$$\Omega = \Omega(E_\text{tot} - E). \tag{1.7}$$

The entropy S is defined as

$$S \equiv k_\text{B}\ln\Omega, \tag{1.8}$$

where k_B is the Boltzmann constant. The temperature T is defined as

$$\frac{1}{T} \equiv \frac{dS}{dE}. \tag{1.9}$$

This is the definition of temperature for a plasma in a near-equilibrium state. However, this definition seems to be a formality. In order to connect this temperature to a familiar quantity in physics, it would be better to consider the kinetic energy of particles. Since the kinetic energy has a certain variance in a near-equilibrium state, one has to think of the probability of a particle having energy E. This is accomplished by considering the entropy S as follows.

$$
\begin{aligned}
S &= k_\text{B}\left[\ln\Omega\left(E_\text{tot} - E\right)\right] \\
&\simeq k_\text{B}\left[\ln\left\{\Omega\left(E_\text{tot}\right)\right\} + \frac{d\left\{\ln(\Omega)\right\}}{dE}(-E)\right] \\
&= k_\text{B}\ln\left\{\Omega\left(E_\text{tot}\right)\right\} - \frac{dS}{dE}E \\
&= k_\text{B}\ln\left\{\Omega\left(E_\text{tot}\right)\right\} - \frac{E}{T}. \tag{1.10}
\end{aligned}
$$

Dividing both sides by k_B gives

$$\ln\Omega\left(E_\text{tot} - E\right) \simeq \ln\left\{\Omega\left(E_\text{tot}\right)\right\} - \frac{E}{k_\text{B}T} \tag{1.11}$$

and exponentiation leads to

$$\Omega\left(E_{\mathrm{tot}} - E\right) \simeq \Omega\left(E_{\mathrm{tot}}\right) \cdot \exp\left(-\frac{E}{k_{\mathrm{B}}T}\right).\tag{1.12}$$

This equation shows that the relative probability of a particle to have the energy E is given by the factor

$$\exp\left(-\frac{E}{k_{\mathrm{B}}T}\right).\tag{1.13}$$

This factor is called the Boltzmann factor. If, for the time being, any potential associated with the position of the particle is ignored, the relative probability of a particle to have its velocity within the volume $dv_x dv_y dv_z$, whose center is (v_x, v_y, v_z) in the three-dimensional velocity space, is given by

$$\exp\left\{\frac{-m\left(v_x^2 + v_y^2 + v_z^2\right)}{2k_{\mathrm{B}}T}\right\} dv_x dv_y dv_z,$$

where m is the mass of the particle. In order to determine the absolute probability P, normalization

$$\int_{-\infty}^{\infty} \exp\left\{\frac{-m\left(v_x^2 + v_y^2 + v_z^2\right)}{2k_{\mathrm{B}}T}\right\} dv_x dv_y dv_z = 1$$

is needed, and P can be written

$$P = \frac{1}{\left(\sqrt{2\pi}v_{\mathrm{t}}\right)^3} \exp\left(-\frac{v^2}{2v_{\mathrm{t}}^2}\right),\tag{1.14}$$

where $v_{\mathrm{t}} \equiv \sqrt{\frac{k_{\mathrm{B}}T}{m}}$ is the thermal velocity. The reason why v_{t} is called the thermal velocity is described later. Although P is considered for a single particle in a near-equilibrium state, a number of particles exist in the real three-dimensional space. Thus, generally, the number density $f(x, y, z, v_x, v_y, v_z)$ of particles in the six-dimensional phase space is defined such that $f(x, y, z, v_x, v_y, v_z)$ represents the number of particles contained in the phase space volume $dx dy dz dv_x dv_y dv_z$. This f is called the distribution function. According to this definition, the three-dimensional integral of f over all velocities, $\boldsymbol{v} = (v_x, v_y, v_z)$, gives the number density of particles per unit volume in the real three-dimensional space. This number density is denoted by $n(x, y, z)$,

$$n = \int f dv_x dv_y dv_z.\tag{1.15}$$

In the equilibrium state, f is expressed using P as

$$f = nP = \frac{n}{\left(\sqrt{2\pi}v_{\mathrm{t}}\right)^3} \exp\left(-\frac{v^2}{2v_{\mathrm{t}}^2}\right).\tag{1.16}$$

This is called the Maxwell-Boltzmann distribution function. Now one can approach the familiar concept of temperature by calculating the average particle kinetic energy for Maxwellian distribution,

$$\left\langle \frac{1}{2}mv^2 \right\rangle_{\mathbf{v}} = \frac{\int \left(\frac{1}{2}mv^2\right) f d^3v}{\int f d^3v} = \frac{3}{2}k_{\mathrm{B}}T.\tag{1.17}$$

For the one dimensional case, for example in the z-direction,

$$\left\langle \frac{1}{2}mv_z^2 \right\rangle_{\mathbf{v}} = \frac{\int \left(\frac{1}{2}mv_z^2\right) f d^3v}{\int f d^3v} = \frac{1}{2}k_{\mathrm{B}}T.\tag{1.18}$$

These two equations indicate that the temperature represents the average particle kinetic energy and, for Maxwellian distribution, the average of any one dimensional component of velocity such as $|v_z|$ is $\sqrt{\frac{k_{\mathrm{B}}T}{m}}$. Thus the velocity

$$v_{\mathrm{t}} = \sqrt{\frac{k_{\mathrm{B}}T}{m}} \tag{1.19}$$

is called the thermal velocity.

1.2.2 Pressure

The pressure is important for considering the equilibrium force balance. In general, pressure is defined as the momentum flux and is viewed as a tensor quantity. The pressure tensor $\boldsymbol{P}$ is defined in index form as

$$
\begin{aligned}
P_{ij} &\equiv mn \left\langle (v_i - u_j)(v_j - u_i) \right\rangle \\
&= mn \left(< v_i v_j > - u_i u_j \right),
\end{aligned} \tag{1.20}
$$

where the definition of the mean velocity $\boldsymbol{u}$, namely $u_i = < v_i >$, is used. It can be confirmed that the velocity relative to the average velocity contributes to the pressure. For the special case of Maxwellian distribution, drifting at a given velocity $\boldsymbol{u}$ (i.e. $f(\boldsymbol{v} - \boldsymbol{u}) = $ Maxwellian), if this system is seen from the coordinate system moving at velocity $\boldsymbol{u}$,

$$P_{ii} = mn \left(\langle v_i^2 \rangle - 0 \right) = mn \frac{k_{\mathrm{B}}T}{m} = n k_{\mathrm{B}} T \tag{1.21}$$

and

$$P_{ij}(i \neq j) = 0 \tag{1.22}$$

are given. If the plasma is immersed in a magnetic field, the temperature depends on the direction and the pressure can be different in different directions. The off-diagonal component describes the viscosity.

1.2.3 Plasma Frequency

In equilibrium without any potential, the plasma is in a state of charge neutrality. If a perturbation is added to the plasma, electrons move much faster than ions because of the large mass ratio (for example, $\frac{m_{\mathrm{i}}}{m_{\mathrm{e}}} \simeq 1837$ where m_{i} and m_{e} are the masses of the proton and the electron, respectively). This breaks charge neutrality and induces an electric field, which introduces a restoring force and the plasma oscillates. To inspect this oscillation, the continuity equation Eq. (1.23) and the equation of motion for electrons Eq. (1.24) are used with three assumptions: the plasma is homogeneous, ions are stationary, and thermal motion can be ignored.

$$\frac{\partial n_{\mathrm{e}}}{\partial t} + \nabla \cdot (n_{\mathrm{e}} \boldsymbol{v_{\mathrm{e}}}) = 0, \tag{1.23}$$

$$m_{\mathrm{e}} \left(\frac{\partial \boldsymbol{v_{\mathrm{e}}}}{\partial t} + \boldsymbol{v_{\mathrm{e}}} \cdot \nabla \boldsymbol{v_{\mathrm{e}}} \right) = -e\boldsymbol{E}, \tag{1.24}$$

where e is the elementary charge, and n_{e} and $\boldsymbol{v_{\mathrm{e}}}$ are the density and the velocity of electrons, respectively. Here, the electric field $\boldsymbol{E}$ is caused by the perturbation. In order to differentiate the stationary component and the perturbed component, order separation is performed as

$$\boldsymbol{E} = \boldsymbol{E_0} + \boldsymbol{E_1} + \boldsymbol{E_2} + \cdots, \tag{1.25}$$

where $\boldsymbol{E_0}$ is the stationary component ($\boldsymbol{E_0} = \boldsymbol{0}$ in this case) and $\boldsymbol{E_1}$ is the first order perturbed component. Higher order components are considered as necessary. Similar order separation can be

performed on n_e and v_e. Assuming that the electron motion is one-dimensional and in the z direction, the continuity equation and the equation of motion reduce to, in first order,

$$\frac{\partial n_{e1}}{\partial t} + \frac{\partial}{\partial z}(n_{e0}v_{e1}) = 0, \tag{1.26}$$

$$m_e\left(\frac{\partial v_{e1}}{\partial t}\right) = -eE_1. \tag{1.27}$$

These two equations are combined to give Coulomb's law, which is, in first order,

$$\frac{\partial E_1}{\partial z} = -\frac{e}{\epsilon_0}n_{e1}, \tag{1.28}$$

where ϵ_0 is the vacuum permittivity. Assuming the first order quantities to vary as $\exp\left[i\left(k_z z - \omega t\right)\right]$ where k_z and ω are the wavenumber along the z direction and the angular frequency, respectively, partial derivatives can be regarded as $\frac{\partial}{\partial t} \mapsto -i\omega$ and $\frac{\partial}{\partial z} \mapsto ik_z$. Three equations above reduce to

$$\begin{cases} -i\omega n_{e1} + ik_z n_{e0}v_{e1} = 0 & (1.29) \\ -i\omega m_e v_{e1} = -eE_1 & (1.30) \\ ik_z E_1 = -\dfrac{e}{\epsilon_0}n_{e1}. & (1.31) \end{cases}$$

Eliminating n_{e1}, v_{e1}, and E_1, the angular frequency ω is given as

$$\omega^2 = \frac{n_{e0}e^2}{\epsilon_0 m_e} \equiv \omega_{pe}^2, \tag{1.32}$$

where ω_{pe} is called the electron plasma angular frequency. Angular frequencies are often simply called frequencies. For a particle of species s, the squared plasma frequency is

$$\omega_{ps}^2 = \frac{n_{s0}\left(Z_s e\right)^2}{\epsilon_0 m_s}, \tag{1.33}$$

where Z_s and m_s are the valence and the mass of the charged particle of species s, respectively. This plasma oscillation is longitudinal with the particle motion in the direction of the wavenumber vector.

1.2.4 Debye Shielding

If a charge exists in vacuum, its potential prevails in space. On the other hand, if a charge is placed in a plasma, other charged particles in the plasma move according to the potential of the charge placed in the plasma, and the potential is weakened or "neutralized". Thus the range that the potential of the charge extends is limited to the vicinity of the charge. This is a fundamental property of the plasma. To derive the distance over which the potential survives, we start from the Boltzmann factor. In this case, an electrostatic potential $\phi(x, y, z)$ is involved and the Boltzmann factor given in (1.13) becomes

$$\exp\left[-\frac{\left(\frac{1}{2}mv^2 + q\phi\right)}{k_B T}\right]. \tag{1.34}$$

Under a near-equilibrium state, since the distribution function f is proportional to the Boltzmann factor, the number density n in the three-dimensional real space is given after integration in three-dimensional velocity space as

$$n \propto \exp\left[-\frac{q\phi(x, y, z)}{k_B T}\right], \tag{1.35}$$

where q is a charge of a charged particle. The case of a planar charge in the y-z plane is considered so that the problem is in one-dimensional. For simplicity, the potential is defined to be zero at infinity,

and charge neutrality $n_\mathrm{e} = Z n_\mathrm{i} \equiv n_\mathrm{e\infty}$ holds where n_i is the ion density. Then, from Eq. (1.35), electron and ion densities are

$$
n_\mathrm{e}(x) \;=\; n_\mathrm{e\infty} \exp\left\{ \frac{e\,\phi(x)}{k_\mathrm{B}T_\mathrm{e}} \right\}, \tag{1.36}
$$

$$
Z n_\mathrm{i}(x) \;=\; n_\mathrm{e\infty} \exp\left\{ -\frac{eZ\,\phi(x)}{k_\mathrm{B}T_\mathrm{i}} \right\}, \tag{1.37}
$$

where T_e and T_i are electron and ion temperatures and they are different in general. Since these two equations stem from the assumption of equilibrium, one must be careful that T_e and T_i are spatially homogeneous, and electrons and ions are in thermal equilibrium separately, i.e., the electrons are in thermal equilibrium among themselves, and so are the ions. The thermal equilibrium between electrons and ions is not necessarily reached because the time for energy equilibration between electrons and ions is much longer than the time scale for energy equilibration among like particles (among electrons, or among ions) due to the large mass discrepancy between electrons and ions. The Poisson equation in one-dimensional planar geometry is

$$
\begin{aligned}
\epsilon_0 \frac{d^2\phi}{dx^2} \;&=\; e n_\mathrm{e\infty} \left[\exp\left\{ \frac{e\,\phi}{k_\mathrm{B}T_\mathrm{e}} \right\} - \exp\left\{ -\frac{eZ\,\phi}{k_\mathrm{B}T_\mathrm{i}} \right\} \right] \\
&\approx\; e n_\mathrm{e\infty} \left[\frac{e\,\phi}{k_\mathrm{B}T_\mathrm{e}} + \frac{eZ\,\phi}{k_\mathrm{B}T_\mathrm{i}} \right].
\end{aligned} \tag{1.38}
$$

In the second line, both $|e\phi| \ll k_\mathrm{B}T_\mathrm{e}$ and $|eZ\phi| \ll k_\mathrm{B}T_\mathrm{i}$ are assumed and Taylor expansion to the first order was performed. These two assumptions limit the validity of the second line to the range not very close to the planer charge. The second line becomes

$$
\frac{d^2\phi}{dx^2} \;\approx\; \frac{e^2 n_\mathrm{e\infty} \left(1 + \frac{Z T_\mathrm{e}}{T_\mathrm{i}} \right)}{\epsilon_0 k_\mathrm{B}T_\mathrm{e}} \phi, \tag{1.39}
$$

which leads to

$$
\phi \propto \exp\left(-\frac{x}{\lambda_D} \right), \tag{1.40}
$$

where

$$
\lambda_\mathrm{D} \equiv \sqrt{ \frac{\epsilon_0 k_\mathrm{B}T_\mathrm{e}}{n_\mathrm{e}e^2 \left(1 + \frac{Z T_\mathrm{e}}{T_\mathrm{i}} \right)} }. \tag{1.41}
$$

Here, the subscript of infinity is dropped from $n_\mathrm{e\infty}$. This λ_D is called the Debye length and represents the characteristic length of the potential decay in space. Note that the Debye length is independent of mass. Often the ion term is not included in the definition of the Debye length, giving

$$
\lambda_\mathrm{D} \equiv \sqrt{ \frac{\epsilon_0 k_\mathrm{B}T_\mathrm{e}}{n_\mathrm{e}e^2} }. \tag{1.42}
$$

Although the temperature has been considered in Kelvin (K) so far, it is more convenient to express the temperature in electron volt (eV), which is defined as the energy gained by an electron across the potential difference of $1\,\mathrm{V}$. By definition,

$$
1\,\mathrm{eV} \equiv e \cdot 1\,\mathrm{J} = 1.6 \times 10^{-19}\,\mathrm{J}, \tag{1.43}
$$

where J stands for Joule. If we denote T measured in eV as T_eV and that measured in K as T_K,

$$
e T_\mathrm{eV} = k_\mathrm{B} T_\mathrm{K} \tag{1.44}
$$

16

holds. From Eq. (1.44), $1\,\mathrm{eV}$ corresponds to

$$T_\mathrm{K} = \frac{e}{k_\mathrm{B}} \cdot 1 = \frac{1.60 \times 10^{-19}}{1.38 \times 10^{-23}} \simeq 11604\,\mathrm{K}. \tag{1.45}$$

Using Eqs. (1.42) and (1.44), the formula for the Debye length is expressed in T_e measured in eV as

$$\lambda_\mathrm{D} = \sqrt{\frac{\epsilon_0 e T_\mathrm{e}}{n_\mathrm{e} e^2}} = \sqrt{\frac{\epsilon_0 T_\mathrm{e}}{n_\mathrm{e} e}}. \tag{1.46}$$

For example, if T_e is $3\,\mathrm{eV}$ and n_e is $10^{16}\,\mathrm{m}^{-3}$, which are typical for the edge region of the initial plasma in fusion devices,

$$\lambda_\mathrm{D} = \sqrt{\frac{(8.85 \times 10^{-12}) \times 3}{10^{16} \times (1.6 \times 10^{-19})}} \simeq 1.3 \times 10^{-4}\,\mathrm{m}\ \ \mathrm{or}\ \ 130\,\mu\mathrm{m}. \tag{1.47}$$

From now on, the temperature T is considered in eV and the thermal energy $k_\mathrm{B}T$ J is simply denoted by T, dropping the Boltzmann constant k_B.

1.2.5 Coulomb Collisions and Plasma Resistivity

Collision Frequency

In a plasma, an electron loses its momentum by making repeated Coulomb collisions with ions. The average electron-ion collision frequency $< \nu_\mathrm{ei} >$ is given by [5]

$$< \nu_\mathrm{ei} > = \frac{2^{\frac{1}{2}} n_\mathrm{i} Z^2 e^4 \ln \Lambda}{12\pi^{\frac{3}{2}} \epsilon_0^2 m_\mathrm{e}^{\frac{1}{2}} T_\mathrm{e}^{\frac{3}{2}}}, \tag{1.48}$$

where n_i is the ion density and $\Lambda \sim \left(\frac{Z}{12\pi} n_\mathrm{e} \lambda_\mathrm{D}^3\right)$. In Eq. (1.48), the ion mass m_i is regarded as infinite and the average is taken over the electron velocity distribution. The average electron-electron and ion-ion collision frequencies $< \nu_\mathrm{ee} >$ and $< \nu_\mathrm{ii} >$ are estimated as

$$< \nu_\mathrm{ee} > \quad \approx \quad \frac{n_\mathrm{e} e^4 \ln \Lambda}{\epsilon_0^2 m_\mathrm{e}^{\frac{1}{2}} T_\mathrm{e}^{\frac{3}{2}}} \approx \frac{< \nu_\mathrm{ei} >}{n_\mathrm{i} Z^2 / n_\mathrm{e}}, \tag{1.49}$$

$$< \nu_\mathrm{ii} > \quad = \quad \frac{n_\mathrm{i} Z^4 e^4 \ln \Lambda}{12\pi^{\frac{3}{2}} \epsilon_0^2 m_\mathrm{i}^{\frac{1}{2}} T_\mathrm{i}^{\frac{3}{2}}}. \tag{1.50}$$

For $T_\mathrm{e} \sim T_\mathrm{i}$ and for low Z, the order of magnitude relationship among $< \nu_\mathrm{ei} >$, $< \nu_\mathrm{ee} >$, and $< \nu_\mathrm{ii} >$ is

$$< \nu_\mathrm{ei} > \quad \sim \quad < \nu_\mathrm{ee} > \quad \sim \quad \sqrt{\frac{m_\mathrm{i}}{m_\mathrm{e}}} < \nu_\mathrm{ii} > . \tag{1.51}$$

Equations (1.48)–(1.50) indicate that the collision frequencies become smaller at higher temperatures. This is an important characteristic of the plasma.

Plasma Resistivity

When an electric field $\boldsymbol{E}$ is applied to a plasma, ions are accelerated in the same direction as $\boldsymbol{E}$ and electrons are accelerated in the opposite direction to $\boldsymbol{E}$, generating an electric current in the plasma. This acceleration is impeded by electron-ion collisions. This is the origin of electric resistivity. In equilibrium, the plasma current density $\boldsymbol{j}$ is proportional to the applied electric field $\boldsymbol{E}$,

$$\boldsymbol{E} = \eta \boldsymbol{j}. \tag{1.52}$$

Equation (1.52) is the Ohm's law. The constant η is the resistivity and is related to the electron-ion collision frequency as [5]

$$\eta = \frac{m_{\mathrm{e}} < \nu_{\mathrm{ei}} >}{n_{\mathrm{e}} e^2}. \tag{1.53}$$

Using Eq. (1.48) and the condition of charge neutrality $n_{\mathrm{i}} Z = n_{\mathrm{e}}$ gives

$$\eta = \frac{2^{\frac{1}{2}} m_{\mathrm{e}}^{\frac{1}{2}} Z e^2 \ln \Lambda}{12 \pi^{\frac{3}{2}} \epsilon_0^2 T_{\mathrm{e}}^{\frac{3}{2}}}. \tag{1.54}$$

The resistivity η decreases as the electron temperature T_{e} increases.

1.3 Plasmas in a Magnetic Field

In fusion applications, the plasma temperature is no less than a few eV, or tens of thousands of K. At such temperatures, no material is useful as a "plasma container" since the plasma will be cooled down when plasma particles come into contact with a material surface. Fortunately, charged particles gyrate around magnetic field lines and thus a closed magnetic field configuration can be utilized as a "plasma container" . In this section, the basic plasma motion in the presence of a magnetic field is outlined.

1.3.1 Larmor Motion

When a plasma is immersed in a stationary magnetic field, charged particles gyrate around the magnetic field lines. This is called the Larmor motion and a center of the Larmor motion is called the guiding center.

If a particle with charge q and mass m moves at a velocity $\boldsymbol{v}$ in a stationary magnetic field $\boldsymbol{B}$, the Lorentz force $\boldsymbol{v} \times \boldsymbol{B}$ acts on the particle. Taking $\boldsymbol{B}$ in the z direction of the Cartesian coordinate system so that

$$\boldsymbol{B} = \begin{pmatrix} 0 \\ 0 \\ B \end{pmatrix}, \tag{1.55}$$

the equation of motion is expressed as

$$\begin{cases} \dfrac{dv_x}{dt} = \dfrac{qB}{m} v_y & \text{(1.56)} \\[2mm] \dfrac{dv_y}{dt} = -\dfrac{qB}{m} v_x & \text{(1.57)} \\[2mm] \dfrac{dv_z}{dt} = 0. & \text{(1.58)} \end{cases}$$

From Eq. (1.58), the motion in the z direction is a uniform motion with constant velocity. From Eqs. (1.56) and (1.57),

$$\frac{d^2 v_x}{dt^2} = -\left(\frac{qB}{m}\right)^2 v_x \tag{1.59}$$

follows. The solution for v_x is given as

$$v_x = v_\perp \exp(-i\Omega t), \tag{1.60}$$

where

$$\Omega = \frac{qB}{m} \tag{1.61}$$

is the cyclotron angular frequency, or simply the cyclotron frequency. Note that the cyclotron frequency changes its sign according to the signs of q and B. Of course the measured value of v_x in real space is given by the real part of Eq. (1.60). Substituting Eq. (1.60) into Eq. (1.56), v_y is given as

$$v_y = iv_\perp \exp(-i\Omega t) = iv_x. \tag{1.62}$$

Since the difference between v_x and v_y is only the factor i, they are simply out of phase by 90° and the amplitudes are equal. Therefore, the particle executes a circular motion at the speed $v_\perp$ in the x-y plane, perpendicular to B. This is why the perpendicular velocity is expressed in terms of $v_\perp$. Looking in the direction of the magnetic field (positive z direction), a particle with positive or negative charge rotates about the magnetic field counter clockwise or clockwise, respectively. In an equilibrium state and in the absence of a potential, $v_\perp$ is determined by the perpendicular temperature $T_\perp$ as

$$\frac{1}{2}mv_\perp^2 = 2 \times \frac{T_\perp}{2} = T_\perp, \tag{1.63}$$

giving

$$v_\perp = \sqrt{\frac{2\,T_\perp}{m}}, \tag{1.64}$$

where the factor 2 in the middle of Eq. (1.63) represents the two degrees of freedom, x and y directions. Using this $v_\perp$ and the cyclotron frequency Ω, the radius of the Larmor motion r_L becomes

$$r_\mathrm{L} = \frac{v_\perp}{\Omega} = \frac{\sqrt{2mT_\perp}}{qB}. \tag{1.65}$$

If $T_{e\perp} = T_{i\perp}$, the ratio of the Larmor radii is

$$\frac{r_{\mathrm{Li}}}{r_{\mathrm{Le}}} = \sqrt{\frac{m_\mathrm{i}}{m_\mathrm{e}}} \approx \sqrt{1873} \simeq 43. \tag{1.66}$$

For a hydrogen plasma with $B = 0.1$ T and $T_{e\perp} = T_{i\perp} = 3$ eV,

$$r_{\mathrm{Le}} = \frac{\sqrt{2 \times (9.11 \times 10^{-31}) \times \{(1.6 \times 10^{-19}) \times 3\}}}{(1.6 \times 10^{-19}) \times 0.1} \simeq 58\,\mu\mathrm{m}, \tag{1.67}$$

$$r_{\mathrm{Li}} = \frac{\sqrt{2 \times (1.67 \times 10^{-27}) \times \{(1.6 \times 10^{-19}) \times 3\}}}{(1.6 \times 10^{-19}) \times 0.1} \simeq 2.5\,\mathrm{mm}. \tag{1.68}$$

In a collisionless plasma in a homogeneous magnetic field and with no potential, the guiding center keeps moving along the magnetic field line at a constant velocity.

1.3.2 Guiding Center Drift

If a stationary electric field also exists, or if the magnetic field has a gradient in its strength or a curvature, the guiding center (center of the Larmor motion) gradually drifts away from the magnetic field line in a direction perpendicular to the magnetic field. The three drift motions are described below [5].

$E \times B$ Drift

In the presence of a uniform electric field in addition to a uniform magnetic field, the guiding center drifts across the magnetic field with velocity

$$\boldsymbol{v}_\mathrm{E} = \frac{\boldsymbol{E} \times \boldsymbol{B}}{B^2}, \tag{1.69}$$

which is called the $\boldsymbol{E} \times \boldsymbol{B}$ drift. From Eq. (1.69), it is found that the perpendicular component of the electric field ($E_\perp$) to $\boldsymbol{B}$ contributes to the $\boldsymbol{E} \times \boldsymbol{B}$ drift and that neither a charge nor a mass of particles are relevant to it.

∇*B* Drift

If the magnetic field is inhomogeneous, other drift motions of the guiding center occur. These drift motions are considered for the case in which the Larmor radius is much smaller than the typical scale length of magnetic field variation,

$$\frac{r_{\mathrm{L}}}{\left(\frac{B}{|\nabla B|}\right)} \ll 1. \tag{1.70}$$

If the variation of B is of the form $\exp(ikx)$ or $\exp(kx)$, Eq. (1.70) yields

$$kr_{\mathrm{L}} \ll 1, \tag{1.71}$$

where kr_{L} is a small expansion parameter. A physical quantity P can then be expanded as

$$P = P_0 + P_1 + P_2 + \cdots, \tag{1.72}$$

where

$$P_i \propto (kr_{\mathrm{L}})^i. \tag{1.73}$$

Expressing $\boldsymbol{B}$ and $\boldsymbol{v}$ in the form of Eq. (1.72) and substituting them into the equation of motion, the drift velocity in the presence of a magnetic field gradient is obtained by equating each order of $(kr_{\mathrm{L}})^i$ as

$$\boldsymbol{v}_{\mathrm{grad}} = \frac{W_\perp}{q} \frac{\boldsymbol{B} \times \nabla B}{B^3}, \tag{1.74}$$

where

$$W_\perp = \frac{1}{2}mv_\perp^2 \tag{1.75}$$

is the component of kinetic energy perpendicular to the magnetic field. This drift is called the gradient B drift.

Curvature Drift

The drift velocity in the presence of a magnetic field curvature is derived based on the same asymptotic expansion. For the vacuum field (magnetic field with very low plasma pressure and current), $\nabla \times \boldsymbol{B} = \boldsymbol{0}$ is approximately satisfied. The curvature drift is given as

$$\boldsymbol{v}_{\mathrm{curv}} = \frac{2W_\parallel}{q} \frac{\boldsymbol{B} \times \nabla B}{B^3}, \tag{1.76}$$

where

$$W_\parallel = \frac{1}{2}mv_\parallel^2 \tag{1.77}$$

is the component of kinetic energy parallel to the magnetic field.

1.4   Magnetic Confinement of Plasmas

In order to realize the fusion reaction, one of the promising methods is to confine the plasma in a closed magnetic field configuration, taking advantage of the Larmor motion of charged particles. In this section, the leading candidate for a magnetic fusion power plant, called the tokamak, and its derivative, the spherical tokamak, are described.
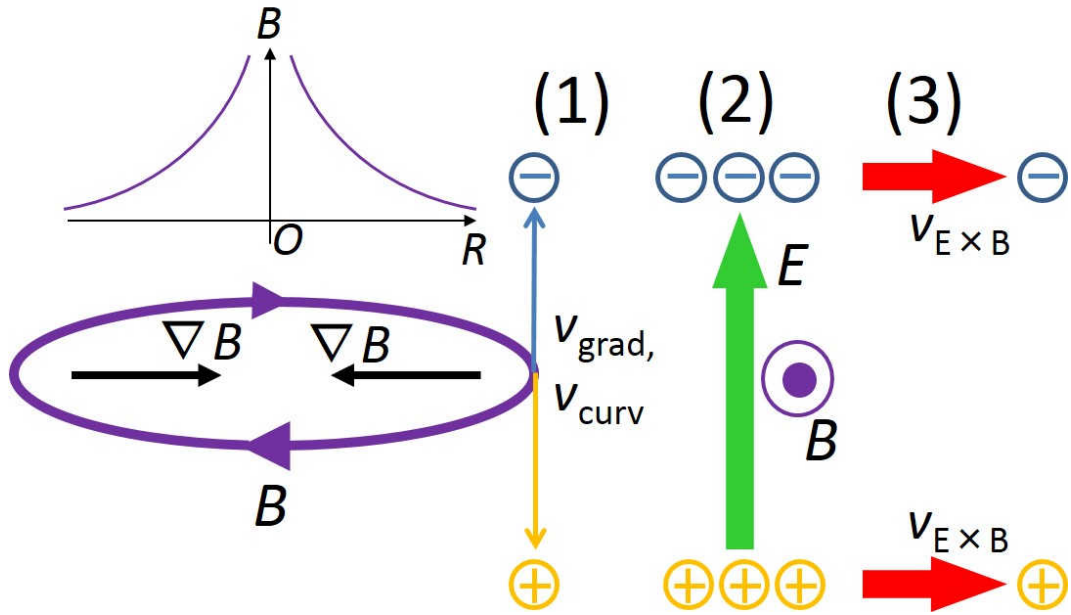
Figure 1.3: Plasma loss when only the toroidal field is present. (1) A charge separation occurs due to the ∇B drift and the curvature drift. (2) An electric field that points upward is induced. (3) Plasma is lost via the outward $\boldsymbol{E} \times \boldsymbol{B}$ drift.

1.4.1 Tokamak

A closed magnetic field configuration in the form of a torus can confine the plasma effectively. The tokamak is an axisymmetric configuration with a large toroidal field and a significant poloidal field generated by the DC toroidal current [2]. The reason why not only the toroidal field but also the DC toroidal current are required for confining the plasma is explained below. An international collaboration project, the ITER project, is also introduced.

Necessity of the Plasma Current for Confining the Plasma

The plasma cannot be confined by the toroidal field alone. This is explained in Fig. 1.3. The toroidal field has both spatial gradient and curvature because it is formed by a current flowing along the symmetry axis of the torus. The toroidal field is inversely proportional to the distance from the symmetry axis (i.e., the major radius) of the torus. Therefore, ∇B is towards the symmetry axis. If the field is as shown in Fig. 1.3, the plasma would be lost by processes (1)–(3) shown in Fig. 1.3: (1) Ions and electrons drift downward and upward, respectively, due to the ∇B drift and the curvature drift according to Eqs. (1.74) and (1.76), causing charge separation. (2) A vertical electric field pointing upward is formed. (3) The plasma would then be lost quickly by the outward $\boldsymbol{E} \times \boldsymbol{B}$ drift according to Eq. (1.69).

To prevent the plasma from being lost, the charge separation must be prevented. This can be achieved by adding another magnetic field that encircles the plasma poloidally to create a helically twisted magnetic field configuration. The helical magnetic field can prevent charge accumulation by connecting the top and the bottom of the torus by magnetic field lines. This additional magnetic field is called the "poloidal field" and is generated by the "plasma current" flowing in the toroidal direction. Since the plasma current is a ring current, a force to expand the toroidal loop is generated. A vertical field must be applied to generate an inward force to balance this expansion force.
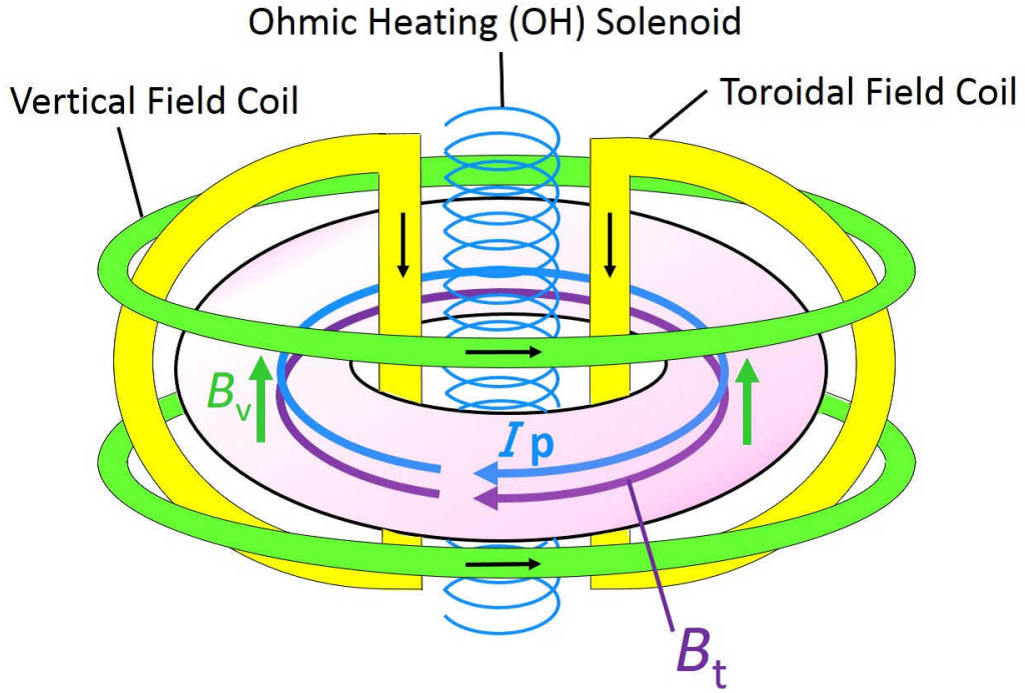
Figure 1.4: Concept of the conventional tokamak.

Tokamak Configuration

There are three fundamental constituent elements for the tokamak: The toroidal field B_{t}, the plasma current I_{p}, and the vertical field B_{v}. Figure 1.4 shows these elements for generating them in conventional tokamaks. The toroidal field B_{t} is produced by the toroidal field coils (yellow). Although only two toroidal field coils are shown in Fig. 1.4, in practice more toroidal field coils are used to ensure axisymmetry of B_{t}. The plasma current I_{p} is induced by temporally varying the current flowing in the Ohmic Heating (OH) solenoid (light blue). The vertical field B_{v} is created by the vertical field coil (light green).

Toroidal Coordinate System

Figure 1.5 shows the coordinate system used for tokamaks. R_0 and a are called the major radius and the minor radius of the torus, respectively, while r is the distance from the center of the plasma cross section. θ is called the poloidal angle. The direction of increase/decrease of θ is called the poloidal direction. Three quantities are defined: the aspect ratio A, the plasma elongation κ, and the safety factor q, which are all relevant for stability of the tokamak plasma. The aspect ratio A is defined as the ratio of the major radius R_0 to the minor radius a of the torus,

$$A = \frac{R_0}{a}. \tag{1.78}$$

The elongation κ is defined as

$$\kappa = \frac{b}{a}. \tag{1.79}$$
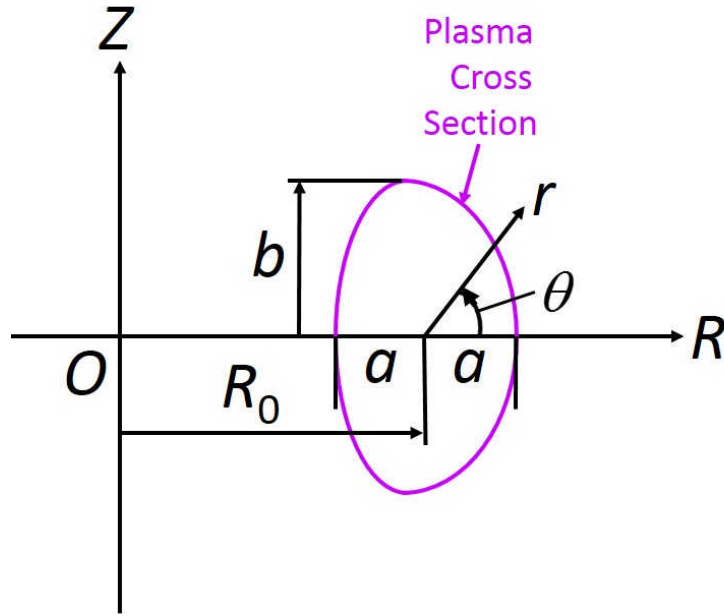
Figure 1.5: Toroidal coordinate system.

The plasma cross section shown in Fig. 1.5 is called the poloidal cross section. Since the magnetic field line draws a helix whose axis is along the toroidal direction, during one rotation of the field line in the poloidal direction, a field line passes through the same poloidal cross section a certain times. The safety factor q is defined as this number, i.e., the number of times a field line passes through the same poloidal cross section in the toroidal direction while it rotates once in the poloidal direction. For example, using the poloidal magnetic field B_p, the safety factor q is given for a circular poloidal cross section tokamak as [2]

$$q(r) = \frac{r B_t(r)}{R_0 B_p(r)} \frac{1}{\sqrt{1 - r^2/R_0^2}}. \tag{1.80}$$

These three quantities, A, κ, and q are used in Subsection 1.4.2.

ITER

Presently, the tokamak is the leading candidate for a fusion reactor and the ITER (International Thermonuclear Experimental Reactor) project is under progress as an international collaboration among the United States of America, China, European Union, India, Korea, Japan, and Russia. The principal aim of the ITER project is to investigate the state of nuclear fusion burning and to achieve the physics gain factor Q of greater than 10 [6], where Q is defined as [2]

$$\begin{aligned} Q &\equiv \frac{\text{net thermal power out}}{\text{heating power in}} \\ &= \frac{\text{total thermal power out} - \text{heating power in}}{\text{heating power in}}. \end{aligned} \tag{1.81}$$

The total fusion power is expected to be $500\,\text{MW}$. The toroidal field and the plasma current are $5.3\,\text{T}$ and $15\,\text{MA}$, respectively, and the major and minor radii are $6.2\,\text{m}$ and $2.0\,\text{m}$, respectively [6]. Figure 1.6 shows a cutaway view of ITER [7]. ITER is being constructed in south France. The construction work
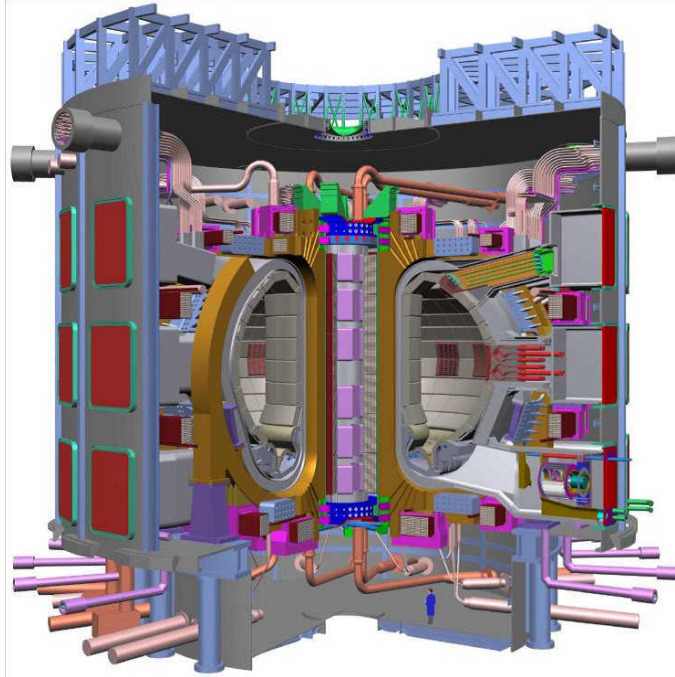
Figure 1.6: ITER [7].

on ITER began in 2010. The first plasma in ITER is scheduled to be obtained in 2020, and deuterium-tritium operation is scheduled to start in 2027 [8]. The cost for building ITER is estimated to be 2755 kIUA. "IUA" is defined as 1 IUA = $1000 (Jan. 1989 value) [7].

One of the great contributions which lead to the initiation of the ITER project was the discovery of an improved confinement mode, called the high confinement mode, or H-mode, in the ASDEX tokamak in 1982 [9]. In H-mode, the energy confinement time τ_{E} becomes larger than that in the usual low confinement mode, or L-mode by a factor of about 2 [10]. The H-mode was observed in plasmas heated by Neutral Beam Injection (NBI), in which high energy neutral atoms are injected into the plasma, ionized by collisions within the plasma, and heat the plasma [11]. With the help of the H-mode, plasma with $Q_{\mathrm{equiv}} \simeq 1$ was studied extensively in large tokamak devices such as TFTR [12], JET [13], and JT-60U [14]. Q_{equiv} is the expected Q if the fuel ions were replaced by a 50%-50% mix of deuterium and tritium. The knowledge obtained through these experiments will be utilized in the ITER project. The JT-60SA tokamak is being constructed in Japan under collaboration with EU to replace JT-60U [15,16]. JT-60SA serves as a "satellite" tokamak of ITER to both support and complement ITER.

1.4.2 Spherical Tokamak

The spherical tokamak (ST) is a small aspect ratio tokamak, with typically $A < 2$. The concept of ST was introduced in 1986 [17]. Figure 1.7 shows the magnetic configuration of the spherical tokamak (sometimes called the spherical torus). As can be seen in Fig. 1.7, the ST plasma extends closer to the symmetry axis of the torus device compared to the conventional tokamak plasma, leading to the potential advantage of being compact. The major advantage of the ST is its superior stability at high plasma β. The plasma β is defined as the ratio of the plasma pressure p to the magnetic field pressure
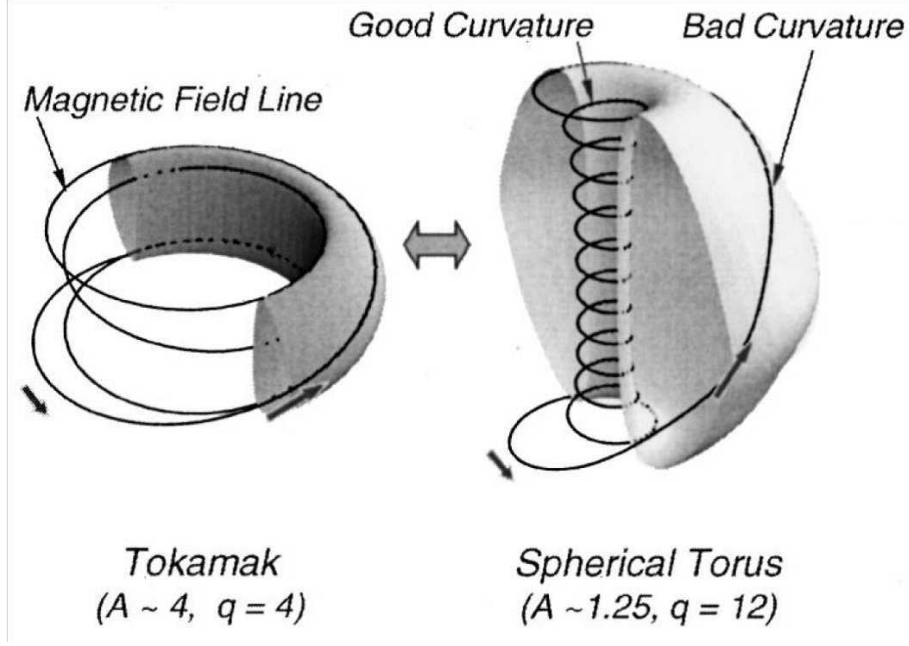
Figure 1.7: Comparison of the conventional tokamak and the spherical tokamak (torus) [18].

$\frac{B^2}{2\mu_0}$,

$$\beta \equiv \frac{p}{B^2/2\mu_0}. \tag{1.82}$$

In high β plasmas, the same plasma pressure (and therefore, fusion power density) can be achieved at a lower confining magnetic field. The volume average β, $\langle\beta\rangle_{\mathrm{v}}$, represents β of the configuration and is denoted by

$$\langle\beta\rangle_{\mathrm{v}} = \frac{\langle p\rangle_{\mathrm{v}}}{\langle B^2\rangle_{\mathrm{v}}/2\mu_0}. \tag{1.83}$$

The toroidal beta

$$\beta_{\mathrm{t}} = \frac{\langle p\rangle_{\mathrm{v}}}{B_{\mathrm{t0}}^2/2\mu_0}, \tag{1.84}$$

is often used in practice where B_{t0} is the toroidal magnetic field at R_0. The stability analysis of tokamak plasmas was pioneered by Sykes [19] and Troyon [20]. Based on their work, the relationship between the maximum attainable β, and the aspect ratio A is approximately given in terms of β_{t} without introducing much error as [18]

$$\langle\beta\rangle_{\mathrm{v, \ max}} \simeq \beta_{\mathrm{t,max}} \approx \beta_{\mathrm{N}} \frac{I_{\mathrm{p}}}{aB_{\mathrm{t0}}} \approx \frac{5\beta_{\mathrm{N}}\kappa}{Aq(a)}, \tag{1.85}$$

where β_{N} is a numerically determined coefficient. Equation (1.85) states that $\langle\beta\rangle_{\mathrm{v, \ max}}$ is approximately inversely proportional to A, signifying the advantage of ST to use the magnetic field more effectively to confine the plasma. This is confirmed experimentally as shown in Fig. 1.8. The attainable β_{t} in ST is nearly 40 %, larger than the highest value achieved in conventional tokamaks of about 13 % by a factor of three.

Therefore, the ST has at least two advantages:

- Plasma position is closer to the symmetry axis of the device compared to conventional tokamaks, leading to the possibility of being compact.

25
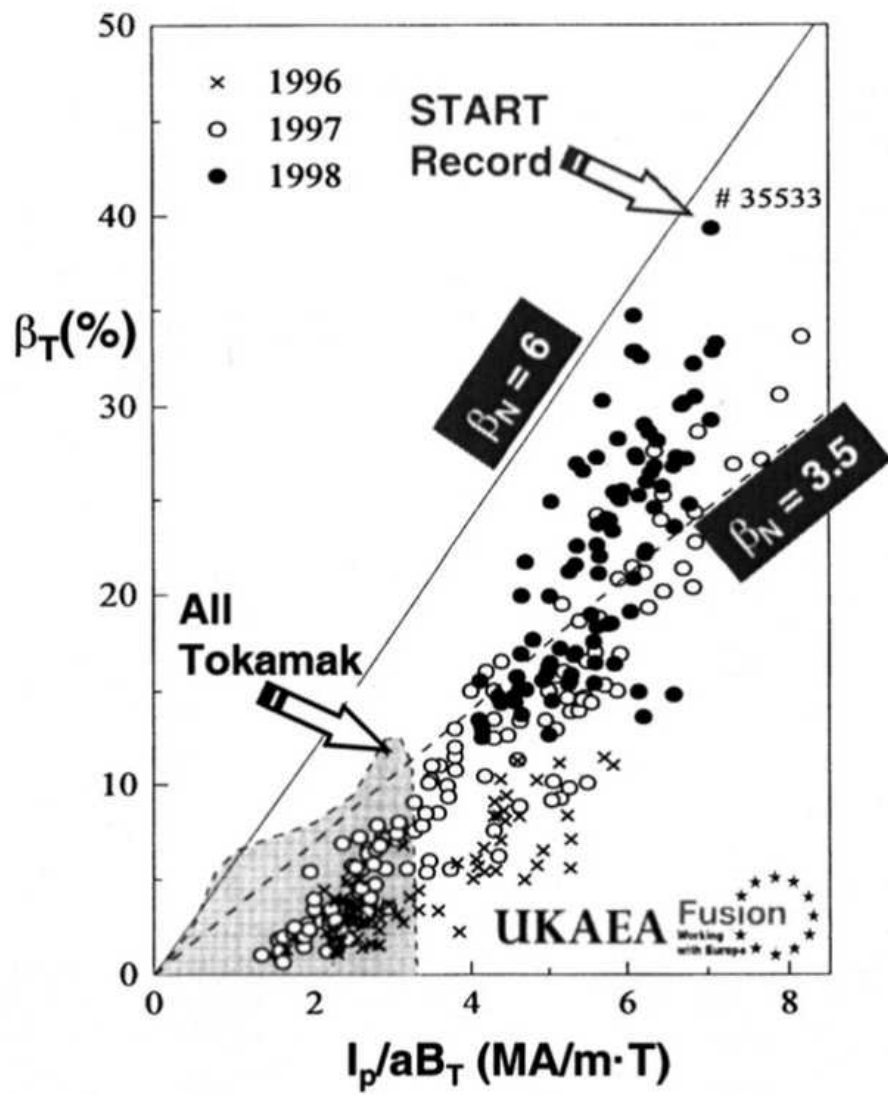
Figure 1.8: Toroidal beta β_t achieved in START during 1996–1998 as a function of I_p/aB_{t0} [18]. β_T and B_T are identical to β_t and B_{t0} used in this thesis.

- The maximum attainable volume average β is larger than that in conventional tokamaks, meaning the required plasma pressure can be achieved with smaller toroidal field, offering the possibility of potentially simpler and less massive magnet structure.

Since ultimately nuclear fusion energy should be produced economically, these features of the spherical tokamak are attractive and desirable.

1.5 Non-Inductive Plasma Current Drive Using the Lower Hybrid Wave

1.5.1 Necessity of Eliminating the OH Solenoid

Since the ST plasma extends close to the symmetry axis of the torus, it is difficult to provide enough space for components such as the OH solenoid, shown in Fig. 1.4. It is desirable to eliminate or at least reduce the size of the OH solenoid [21, 22]. Although the OH solenoid has been used to drive the plasma current, which is indispensable for the tokamaks, in virtually all tokamaks so far, there are two fatal disadvantages:

- Since the OH solenoid drives the plasma current by electromagnetic induction and requires the solenoid current to keep changing in one direction, it cannot be used for steady state current drive.

- At high plasma temperature, resistive heating of the plasma by the inductively driven current decreases rapidly because the plasma resistivity, shown in Eq. (1.54), is inversely proportional to $T_\mathrm{e}^{\frac{3}{2}}$, though this is not directly relevant to the ability to drive the plasma current.

For these reasons, the development of a method to drive the plasma current non-inductively (in steady state) without the use of the OH solenoid is highly desired.

1.5.2 Current Drive Efficiencies

Various method of non-inductive current drive have been studied, momentum transfer from waves or injected particles. The current drive efficiencies using various waves and particle injection are summarized in Fig. 1.9 [23]. The abscissa is U_0, which is the wave phase velocity $\omega/k_\parallel$ or the particle velocity v_0, normalized by the electron velocity v_e. The reason for comparing with the electron velocity is that the electrons are much more effective in contributing to the plasma current because the electron mass is much smaller than the ion mass. The ordinate is J/P, referred to as the normalized efficiency factor, where J is the current density and P is the power density required to maintain the current.

It can be seen from Fig. 1.9 that the current drive efficiency is high for $U_0 < 10^{-1}$ or $4 < U_0$. In these regions, among the various waves, the lower hybrid wave (LHW) has the second largest current drive efficiency. The compressional Alfvén wave and the fast magnetosonic wave have slightly higher efficiencies, but are less well developed. Therefore, the LHW is commonly used to drive the plasma current.

1.5.3 Non-Inductive Current Drive Experiments Using the LHW

The possibility of using the LHW to drive the plasma current in steady state was pointed out by Fisch [24–26]. The LHW has been used for plasma current sustainment and/or ramp-up in conventional tokamaks. During the last decade, current drive experiments using the LHW are also conducted in ST devices.
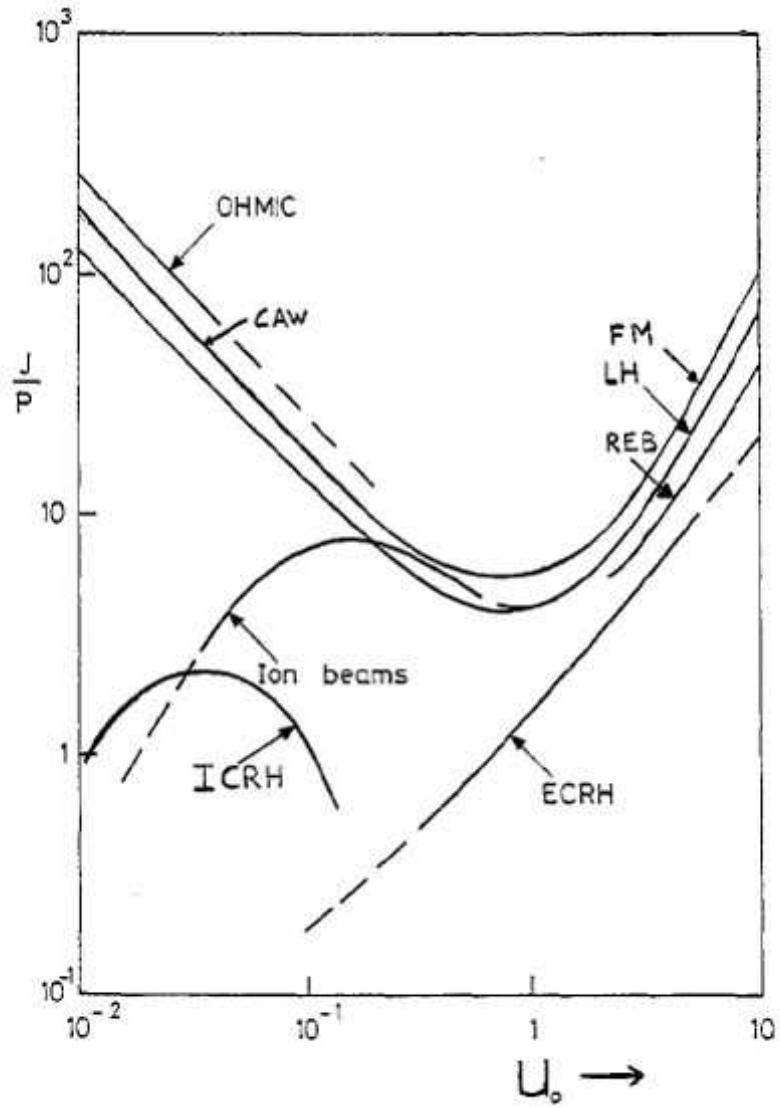
Figure 1.9: Normalized efficiency factor versus $U_0 = \omega / \left(k_\parallel v_e\right)$ for waves or v_0/v_e for particle injection at velocity v_0 [23]. The abbreviations are. OHMIC: OH solenoid, CAW: Compressional Alfvén Wave, REB: Relativistic Electron Beam, LH: Lower Hybrid Wave, FM: Fast Magnetosonic Wave, ECRH: Electron Cyclotron Resonance Heating, ICRH: Ion Clotron Minority Heating.

Plasma Current Sustainment by LHW in PLT

In one of the early successful experiments the plasma current was sustained by the LHW in the Princeton Large Torus (PLT, $R = 1.32\,\text{m}$, $a = 0.4\,\text{m}$, $B_t = 3\,\text{T}$) [27, 28] in 1982. Figure 1.10 shows a schematic diagram of PLT and the lower hybrid apparatus. The LHW with an RF power of up to $500\,\text{kW}$ at $800\,\text{MHz}$ was excited in the plasma by means of a radiating antenna consisting of a six-element waveguide array, called the grill antenna. Figure 1.11 shows the behaviors of the plasma current in deuterium discharges in PLT with and without (solid and dashed lines) RF power. The plasma current was maintained at $240\,\text{kA}$ for 1 second with $130\,\text{kW}$ of RF power. The phase difference between adjacent waveguides of the grill antenna was set to $90°$ and the toroidal field was $3.1\,\text{T}$. With the same setting for the phase difference, a plasma current of $165\,\text{kA}$ was sustained for ~ 3.5 second with up to $70\,\text{kW}$ of RF power at the toroidal field of $2.3\,\text{T}$. This experiment demonstrated the capability of the LHW to sustain the plasma current.

Plasma Current Ramp-Up by LHW in JT-60U

In order to eliminate the OH solenoid, plasma current ramp-up to high enough level to confine energetic ions must be demonstrated without the use of the OH solenoid. An experiment to demonstrate such an operation was performed in the JT-60U tokamak in 2002 [29–31]. Figure 1.12 shows the coil system of JT-60U. A successful ramp-up scenario was demonstrated as shown in Fig. 1.13.

The discharge number E041711 consists of three phases, described at the top of Fig. 1.13: (1) Initial plasma current formation by using induction from the triangularity control coil current (I_{VT}). (2) Non-inductive I_p ramp-up using the LHW ($2\,\text{GHz}$) with the electron cyclotron wave (ECW) ($110\,\text{GHz}$). (3) Transition to the advanced tokamak phase [32, 33] using neutral beam injection (NBI).

The advanced tokamak is a concept to improve the tokamak toward steady-state operation. In the advanced tokamak, the plasma current is maintained mainly by the self-generated bootstrap current [34]. The advanced tokamak phase is initiated by NBI, which needs sufficient plasma current and density to ionize the neutral beam and confine these energetic ions. The plasma confinement improves as the plasma current increases because the higher poloidal magnetic field reduces the deviation of ion orbits from the flux surface (determined by the poloidal Larmor radius), as shown in Eq. (1.65). Since the smaller poloidal Larmor radius reduces plasma transport across the magnetic field [5], higher plasma current provides improved plasma confinement.

The significance of this experiment is in the demonstration of an integrated scenario from the initial plasma to a state with high enough plasma current for NBI, which is required for a successful transition to the advanced tokamak phase without the use of the OH solenoid (see the zero value of I_F shown by the blue dashed line in Fig. 1.13). Note that I_{VR} and I_{VT} also increase as I_p increases to keep the plasma in equilibrium (radial position and shape) and contributes to plasma current ramp-up, their contribution is about $20\,\%$ in terms of the poloidal magnetic flux, and therefore the current is dominantly driven by the LHW, assisted by the ECW (same as ECRH in Fig. 1.9). The role of ECW in this experiment is not to contribute to current drive, but to keep the electron temperature high. This successful result gives a great encouragement to the ST fusion reactor for which the elimination of the OH solenoid is a necessity [31].

Plasma Current Ramp-Up by LHW in Spherical Tokamaks

In order to demonstrate ST operation without the use of the OH solenoid, non-inductive current drive experiments using the LHW are being conducted on ST devices. In the Tokyo Spherical Tokamak-2 (TST-2) device, non-inductive current drive experiments using waves at a frequency of $200\,\text{MHz}$ (LHW frequency range) have been conducted using an inductively-coupled combline antenna [35] and a dielectric-loaded waveguide array (grill) antenna [36]. Detailed information on TST-2 is given in Chapter 4.

Figure 1.14 shows typical discharge waveforms of a plasma driven non-inductively by waves in the LHW frequency range using the inductively-coupled combline antenna, which was used on the JFT-2M
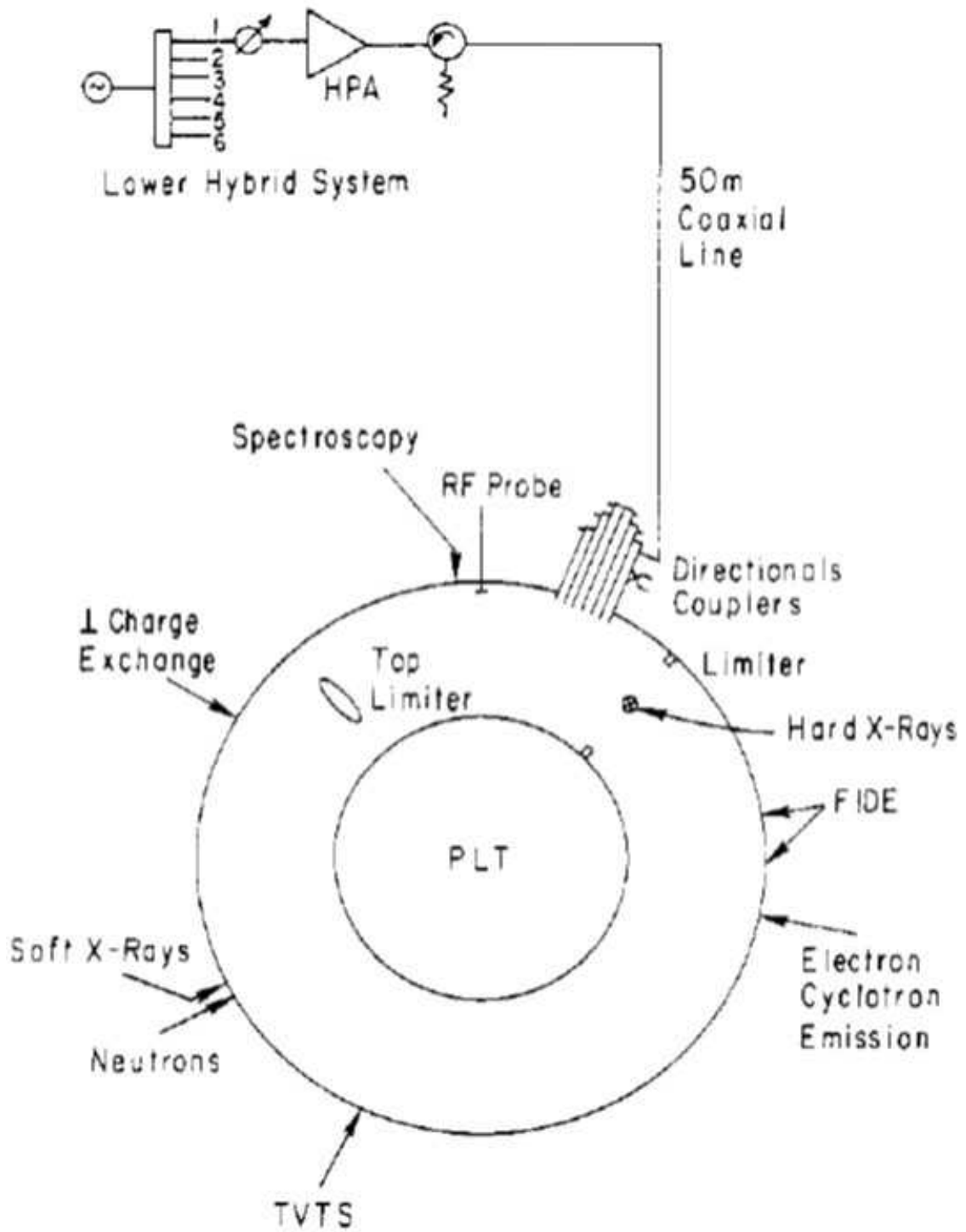
Figure 1.10: Schematic diagram of PLT, RF system, and locations of various diagnostics [28].
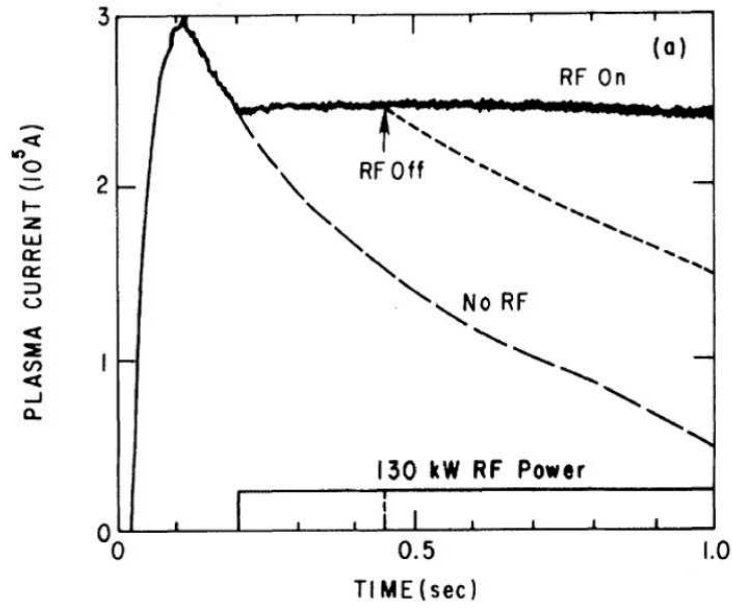
Figure 1.11: Waveforms of the plasma current in PLT with and without (solid and dashed lines) RF power [27].
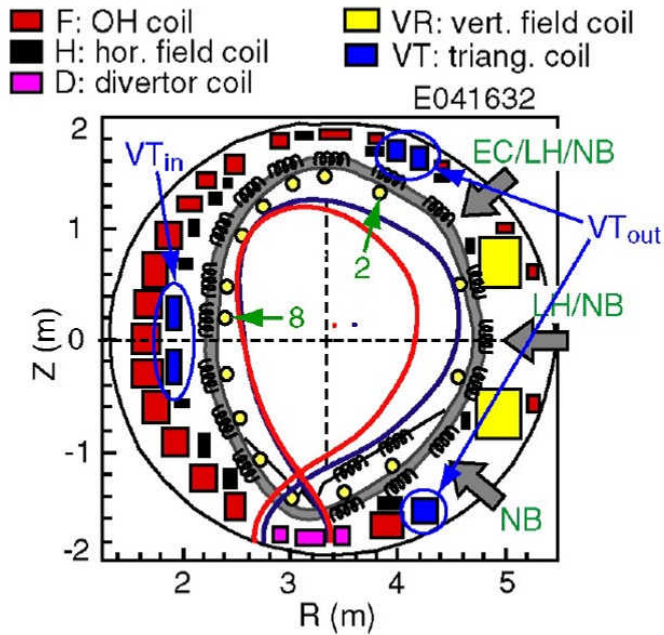
Figure 1.12: JT-60U coil configuration and typical equilibria for the lower hybrid current drive phase (blue) and the neutral beam heating phase (red). The OH solenoid (F coil) was not used in this experiment. Locations of flux loops and poloidal field pick-up coils are also shown [29].
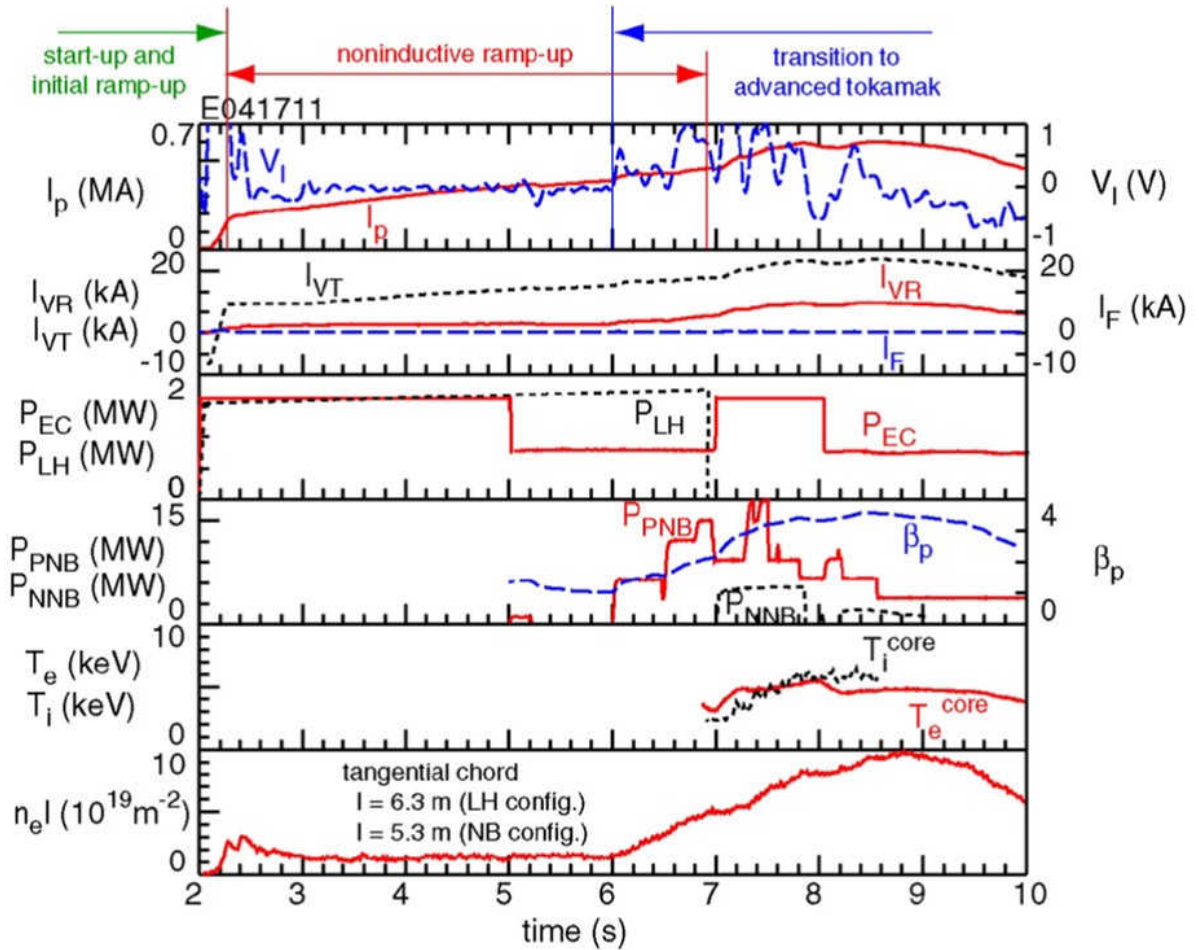
Figure 1.13: Integrated scenario from plasma start-up to the achievement of an advanced tokamak plasma without the use of the OH solenoid [29]. I_{p}: plasma current, I_{VT}: triangularity control coil current, I_{F}: OH solenoid current, P_{LH}: LHW power, P_{PNB} and P_{NNB}: positive/negative ion based neutral beam powers, and $n_{\mathrm{e}}l$: line integrated electron density (l is given in the figure).
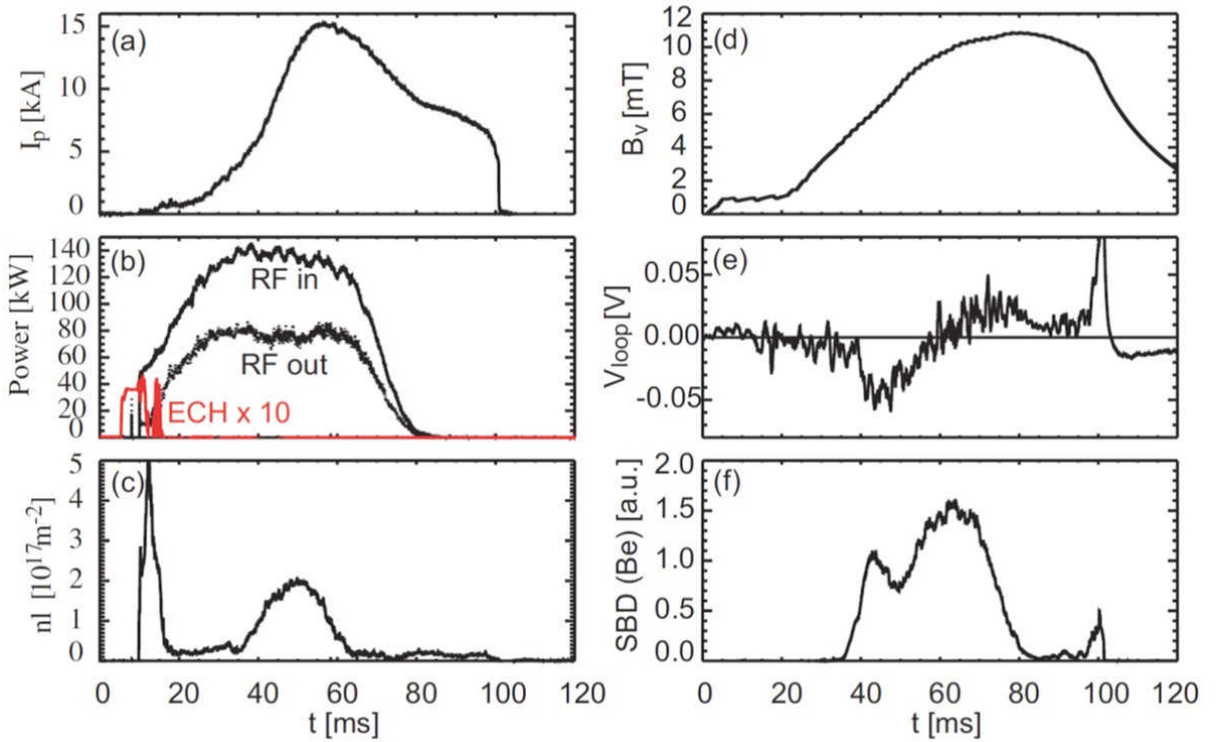
Figure 1.14: Typical waveforms of a TST-2 discharge ramped up by the LHW. (a) Plasma current, (b) ECH and RF powers, (c) line-integrated density (typical path length is 0.88 m), (d) vertical field, (e) loop voltage, (f) soft x-ray emission [35].

tokamak for current drive experiments [37], and was subsequently modified for use on TST-2. Plasma currents of up to 15 kA were achieved at B_{t0} of about 0.1 T. Similar plasma currents were obtained using the dielectric-loaded grill antenna [36] and the dependence of the hard x-ray emission from the plasma on the launched wavenumber spectrum was studied.

Another non-inductive current drive experiment was conducted on the Globus-M spherical tokamak ($R = 0.36$ m, $a = 0.24$ m, and $R/a = 1.5$) [38]. Plasma currents of up to 21 kA were achieved using the LHW with RF power of 100 kW at 900 MHz at $B_{t0} \sim 0.4$ T [39]. It is desirable for STs of the scale of TST-2 and Globus-M to demonstrate non-inductive ramp-up to a level of order 100 kA.

Currently, the achieved value of non-inductively driven current using the LHW is about 20 kA, considerably smaller than the desired value of 100 kA. In order to improve the amount of driven current, a further understanding of the physics of start-up plasmas driven by the LHW is necessary. As will be described in Chapter 2, the wavenumber determines wave propagation in the plasma and interaction with the plasma. A measurement of the wavenumber can help clarify the physical picture of non-inductive start-up plasmas using the LHW, and is therefore important.

1.6 Review of Preceding Studies on LHW Wavenumber Measurement

In this section, three preceding studies on LHW wavenumber measurement are reviewed.

1.6.1 Electrostatic Probe Measurement in a Linear Device

The LHW was excited by a meander-line antenna in a linear device at Nagoya University, and the wavenumber components parallel and perpendicular to the static magnetic field ($k_\parallel$ and $k_\perp$) were measured by interferometric method and by a double-tip electrostatic probe, respectively [40, 41]. In this experiment, argon plasma was produced by LHW at a frequency of 289 MHz or 432 MHz with RF power of up to 100 W at a pressure of 2–3×10^{-4} Torr. The plasma column is 13 cm in diameter and 130 cm in length. Typical plasma parameters were: electron density 10^{16}–$10^{17}\,\mathrm{m}^{-3}$, electron temperature 3–4 eV, and static magnetic field 0.07 T.

Figure 1.15 shows the meander-line antenna used in this experiment. Figure 1.16 shows (a) the waveforms along the static magnetic field (along the z-axis) measured by the interferometric method [40] and (b) a movable z-r double-tip electrostatic probe [41]. As shown in Fig. 1.16(a), the wavelength along the static magnetic field λ_z was measured from the interferogram and was converted to $k_\parallel$. The wavelength perpendicular to the static magnetic field was measured by the z-r double-tip electrostatic probe tips and was converted to $k_\perp$. In this experiment, the meander-line antenna shown in Fig. 1.15 was used instead of the helical antenna shown in Fig. 1.16(b). Figure 1.17 shows the relationship between the ratio $k_\perp/k_\parallel$ and the wave angular frequency for the LHW. This relationship is the dispersion relation, explained in Chapter 2. Experimental data points showed good agreement with the theoretical curve of the cold plasma dispersion relation for the LHW.

1.6.2 CO_2 Laser Scattering Measurement in Alcator-C

The wavenumber of the LHW was measured using CO_2 laser scattering in the Alcator-C tokamak [42]. The purpose of this experiment was to investigate the deterioration of heating and current drive by the LHW due to the parametric decay instability [43, 44], in which a fraction of the LHW is converted to another wave with different frequency and wavenumber.

Figure 1.18 shows the experimental setup. The LHW was launched from two 4×4 waveguide arrays (MW1 and MW2). Each waveguide array was fed by four 250 kW, 4.6 GHz klystrons, and adjacent columns of waveguides were phased 180° (90°) relative to each other for heating (current drive) [45, 46]. Plasma parameters were: toroidal magnetic field $B = 8$ T, line averaged electron density $1.8 \times 10^{20}\,\mathrm{m}^{-3} < \overline{n}_\mathrm{e} < 2.4 \times 10^{20}\,\mathrm{m}^{-3}$, launched LHW power $P_\mathrm{rf} = 260$ kW from MW2 alone. The measurement was performed along a vertical chord at $x \equiv R - R_0 = +12$ cm at E port (Fig. 1.18), where R_0 is the major radial location of the plasma center.

Figure 1.19 shows the principle of wavenumber measurement using CO_2 laser scattering [47]. The incident CO_2 laser beam is split by the first beam splitter (BS1). Majority of the beam is passed through the plasma. A small fraction of the incident beam is scattered by a small angle ϕ_B due to the density fluctuation in the plasma. Since the density fluctuation includes frequency and wavenumber components of the LHW (both the externally excited pump wave and the decay wave produced by parametric decay), information of the LHW is contained in the scattered signal.

Since the wavelength of the CO_2 laser is 10.6 μm, its frequency is about 30 THz, much larger than the electron plasma frequency so that the propagation path of the CO_2 laser beam is unaffected by the presence of the plasma. The wavenumbers of both the incident wave and the scattered wave ($\left|\overrightarrow{k}_0\right|$ and $\left|\overrightarrow{k}_\mathrm{s}\right|$) are typically much larger than the wavenumber of the density fluctuations in the plasma $\left|\overrightarrow{k}_\mathrm{d}\right|$, so the scattering angle ϕ_B is small (forward scattering) and $\overrightarrow{k}_\mathrm{d}$ is oriented nearly perpendicular to the incident wavevector $\overrightarrow{k}_0$. The scattering wavenumber $\left|\overrightarrow{k}_\mathrm{d}\right|$ can be chosen by adjusting the rotatable mirror (RM) so that the scattered beam with scattering angle ϕ_B is made collinear with the LO beam and detected by the detector D. Since the frequency of the CO_2 laser beam is too high to be sampled by the detector, the frequency of the scattered beam is down-converted by heterodyne mixing with the LO beam and mixed at the detector D.

The scattered signals were obtained for a range of $k_\mathrm{d} \equiv \left|\overrightarrow{k}_\mathrm{d}\right|$, and the wavenumber spectra were
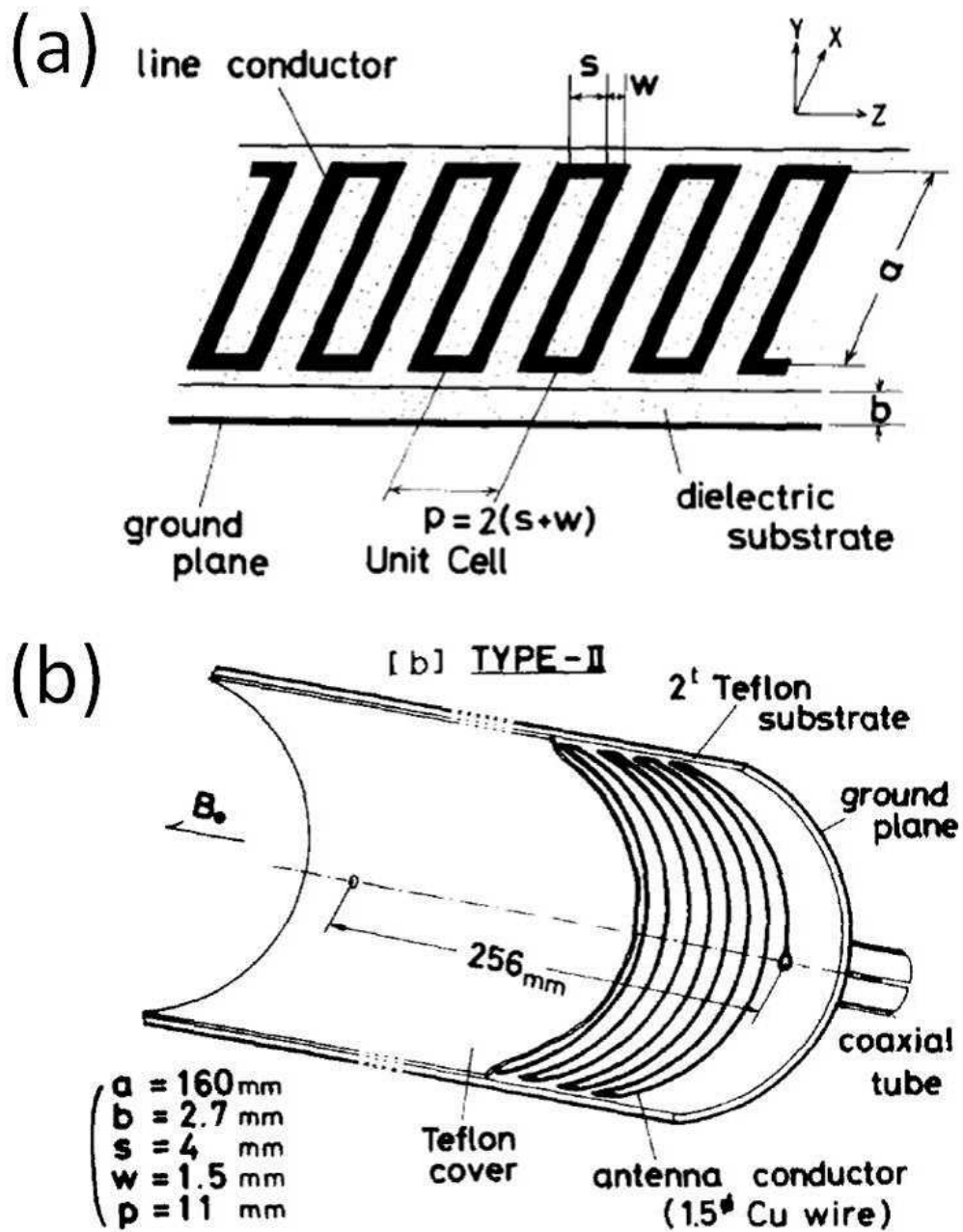
Figure 1.15: Meander-line antenna [40]. (a) Microstrip meander line. p is the pitch of the periodic structure, s is the spacing between two neighboring strip lines, w is the width of the microstrip line, and b is the thickness of dielectric substrate. (b) Meander-line antenna used in the experiment.
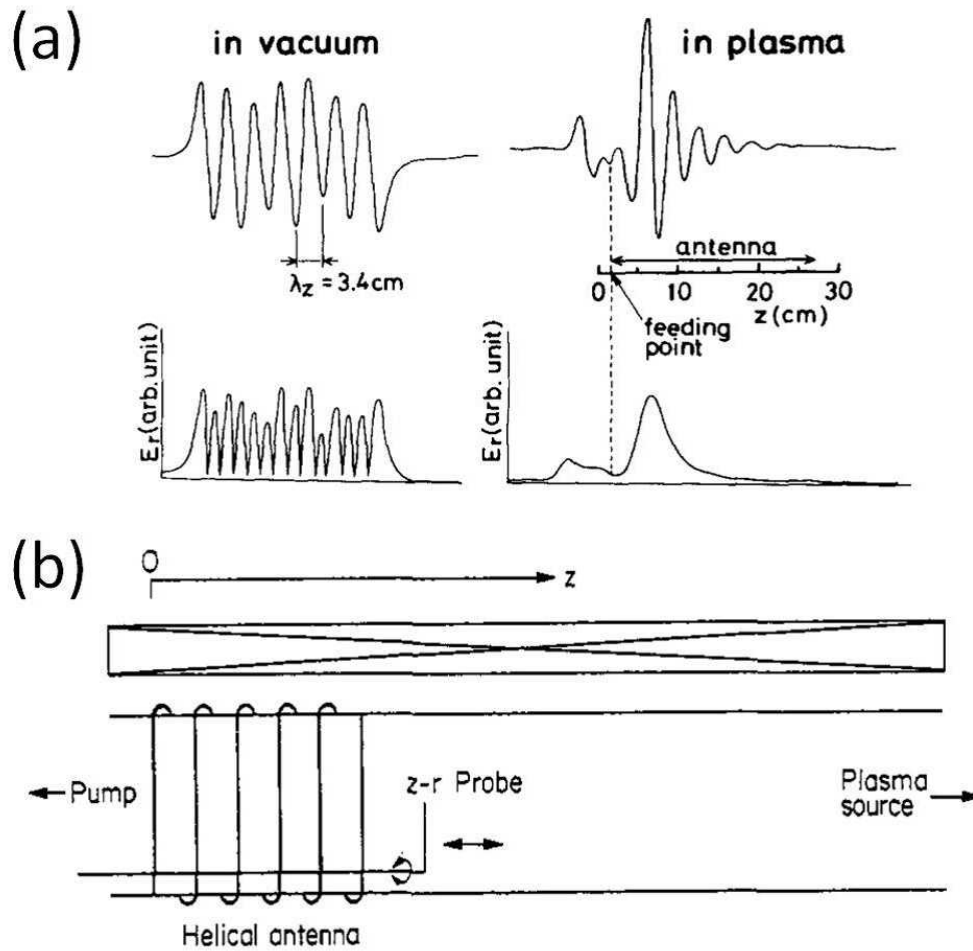
Figure 1.16: (a) Interferograms of LHW along the z-axis and the radial electric field E_r [40]. (b) z-r probe used to measure the perpendicular wavenumber $k_\perp$ [41]. The meander-line antenna shown in Fig. 1.15(b) was used instead of the helical antenna shown in this figure.
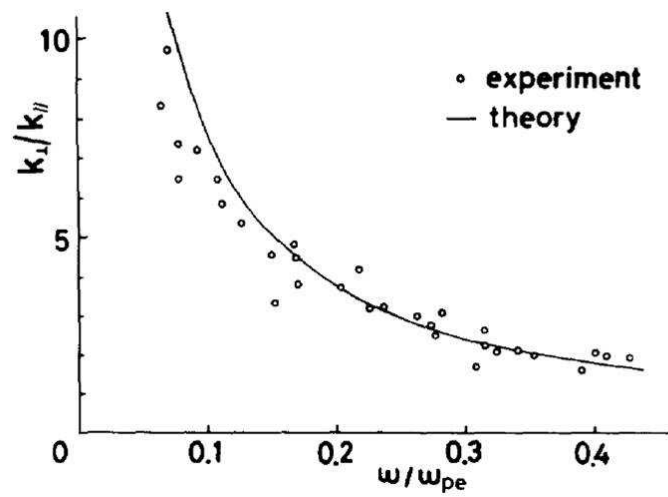
Figure 1.17: Dispersion curve of the excited wave. $\omega_{\mathrm{pe}}^2/\Omega_{\mathrm{e}}^2 = 1.3$ [40].
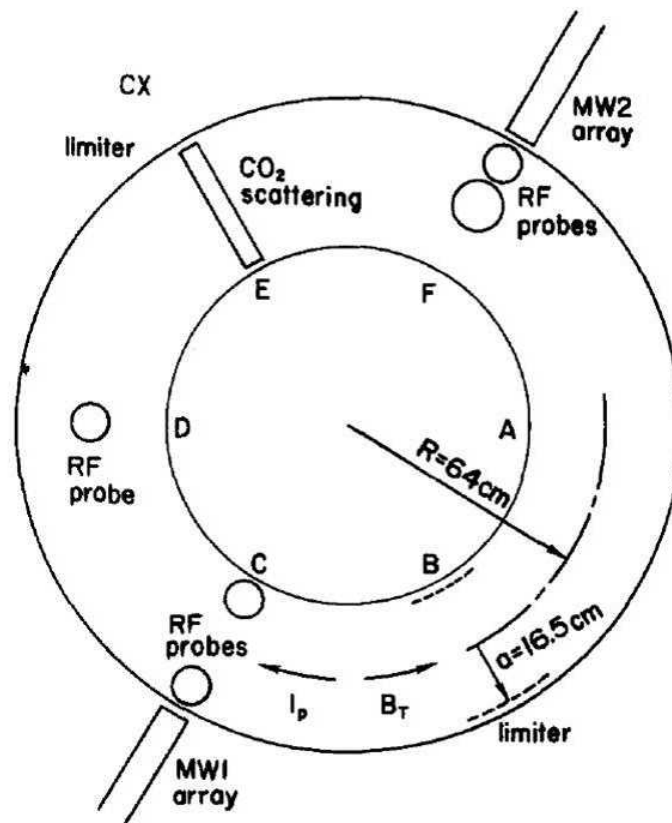
Figure 1.18: Locations of the waveguide arrays, limiters, and relevant diagnostics in Alcator-C [42].
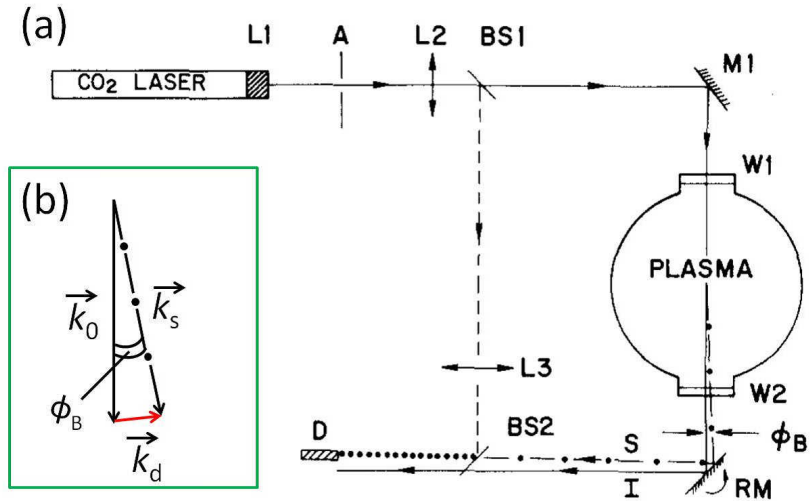
Figure 1.19: (a) A schematic diagram of small angle CO_2 laser scattering from a plasma. The laser beam is shaped by lenses L1 and L2. Aperture A is used to eliminate higher order modes. The dashed line shows the local oscillator (LO) path from beam splitters BS1 and BS2 to the detector D. Mirror RM is used to align the scattered radiation S (at angle ϕ_B from the incident beam) with the LO beam at BS2 [47]. (b) Diagram showing the relationship among the incident wavevector $\vec{k}_0$, the scattered wavevector $\vec{k}_s$, and the scattering wavevector $\vec{k}_d$ of the density fluctuation.

obtained for the pump wave and the decay wave. The wavenumber spectra can be plotted in terms of $N_\parallel = \frac{c}{\omega} k_\parallel$, where $k_\parallel$ is converted from the measured $k_d \cong k_\perp$ using the warm plasma dispersion relation. As pointed out in Ref. [42], since the vertical extent of the scattering volume is large (especially for small scattering angles), a unique mapping of $k_\perp$ into $N_\parallel$ cannot be made. The authors of Ref. [42] introduced $N_\parallel^*$ as the value of $N_\parallel$ obtained using the electron density on the midplane of the torus. $N_\parallel^*$ gives a lower bound on the true value of $N_\parallel$. Figure 1.20 shows the wavenumber spectra for the pump wave and the decay wave in terms of $N_\parallel^*$. The power density for the pump wave increases as $N_\parallel^*$ decreases to 3, which is consistent with the peak value of $N_\parallel = 2.6$ of the launched pump wave spectrum for 180° phasing used in this experiment.

1.6.3 Magnetic Probe Measurement in TST-2

In the TST-2 spherical tokamak, wavenumber components of the LHW at 200 MHz were measured in RF start-up plasmas using an array of five radio frequency magnetic probes (RFMPs) shown in Fig. 1.21 [35, 48]. The RFMP detects the RF magnetic field component parallel to the slit in front of each magnetic probe. Figure 1.22 shows (a) the midplane cross section of TST-2 for this experiment, (b) the parallel wavenumber spectrum excited by the grill antenna (not optimized for current drive), and (c) the result of wave identification calculation. The grill antenna shown schematically in Fig. 1.22(a) is identical to that used in Ref. [36]. The three components of the wavevector (toroidal, poloidal, and radial) were measured using this probe array. The radial component was measured by scanning the position of the RFMP array radially and measuring the phase shift with respect to the reference signal sampled from the incident wave to the grill antenna. From these components, both $k_\parallel$ and $k_\perp$ can be evaluated. The measured value of $k_\parallel$ was used to calculate $k_\perp$ using the cold plasma dispersion relation for the electron plasma densities typical in RF start-up plasmas in TST-2 as shown in Fig. 1.22(c) by black and red solid lines. SW (black) and FW (red) represent the two solutions
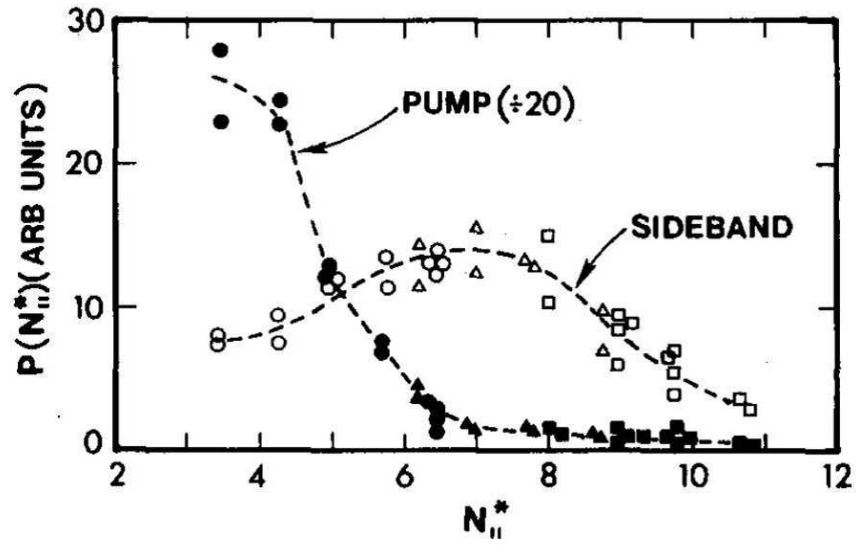
Figure 1.20: Wavenumber spectra $P(N_\parallel^*)$ for the pump wave and for the decay wave deduced from the experimentally measured $k_{\mathrm{d}} \cong k_\perp$ spectra. Deuterium, $B = 8\,\mathrm{T}$, $1.8 \leq \bar{n}_{\mathrm{e}}\left(10^{20}\,\mathrm{m}^{-3}\right) \leq 2.4$, $P_{\mathrm{rf}} = 260\,\mathrm{kW}$, and $x = +12\,\mathrm{cm}$. The pump wave data points are scaled down by a factor of 20 [42].
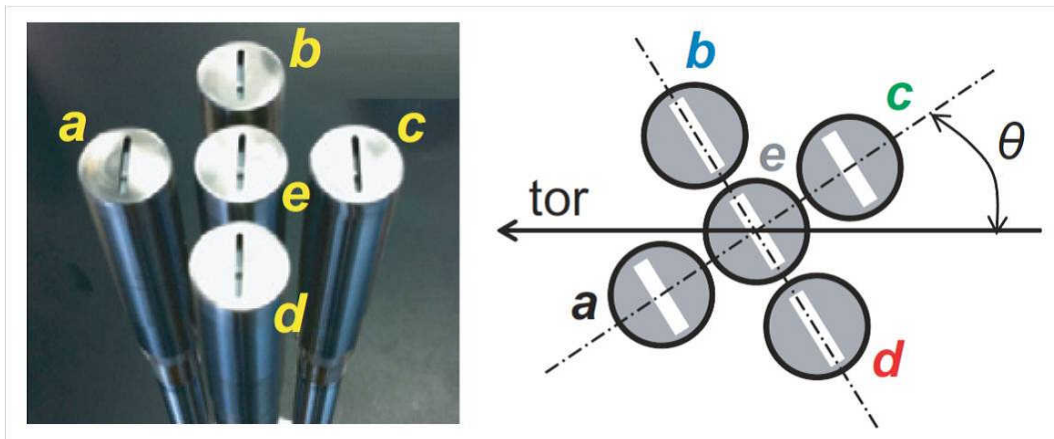
Figure 1.21: Magnetic probe array. The entire assembly can be turned around its axis to measure the RF poloidal magnetic field (when $\theta = 0°$), RF toroidal magnetic field (when $\theta = 90°$), or their linear combination [35].
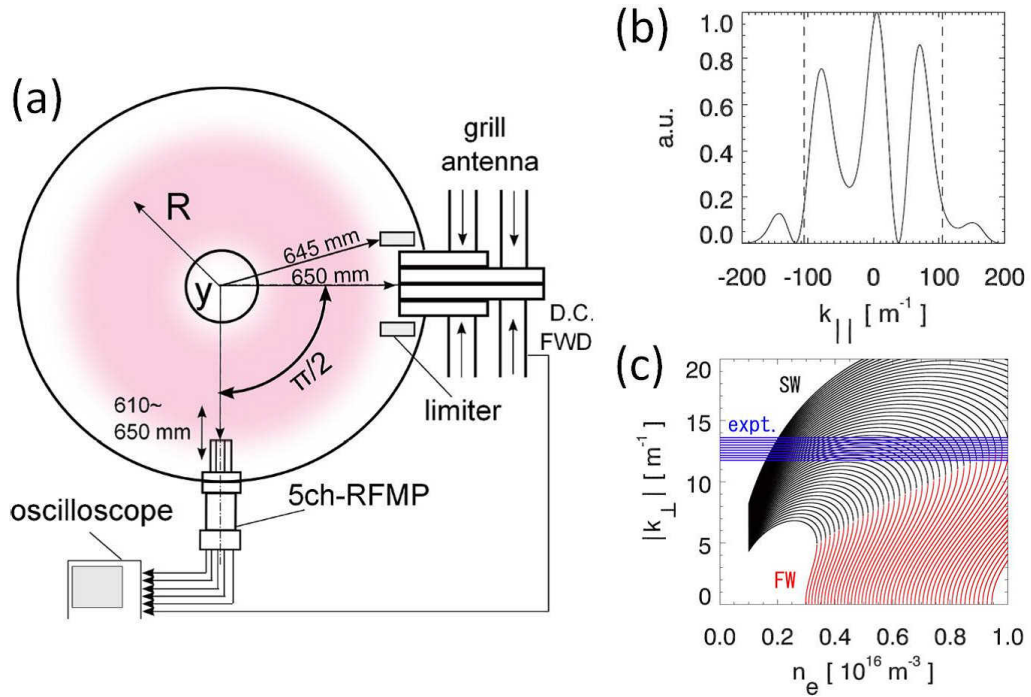
Figure 1.22: Wavenumber measurement using the RF magnetic probe array [48]. (a) Midplane cross section showing the 5-channel RFMP and the grill antenna. (b) Parallel wavenumber ($k_\parallel$) spectrum in front of the grill antenna. (The 5ch-RFMP can detect waves in the range $|k_\parallel| < 105\,\mathrm{m}^{-1}$.) (c) Cold plasma dispersion calculation. Black lines represent the slow wave (SW) and red lines represent the fast wave (FW). $|k_\perp|$ is calculated using the measured $k_\parallel$ at $R = 0.63\,\mathrm{m}$, $B_\mathrm{t} = 0.04\,\mathrm{T}$, and the electron density n_e in the range 10^{15}–$10^{16}\,\mathrm{m}^{-3}$. The blue lines mark the range of measured $|k_\perp|$ at $R = 0.63\,\mathrm{m}$.

of the cold plasma dispersion relation, i.e., the slow wave and the fast wave, respectively. As will be described in Subsection 2.5, the slow wave is the LHW. The measured $k_\perp$, shown by the blue region, is located in the region of the slow wave (LHW).

1.7   Thesis Objective and Original Contribution

In Section 1.4, the spherical tokamak (ST) was introduced to have two advantages over conventional tokamaks: being more compact and having better stability at high β. In Section 1.5, it was explained that the elimination of the OH solenoid was necessary for realizing the ST fusion power plant and that the lower hybrid wave (LHW) was a promising candidate for driving the plasma current non-inductively. Successful uses of the LHW to drive current in tokamaks and the current situation in STs were reviewed, It was pointed out that further understanding of RF start-up ST plasmas driven by the LHW is essential for improving the current drive performance. Direct measurements of the LHW wavenumber in ST devices can make a great contribution to the understanding because the wavenumber determines wave propagation and absorption in the plasma.

The objective of this thesis is to measure the wavenumber of the LHW in RF start-up plasmas at a frequency of 200 MHz used in TST-2 by an array of electrostatic probes. This thesis reports the first application of the electrostatic probe to the measurement of the LHW wavenumber in RF start-up ST plasmas, and will add new knowledge on RF wavenumber measurement. Table 1.1 shows a comparison of preceding studies of LHW wavenumber measurement and this thesis. Although LHW wavenumber measurement has already been conducted using an array of RF magnetic probes in TST-2, the significance of using an array of electrostatic probes is explained as follows. As will be explained in Section 2.5, the LHW is the slow wave, and as explained in Subsection 2.4.2, the slow wave is an oscillation of the electrostatic potential ϕ_p. While the magnetic probe measures the RF magnetic field accompanying the temporal variation of ϕ_p, the electrostatic probe can measure the potential directly. Therefore, the electrostatic probe is expected to measure the temporal variation of ϕ_p associated with the LHW more directly.

A unique point of this research is the use of an embedded high impedance resistor just after the electrode of the electrostatic probe. The reason for using a high impedance resistor is to reduce the current drawn from the plasma to suppress the perturbation caused by the probe. Also, as will be shown in Chapter 3, ϕ_p is linearly related to the floating potential V_f, which is measured by the electrostatic probe with high impedance. Although the simple linear relationship between ϕ_p and V_f is proven in low frequency regimes, much smaller than 200 MHz, even at high frequencies such as 200 MHz, the use of a high impedance resistor is expected to enable measurement of V_f, through which the temporal variation of ϕ_p (the LHW) is detected. By measuring the phase difference between signals detected by such high-impedance-embedded electrostatic probes, the wavenumber of the LHW can be measured.

Although the idea of using a high impedance resistor just after the electrode of an electrostatic probe existed previously [49,50], this is the first time to apply this type of electrostatic probe (referred to as "Modified Electrostatic Probe" in Table 1.1) to the high frequency range of 200 MHz.

Table 1.1: Comparison of preceding studies and this thesis.

Research	Subsection 1.6.1	Subsection 1.6.2	Subsection 1.6.3	This Thesis
Device	Linear Device	Alcator-C Tokamak	TST-2 Spherical Tokamak	TST-2 Spherical Tokamak
Measuring Instrument	Electrostatic Probe	CO_2 Laser Scattering	Magnetic Probe	Modified Electrostatic Probe
Frequency	289 MHz	4.6 GHz	200 MHz	200 MHz

Chapter 2

Theory of Waves in Cold Plasmas

Waves in a cold plasma are described in this Chapter [51]. The modifier "cold" means that finite temperature effects can be neglected. This assumption is usually valid when describing waves propagating in plasmas whose temperature is in the range of a few eV to tens of eV.

2.1 Wave Equation in a Cold Plasma

2.1.1 Background and Assumptions

Waves considered here are waves with an oscillating electric field and a magnetic field. The dynamics of these waves are governed by the wave equation, which is derived from Maxwell equations,

$$\nabla \cdot \boldsymbol{D} = \rho, \tag{2.1}$$

$$\nabla \times \boldsymbol{E} = -\frac{\partial \boldsymbol{B}}{\partial t}, \tag{2.2}$$

$$\nabla \cdot \boldsymbol{B} = 0, \tag{2.3}$$

$$\nabla \times \boldsymbol{H} = \boldsymbol{j} + \frac{\partial \boldsymbol{D}}{\partial t}, \tag{2.4}$$

where, in the SI unit system, ρ, $\boldsymbol{H}$, $\boldsymbol{j}$, and $\boldsymbol{D}$ are the net charge density [C/m^3], magnetic field [T], current density [C/ $\left(\mathrm{m}^2\mathrm{s}\right)$], and electric displacement [C/m^2], respectively. Although $\boldsymbol{B}$ is called the magnetic field in this thesis, the formal nomenclature is that $\boldsymbol{H}$ is the magnetic field and $\boldsymbol{B}$ is the magnetic flux density [T]. In Section 2.1, the terminology follows the formal nomenclature, but in other sections, $\boldsymbol{B}$ is called the magnetic field. These four equations have to be applied to the cold plasma, which is characterized by

- zero-temperature,

- approximately charge neutral,

- frictionless fluids of ions and electrons.

The zero-temperature assumption makes the thermal velocity zero, so the plasma is stationary on its own, but the particle inertia is taken into account. The background magnetic field, as well as the density and composition of the plasma are assumed to be stationary in time and homogeneous in space.

2.1.2 Order Separation between Wave Components

In considering waves in such a plasma, waves are regarded as perturbations in the plasma which is assumed to be a stationary medium. To handle this situation, it is helpful to perform order separation. This is already partly mentioned in Subsection 1.2.3 where stationary quantities are regarded as zeroth order, and wave quantities are regarded as first order perturbations. Physical quantities are expressed as

$$\boldsymbol{v}_s = \boldsymbol{v_0}_s + \boldsymbol{v_1}_s = \boldsymbol{0} + \boldsymbol{v_1}_s = \boldsymbol{v_1}_s, \tag{2.5}$$

$$\boldsymbol{B} = \boldsymbol{B_0} + \boldsymbol{B_1}, \tag{2.6}$$

$$\boldsymbol{n}_s = \boldsymbol{n_0}_s + \boldsymbol{n_1}_s, \tag{2.7}$$

$$\boldsymbol{E} = \boldsymbol{E_0} + \boldsymbol{E_1} = \boldsymbol{0} + \boldsymbol{E_1} = \boldsymbol{E_1}, \tag{2.8}$$

where the index s represents the particle species. All the first order quantities are assumed to vary as

$$\exp\left[i\left(\boldsymbol{k}\cdot\boldsymbol{r} - \omega\, t\right)\right],$$

where $\boldsymbol{k}$, $\boldsymbol{r}$, and ω are the wavenumber vector (or wave vector), the position vector in real space, and the angular frequency of the wave, respectively. The reason why the phase factor $(\boldsymbol{k}\cdot\boldsymbol{r} - \omega\, t)$ is chosen rather than $(\omega\, t - \boldsymbol{k}\cdot\boldsymbol{r})$ is that, in quantum mechanics, the operator $\hat{U}$ of time evolution is defined as

$$\hat{U}(t) = \exp\left(-i\frac{\hat{H}}{\hbar}t\right),$$

where $\hbar$ and $\hat{H}$ are the Planck constant divided by 2π and the time-independent Hamiltonian. Taking $(\boldsymbol{k}\cdot\boldsymbol{r} - \omega\, t)$ as the phase factor, it can be proven that $\exp\left[i\left(\boldsymbol{k}\cdot\boldsymbol{r}\right)\right]$ is an eigenfunction of a state moving in the direction of $\boldsymbol{k}$ in real three-dimensional space, consistent with quantum mechanics.

2.1.3 Maxwell Equations in a Cold Plasma

Maxwell equations can be arranged in a simpler form for the cold plasma case by using the assumption of approximate charge neutrality. This assumption requires that a net charge density ρ in Eq. (2.1) must vanish. An external current $\boldsymbol{j}$ in Eq. (2.4), which is the current generated by sources not related to the plasma, must also vanish. On the other hand, an internal current, which is caused by polarization of the plasma must be taken into consideration. The effect of plasma polarization is included in the electric displacement $\boldsymbol{D}$ in Eq. (2,4), defined as

$$\boldsymbol{D} \equiv \epsilon_0 \boldsymbol{E} + \boldsymbol{P}, \tag{2.9}$$

where $\boldsymbol{P}$ is the polarization vector and is given as

$$\boldsymbol{P} = \sum_{\mathrm{s}} n_s q_s \boldsymbol{x}_s, \tag{2.10}$$

in which $\boldsymbol{x}_s$ denotes the position of particles of species s. Thus, when considering $\boldsymbol{D}$, both the electric field $\boldsymbol{E}$ and the first order motion of charged particles must be included. For the magnetic flux density $\boldsymbol{B}$, it is sufficient to consider only the contribution of the magnetic field $\boldsymbol{H}$, because there is no magnetic monopole. Although the plasma can exhibit diamagnetism by the Larmor motion of charged particles, under the cold plasma assumption there is no zeroth order Larmor motion, and thus the cold plasma can be regarded as exhibiting paramagnetism. Therefore the permeability μ is equal to μ_0, the permeability in vacuum, and

$$\boldsymbol{B} = \mu_0 \boldsymbol{H} \tag{2.11}$$

holds in a cold plasma. Therefore, in a cold plasma,

$$\rho = 0, \tag{2.12}$$

$$\boldsymbol{j} = \boldsymbol{0}, \tag{2.13}$$

$$\boldsymbol{B} = \mu_0 \boldsymbol{H}, \tag{2.14}$$

are satisfied and Maxwell equations reduce to

$$\nabla \cdot \boldsymbol{D} = 0, \tag{2.15}$$

$$\nabla \times \boldsymbol{E} = -\frac{\partial \boldsymbol{B}}{\partial t}, \tag{2.16}$$

$$\nabla \cdot \boldsymbol{B} = 0, \tag{2.17}$$

$$\nabla \times \boldsymbol{B} = \mu_0 \frac{\partial \boldsymbol{D}}{\partial t}, \tag{2.18}$$

where

$$\boldsymbol{D} \equiv \epsilon_0 \boldsymbol{E} + \boldsymbol{P} = \epsilon_0 \boldsymbol{E} + \sum_s n_s q_s \boldsymbol{x}_s. \tag{2.19}$$

The partial time derivative of $\boldsymbol{D}$ in Eq. (2.18) is

$$\frac{\partial \boldsymbol{D}}{\partial t} = \epsilon_0 \frac{\partial \boldsymbol{E}}{\partial t} + \frac{\partial}{\partial t} \left(\sum_s n_s q_s \boldsymbol{x}_s \right) = \epsilon_0 \frac{\partial \boldsymbol{E}}{\partial t} + \sum_s n_s q_s \boldsymbol{v}_s. \tag{2.20}$$

Here, the second term in the rightmost side of Eq. (2.20) represents the plasma response consisting of the summation of the first order internal (polarization) current $\boldsymbol{j}_s = n_s q_s \boldsymbol{v}_s$ for each species.

2.1.4   Dielectric Tensor

In principle, combining Eqs. (2.15)–(2.18) gives waves we are seeking. But the electric displacement $\boldsymbol{D}$ includes the effects of not only the electric field $\boldsymbol{E}$ but also the motions of charged particles. It is convenient to express $\boldsymbol{D}$ only by $\boldsymbol{E}$. This is possible because the velocities of charged particles are linearly dependent on $\boldsymbol{E}$ through the equation of motion. Thus the dielectric tensor $\boldsymbol{\epsilon}$ is defined as

$$\boldsymbol{D} = \boldsymbol{\epsilon}\, \epsilon_0 \cdot \boldsymbol{E} \tag{2.21}$$

and for a cold plasma, from Eq. (2.19),

$$\boldsymbol{\epsilon}\, \epsilon_0 \cdot \boldsymbol{E} = \boldsymbol{D} = \epsilon_0 \boldsymbol{E} + \sum_s n_s q_s \boldsymbol{x}_s \tag{2.22}$$

follows. The dielectric tensor represents the relative dielectric in three-dimensional space and is dimensionless. Remembering that only $\boldsymbol{B}_0$, $\boldsymbol{n}_{0s}$ and $\boldsymbol{x}_{0s}$ are finite in the zeroth order, and all the first order quantities vary as $\exp\left[i\left(\boldsymbol{k}\cdot\boldsymbol{r} - \omega\, t\right)\right]$, Eq. (2.22) in the first order is

$$\boldsymbol{\epsilon}\, \epsilon_0 \cdot \boldsymbol{E}_1 = \epsilon_0 \boldsymbol{E}_1 + \sum_s n_s q_s \boldsymbol{x}_{s1}, \tag{2.23}$$

leading to

$$\boldsymbol{\epsilon} \cdot \boldsymbol{E}_1 = \boldsymbol{E}_1 + \frac{i}{\epsilon_0 \omega} \sum_s n_s q_s \boldsymbol{v}_{s1}, \tag{2.24}$$

where

$$\boldsymbol{v}_{s1} = \frac{d\boldsymbol{x}_{s1}}{dt} = -i\omega \boldsymbol{x}_{s1} \tag{2.25}$$

44

has been used.

Note that the first order quantities such as $\boldsymbol{E}_1$ and $\boldsymbol{v}_{s1}$ in Eq. (2.24) are in the form of

$$\boldsymbol{E}_1\left(t, \boldsymbol{r}\right) = \frac{1}{\left(\sqrt{2\pi}\right)^4} \int d\omega \int d\boldsymbol{k} \; \boldsymbol{E}_1\left(\omega, \boldsymbol{k}\right) \exp\left[i\left(\boldsymbol{k} \cdot \boldsymbol{r} - \omega \, t\right)\right]. \tag{2.26}$$

$\boldsymbol{E}_1\left(\omega, \boldsymbol{k}\right)$ is the complex amplitude of the electric field whose frequency and wavenumber vector are ω and $\boldsymbol{k}$. $\boldsymbol{E}_1\left(\omega, \boldsymbol{k}\right)$ is given by the inverse transform

$$\boldsymbol{E}_1\left(\omega, \boldsymbol{k}\right) = \frac{1}{\left(\sqrt{2\pi}\right)^4} \int dt \int d\boldsymbol{r} \; \boldsymbol{E}_1\left(t, \boldsymbol{r}\right) \exp\left[-i\left(\boldsymbol{k} \cdot \boldsymbol{r} - \omega \, t\right)\right]. \tag{2.27}$$

From now on, $\boldsymbol{E}_1\left(\omega, \boldsymbol{k}\right)$ is considered in the $(\omega, \boldsymbol{k})$ domain, since the dependence of the amplitude of the electric field $\boldsymbol{E}_1$ on ω and $\boldsymbol{k}$ is of interest. Performing the inverse Fourier transform of Eq. (2.24) leads to

$$\boldsymbol{\epsilon}(\omega, \boldsymbol{k}) \cdot \boldsymbol{E}(\omega, \boldsymbol{k}) = \boldsymbol{E}(\omega, \boldsymbol{k}) + \frac{i}{\epsilon_0 \omega} \sum_s n_s q_s \boldsymbol{v}_s(\omega, \boldsymbol{k}), \tag{2.28}$$

where the subscript 1 indicating the first order is omitted. From this equation, the dielectric tensor can be expressed as

$$\boldsymbol{\epsilon}(\omega, \boldsymbol{k}) = \boldsymbol{1} + \sum_s \boldsymbol{\chi}_s(\omega, \boldsymbol{k}), \tag{2.29}$$

where $\boldsymbol{1}$ is the 3×3 identity matrix and $\boldsymbol{\chi}_s(\omega, \boldsymbol{k})$ is the susceptivity tensor for particle species s. Substituting Eq. (2.29) in Eq. (2.28) and comparing both sides, it is shown that the contributions of charged particle motions appear in $\boldsymbol{\chi}_s(\omega, \boldsymbol{k})$ as

$$\boldsymbol{\chi}_s(\omega, \boldsymbol{k}) \cdot \boldsymbol{E}(\omega, \boldsymbol{k}) = \frac{i}{\epsilon_0 \omega} n_s q_s \boldsymbol{v}_s(\omega, \boldsymbol{k}). \tag{2.30}$$

This means that if $\boldsymbol{v}_s(\omega, \boldsymbol{k})$ could be expressed linearly in $\boldsymbol{E}(\omega, \boldsymbol{k})$, the effects of the first order motions of charged particles are included in the dielectric tensor $\boldsymbol{\epsilon}(\omega, \boldsymbol{k})$ through $\boldsymbol{\chi}_s(\omega, \boldsymbol{k})$ and the wave equation is obtained.

From the assumption that a cold plasma consists of frictionless fluids of ions and electrons, the equation of motion for the fluid of species s is

$$n_s m_s \frac{d\boldsymbol{v}_s}{dt} = n_s m_s \left(\frac{\partial \boldsymbol{v}_s}{\partial t} + \boldsymbol{v}_s \cdot \nabla \boldsymbol{v}_s\right) = n_s q_s \left(\boldsymbol{E} + \boldsymbol{v}_s \times \boldsymbol{B}\right) - \nabla \cdot \boldsymbol{\Phi}_s, \tag{2.31}$$

where $\boldsymbol{\Phi}_s$ is the fluid stress tensor which is zero under the cold plasma assumption. Collisions are also neglected due to the assumption of frictionless fluid. Therefore, Eq. (2.31) reduces to

$$m_s \frac{d\boldsymbol{v}_s}{dt} = q_s(\boldsymbol{E} + \boldsymbol{v}_s \times \boldsymbol{B}). \tag{2.32}$$

This equation is solved in each order of perturbation. Since $\boldsymbol{v}_{s0}$ and $\boldsymbol{E}_0$ are zero, this equation is trivially satisfied in the zeroth order. In the first order, omitting the subscript 1 indicating the first order,

$$m_s \frac{d\boldsymbol{v}_s}{dt} = q_s(\boldsymbol{E} + \boldsymbol{v}_s \times \boldsymbol{B}_0) \tag{2.33}$$

holds. Note that this is an equation in the $(t, \boldsymbol{r})$ domain. From Eq. (2.26), the time derivative on $\boldsymbol{v}_s$ generates a factor $-i\omega$, and performing the inverse Fourier transform gives

$$-i\omega m_s \boldsymbol{v}_s(\omega, \boldsymbol{k}) = q_s \left\{\boldsymbol{E}(\omega, \boldsymbol{k}) + \boldsymbol{v}_s(\omega, \boldsymbol{k}) \times \boldsymbol{B}_0\right\}. \tag{2.34}$$

Recalling that the direction of the magnetic field is in the z direction:

$$\boldsymbol{B} = \begin{pmatrix} 0 \\ 0 \\ B_0 \end{pmatrix}, \tag{2.35}$$

the solution $\boldsymbol{v}_s$ is given in terms of $\boldsymbol{E}(\omega, \boldsymbol{k})$ as

$$\boldsymbol{v}_s(\omega, \boldsymbol{k}) = \begin{pmatrix} v_{sx}(\omega, \boldsymbol{k}) \\ v_{sy}(\omega, \boldsymbol{k}) \\ v_{sz}(\omega, \boldsymbol{k}) \end{pmatrix} = -\frac{iq_s}{m_s} \begin{pmatrix} -\dfrac{\omega}{\omega^2 - \Omega_s^2} & -i\dfrac{\Omega_s}{\omega^2 - \Omega_s^2} & 0 \\[3mm] i\dfrac{\Omega_s}{\omega^2 - \Omega_s^2} & -\dfrac{\omega}{\omega^2 - \Omega_s^2} & 0 \\[3mm] 0 & 0 & -\dfrac{1}{\omega} \end{pmatrix} \begin{pmatrix} E_x(\omega, \boldsymbol{k}) \\ E_y(\omega, \boldsymbol{k}) \\ E_z(\omega, \boldsymbol{k}) \end{pmatrix}. \tag{2.36}$$

Thus, from Eq. (2.30),

$$\begin{aligned}
\boldsymbol{\chi}(\omega, \boldsymbol{k})_s \cdot \boldsymbol{E}(\omega, \boldsymbol{k}) &= \frac{i}{\epsilon_0 \omega} n_s q_s \boldsymbol{v}_s(\omega, \boldsymbol{k}) \\[3mm]
&= \frac{n_s q_s^2}{\epsilon_0 m_s} \begin{pmatrix} -\dfrac{1}{\omega^2 - \Omega_s^2} & -i\dfrac{\Omega_s}{\omega(\omega^2 - \Omega_s^2)} & 0 \\[3mm] i\dfrac{\Omega_s}{\omega(\omega^2 - \Omega_s^2)} & -\dfrac{1}{\omega^2 - \Omega_s^2} & 0 \\[3mm] 0 & 0 & -\dfrac{1}{\omega^2} \end{pmatrix} \begin{pmatrix} E_x(\omega, \boldsymbol{k}) \\ E_y(\omega, \boldsymbol{k}) \\ E_z(\omega, \boldsymbol{k}) \end{pmatrix} \\[3mm]
&= \begin{pmatrix} -\dfrac{\omega_{\mathrm{p}s}^2}{\omega^2 - \Omega_s^2} & -i\dfrac{\Omega_s}{\omega}\dfrac{\omega_{\mathrm{p}s}^2}{\omega^2 - \Omega_s^2} & 0 \\[3mm] i\dfrac{\Omega_s}{\omega}\dfrac{\omega_{\mathrm{p}s}^2}{\omega^2 - \Omega_s^2} & -\dfrac{\omega_{\mathrm{p}s}^2}{\omega^2 - \Omega_s^2} & 0 \\[3mm] 0 & 0 & -\dfrac{\omega_{\mathrm{p}s}^2}{\omega^2} \end{pmatrix} \cdot \boldsymbol{E}(\omega, \boldsymbol{k}),
\end{aligned} \tag{2.37}$$

where $\omega_{\mathrm{p}s}$ is the plasma frequency defined in Eq. (1.33). The dielectric tensor

$$\boldsymbol{\epsilon}(\omega, \boldsymbol{k}) = \mathbf{1} + \sum_s \boldsymbol{\chi}_s(\omega, \boldsymbol{k})$$

is then obtained as

$$\boldsymbol{\epsilon}(\omega, \boldsymbol{k}) \cdot \boldsymbol{E}(\omega, \boldsymbol{k}) = \begin{pmatrix} S & -iD & 0 \\ iD & S & 0 \\ 0 & 0 & P \end{pmatrix} \begin{pmatrix} E_x(\omega, \boldsymbol{k}) \\ E_y(\omega, \boldsymbol{k}) \\ E_z(\omega, \boldsymbol{k}) \end{pmatrix}, \tag{2.38}$$

where

$$S = 1 - \sum_s \frac{\omega_{\mathrm{p}s}^2}{\omega^2 - \Omega_s^2} \tag{2.39}$$

$$D = \sum_s \frac{\Omega_s}{\omega} \frac{\omega_{\mathrm{p}s}^2}{\omega^2 - \Omega_s^2} \tag{2.40}$$

$$P = 1 - \sum_s \frac{\omega_{\mathrm{p}s}^2}{\omega^2}. \tag{2.41}$$

The two parameters R and L are also used for describing the property of waves in a cold plasma:

$$R = 1 - \sum_s \frac{\omega_{ps}^2}{\omega(\omega + \Omega_s)}, \tag{2.42}$$

$$L = 1 - \sum_s \frac{\omega_{ps}^2}{\omega(\omega - \Omega_s)}, \tag{2.43}$$

which can express S and D as

$$S = \frac{1}{2}(R + L), \tag{2.44}$$

$$D = \frac{1}{2}(R - L). \tag{2.45}$$

Parameters R, L, P, S, and D are called the Stix parameters [51].

2.1.5 Wave Equation in a Cold Plasma

Now that the effects of charged particle motions are included in the dielectric tensor, the wave equation in a cold plasma can be obtained. The two Maxwell equations for a cold plasma, Eqs. (2.16) and (2.18), give

$$\nabla \times (\nabla \times \boldsymbol{E}) = -\frac{\partial}{\partial t}(\nabla \times \boldsymbol{B}) = -\mu_0 \frac{\partial^2 \boldsymbol{D}}{\partial t^2}, \tag{2.46}$$

where $\boldsymbol{D} = \boldsymbol{\epsilon}\,\epsilon_0 \cdot \boldsymbol{E}$. For the Fourier amplitude $\boldsymbol{E}(\omega, \boldsymbol{k})$, differentiation (i.e. $\nabla \times \mapsto i\boldsymbol{k}\times$ and $\frac{\partial}{\partial t} \mapsto -i\omega$) leads to

$$-\boldsymbol{k} \times \{\boldsymbol{k} \times \boldsymbol{E}(\omega, \boldsymbol{k})\} = \mu_0 \omega^2 \epsilon_0 \boldsymbol{\epsilon}(\omega, \boldsymbol{k}) \cdot \boldsymbol{E}(\omega, \boldsymbol{k}), \tag{2.47}$$

resulting in

$$\boldsymbol{k} \times (\boldsymbol{k} \times \boldsymbol{E}) + \frac{\omega^2}{c^2}\boldsymbol{\epsilon} \cdot \boldsymbol{E} = \boldsymbol{0} \tag{2.48}$$

with $(\omega, \boldsymbol{k})$ omitted and $c = \frac{1}{\sqrt{\epsilon_0 \mu_0}}$ is the speed of light. It is convenient to introduce a dimensionless vector $\boldsymbol{n}$ which has the direction of the propagation vector $\boldsymbol{k}$ and the magnitude of the refractive index:

$$\boldsymbol{n} \equiv \frac{\boldsymbol{k}c}{\omega}. \tag{2.49}$$

The magnitude of $\boldsymbol{n}$ is

$$|\boldsymbol{n}| = \frac{c}{\left(\frac{\omega}{|\boldsymbol{k}|}\right)}, \tag{2.50}$$

where the denominator $\frac{\omega}{|\boldsymbol{k}|}$ is the phase velocity. Using $\boldsymbol{n}$, the wave equation Eq. (2.48) becomes

$$\boldsymbol{n} \times (\boldsymbol{n} \times \boldsymbol{E}) + \boldsymbol{\epsilon} \cdot \boldsymbol{E} = \boldsymbol{0}. \tag{2.51}$$

Using the angle θ between $\boldsymbol{B}_0 = \hat{\boldsymbol{z}}\,B_0$ and $\boldsymbol{n}$ where $\hat{\boldsymbol{z}}$ is a unit vector along the z-axis, and assuming $\boldsymbol{n}$ to lie in the x-z plane, Eq. (2.51) becomes

$$\begin{pmatrix} S - n^2\cos^2\theta & -iD & n^2\cos\theta\sin\theta \\ iD & S - n^2 & 0 \\ n^2\cos\theta\sin\theta & 0 & P - n^2\sin^2\theta \end{pmatrix} \begin{pmatrix} E_x \\ E_y \\ E_z \end{pmatrix} = \boldsymbol{0}, \tag{2.52}$$

where the coordinate system shown in Fig. 2.1 is used. This is the wave equation in a cold plasma.
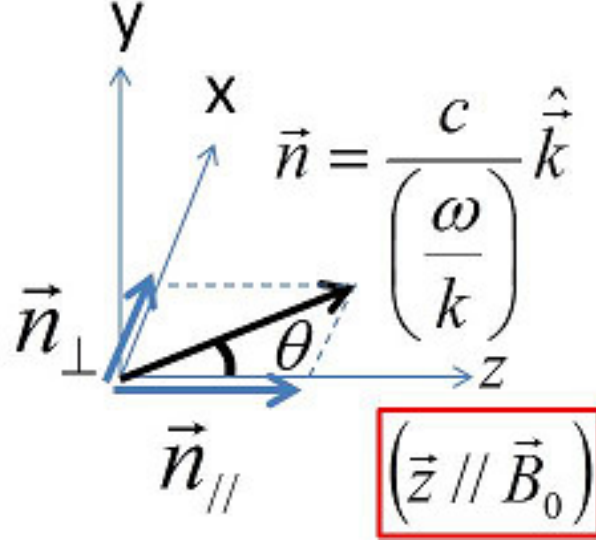
Figure 2.1: Coordinate system.

2.2 Cold Plasma Dispersion Relation

The condition for $\boldsymbol{n}$ of a propagating wave is obtained by setting the determinant of the coefficient matrix $\boldsymbol{M}$ of $\boldsymbol{E}$ in Eq. (2.52) to zero,

$$\det \boldsymbol{M} = 0, \tag{2.53}$$

otherwise $\boldsymbol{E}$ has only a trivial solution $\boldsymbol{E}(\omega, \boldsymbol{k}) = \boldsymbol{0}$. Considering that $\boldsymbol{n}$ is written explicitly as

$$\boldsymbol{n} = \begin{pmatrix} n\sin\theta \\ 0 \\ n\cos\theta \end{pmatrix} \equiv \begin{pmatrix} n_\perp \\ 0 \\ n_\parallel \end{pmatrix}, \tag{2.54}$$

where the indices $_\parallel$ and $_\perp$ denote the parallel and perpendicular directions with respect to $\boldsymbol{B}_0$, and that $n_\parallel$ is fixed by the boundary condition specified by the antenna, it is more practical to regard the condition $\det \boldsymbol{M} = 0$ as the condition for $n_\perp$ for a given $n_\parallel$. The wave equation Eq. (2.52) is rewritten in terms of $n_\parallel$ and $n_\perp$ as

$$\begin{pmatrix} S - n_\parallel^2 & -iD & n_\parallel n_\perp \\ iD & S - n^2 & 0 \\ n_\parallel n_\perp & 0 & P - n_\perp^2 \end{pmatrix} \begin{pmatrix} E_x \\ E_y \\ E_z \end{pmatrix} = \boldsymbol{0} \tag{2.55}$$

and the condition $\det \boldsymbol{M} = 0$ gives the cold-plasma dispersion relation

$$a n_\perp^4 - b n_\perp^2 + c = 0, \tag{2.56}$$

where

$$a \equiv S \tag{2.57}$$

$$b \equiv RL + PS - (P + S) n_\parallel^2 \tag{2.58}$$

$$c \equiv P\left(RL - 2S n_\parallel^2 + n_\parallel^4\right). \tag{2.59}$$

48

2.3 Properties of a Propagating Wave

2.3.1 Fast Wave and Slow Wave

There are two solutions for the cold-plasma dispersion relation Eq. (2.56):

$$n_\perp^2 = \frac{b \pm \sqrt{b^2 - 4ac}}{2a}. \tag{2.60}$$

The two solutions correspond to the slow wave and the fast wave. The nomenclatures of slow and fast are based on the phase velocity

$$v_{\text{ph}} = \frac{\omega}{|\boldsymbol{k}|}, \tag{2.61}$$

and

$$v_{\text{ph,fast}} > v_{\text{ph,slow}} \tag{2.62}$$

holds by definition. From Eqs. (2.50) and (2.61),

$$|\boldsymbol{n}| = \frac{c}{\left(\frac{\omega}{|\boldsymbol{k}|}\right)} = \frac{c}{v_{\text{ph}}} \tag{2.63}$$

is satisfied and the relation $v_{\text{ph,fast}} > v_{\text{ph,slow}}$ leads to

$$|\boldsymbol{n}|_{\text{fast}} < |\boldsymbol{n}|_{\text{slow}}. \tag{2.64}$$

Thus, for a given $n_\parallel$, two solutions of Eq. (2.60) are

$$n_{\perp,\text{slow}}^2 = \frac{b + \sqrt{b^2 - 4ac}}{2a}, \tag{2.65}$$

$$n_{\perp,\text{fast}}^2 = \frac{b - \sqrt{b^2 - 4ac}}{2a}. \tag{2.66}$$

2.3.2 Propagation and Evanescence

Note that $n_\perp^2$ can be negative or complex, in which case $n_\perp$ has an imaginary component. For example, if $n_\perp^2 < 0$, $n_\perp$ and thus $k_\perp$ is purely imaginary for positive ω. In this case, $k_\perp$ is denoted by $k_\perp = \pm i\kappa_\perp$ where $\kappa_\perp \in \mathbb{R}$, and the wave solution is expressed as

$$\exp\left[i\left(\boldsymbol{k} \cdot \boldsymbol{r} - \omega\, t\right)\right] = \exp\left(\mp\kappa_\perp x\right) \cdot \exp\left[i\left(k_\parallel z - \omega\, t\right)\right], \tag{2.67}$$

where the x direction is perpendicular to $\boldsymbol{B}_0$. Without any mechanism of amplifying the wave, the solution that attenuates in the x direction is chosen. This decaying wave is called an evanescent wave. In order for a wave to exist as a propagating wave in space, both

$$b^2 - 4ac \geq 0 \tag{2.68}$$

and

$$n_\perp^2 \geq 0 \tag{2.69}$$

must be satisfied for our definition of $\boldsymbol{n}$.

2.3.3 Relations Among the Electric and Magnetic Field Components

The difference in $\boldsymbol{n}$ between the fast wave and the slow wave features their "characters". The magnitude relations among the six components of the wave, i.e., E_x, E_y, E_z, B_x, B_y, and B_z can be derived from the wave equation Eq. (2.55):

$$\begin{pmatrix} S - n_\parallel^2 & -iD & n_\parallel n_\perp \\ iD & S - n^2 & 0 \\ n_\parallel n_\perp & 0 & P - n_\perp^2 \end{pmatrix} \begin{pmatrix} E_x(\omega, \boldsymbol{k}) \\ E_y(\omega, \boldsymbol{k}) \\ E_z(\omega, \boldsymbol{k}) \end{pmatrix} = \boldsymbol{0},$$

which is expressed in terms of $\boldsymbol{E}(\omega, \boldsymbol{k})$. Recalling that the physical quantities can be perceived in the form of $\mathrm{Re}\left[\boldsymbol{E}(t, \boldsymbol{r})\right]$ in experiments, it is important to verify the relationship between $\mathrm{Re}\left[\boldsymbol{E}(t, \boldsymbol{r})\right]$ and $\boldsymbol{E}(\omega, \boldsymbol{k})$. Starting from Eq. (2.26):

$$\boldsymbol{E}_1(t, \boldsymbol{r}) = \frac{1}{\left(\sqrt{2\pi}\right)^4} \int d\omega \int d\boldsymbol{k} \, \boldsymbol{E}_1(\omega, \boldsymbol{k}) \exp\left[i\left(\boldsymbol{k} \cdot \boldsymbol{r} - \omega t\right)\right],$$

where $\boldsymbol{E}_1(t, \boldsymbol{r})$ and $\boldsymbol{E}_1(\omega, \boldsymbol{k})$ are complex vectors, this equation gives

$$\mathrm{Re}\left[\boldsymbol{E}_1(t, \boldsymbol{r})\right] = \frac{1}{\left(\sqrt{2\pi}\right)^4} \int d\omega \int d\boldsymbol{k} \, \mathrm{Re}\left\{\boldsymbol{E}_1(\omega, \boldsymbol{k}) \exp\left[i\left(\boldsymbol{k} \cdot \boldsymbol{r} - \omega t\right)\right]\right\}. \tag{2.70}$$

For the x-component, after dropping the subscript 1 and expressing $E_x(\omega, \boldsymbol{k})$ as

$$E_x(\omega, \boldsymbol{k}) = E_{x\mathrm{r}}(\omega, \boldsymbol{k}) + iE_{x\mathrm{i}}(\omega, \boldsymbol{k}), \tag{2.71}$$

where $E_{x\mathrm{r}}(\omega, \boldsymbol{k})$ and $E_{x\mathrm{i}}(\omega, \boldsymbol{k})$ are real numbers. The integrand of the x-component of Eq. (2.70) is

$$
\begin{aligned}
&\mathrm{Re}\left\{E_x(\omega, \boldsymbol{k}) \exp\left[i\left(\boldsymbol{k} \cdot \boldsymbol{r} - \omega t\right)\right]\right\} \\
=\ & E_{x\mathrm{r}}(\omega, \boldsymbol{k})\cos\left(\boldsymbol{k} \cdot \boldsymbol{r} - \omega t\right) - E_{x\mathrm{i}}(\omega, \boldsymbol{k})\sin\left(\boldsymbol{k} \cdot \boldsymbol{r} - \omega t\right) \\
=\ & \sqrt{E_{x\mathrm{r}}^2(\omega, \boldsymbol{k}) + E_{x\mathrm{i}}^2(\omega, \boldsymbol{k})}\cos\left(\boldsymbol{k} \cdot \boldsymbol{r} - \omega t + \delta_x\right) \\
=\ & |E_x(\omega, \boldsymbol{k})| \cos\left(\boldsymbol{k} \cdot \boldsymbol{r} - \omega t + \delta_x\right),
\end{aligned}
\tag{2.72}
$$

where $\tan \delta_x = \frac{E_{x\mathrm{i}}(\omega, \boldsymbol{k})}{E_{x\mathrm{r}}(\omega, \boldsymbol{k})}$. Thus, for the x-component,

$$\mathrm{Re}\left[E_x(t, \boldsymbol{r})\right] = \frac{1}{\left(\sqrt{2\pi}\right)^4} \int d\omega \int d\boldsymbol{k} \, |E_x(\omega, \boldsymbol{k})| \cos\left(\boldsymbol{k} \cdot \boldsymbol{r} - \omega t + \delta_x\right) \tag{2.73}$$

is satisfied. Similarly for the y and the z components,

$$\mathrm{Re}\left[\begin{pmatrix} E_x(t, \boldsymbol{k}) \\ E_y(t, \boldsymbol{k}) \\ E_z(t, \boldsymbol{k}) \end{pmatrix}\right] = \frac{1}{\left(\sqrt{2\pi}\right)^4} \int d\omega \int d\boldsymbol{k} \begin{pmatrix} |E_x(\omega, \boldsymbol{k})| \cos\left(\boldsymbol{k} \cdot \boldsymbol{r} - \omega t + \delta_x\right) \\ |E_y(\omega, \boldsymbol{k})| \cos\left(\boldsymbol{k} \cdot \boldsymbol{r} - \omega t + \delta_y\right) \\ |E_z(\omega, \boldsymbol{k})| \cos\left(\boldsymbol{k} \cdot \boldsymbol{r} - \omega t + \delta_z\right) \end{pmatrix} \tag{2.74}$$

is obtained. Therefore, the absolute value of $E(\omega, \boldsymbol{k})$, or $|E(\omega, \boldsymbol{k})|$, can be regarded as being proportional to the amplitude of the measured quantity for the $(\omega, \boldsymbol{k})$ component with a common constant of proportionality.

Now back to the wave equation

$$\begin{pmatrix} S - n_\parallel^2 & -iD & n_\parallel n_\perp \\ iD & S - n^2 & 0 \\ n_\parallel n_\perp & 0 & P - n_\perp^2 \end{pmatrix} \begin{pmatrix} E_x(\omega, \boldsymbol{k}) \\ E_y(\omega, \boldsymbol{k}) \\ E_z(\omega, \boldsymbol{k}) \end{pmatrix} = \boldsymbol{0},$$

the second and the third rows give $E_y(\omega, \boldsymbol{k})$ and $E_z(\omega, \boldsymbol{k})$ in terms of $E_x(\omega, \boldsymbol{k})$ and

$$
\begin{pmatrix} E_x(\omega, \boldsymbol{k}) \\ E_y(\omega, \boldsymbol{k}) \\ E_z(\omega, \boldsymbol{k}) \end{pmatrix} = E_x(\omega, \boldsymbol{k}) \begin{pmatrix} 1 \\ i\frac{D}{n^2 - S} \\ \frac{n_\parallel n_\perp}{n_\perp^2 - P} \end{pmatrix} \tag{2.75}
$$

follows. It can be shown that Eq. (2.75) satisfies the first row of the wave equation. $\boldsymbol{B}(\omega, \boldsymbol{k})$ is obtained from Faraday's law:

$$
\nabla \times \boldsymbol{E} = -\frac{\partial \boldsymbol{B}}{\partial t},
$$

which can be written in Fourier representation as

$$
i\boldsymbol{k} \times \boldsymbol{E}(\omega, \boldsymbol{k}) = -(-i\omega)\boldsymbol{B}(\omega, \boldsymbol{k}),
$$

i.e.,

$$
c\boldsymbol{B}(\omega, \boldsymbol{k}) = \boldsymbol{n} \times \boldsymbol{E}(\omega, \boldsymbol{k}). \tag{2.76}
$$

Equations (2.54), (2.75), and (2.76) give

$$
\begin{aligned}
\begin{pmatrix} cB_x(\omega, \boldsymbol{k}) \\ cB_y(\omega, \boldsymbol{k}) \\ cB_z(\omega, \boldsymbol{k}) \end{pmatrix} &= \begin{pmatrix} n_\parallel E_y(\omega, \boldsymbol{k}) \\ n_\parallel E_x(\omega, \boldsymbol{k}) - n_\perp E_z(\omega, \boldsymbol{k}) \\ n_\perp E_y(\omega, \boldsymbol{k}) \end{pmatrix} \\
&= E_x(\omega, \boldsymbol{k}) \begin{pmatrix} n_\parallel i \frac{D}{n^2 - S} \\ n_\parallel - n_\perp \frac{n_\parallel n_\perp}{n_\perp^2 - P} \\ n_\perp i \frac{D}{n^2 - S} \end{pmatrix} \\
&= E_x(\omega, \boldsymbol{k}) \begin{pmatrix} i\frac{n_\parallel D}{n^2 - S} \\ -\frac{n_\parallel P}{n_\perp^2 - P} \\ i\frac{n_\perp D}{n^2 - S} \end{pmatrix}.
\end{aligned} \tag{2.77}
$$

So, from Eqs. (2.75) and (2.77), the relative amplitudes are expressed with reference to $|E_x(\omega, \boldsymbol{k})|$ as

$$
\begin{aligned}
&(|E_x(\omega, \boldsymbol{k})|, |E_y(\omega, \boldsymbol{k})|, |E_z(\omega, \boldsymbol{k})|, |cB_x(\omega, \boldsymbol{k})|, |cB_y(\omega, \boldsymbol{k})|, |cB_z(\omega, \boldsymbol{k})|) \\
&= |E_x(\omega, \boldsymbol{k})| \left(1, \left|\frac{D}{n^2 - S}\right|, \left|\frac{n_\parallel n_\perp}{n_\perp^2 - P}\right|, \left|\frac{n_\parallel D}{n^2 - S}\right|, \left|\frac{n_\parallel P}{n_\perp^2 - P}\right|, \left|\frac{n_\perp D}{n^2 - S}\right| \right).
\end{aligned} \tag{2.78}
$$

This is the amplitude relationship among the field components.

2.4 Application of Theory

2.4.1 Electric and Magnetic Field Components

Properties of cold plasma waves are analyzed for specific conditions. For the initial plasma created by RF power, which can be regarded as a cold plasma, four quantities such as the perpendicular refractive index $n_\perp$, the perpendicular wavenumber $k_\perp$, the perpendicular wavelength $\lambda_\perp$, and the angle θ that the wavenumber vector makes with the direction of the toroidal magnetic field, are plotted for the fast wave and the slow wave against the electron density in Fig. 2.2 for a wave frequency of $f = \frac{\omega}{2\pi} = 200\,\text{MHz}$, $B_0 = 0.15\,\text{T}$ and $n_\parallel = -9.5$. In this thesis, the wave frequency is taken to be $200\,\text{MHz}$, the frequency used in the TST-2 experiment. $B_0 = 0.15\,\text{T}$ is the toroidal magnetic field strength in the plasma core at a major radius of $R = 380\,\text{mm}$. $n_\parallel = -9.5$ is the parallel refractive index of the main peak of the wave launched by the grill antenna used in the TST-2 experiment in this thesis in the direction opposite to the toroidal magnetic field.
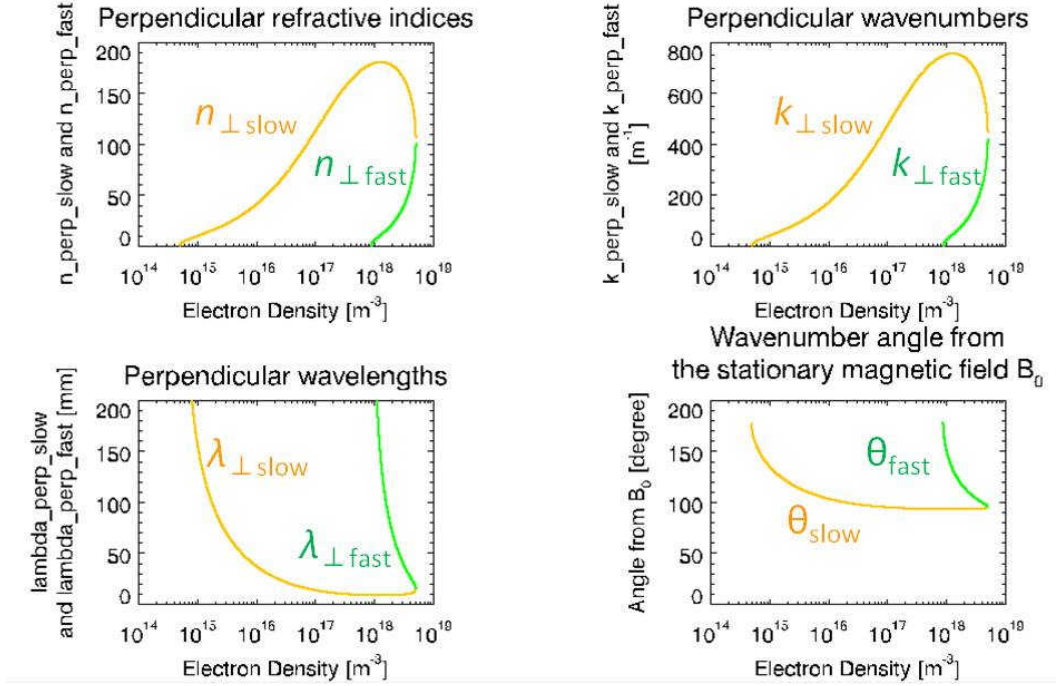
Figure 2.2: Perpendicular refractive indices $n_\perp$, perpendicular wavenumbers $k_\perp$, perpendicular wavelengths $\lambda_\perp$, and the angles θ that the wavenumber vector makes with the toroidal magnetic field for the slow wave and the fast wave for $B_0 = 0.15\,\mathrm{T}$ and $n_\parallel = -9.5$.

For $B_0 = 0.15\,\mathrm{T}$ and $n_\parallel = -9.5$, when the discriminant $b^2 - 4ac$ in the cold plasma dispersion relation Eq. (2.56) is positive and for densities above the respective cutoff densities, the fast wave and the slow wave exist as propagating waves. For the density range 10^{16} to $10^{18}\,\mathrm{m}^{-3}$ typical of the initial plasma, the slow wave is propagating whereas the fast wave is virtually evanescent. Thus, the slow wave can be used effectively to drive the plasma current. The perpendicular wavelengths $\lambda_{\perp\mathrm{slow}}$ and $\lambda_{\perp\mathrm{fast}}$ shown in Fig. 2.2 were calculated as

$$\lambda_\perp = \frac{2\pi}{k_\perp}. \tag{2.79}$$

These perpendicular wavelengths were used in determining the electrode length of the Langmuir probe.

From Eq. (2.78), the field amplitudes relative to $|E_x(\omega, \boldsymbol{k})|$ were obtained using the calculated $n_{\perp\mathrm{slow}}$ and $n_{\perp\mathrm{fast}}$. These ratios are plotted in Fig. 2.3 where the top figures are for the slow wave and the bottom figures are for the fast wave. Note that the scales of $\boldsymbol{E}(\omega, \boldsymbol{k})$ and $c\boldsymbol{B}(\omega, \boldsymbol{k})$ are common in these plots so the amplitudes of different components can be compared directly.

The same evaluation was applied to the case with $B_0 = 0.055\,\mathrm{T}$, which is the magnetic field strength at $R = 590\,\mathrm{mm}$ where the probe assembly was located for wavenumber measurement. The results are plotted in Figs. 2.4 and 2.5. Although both the fast wave and the slow wave become less propagative at high densities than for the case with $B_0 = 0.15\,\mathrm{T}$, overall wave propagation characteristics remain the same. The red broken line in Figs. 2.3 and 2.5 will be discussed in Subsection 2.4.2.

The amplitude relation is roughly summarized in Table 2.1. Roughly speaking, the slow wave is dominantly electric and the fast wave is dominantly magnetic. For the slow wave, E_z is the largest next to E_x and this E_z of the slow wave works effectively in driving a toroidal plasma current, which is in the z direction. Therefore the slow wave is used for the non-inductive plasma current drive in
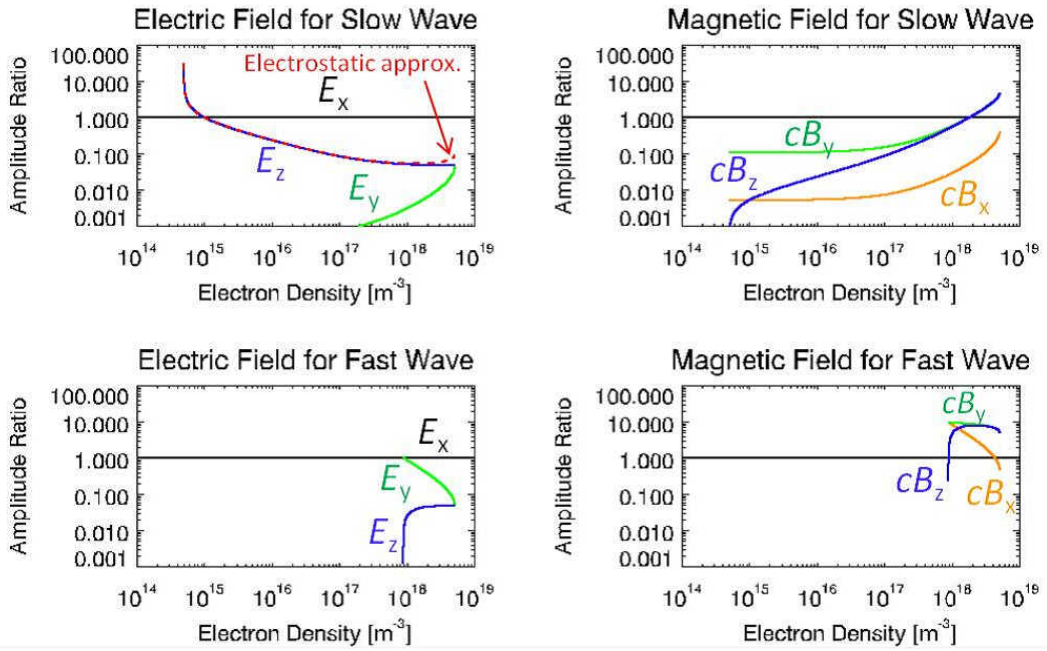
Figure 2.3: Field amplitudes relative to $|E_x(\omega, \boldsymbol{k})|$ for the slow wave and the fast wave for $B_0 = 0.15\,\mathrm{T}$ and $n_\parallel = -9.5$.
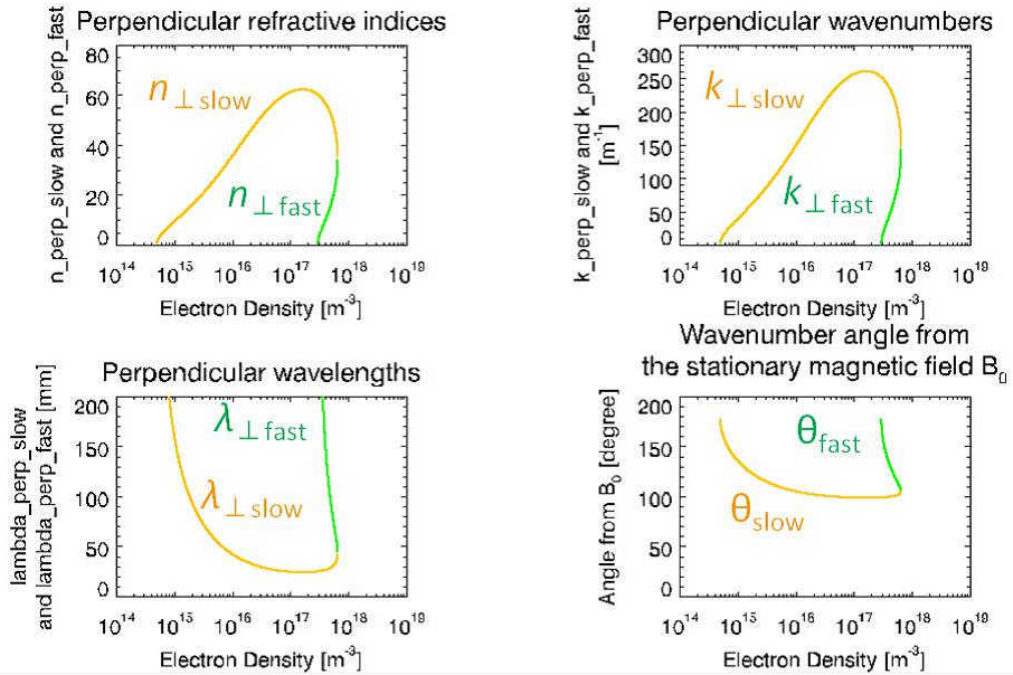
Figure 2.4: Perpendicular refractive indices $n_\perp$, perpendicular wavenumbers $k_\perp$, perpendicular wavelengths $\lambda_\perp$, and the angles θ that the wavenumber vector makes with the toroidal magnetic field for the slow wave and the fast wave for $B_0 = 0.055\,\mathrm{T}$ and $n_\parallel = -9.5$.
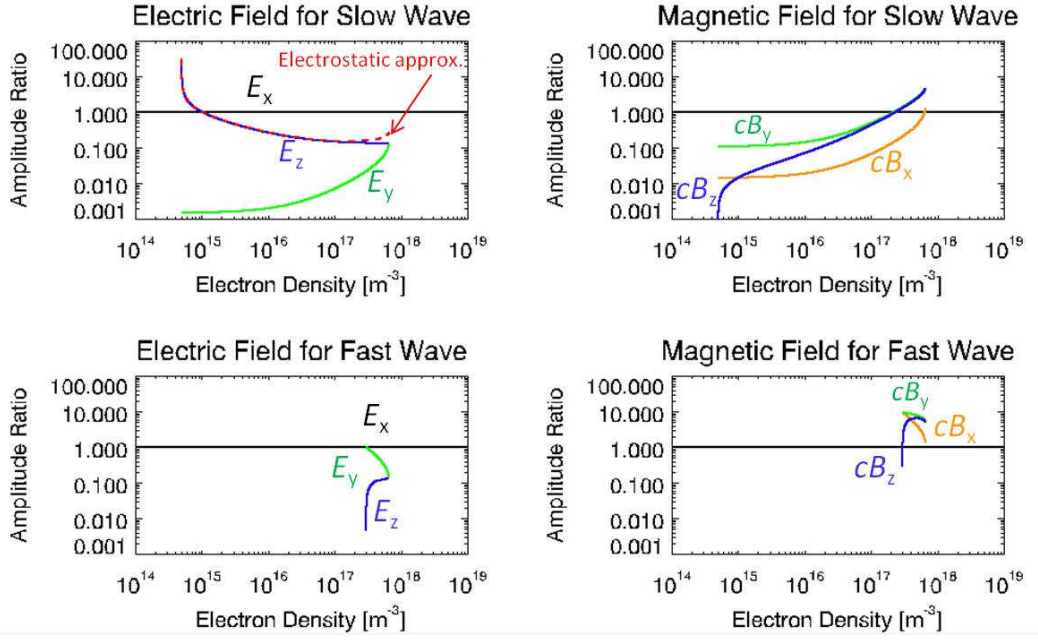
Figure 2.5: Field amplitudes relative to $|E_x(\omega, \boldsymbol{k})|$ for the slow wave and the fast wave for $B_0 = 0.055\,\mathrm{T}$ and $n_\parallel = -9.5$.

Table 2.1: Amplitude relation of wave components with reference to $E_x = 1$.

Wave component	Slow wave	Fast wave
E_x	1	1
E_y	$0.001 \sim 0.01$	$0.1 \sim 1$
E_z	$0.1 \sim 1$	0.1
cB_x	$0.01 \sim 0.1$	$1 \sim 10$
cB_y	$0.1 \sim 1$	10
cB_z	$0.01 \sim 1$	$1 \sim 10$

tokamaks and spherical tokamaks.

2.4.2 Electrostatic Wave

Since the slow wave is used for the plasma current drive and is electric field-dominant in the initial plasma for 200 MHz, it is helpful to consider the electric field in more detail. The electric field is given by

$$\boldsymbol{E} = -\nabla \phi - \frac{\partial \boldsymbol{A}}{\partial t}, \tag{2.80}$$

where ϕ is a scalar potential and $\boldsymbol{A}$ is a vector potential, which is related to a magnetic field $\boldsymbol{B}$ as

$$\boldsymbol{B} = \nabla \times \boldsymbol{A}. \tag{2.81}$$

54

The case in which the contribution from the time varying magnetic field vanishes, $\frac{\partial \boldsymbol{A}}{\partial t} = \boldsymbol{0}$, is called electrostatic. In this case, the electric field is simply written as

$$\boldsymbol{E} = -\nabla\phi. \tag{2.82}$$

Although this situation is called electrostatic, it does not mean that the charged particles are stationary. Since ϕ is determined by the spatial distribution of charged particles, their motion causes a time variation of ϕ and $\boldsymbol{E}$ changes in time. The term electrostatic means that the second term on the right hand side of Eq. (2.80) can be ignored compared to the first term.

Under the coordinate system adopted in this thesis, Eq. (2.82) gives

$$\boldsymbol{E}(\omega, \boldsymbol{k}) = -i\boldsymbol{k}\phi(\omega, \boldsymbol{k}) = -i\phi(\omega, \boldsymbol{k})\begin{pmatrix} k_\perp \\ 0 \\ k_\parallel \end{pmatrix} = -i\phi(\omega, \boldsymbol{k})k\begin{pmatrix} \sin\theta \\ 0 \\ \cos\theta \end{pmatrix}, \tag{2.83}$$

leading to

$$|E_y(\omega, \boldsymbol{k})| = 0 \tag{2.84}$$

and

$$\frac{|E_z(\omega, \boldsymbol{k})|}{|E_x(\omega, \boldsymbol{k})|} = \frac{1}{\tan\theta}. \tag{2.85}$$

The ratio $\frac{1}{\tan\theta}$, which is the ratio of electric field component magnitudes $|E_z(\omega, \boldsymbol{k})|$ to $|E_x(\omega, \boldsymbol{k})|$, is plotted in Figs. 2.3 and 2.5 in a red broken line, where θ_{slow} in Figs. 2.2 and 2.4 are used for θ, respectively. $|E_z(\omega, \boldsymbol{k})|$ shown by the purple line (slow wave as a solution of the cold-plasma dispersion relation) and by the red broken line (in the electrostatic approximation) agree with each other up to the density of at least $10^{17}\,\text{m}^{-3}$. In addition, Eq. (2.84) is consistent with the smallness of E_y for slow wave. These agreements state that the slow wave can be regarded as an electrostatic wave up to that density.

For grater densities, the slow wave deviates from the electrostatic approximation. As for Fig. 2.3, for example, this happens for densities of greater than $10^{18}\,\text{m}^{-3}$. This is because the two propagating waves, the slow wave ($\boldsymbol{E}$ dominant) and the fast wave ($\boldsymbol{B}$ dominant) become closer in quality, and a mode conversion between them occurs [51].

2.5 Physical Picture of the Lower Hybrid Wave

The slow wave at a frequency of 200 MHz used in the TST-2 experiment is classified as the Lower Hybrid Wave (LHW). In this section, the meaning of the name "Lower Hybrid Wave" and the particle motion under the influence of the LHW are described.

2.5.1 Hybrid Waves

In a magnetic confinement fusion device, both the plasma density and the static magnetic field are finite. Recalling Eq. (1.33) and Eq. (1.61), the plasma density and the static magnetic field give rise to the plasma frequency $\omega_{\text{p}s}$ and the cyclotron frequency Ω_s, respectively. These are fundamental frequencies for plasmas in a magnetic field.

Considering a perturbative displacement of the position of a charged particle purely parallel to the static magnetic field, only the longitudinal electrostatic restoring force acts on the charged particle. In this case, the particle exhibits the plasma oscillation at $\omega_{\text{p}s}$. If the perturbative displacement has a finite component perpendicular to the static magnetic field, the charged particle experiences a "hybrid" force consisting of the transverse Lorentz force and the longitudinal electrostatic force. This is the physical picture of hybrid waves. The characteristic frequencies of hybrid waves deviate from the plasma frequency $\omega_{\text{p}s}$ and the correction term is given in terms of the cyclotron frequency Ω_s.

Table 2.2: Frequencies [MHz] for the plasma core and the plasma edge of a typical initial plasma in TST-2.

frequency	in the plasma core [MHz] ($B_0 = 0.15\,\mathrm{T}$ and $n_e = 5 \times 10^{17}\,\mathrm{m^{-3}}$)	in the plasma edge [MHz] ($B_0 = 0.055\,\mathrm{T}$ and $n_e = 1 \times 10^{16}\,\mathrm{m^{-3}}$)
$\omega_{\mathrm{UH}}/(2\pi)$	7608	1782
$\omega_{\mathrm{pe}}/(2\pi)$	6345	897
$|\Omega_{\mathrm{e}}|/(2\pi)$	4197	1539
$\omega_{\mathrm{pi}}/(2\pi)$	104.7	14.8
$\omega_{\mathrm{LH}}/(2\pi)$	57.8	12.8
$\Omega_{\mathrm{i}}/(2\pi)$	1.1	0.4

Lower Hybrid and Upper Hybrid Resonance Frequencies

The two main types of hybrid waves, the lower hybrid wave and the upper hybrid wave have characteristic frequencies in the vicinities of the lower hybrid resonance frequency ω_{LH} and the upper hybrid resonance frequency ω_{UH}, respectively, where $\omega_{\mathrm{LH}} < \omega_{\mathrm{UH}}$. They are defined for perpendicular propagation ($\theta = \frac{\pi}{2}$) and are given by the two solutions for $S = 0$, where S is the Stix S parameter defined in Eq. (2.44):

$$S = \frac{R + L}{2} \simeq \frac{\omega^4 - \left(\Omega_{\mathrm{i}}^2 + \Omega_{\mathrm{e}}^2 + \omega_{\mathrm{pe}}^2\right)\omega^2 - \Omega_{\mathrm{i}}\Omega_{\mathrm{e}}\left(\omega_{\mathrm{pe}}^2 - \Omega_{\mathrm{i}}\Omega_{\mathrm{e}}\right)}{\left(\omega^2 - \Omega_{\mathrm{i}}^2\right)\left(\omega^2 - \Omega_{\mathrm{e}}^2\right)}, \tag{2.86}$$

where the approximation

$$\frac{\omega_{\mathrm{pi}}^2}{\omega_{\mathrm{pe}}^2} = \left|\frac{\Omega_{\mathrm{i}}}{\Omega_{\mathrm{e}}}\right| = \frac{Zm_{\mathrm{e}}}{m_{\mathrm{i}}} \ll 1 \tag{2.87}$$

for $Z = 1$ was used. Solving $S = 0$ under the approximation Eq. (2.87) yields [52],

$$\frac{1}{\omega_{\mathrm{LH}}^2} = \frac{1}{\Omega_{\mathrm{i}}^2 + \omega_{\mathrm{pi}}^2} + \frac{1}{|\Omega_{\mathrm{i}}\Omega_{\mathrm{e}}|}, \tag{2.88}$$

and

$$\omega_{\mathrm{UH}}^2 = \Omega_{\mathrm{e}}^2 + \omega_{\mathrm{pe}}^2. \tag{2.89}$$

In Eq. (2.88), $\omega_{\mathrm{LH}}^2 \simeq \Omega_{\mathrm{i}}^2 + \omega_{\mathrm{pi}}^2$ for $\omega_{\mathrm{pe}} \ll \Omega_{\mathrm{e}}$ whereas $\omega_{\mathrm{LH}}^2 \simeq |\Omega_{\mathrm{i}}\Omega_{\mathrm{e}}|$ for $\omega_{\mathrm{pe}} \gg \Omega_{\mathrm{e}}$. For $\theta = \frac{\pi}{2}$, $n_\parallel = 0$ follows from Eq. (2.54), and from Eqs. (2.57)–(2.60), the perpendicular refractive index $n_\perp$ is given as

$$n_\perp^2 = \frac{RL}{S}. \tag{2.90}$$

As S approaches to zero, $n_\perp^2$ (and therefore $k_\perp^2$) goes to infinity, and both the phase velocity and the group velocity go to zero, resulting in wave energy pile up in a localized space. This is called the resonance. From the plasma current drive point of view, the resonance is not necessarily favorable, because the wave energy becomes concentrated and as the wavelength shortens the wave can be converted to another wave which is less suitable for current drive [51].

Comparison of Frequencies

The characteristic frequencies Ω_s, $\omega_{\mathrm{p}s}$, ω_{LH}, and ω_{UH} are tabulated for the core plasma and the edge plasma (where the wavenumber measurement is conducted) of a typical initial plasma in TST-2 in Table 2.2. The frequency of 200 MHz used in TST-2 is close to the ion plasma frequency ω_{pi} and the lower hybrid resonance frequency ω_{LH}. In the presence of the magnetic field, the ion plasma oscillation is modified as described in the next subsection, and the wave is called the lower hybrid wave.

2.5.2 Motion of Charged Particles in the Lower Hybrid Wave

Since the 200 MHz slow wave in an initial TST-2 plasma is an electrostatic wave, as shown in Figs. 2.3 and 2.5, E_y can be set to zero as in Eq. (2.84). For $E_y = 0$, the solution of the equation of motion Eq. (2.36) reduces to

$$
\begin{cases}
v_{sx}(\omega, \boldsymbol{k}) = i\omega \dfrac{q_s}{m_s\left(\omega^2 - \Omega_s^2\right)} E_x(\omega, \boldsymbol{k}) & (2.91) \\[3mm]
v_{sy}(\omega, \boldsymbol{k}) = \Omega_s \dfrac{q_s}{m_s\left(\omega^2 - \Omega_s^2\right)} E_x(\omega, \boldsymbol{k}) & (2.92) \\[3mm]
v_{sz}(\omega, \boldsymbol{k}) = i\dfrac{q_s}{m_s\omega} E_z(\omega, \boldsymbol{k}). & (2.93)
\end{cases}
$$

Using a shortcut representation [51] with single values for ω and $\boldsymbol{k}$, the velocity of the charged particle $\boldsymbol{v}(t, \boldsymbol{r})$ can be written as

$$
\boldsymbol{v}_s(t, \boldsymbol{r}) \sim \mathrm{Re}\left[\boldsymbol{v}_s(\omega, \boldsymbol{k})e^{i(\boldsymbol{k}\cdot\boldsymbol{r} - \omega t)}\right]. \tag{2.94}
$$

Equations (2.91)–(2.93) give

$$
\begin{cases}
v_{sx}(t, \boldsymbol{r}) = A_0 \dfrac{q_s\omega}{m_s\left(\omega^2 - \Omega_s^2\right)} \mathrm{Re}\left[iE_x(\omega, \boldsymbol{k})e^{i(\boldsymbol{k}\cdot\boldsymbol{r} - \omega t)}\right] & (2.95) \\[3mm]
v_{sy}(t, \boldsymbol{r}) = A_0 \dfrac{q_s\Omega_s}{m_s\left(\omega^2 - \Omega_s^2\right)} \mathrm{Re}\left[E_x(\omega, \boldsymbol{k})e^{i(\boldsymbol{k}\cdot\boldsymbol{r} - \omega t)}\right] & (2.96) \\[3mm]
v_{sz}(t, \boldsymbol{r}) = D_0 \dfrac{q_s}{m_s\omega} \mathrm{Re}\left[iE_z(\omega, \boldsymbol{k})e^{i(\boldsymbol{k}\cdot\boldsymbol{r} - \omega t)}\right], & (2.97)
\end{cases}
$$

where A_0 and D_0 are real correction coefficients due to the shortcut representation. A_0 in Eq. (2.95) and A_0 in Eq. (2.96) are the same because the operation Re[ ] is applied to $iE_x(\omega, \boldsymbol{k})$ and $E_x(\omega, \boldsymbol{k})$, which have the same absolute values $|E_x(\omega, \boldsymbol{k})|$. Using

$$
\mathrm{Re}\left[iE_j(\omega, \boldsymbol{k})e^{i(\boldsymbol{k}\cdot\boldsymbol{r} - \omega t)}\right] = |E_j(\omega, \boldsymbol{k})|\cos\left\{\boldsymbol{k}\cdot\boldsymbol{r} - \omega t + \arg\left[E_j(\omega, \boldsymbol{k})\right] + \frac{\pi}{2}\right\} \text{ for } j = x \text{ and } z,
$$
$$\tag{2.98}$$

$$
\mathrm{Re}\left[E_x(\omega, \boldsymbol{k})e^{i(\boldsymbol{k}\cdot\boldsymbol{r} - \omega t)}\right] = |E_x(\omega, \boldsymbol{k})|\cos\left\{\boldsymbol{k}\cdot\boldsymbol{r} - \omega t + \arg\left[E_x(\omega, \boldsymbol{k})\right]\right\}, \tag{2.99}
$$

and defining real lengths R_s and R_{sz} as

$$
R_s = A_0 \frac{q_s|E_x(\omega, \boldsymbol{k})|}{m_s\left(\omega^2 - \Omega_s^2\right)}, \tag{2.100}
$$

$$
R_{sz} = D_0 \frac{q_s|E_z(\omega, \boldsymbol{k})|}{m_s\omega^2}, \tag{2.101}
$$

Eqs. (2.95)–(2.97) lead to

$$
\begin{cases}
v_{sx} = -\omega R_s \sin\left\{\boldsymbol{k}\cdot\boldsymbol{r} - \omega t + \arg\left[E_x(\omega, \boldsymbol{k})\right]\right\} & (2.102) \\[2mm]
v_{sy} = \Omega_s R_s \cos\left\{\boldsymbol{k}\cdot\boldsymbol{r} - \omega t + \arg\left[E_x(\omega, \boldsymbol{k})\right]\right\} & (2.103) \\[2mm]
v_{sz} = -\omega R_{sz} \sin\left\{\boldsymbol{k}\cdot\boldsymbol{r} - \omega t + \arg\left[E_z(\omega, \boldsymbol{k})\right]\right\}. & (2.104)
\end{cases}
$$

and integrating by time t gives the position of the charged particle as

$$
\begin{cases}
x_{sx} - x_0 = -R_s \cos\left\{\boldsymbol{k}\cdot\boldsymbol{r} - \omega t + \arg\left[E_x(\omega, \boldsymbol{k})\right]\right\} & (2.105) \\[2mm]
y_{sy} - y_0 = -\dfrac{\Omega_s}{\omega} R_s \sin\left\{\boldsymbol{k}\cdot\boldsymbol{r} - \omega t + \arg\left[E_x(\omega, \boldsymbol{k})\right]\right\} & (2.106) \\[2mm]
z_{sz} - z_0 = -R_{sz} \cos\left\{\boldsymbol{k}\cdot\boldsymbol{r} - \omega t + \arg\left[E_z(\omega, \boldsymbol{k})\right]\right\}. & (2.107)
\end{cases}
$$
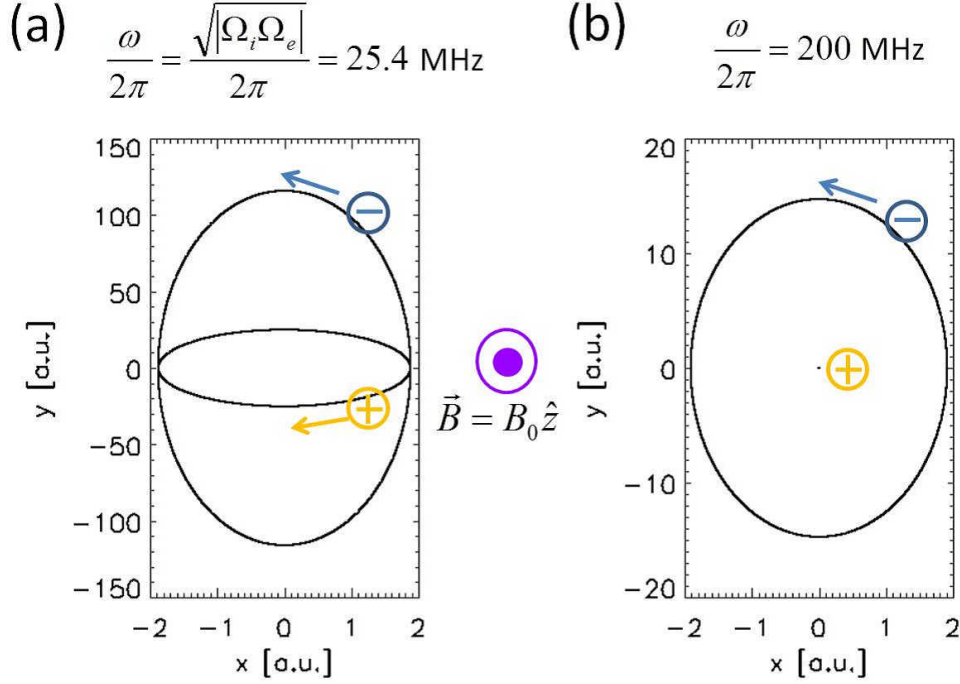
Figure 2.6: Particle orbits in the presence of the LHW for $B_0 = 0.055\,\mathrm{T}$. (a) For $\omega / (2\pi) = \sqrt{|\Omega_i \Omega_e|} / (2\pi) = 25.4\,\mathrm{MHz}$. Ion motion is enlarged in the y direction by a factor 5×10^4. (b) For $\omega / (2\pi) = 200\,\mathrm{MHz}$.

The initial position ${}^t\boldsymbol{r}_0 = (x_0, y_0, z_0)$ is common to ions $(s = \mathrm{i})$ and electrons $(s = \mathrm{e})$ due to the charge neutrality of the plasma. From Eq. (2.75), since $E_z(\omega, \boldsymbol{k})$ is given by multiplying $E_x(\omega, \boldsymbol{k})$ by $\frac{n_\parallel n_\perp}{n_\perp^2 - P}$ which is real in the propagating region, $E_x(\omega, \boldsymbol{k})$ and $E_z(\omega, \boldsymbol{k})$ are in phase. Thus $\arg [E_x(\omega, \boldsymbol{k})]$ and $\arg [E_z(\omega, \boldsymbol{k})]$ can be dropped, resulting in

$$
\begin{cases}
x_{sx} - x_0 = -R_s \cos (\boldsymbol{k} \cdot \boldsymbol{r} - \omega t) & (2.108) \\[2mm]
y_{sy} - y_0 = -\dfrac{\Omega_s}{\omega} R_s \sin (\boldsymbol{k} \cdot \boldsymbol{r} - \omega t) & (2.109) \\[2mm]
z_{sz} - z_0 = -R_{sz} \cos (\boldsymbol{k} \cdot \boldsymbol{r} - \omega t). & (2.110)
\end{cases}
$$

These equations state that the charged particle trajectory is an ellipse with major and minor radii R_s and $\frac{\Omega_s}{\omega} R_s$ in the x-y plane and oscillates in the z direction (in the direction of $\boldsymbol{B}_0$) with an amplitude of R_{sz}. The shapes of orbits for ions and electrons in the x-y plane are shown in Fig. 2.6 for $\omega = \sqrt{|\Omega_i \Omega_e|}$ and $\omega / (2\pi) = 200\,\mathrm{MHz}$ for $B_0 = 0.055\,\mathrm{T}$. For $\omega = \sqrt{|\Omega_i \Omega_e|}$, the radii for the ion and the electron in the x direction are same. At 200 MHz, ions are nearly fixed to the magnetic field line because the ion inertia is too large to follow the oscillation at such high frequency. On the other hand, electrons mainly exhibit the $\boldsymbol{E} \times \boldsymbol{B}$ motion. It should be noted that the center of particle orbit does not move in a cold plasma.

2.6 Wave Energy Density and Group Velocity

Although the center of the orbit of a charged particle moving under the influence of the LHW does not move in a cold plasma, the wave energy associated with the LHW propagates in the plasma. In

this section, the wave energy density W is defined and the velocity of wave energy propagation, called the group velocity $\boldsymbol{v}_{\mathrm{g}}$ [51], is calculated for the LHW. Both W and $\boldsymbol{v}_{\mathrm{g}}$ are important quantities for evaluating damping of wave energy.

2.6.1 Wave Energy Density

The purpose of this subsection is to express the wave energy density W and some related quantities in terms of $\boldsymbol{E}(\omega, \boldsymbol{k})$, $\boldsymbol{B}(\omega, \boldsymbol{k})$, and $\boldsymbol{\epsilon}(\omega, \boldsymbol{k})$ since the wave energy of the LHW for a particular $(\omega, \boldsymbol{k})$ is of interest.

Poynting Theorem

The power given to charged particles by the electromagnetic field is given by $\boldsymbol{j} \cdot \boldsymbol{E}$, since the Lorentz force $\boldsymbol{v} \times \boldsymbol{B}$ does not do work. Equation (2.4) is used to rewrite $\boldsymbol{j} \cdot \boldsymbol{E}$ as

$$\boldsymbol{j} \cdot \boldsymbol{E} = \boldsymbol{E} \cdot (\nabla \times \boldsymbol{H}) - \boldsymbol{E} \cdot \frac{\partial \boldsymbol{D}}{\partial t}. \tag{2.111}$$

Using the vector identity

$$\nabla \cdot (\boldsymbol{E} \times \boldsymbol{H}) = \boldsymbol{H} \cdot (\nabla \times \boldsymbol{E}) - \boldsymbol{E} \cdot (\nabla \times \boldsymbol{H}) \tag{2.112}$$

and Faraday's law Eq. (2.2), Eq. (2.111) leads to

$$\boldsymbol{j} \cdot \boldsymbol{E} = - \left\{ \nabla \cdot (\boldsymbol{E} \times \boldsymbol{H}) + \boldsymbol{E} \cdot \frac{\partial \boldsymbol{D}}{\partial t} + \boldsymbol{H} \cdot \frac{\partial \boldsymbol{B}}{\partial t} \right\}. \tag{2.113}$$

This is the Poynting Theorem. The Poynting vector $\boldsymbol{S}'$ is defined as

$$\boldsymbol{S}' = \boldsymbol{E} \times \boldsymbol{H}. \tag{2.114}$$

Considering a plasma with no external current density, the current density in the plasma is regarded as an internal response of the plasma to the electromagnetic field. The effect of this internal current density is included in the electric and magnetic field terms, leading to $\boldsymbol{j} = \boldsymbol{0}$. For this case, Eq. (2.113) reduces to

$$\nabla \cdot \boldsymbol{S}' + \left(\boldsymbol{E} \cdot \frac{\partial \boldsymbol{D}}{\partial t} + \boldsymbol{H} \cdot \frac{\partial \boldsymbol{B}}{\partial t} \right) = 0. \tag{2.115}$$

Equation (2.115) is an energy conservation equation for waves in plasmas with no external current.

Expression of Wave Energy Density using Complex Wave Amplitudes $\boldsymbol{E}(\omega, \boldsymbol{k})$ and $\boldsymbol{B}(\omega, \boldsymbol{k})$

In order to express the energy conservation equation (2.115) given for $(t, \boldsymbol{r})$ in terms of $(\omega, \boldsymbol{k})$, the shortcut representation Eq. (2.94) is used such that

$$\boldsymbol{E}(t, \boldsymbol{r}) = \mathrm{Re} \left[\boldsymbol{E}(\omega, \boldsymbol{k}) e^{-i\phi(t, \boldsymbol{r})} \right], \tag{2.116}$$

where the equal sign is used [51]. The phase factor $\phi(t, \boldsymbol{r})$ is called the "eikonal" and is expressed as

$$\begin{aligned}
\phi(t, \boldsymbol{r}) &\equiv -\boldsymbol{k} \cdot \boldsymbol{r} + \omega t \\
&= -(\boldsymbol{k}_{\mathrm{r}} + i\boldsymbol{k}_{\mathrm{i}}) \cdot \boldsymbol{r} + (\omega_{\mathrm{r}} + i\omega_{\mathrm{i}}) t \\
&= (-\boldsymbol{k}_{\mathrm{r}} \cdot \boldsymbol{r} + \omega_{\mathrm{r}} t) + i(-\boldsymbol{k}_{\mathrm{i}} \cdot \boldsymbol{r} + \omega_{\mathrm{i}} t) \\
&\equiv \phi_{\mathrm{r}}(t, \boldsymbol{r}) + i\phi_{\mathrm{i}}(t, \boldsymbol{r}),
\end{aligned} \tag{2.117}$$

59

where $\boldsymbol{k}_i$ and ω_i are imaginary parts of $\boldsymbol{k}$ and ω given by

$$\boldsymbol{k}_i = -\nabla\phi_i(t, \boldsymbol{r}), \tag{2.118}$$

$$\omega_i = \frac{\partial}{\partial t}\phi_i(t, \boldsymbol{r}). \tag{2.119}$$

The imaginary part $\phi_i(t, \boldsymbol{r})$ describes temporal/spatial variations of the wave amplitude over several periods/wavelengths. Note that Eq. (2.115) consists of products of vector quantities with a common phase. The product between vectors $\boldsymbol{X}(t, \boldsymbol{r})$ and $\boldsymbol{Y}(t, \boldsymbol{r})$ with a common $\phi(t, \boldsymbol{r})$ is expressed as

$$
\begin{aligned}
\boldsymbol{X}(t, \boldsymbol{r})\boldsymbol{Y}(t, \boldsymbol{r}) &= \mathrm{Re}\left[\boldsymbol{X}(\omega, \boldsymbol{k})e^{-i\phi(t, \boldsymbol{r})}\right]\mathrm{Re}\left[\boldsymbol{Y}(\omega, \boldsymbol{k})e^{-i\phi(t, \boldsymbol{r})}\right] \\
&= \frac{1}{2}\left(\boldsymbol{X}e^{-i\phi} + \overline{\boldsymbol{X}e^{-i\phi}}\right)\frac{1}{2}\left(\boldsymbol{Y}e^{-i\phi} + \overline{\boldsymbol{Y}e^{-i\phi}}\right) \\
&= \frac{1}{4}\left(\boldsymbol{XY}e^{-2i\phi} + \overline{\boldsymbol{XY}}e^{2i\overline{\phi}} + \boldsymbol{X}\overline{\boldsymbol{Y}}e^{2\phi_i} + \overline{\boldsymbol{X}}\boldsymbol{Y}e^{2\phi_i}\right),
\end{aligned} \tag{2.120}
$$

where $(\omega, \boldsymbol{k})$ and $(t, \boldsymbol{r})$ were omitted from the second row. From Eq. (2.117), the first and second terms in Eq. (2.120) are proportional to $\exp\{\pm i\left[\phi_r(t, \boldsymbol{r})\right]\}$. If $\exp\{\pm i\left[\phi_r(t, \boldsymbol{r})\right]\}$ were periodic in time or space, averaging Eq. (2.120) over several periods or wavelengths gives

$$\langle\boldsymbol{X}(t, \boldsymbol{r})\boldsymbol{Y}(t, \boldsymbol{r})\rangle_{\text{ave.}} = \frac{1}{4}\left\{\boldsymbol{X}(\omega, \boldsymbol{k})\overline{\boldsymbol{Y}(\omega, \boldsymbol{k})} + \overline{\boldsymbol{X}(\omega, \boldsymbol{k})}\boldsymbol{Y}(\omega, \boldsymbol{k})\right\}\exp\left[2\phi_i(t, \boldsymbol{r})\right]. \tag{2.121}$$

Equation (2.121) provides a fundamental relationship between periodically averaged values and amplitudes expressed in $(\omega, \boldsymbol{k})$.

Using Eq. (2.121), the average of Eq. (2.115) over several periods is written as

$$\nabla\cdot\langle\boldsymbol{S'}\rangle_{\text{ave.}} + \left\langle\boldsymbol{E}\cdot\frac{\partial\boldsymbol{D}}{\partial t}\right\rangle_{\text{ave.}} + \left\langle\boldsymbol{H}\cdot\frac{\partial\boldsymbol{B}}{\partial t}\right\rangle_{\text{ave.}} = 0. \tag{2.122}$$

$\langle\boldsymbol{S'}\rangle_{\text{ave.}}$ in the first term in Eq. (2.122) is given using Eqs. (2.114), (2.11), and (2.121) as

$$\langle\boldsymbol{S'}\rangle_{\text{ave.}} = \left\langle\boldsymbol{E}\times\frac{\boldsymbol{B}}{\mu_0}\right\rangle_{\text{ave.}} = \frac{1}{4\mu_0}\left\{\boldsymbol{E}(\omega, \boldsymbol{k})\times\overline{\boldsymbol{B}(\omega, \boldsymbol{k})} + \overline{\boldsymbol{E}(\omega, \boldsymbol{k})}\times\boldsymbol{B}(\omega, \boldsymbol{k})\right\}\exp\left[2\phi_i(t, \boldsymbol{r})\right]. \tag{2.123}$$

The second term $\left\langle\boldsymbol{E}\cdot\frac{\partial\boldsymbol{D}}{\partial t}\right\rangle_{\text{ave.}}$ on the left-hand side of Eq. (2.122) is calculated as follows. $\frac{\partial\boldsymbol{D}(t, \boldsymbol{r})}{\partial t}$ is expressed as

$$
\begin{aligned}
\frac{\partial\boldsymbol{D}(t, \boldsymbol{r})}{\partial t} &= \frac{\partial}{\partial t}\mathrm{Re}\left[\boldsymbol{D}(\omega, \boldsymbol{k})e^{-i\phi(t, \boldsymbol{r})}\right] \\
&= \mathrm{Re}\left[\boldsymbol{D}(\omega, \boldsymbol{k})\frac{\partial}{\partial t}e^{-i\phi(t, \boldsymbol{r})}\right] \\
&= \mathrm{Re}\left[\epsilon_0\boldsymbol{\epsilon}(\omega, \boldsymbol{k})\cdot\boldsymbol{E}(\omega, \boldsymbol{k})\left\{-i\left(\omega_r + i\omega_i\right)\right\}e^{-i\phi(t, \boldsymbol{r})}\right],
\end{aligned} \tag{2.124}
$$

where Eqs. (2.21) and (2.117) were used. Referring to Eqs. (2.121) and (2.124), $\left\langle\boldsymbol{E}\cdot\frac{\partial\boldsymbol{D}}{\partial t}\right\rangle_{\text{ave.}}$ is given by substituting in Eq. (2.121) as

$$\boldsymbol{E}(\omega, \boldsymbol{k})\mapsto\boldsymbol{X}(\omega, \boldsymbol{k}),$$

$$\epsilon_0\boldsymbol{\epsilon}(\omega, \boldsymbol{k})\cdot\boldsymbol{E}(\omega, \boldsymbol{k})\left(\omega_i - i\omega_r\right)\mapsto\boldsymbol{Y}(\omega, \boldsymbol{k}),$$

with the result

$$\left\langle\boldsymbol{E}\cdot\frac{\partial\boldsymbol{D}}{\partial t}\right\rangle_{\text{ave.}} = \frac{1}{4}\epsilon_0\left\{\omega_i\overline{\boldsymbol{E}}\cdot\left(\boldsymbol{\epsilon} + \boldsymbol{\epsilon}^\dagger\right)\cdot\boldsymbol{E} + \omega_r\overline{\boldsymbol{E}}\cdot\left(-i\boldsymbol{\epsilon} + i\boldsymbol{\epsilon}^\dagger\right)\cdot\boldsymbol{E}\right\}\exp\left[2\phi_i(t, \boldsymbol{r})\right], \tag{2.125}$$

where $(\omega, \boldsymbol{k})$ is omitted and

$$\overline{\boldsymbol{\epsilon}(\omega, \boldsymbol{k}) \cdot \boldsymbol{E}(\omega, \boldsymbol{k})} = \overline{\boldsymbol{\epsilon}(\omega, \boldsymbol{k})} \cdot \overline{\boldsymbol{E}(\omega, \boldsymbol{k})},$$
$$\boldsymbol{E}(\omega, \boldsymbol{k}) \cdot \overline{\boldsymbol{\epsilon}(\omega, \boldsymbol{k})} \cdot \overline{\boldsymbol{E}(\omega, \boldsymbol{k})} = \overline{\boldsymbol{E}(\omega, \boldsymbol{k})} \cdot \boldsymbol{\epsilon}^\dagger(\omega, \boldsymbol{k}) \cdot \boldsymbol{E}(\omega, \boldsymbol{k}),$$

were used. $\boldsymbol{\epsilon}^\dagger(\omega, \boldsymbol{k})$ is the complex conjugate of the transposed matrix of $\boldsymbol{\epsilon}(\omega, \boldsymbol{k})$.

Similarly, the third term $\left\langle \boldsymbol{H} \cdot \frac{\partial \boldsymbol{B}}{\partial t} \right\rangle_{\text{ave.}}$ on the left-hand side of Eq. (2.122) is given by substituting in Eq. (2.121) as

$$\frac{\boldsymbol{B}(\omega, \boldsymbol{k})}{\mu_0} \mapsto \boldsymbol{X}(\omega, \boldsymbol{k}),$$
$$\boldsymbol{B}(\omega, \boldsymbol{k})\,(\omega_{\mathrm{i}} - i\omega_{\mathrm{r}}) \mapsto \boldsymbol{Y}(\omega, \boldsymbol{k}),$$

with the result

$$\left\langle \boldsymbol{H} \cdot \frac{\partial \boldsymbol{B}}{\partial t} \right\rangle_{\text{ave.}} = \frac{1}{4\mu_0} \left\{ 2\omega_{\mathrm{i}} \overline{\boldsymbol{B}(\omega, \boldsymbol{k})} \cdot \boldsymbol{B}(\omega, \boldsymbol{k}) \right\} \exp\left[2\phi_{\mathrm{i}}(t, \boldsymbol{r})\right]. \tag{2.126}$$

Thus, the energy conservation Eq. (2.122) is expressed in terms of Eqs. (2.123), (2.125), and (2.126).

Simplification under the Condition $|\omega_{\mathrm{i}}| \ll |\omega|$ and $|\boldsymbol{k}_{\mathrm{i}}| \ll |\boldsymbol{k}|$

For $|\omega_{\mathrm{i}}| \ll |\omega|$ and $|\boldsymbol{k}_{\mathrm{i}}| \ll |\boldsymbol{k}|$, Eq. (2.125) can be simplified as follows. $\boldsymbol{\epsilon}(\omega, \boldsymbol{k})$ is decomposed into the Hermitian component $\boldsymbol{\epsilon}_{\mathrm{h}}(\omega, \boldsymbol{k}) \left(= \boldsymbol{\epsilon}_{\mathrm{h}}^\dagger(\omega, \boldsymbol{k})\right)$ and the anti-Hermitian component $i\boldsymbol{\epsilon}_{\mathrm{a}}(\omega, \boldsymbol{k})$ as

$$\boldsymbol{\epsilon}(\omega, \boldsymbol{k}) = \boldsymbol{\epsilon}_{\mathrm{h}}(\omega, \boldsymbol{k}) + i\boldsymbol{\epsilon}_{\mathrm{a}}(\omega, \boldsymbol{k}), \tag{2.127}$$
$$\boldsymbol{\epsilon}^\dagger(\omega, \boldsymbol{k}) = \boldsymbol{\epsilon}_{\mathrm{h}}^\dagger(\omega, \boldsymbol{k}) - i\boldsymbol{\epsilon}_{\mathrm{a}}(\omega, \boldsymbol{k}), \tag{2.128}$$

where

$$\left\{i\boldsymbol{\epsilon}_{\mathrm{a}}(\omega, \boldsymbol{k})\right\}^\dagger = -i\boldsymbol{\epsilon}_{\mathrm{a}}(\omega, \boldsymbol{k})$$

was used. For $\boldsymbol{\epsilon}_{\mathrm{h}}(\omega, \boldsymbol{k})$, under the condition $|\omega_{\mathrm{i}}| \ll |\omega|$ and $|\boldsymbol{k}_{\mathrm{i}}| \ll |\boldsymbol{k}|$, analytical continuation by a small distance into the complex $\omega, \boldsymbol{k}$ planes gives

$$\boldsymbol{\epsilon}_{\mathrm{h}}(\omega_{\mathrm{r}} + i\omega_{\mathrm{i}},\ \boldsymbol{k}_{\mathrm{r}} + i\boldsymbol{k}_{\mathrm{i}}) = \left[\boldsymbol{\epsilon}_{\mathrm{h}} + i\omega_{\mathrm{i}}\frac{\partial}{\partial \omega}\boldsymbol{\epsilon}_{\mathrm{h}} + i\boldsymbol{k}_{\mathrm{i}} \cdot \frac{\partial}{\partial \boldsymbol{k}}\boldsymbol{\epsilon}_{\mathrm{h}}\right]_{\omega_{\mathrm{r}},\ \boldsymbol{k}_{\mathrm{r}}} + \cdots, \tag{2.129}$$

$$\boldsymbol{\epsilon}_{\mathrm{h}}^\dagger(\omega_{\mathrm{r}} + i\omega_{\mathrm{i}},\ \boldsymbol{k}_{\mathrm{r}} + i\boldsymbol{k}_{\mathrm{i}}) = \left[\boldsymbol{\epsilon}_{\mathrm{h}} - i\omega_{\mathrm{i}}\frac{\partial}{\partial \omega}\boldsymbol{\epsilon}_{\mathrm{h}} - i\boldsymbol{k}_{\mathrm{i}} \cdot \frac{\partial}{\partial \boldsymbol{k}}\boldsymbol{\epsilon}_{\mathrm{h}}\right]_{\omega_{\mathrm{r}},\ \boldsymbol{k}_{\mathrm{r}}} + \cdots. \tag{2.130}$$

Using Eqs. (2.127)–(2.130), $\left(\boldsymbol{\epsilon} + \boldsymbol{\epsilon}^\dagger\right)$ and $\left(-i\boldsymbol{\epsilon} + i\boldsymbol{\epsilon}^\dagger\right)$ in Eq. (2.125) can be calculated as

$$\begin{aligned}
&\boldsymbol{\epsilon} + \boldsymbol{\epsilon}^\dagger \\
={}& \boldsymbol{\epsilon}(\omega_{\mathrm{r}} + i\omega_{\mathrm{i}},\ \boldsymbol{k}_{\mathrm{r}} + i\boldsymbol{k}_{\mathrm{i}}) + \boldsymbol{\epsilon}^\dagger(\omega_{\mathrm{r}} + i\omega_{\mathrm{i}},\ \boldsymbol{k}_{\mathrm{r}} + i\boldsymbol{k}_{\mathrm{i}}) \\
={}& \boldsymbol{\epsilon}_{\mathrm{h}}(\omega_{\mathrm{r}} + i\omega_{\mathrm{i}},\ \boldsymbol{k}_{\mathrm{r}} + i\boldsymbol{k}_{\mathrm{i}}) + \boldsymbol{\epsilon}_{\mathrm{h}}^\dagger(\omega_{\mathrm{r}} + i\omega_{\mathrm{i}},\ \boldsymbol{k}_{\mathrm{r}} + i\boldsymbol{k}_{\mathrm{i}}) \\
\simeq{}& 2\boldsymbol{\epsilon}_{\mathrm{h}}(\omega_{\mathrm{r}},\ \boldsymbol{k}_{\mathrm{r}})
\end{aligned} \tag{2.131}$$

and

$$\begin{aligned}
&-i\boldsymbol{\epsilon} + i\boldsymbol{\epsilon}^\dagger \\
={}& -i\boldsymbol{\epsilon}(\omega_{\mathrm{r}} + i\omega_{\mathrm{i}},\ \boldsymbol{k}_{\mathrm{r}} + i\boldsymbol{k}_{\mathrm{i}}) + i\boldsymbol{\epsilon}^\dagger(\omega_{\mathrm{r}} + i\omega_{\mathrm{i}},\ \boldsymbol{k}_{\mathrm{r}} + i\boldsymbol{k}_{\mathrm{i}}) \\
={}& -i\left\{\boldsymbol{\epsilon}_{\mathrm{h}}(\omega_{\mathrm{r}} + i\omega_{\mathrm{i}},\ \boldsymbol{k}_{\mathrm{r}} + i\boldsymbol{k}_{\mathrm{i}}) - \boldsymbol{\epsilon}_{\mathrm{h}}^\dagger(\omega_{\mathrm{r}} + i\omega_{\mathrm{i}},\ \boldsymbol{k}_{\mathrm{r}} + i\boldsymbol{k}_{\mathrm{i}})\right\} + 2\boldsymbol{\epsilon}_{\mathrm{a}}(\omega_{\mathrm{r}},\ \boldsymbol{k}_{\mathrm{r}}) \\
\simeq{}& 2\omega_{\mathrm{i}}\frac{\partial}{\partial \omega}\boldsymbol{\epsilon}_{\mathrm{h}}(\omega_{\mathrm{r}},\ \boldsymbol{k}_{\mathrm{r}}) + 2\boldsymbol{k}_{\mathrm{i}} \cdot \frac{\partial}{\partial \boldsymbol{k}}\boldsymbol{\epsilon}_{\mathrm{h}}(\omega_{\mathrm{r}},\ \boldsymbol{k}_{\mathrm{r}}) + 2\boldsymbol{\epsilon}_{\mathrm{a}}(\omega_{\mathrm{r}},\ \boldsymbol{k}_{\mathrm{r}}).
\end{aligned} \tag{2.132}$$

Substituting Eqs. (2.131) and (2.132) into Eq. (2.125) gives

$$\left\langle \boldsymbol{E} \cdot \frac{\partial \boldsymbol{D}}{\partial t} \right\rangle_{\text{ave.}} = \frac{1}{4}\epsilon_0 \left\{ 2\omega_i \overline{\boldsymbol{E}} \cdot \boldsymbol{\epsilon}_{\text{h}} \cdot \boldsymbol{E} + 2\omega_r \overline{\boldsymbol{E}} \cdot \left(\omega_i \frac{\partial}{\partial \omega} \boldsymbol{\epsilon}_{\text{h}} + \boldsymbol{k}_i \cdot \frac{\partial}{\partial \boldsymbol{k}} \boldsymbol{\epsilon}_{\text{h}} + \boldsymbol{\epsilon}_{\text{a}} \right) \cdot \boldsymbol{E} \right\} \exp\left[2\phi_i(t,\boldsymbol{r})\right]. \tag{2.133}$$

The wave energy conservation equation (2.122) is now expressed in terms of $\boldsymbol{k}_i$ and ω_i using Eqs. (2.123), (2.126), and (2.133). $\nabla \cdot \langle \boldsymbol{S}' \rangle_{\text{ave.}}$ in Eq. (2.122) is expressed using Eqs. (2.118) and (2.123) as

$$\nabla \cdot \langle \boldsymbol{S}' \rangle_{\text{ave.}} = -2\left(\boldsymbol{k}_i \cdot \boldsymbol{S}\right) \exp\left[2\phi_i(t,\boldsymbol{r})\right], \tag{2.134}$$

where $\boldsymbol{S}$ is in the form of

$$\boldsymbol{S} \equiv \frac{1}{4\mu_0} \left(\boldsymbol{E} \times \overline{\boldsymbol{B}} + \overline{\boldsymbol{E}} \times \boldsymbol{B} \right) \tag{2.135}$$

and is discussed below.

Equations (2.134), (2.133), and (2.126) are substituted into the energy conservation equation (2.122), with the common coefficient $\exp\left[2\phi_i(t,\boldsymbol{r})\right]$ dropped, to give

$$\begin{aligned}
0 &= \nabla \cdot \langle \boldsymbol{S}' \rangle_{\text{ave.}} + \left\langle \boldsymbol{E} \cdot \frac{\partial \boldsymbol{D}}{\partial t} \right\rangle_{\text{ave.}} + \left\langle \boldsymbol{H} \cdot \frac{\partial \boldsymbol{B}}{\partial t} \right\rangle_{\text{ave.}} \\
&= -2\boldsymbol{k}_i \cdot \left(\boldsymbol{S} - \frac{1}{4}\epsilon_0 \omega_r \overline{\boldsymbol{E}} \cdot \frac{\partial}{\partial \boldsymbol{k}} \boldsymbol{\epsilon}_{\text{h}} \cdot \boldsymbol{E} \right) + 2\omega_i \cdot \frac{1}{4} \left\{ \frac{\overline{\boldsymbol{B}} \cdot \boldsymbol{B}}{\mu_0} + \epsilon_0 \overline{\boldsymbol{E}} \cdot \left(\boldsymbol{\epsilon}_{\text{h}} + \omega_r \frac{\partial}{\partial \omega} \boldsymbol{\epsilon}_{\text{h}} \right) \cdot \boldsymbol{E} \right\} \\
&\quad + \frac{1}{2}\epsilon_0 \omega_r \overline{\boldsymbol{E}} \cdot \boldsymbol{\epsilon}_{\text{a}} \cdot \boldsymbol{E} \\
&\equiv -2\boldsymbol{k}_i \cdot (\boldsymbol{S} + \boldsymbol{T}) + 2\omega_i W + \left(\frac{\partial W}{\partial t} \right)_{\text{lossy}}, \tag{2.136}
\end{aligned}$$

where

$$\boldsymbol{S} \equiv \frac{1}{4\mu_0} \left(\boldsymbol{E} \times \overline{\boldsymbol{B}} + \overline{\boldsymbol{E}} \times \boldsymbol{B} \right)$$

is the flux density of electromagnetic energy defined in Eq. (2.135),

$$\boldsymbol{T} \equiv -\frac{1}{4}\epsilon_0 \omega \overline{\boldsymbol{E}} \cdot \frac{\partial}{\partial \boldsymbol{k}} \boldsymbol{\epsilon}_{\text{h}} \cdot \boldsymbol{E} \tag{2.137}$$

is the flux density of acoustic energy,

$$W \equiv \frac{1}{4} \left\{ \frac{\overline{\boldsymbol{B}} \cdot \boldsymbol{B}}{\mu_0} + \epsilon_0 \overline{\boldsymbol{E}} \cdot \frac{\partial}{\partial \omega} \left(\omega \boldsymbol{\epsilon}_{\text{h}} \right) \cdot \boldsymbol{E} \right\} \tag{2.138}$$

is the wave energy density, and

$$\left(\frac{\partial W}{\partial t} \right)_{\text{lossy}} = \frac{1}{2}\epsilon_0 \omega \overline{\boldsymbol{E}} \cdot \boldsymbol{\epsilon}_{\text{a}} \cdot \boldsymbol{E} \tag{2.139}$$

represents dissipation or absorption of energy density. In Eqs. (2.137)–(2.139), ω_r is replaced by ω under the assumption $|\omega_i| \ll |\omega|$. The quantities $\boldsymbol{S}$, $\boldsymbol{T}$, W, and $\left(\frac{\partial W}{\partial t}\right)_{\text{lossy}}$ are expressed in terms of $\boldsymbol{E}(\omega,\boldsymbol{k})$, $\boldsymbol{B}(\omega,\boldsymbol{k})$, $\boldsymbol{\epsilon}_{\text{h}}(\omega,\boldsymbol{k})$, and $\boldsymbol{\epsilon}_{\text{a}}(\omega,\boldsymbol{k})$. Using Eqs. (2.127) and (2.128) with $\boldsymbol{\epsilon}_{\text{h}}^{\dagger}(\omega,\boldsymbol{k}) = \boldsymbol{\epsilon}_{\text{h}}(\omega,\boldsymbol{k})$, $\boldsymbol{\epsilon}_{\text{h}}(\omega,\boldsymbol{k})$ and $\boldsymbol{\epsilon}_{\text{a}}(\omega,\boldsymbol{k})$ are given as

$$\boldsymbol{\epsilon}_{\text{h}}(\omega,\boldsymbol{k}) = \frac{\boldsymbol{\epsilon}(\omega,\boldsymbol{k}) + \boldsymbol{\epsilon}^{\dagger}(\omega,\boldsymbol{k})}{2}, \tag{2.140}$$

$$\boldsymbol{\epsilon}_{\text{a}}(\omega,\boldsymbol{k}) = \frac{\boldsymbol{\epsilon}(\omega,\boldsymbol{k}) - \boldsymbol{\epsilon}^{\dagger}(\omega,\boldsymbol{k})}{2i}. \tag{2.141}$$

2.6.2　Group Velocity

In a plasma, the direction of wave energy propagation is not necessarily the same as the direction of phase propagation, or the wavenumber vector $\boldsymbol{k}$. The velocity of wave energy propagation is called the group velocity $\boldsymbol{v}_{\mathrm{g}}$, and is defined using $\boldsymbol{S}$, $\boldsymbol{T}$, and W given in Subsection 2.6.1 as [51]

$$\boldsymbol{v}_{\mathrm{g}} = \frac{\boldsymbol{S} + \boldsymbol{T}}{W} = \frac{\text{total energy flux density}}{\text{total energy density}}. \tag{2.142}$$

It can be shown that [51]

$$\boldsymbol{v}_{\mathrm{g}} = \frac{\partial \omega\left(\boldsymbol{k}\right)}{\partial \boldsymbol{k}}. \tag{2.143}$$

2.6.3　Group Velocity of a Cold Plasma Electrostatic Wave

Since the LHW is an electrostatic wave, the group velocity is evaluated for an electrostatic wave. Referring to Eqs. (2.82) and (2.83), the electric field $\boldsymbol{E}$ for an electrostatic wave is expressed as

$$\boldsymbol{E} = -\nabla\phi = -i\phi\boldsymbol{k} = -i\phi \begin{pmatrix} k_\perp \\ 0 \\ k_\parallel \end{pmatrix}, \tag{2.144}$$

where $\boldsymbol{k}$ is real and $(\omega, \boldsymbol{k})$ is omitted. In the rest of this subsection, $(\omega, \boldsymbol{k})$ is omitted.

The plasma is assumed to be cold. The dielectric tensor $\boldsymbol{\epsilon}$ for a cold plasma is given by Eq. (2.38):

$$\boldsymbol{\epsilon} = \begin{pmatrix} S & -iD & 0 \\ iD & S & 0 \\ 0 & 0 & P \end{pmatrix}$$

and $\boldsymbol{\epsilon}^\dagger = \boldsymbol{\epsilon}$ holds. Therefore Eqs. (2.140) and (2.141) give $\boldsymbol{\epsilon}_{\mathrm{h}}$ and $\boldsymbol{\epsilon}_{\mathrm{a}}$ as

$$\boldsymbol{\epsilon}_{\mathrm{h}} = \begin{pmatrix} S & -iD & 0 \\ iD & S & 0 \\ 0 & 0 & P \end{pmatrix} = \boldsymbol{\epsilon}, \tag{2.145}$$

$$\boldsymbol{\epsilon}_{\mathrm{a}} = \begin{pmatrix} 0 & 0 & 0 \\ 0 & 0 & 0 \\ 0 & 0 & 0 \end{pmatrix}. \tag{2.146}$$

Since $\boldsymbol{\epsilon}_{\mathrm{h}}$ is independent of $\boldsymbol{k}$ in a cold plasma, Eq. (2.137) gives zero acoustic energy flux density

$$\boldsymbol{T} = \boldsymbol{0}. \tag{2.147}$$

Equations (2.139) and (2.146) give the dissipative or absorptive energy component $\left(\frac{\partial W}{\partial t}\right)_{\mathrm{lossy}}$ as

$$\left(\frac{\partial W}{\partial t}\right)_{\mathrm{lossy}} = 0, \tag{2.148}$$

meaning that a cold plasma is loss-free. Therefore, $\boldsymbol{v}_{\mathrm{g}}$ reduces to

$$\boldsymbol{v}_{\mathrm{g}} = \frac{\boldsymbol{S}}{W}. \tag{2.149}$$

Electromagnetic Energy Flux Density S

From Eq. (2.135), the magnetic field $\boldsymbol{B}$ is necessary for deriving $\boldsymbol{S}$. Starting from Eq. (2.18):

$$\nabla \times \boldsymbol{B} = \mu_0 \frac{\partial \boldsymbol{D}}{\partial t}$$

and Eq. (2.21):

$$\boldsymbol{D} = \boldsymbol{\epsilon}\,\epsilon_0 \cdot \boldsymbol{E},$$

the following equation

$$i\boldsymbol{k} \times \boldsymbol{B} = \mu_0 \left(-i\omega\right) \epsilon_0 \boldsymbol{\epsilon} \cdot \boldsymbol{E} \tag{2.150}$$

is derived. Taking the cross product of $\boldsymbol{k}$ with Eq. (2.150) gives

$$\boldsymbol{B} = \frac{\epsilon_0 \mu_0 \omega}{k^2} \boldsymbol{k} \times \left(\boldsymbol{\epsilon} \cdot \boldsymbol{E}\right), \tag{2.151}$$

where $\nabla \cdot \boldsymbol{B} = i\boldsymbol{k} \cdot \boldsymbol{B} = 0$ was used. Using Eqs. (2.135) and (2.151), $\boldsymbol{S}$ is calculated as

$$
\begin{aligned}
\boldsymbol{S} &= \frac{1}{4\mu_0}\left(\boldsymbol{E} \times \overline{\boldsymbol{B}} + \overline{\boldsymbol{E}} \times \boldsymbol{B}\right) \\
&= \frac{\omega\epsilon_0}{4k^2}\left\{\overline{\boldsymbol{E}} \times \left[\boldsymbol{k} \times (\boldsymbol{\epsilon} \cdot \boldsymbol{E})\right] + \boldsymbol{E} \times \overline{\left[\boldsymbol{k} \times (\boldsymbol{\epsilon} \cdot \boldsymbol{E})\right]}\right\} \\
&= \frac{\omega\epsilon_0}{4k^2}\left\{\overline{\boldsymbol{E}} \times \left[\boldsymbol{k} \times (\boldsymbol{\epsilon} \cdot \boldsymbol{E})\right] + \boldsymbol{E} \times \left[\overline{\boldsymbol{k}} \times \left(\overline{\boldsymbol{\epsilon}} \cdot \overline{\boldsymbol{E}}\right)\right]\right\} \\
&= \frac{\omega\epsilon_0}{4k^2}\left\{\left[\left(\overline{\boldsymbol{E}} \cdot \boldsymbol{\epsilon} \cdot \boldsymbol{E}\right)\boldsymbol{k} - \left(\overline{\boldsymbol{E}} \cdot \boldsymbol{k}\right)(\boldsymbol{\epsilon} \cdot \boldsymbol{E})\right] + \left[\left(\boldsymbol{E} \cdot \overline{\boldsymbol{\epsilon}} \cdot \overline{\boldsymbol{E}}\right)\overline{\boldsymbol{k}} - \left(\boldsymbol{E} \cdot \overline{\boldsymbol{k}}\right)\left(\overline{\boldsymbol{\epsilon}} \cdot \overline{\boldsymbol{E}}\right)\right]\right\}. \tag{2.152}
\end{aligned}
$$

Since $\boldsymbol{k}$ is real and $\boldsymbol{E} \cdot \overline{\boldsymbol{\epsilon}} \cdot \overline{\boldsymbol{E}} = \overline{\boldsymbol{E}} \cdot \boldsymbol{\epsilon}^\dagger \cdot \boldsymbol{E}$ holds, the first and the third terms in Eq. (2.152) can be combined, and $\boldsymbol{S}$ reduces to

$$
\begin{aligned}
\boldsymbol{S} &= \frac{\omega\epsilon_0}{4k^2}\left\{\left[\overline{\boldsymbol{E}} \cdot \left(\boldsymbol{\epsilon} + \boldsymbol{\epsilon}^\dagger\right) \cdot \boldsymbol{E}\right] - \left(\overline{\boldsymbol{E}} \cdot \boldsymbol{k}\right)(\boldsymbol{\epsilon} \cdot \boldsymbol{E}) - (\boldsymbol{E} \cdot \boldsymbol{k})\left(\overline{\boldsymbol{\epsilon}} \cdot \overline{\boldsymbol{E}}\right)\right\} \\
&= \frac{\omega\epsilon_0}{4k^2}\left\{\left[\overline{\boldsymbol{E}} \cdot (2\boldsymbol{\epsilon}_{\mathrm{h}}) \cdot \boldsymbol{E}\right] - \left(\overline{\boldsymbol{E}} \cdot \boldsymbol{k}\right)(\boldsymbol{\epsilon} \cdot \boldsymbol{E}) - (\boldsymbol{E} \cdot \boldsymbol{k})\left(\overline{\boldsymbol{\epsilon}} \cdot \overline{\boldsymbol{E}}\right)\right\}, \tag{2.153}
\end{aligned}
$$

where Eq. (2.140) was used. Substituting Eq. (2.144) or $\boldsymbol{E} = -i\phi\boldsymbol{k}$ into Eq. (2.153) gives

$$
\begin{aligned}
\boldsymbol{S} &= \frac{\omega\epsilon_0}{4k^2}\left\{2|\phi|^2\left(\boldsymbol{k} \cdot \boldsymbol{\epsilon}_{\mathrm{h}} \cdot \boldsymbol{k}\right) - |\phi|^2 k^2 (\boldsymbol{\epsilon} \cdot \boldsymbol{k}) - |\phi|^2 k^2 \left(\overline{\boldsymbol{\epsilon}} \cdot \boldsymbol{k}\right)\right\} \\
&= \frac{\omega\epsilon_0|\phi|^2}{4k^2}\left\{2\left(\boldsymbol{k} \cdot \boldsymbol{\epsilon}_{\mathrm{h}} \cdot \boldsymbol{k}\right) - k^2(\boldsymbol{\epsilon} + \overline{\boldsymbol{\epsilon}}) \cdot \boldsymbol{k}\right\}. \tag{2.154}
\end{aligned}
$$

The first term in Eq. (2.154) vanishes as follows. The zero divergence of Eq. (2.18):

$$
\begin{aligned}
0 = \nabla \cdot (\nabla \times \boldsymbol{B}) &= \nabla \cdot \left(\mu_0 \frac{\partial \boldsymbol{D}}{\partial t}\right) \\
&= \mu_0 (i\boldsymbol{k})(-i\omega) \cdot \boldsymbol{D} \\
&= \mu_0 \omega \epsilon_0 (\boldsymbol{k} \cdot \boldsymbol{\epsilon} \cdot \boldsymbol{k}) \tag{2.155}
\end{aligned}
$$

and Eq. (2.145) give

$$\boldsymbol{k} \cdot \boldsymbol{\epsilon}_{\mathrm{h}} \cdot \boldsymbol{k} = \boldsymbol{k} \cdot \boldsymbol{\epsilon} \cdot \boldsymbol{k} = 0. \tag{2.156}$$

Therefore, $\boldsymbol{S}$ is expressed as

$$
\begin{aligned}
\boldsymbol{S} &= -\frac{1}{4}\omega\epsilon_0|\phi|^2(\boldsymbol{\epsilon} + \overline{\boldsymbol{\epsilon}}) \cdot \boldsymbol{k} = -\frac{1}{4}\omega\epsilon_0|\phi|^2 \begin{pmatrix} 2S & 0 & 0 \\ 0 & 2S & 0 \\ 0 & 0 & 2P \end{pmatrix} \begin{pmatrix} k_\perp \\ 0 \\ k_\parallel \end{pmatrix} \\
&= -\frac{1}{2}\omega\epsilon_0|\phi|^2 \begin{pmatrix} Sk_\perp \\ 0 \\ Pk_\parallel \end{pmatrix}. \tag{2.157}
\end{aligned}
$$

64

Wave Energy Density W

From Eq. (2.138), W is expressed as

$$W = \frac{1}{4} \left\{ \frac{\overline{\boldsymbol{B}} \cdot \boldsymbol{B}}{\mu_0} + \epsilon_0 \overline{\boldsymbol{E}} \cdot \frac{\partial}{\partial \omega} \left(\omega \boldsymbol{\epsilon}_{\mathrm{h}} \right) \cdot \boldsymbol{E} \right\}.$$

First, the magnetic field $\boldsymbol{B}$ is calculated explicitly by substituting the electrostatic notation $\boldsymbol{E} = -i\phi\boldsymbol{k}$ into Eq. (2.151) as

$$
\begin{aligned}
\boldsymbol{B} &= \frac{\epsilon_0 \mu_0 \omega}{k^2} \boldsymbol{k} \times (\boldsymbol{\epsilon} \cdot \boldsymbol{E}) \\
&= \frac{\epsilon_0 \mu_0 \omega}{k^2} (-i\phi) \, \boldsymbol{k} \times (\boldsymbol{\epsilon} \cdot \boldsymbol{k}) \\
&= \frac{\epsilon_0 \mu_0 \omega}{k^2} (-i\phi) \begin{pmatrix} k_\perp \\ 0 \\ k_\parallel \end{pmatrix} \times \begin{pmatrix} S & -iD & 0 \\ iD & S & 0 \\ 0 & 0 & P \end{pmatrix} \begin{pmatrix} k_\perp \\ 0 \\ k_\parallel \end{pmatrix} \\
&= \frac{\epsilon_0 \mu_0 \omega}{k^2} (-i\phi) \begin{pmatrix} k_\perp \\ 0 \\ k_\parallel \end{pmatrix} \times \begin{pmatrix} Sk_\perp \\ iDk_\perp \\ Pk_\parallel \end{pmatrix} \\
&= \frac{\epsilon_0 \mu_0 \omega}{k^2} (-i\phi) \begin{pmatrix} -iDk_\parallel k_\perp \\ (S-P)\,k_\parallel k_\perp \\ iDk_\perp^2 \end{pmatrix}.
\end{aligned} \tag{2.158}
$$

Using Eq. (2.158), the first term $\frac{\overline{\boldsymbol{B}} \cdot \boldsymbol{B}}{\mu_0}$ in W is calculated as

$$
\begin{aligned}
\frac{\overline{\boldsymbol{B}} \cdot \boldsymbol{B}}{\mu_0} &= \mu_0 \left(\frac{\epsilon_0 \omega}{k^2} \right)^2 \overline{(-i\phi) \begin{pmatrix} -iDk_\parallel k_\perp \\ (S-P)\,k_\parallel k_\perp \\ iDk_\perp^2 \end{pmatrix}} \cdot (-i\phi) \begin{pmatrix} -iDk_\parallel k_\perp \\ (S-P)\,k_\parallel k_\perp \\ iDk_\perp^2 \end{pmatrix} \\
&= \mu_0 \left(\frac{\epsilon_0 \omega}{k^2} \right)^2 |\phi|^2 \begin{pmatrix} iDk_\parallel k_\perp \\ (S-P)\,k_\parallel k_\perp \\ -iDk_\perp^2 \end{pmatrix} \cdot \begin{pmatrix} -iDk_\parallel k_\perp \\ (S-P)\,k_\parallel k_\perp \\ iDk_\perp^2 \end{pmatrix} \\
&= \mu_0 \left(\frac{\epsilon_0 \omega}{k^2} \right)^2 |\phi|^2 \left\{ D^2 k_\parallel^2 k_\perp^2 + (S-P)^2 \, k_\parallel^2 k_\perp^2 + D^2 k_\perp^4 \right\} \\
&= \mu_0 \epsilon_0^2 \omega^2 |\phi|^2 \frac{k_\perp^2 \left\{ D^2 k^2 + (S-P)^2 \, k_\parallel^2 \right\}}{k^4},
\end{aligned} \tag{2.159}
$$

where $k_\parallel^2 + k_\perp^2 = k^2$ was used to obtain the last row.

The second term $\epsilon_0 \overline{\boldsymbol{E}} \cdot \frac{\partial}{\partial \omega} \left(\omega \boldsymbol{\epsilon}_{\mathrm{h}} \right) \cdot \boldsymbol{E}$ in W is evaluated as follows. Using Eq. (2.145) and Stix parameters S, D, and P defined by Eqs. (2.39)–(2.41), $\frac{\partial}{\partial \omega} \left(\omega \boldsymbol{\epsilon}_{\mathrm{h}} \right)$ is given as

$$\frac{\partial}{\partial \omega} \left(\omega \boldsymbol{\epsilon}_{\mathrm{h}} \right) = \frac{\partial}{\partial \omega} \left[\omega \begin{pmatrix} S & -iD & 0 \\ iD & S & 0 \\ 0 & 0 & P \end{pmatrix} \right] = \begin{pmatrix} F & -iG & 0 \\ iG & F & 0 \\ 0 & 0 & H \end{pmatrix}, \tag{2.160}$$

where F, G, and H are defined as

$$F \equiv \frac{\partial}{\partial \omega} \left(\omega S \right) = 1 + \sum_s \frac{\omega_{\mathrm{p}s}^2 \left(\omega^2 + \Omega_s^2 \right)}{\left(\omega^2 - \Omega_s^2 \right)^2} \tag{2.161}$$

$$G \equiv \frac{\partial}{\partial \omega} \left(\omega D \right) = -2 \sum_s \frac{\omega \Omega_s \omega_{\mathrm{p}s}^2}{\left(\omega^2 - \Omega_s^2 \right)^2} \tag{2.162}$$

$$H \equiv \frac{\partial}{\partial \omega} \left(\omega P \right) = 1 + \sum_s \frac{\omega_{\mathrm{p}s}^2}{\omega^2}. \tag{2.163}$$

Using Eq. (2.160) and $\boldsymbol{E} = -i\phi\boldsymbol{k}$, $\epsilon_0\overline{\boldsymbol{E}} \cdot \frac{\partial}{\partial\omega}(\omega\boldsymbol{\epsilon}_{\mathrm{h}}) \cdot \boldsymbol{E}$ is calculated for real $\boldsymbol{k}$ as

$$
\begin{aligned}
\epsilon_0\overline{\boldsymbol{E}} \cdot \frac{\partial}{\partial\omega}(\omega\boldsymbol{\epsilon}_{\mathrm{h}}) \cdot \boldsymbol{E} &= \epsilon_0|\phi|^2\boldsymbol{k} \cdot \frac{\partial}{\partial\omega}(\omega\boldsymbol{\epsilon}_{\mathrm{h}}) \cdot \boldsymbol{k} \\
&= \epsilon_0|\phi|^2 \begin{pmatrix} k_\perp \\ 0 \\ k_\parallel \end{pmatrix} \cdot \begin{pmatrix} F & -iG & 0 \\ iG & F & 0 \\ 0 & 0 & H \end{pmatrix} \begin{pmatrix} k_\perp \\ 0 \\ k_\parallel \end{pmatrix} \\
&= \epsilon_0|\phi|^2 \begin{pmatrix} k_\perp \\ 0 \\ k_\parallel \end{pmatrix} \cdot \begin{pmatrix} Fk_\perp \\ iGk_\perp \\ Hk_\parallel \end{pmatrix} \\
&= \epsilon_0|\phi|^2\left(Fk_\perp^2 + Hk_\parallel^2\right).
\end{aligned} \tag{2.164}
$$

Eqs. (2.159) and (2.164) give the wave energy density W for a cold plasma electrostatic wave as

$$
\begin{aligned}
W &= \frac{1}{4}\left\{\frac{\overline{\boldsymbol{B}} \cdot \boldsymbol{B}}{\mu_0} + \epsilon_0\overline{\boldsymbol{E}} \cdot \frac{\partial}{\partial\omega}(\omega\boldsymbol{\epsilon}_{\mathrm{h}}) \cdot \boldsymbol{E}\right\} \\
&= \frac{1}{4}\epsilon_0|\phi|^2\left\{\mu_0\epsilon_0\omega^2\frac{k_\perp^2\left[D^2k^2 + (S-P)^2k_\parallel^2\right]}{k^4} + \left(Fk_\perp^2 + Hk_\parallel^2\right)\right\} \\
&= \frac{1}{4}\epsilon_0|\phi|^2\left\{\frac{\omega^2}{c^2}\frac{k_\perp^2\left[D^2k^2 + (S-P)^2k_\parallel^2\right]}{k^4} + \left(Fk_\perp^2 + Hk_\parallel^2\right)\right\}.
\end{aligned} \tag{2.165}
$$

Explicit Notation for Group Velocity $\boldsymbol{v}_{\mathrm{g}}$

From Eqs. (2.149), (2.157) and (2.165), the group velocity $\boldsymbol{v}_{\mathrm{g}}$ for a cold plasma electrostatic wave is given as

$$
\begin{aligned}
\boldsymbol{v}_{\mathrm{g}} = \frac{\boldsymbol{S}}{W} &= \frac{-\frac{1}{2}\omega\epsilon_0|\phi|^2 \begin{pmatrix} Sk_\perp \\ 0 \\ Pk_\parallel \end{pmatrix}}{\frac{1}{4}\epsilon_0|\phi|^2\left\{\frac{\omega^2}{c^2}\frac{k_\perp^2\left[D^2k^2 + (S-P)^2k_\parallel^2\right]}{k^4} + \left(Fk_\perp^2 + Hk_\parallel^2\right)\right\}} \\
&= -\frac{2\omega}{\frac{\omega^2}{c^2}\frac{k_\perp^2\left[D^2k^2 + (S-P)^2k_\parallel^2\right]}{k^4} + \left(Fk_\perp^2 + Hk_\parallel^2\right)}\begin{pmatrix} Sk_\perp \\ 0 \\ Pk_\parallel \end{pmatrix} \\
&= -\frac{2c}{\frac{n_\perp^2\left[D^2n^2 + (S-P)^2n_\parallel^2\right]}{n^4} + \left(Fn_\perp^2 + Hn_\parallel^2\right)}\begin{pmatrix} Sn_\perp \\ 0 \\ Pn_\parallel \end{pmatrix},
\end{aligned}
$$

(2.166) and (2.167)

where the notation $\boldsymbol{n} = \frac{c}{\omega}\boldsymbol{k}$ was used. Eqs. (2.166) and (2.167) are expressions for $\boldsymbol{v}_{\mathrm{g}}$ in terms of $\boldsymbol{k}$ and $\boldsymbol{n}$, respectively.

It is worth noting that $\boldsymbol{k}$ and $\boldsymbol{v}_{\mathrm{g}}$ are perpendicular to each other. This is shown as follows. From Eq. (2.156), a short calculation yields

$$
0 = \boldsymbol{k} \cdot \boldsymbol{\epsilon} \cdot \boldsymbol{k} = Sk_\perp^2 + Pk_\parallel^2 \tag{2.168}
$$

and therefore, from Eq. (2.166),

$$
\boldsymbol{k} \cdot \boldsymbol{v}_{\mathrm{g}} \propto \begin{pmatrix} k_\perp \\ 0 \\ k_\parallel \end{pmatrix} \cdot \begin{pmatrix} Sk_\perp \\ 0 \\ Pk_\parallel \end{pmatrix} = Sk_\perp^2 + Pk_\parallel^2 = 0. \tag{2.169}
$$

2.7 Landau Damping

An electrostatic wave can interact with charged particles and exchange energy. An important energy exchange processes was suggested by Landau in 1946 [53]. This is called Landau damping. In this section, the physical picture of the Landau damping is described [51, 54, 55] and the temporal wave energy damping rate by Landau damping is evaluated.

2.7.1 Physical Picture of Landau Damping

Temporal Variation of the Particle Kinetic Energy

Consider a 1-dimensional electrostatic (longitudinal) wave with $\boldsymbol{E} \parallel \boldsymbol{k}$ in the absence of magnetic field (or in the direction of the magnetic field). Taking $\boldsymbol{v} = \hat{\boldsymbol{z}} v$ and $\boldsymbol{E} = \hat{\boldsymbol{z}} E \cos(kz - \omega t)$ where $\hat{\boldsymbol{z}}$ is the unit vector in the z direction, the single-particle equation of motion is written as

$$m \frac{dv}{dt} = qE \cos(kz - \omega t), \tag{2.170}$$

where E is real and is taken to be a first order quantity. Expanding v and z as

$$v = v_0 + v_1 + v_2 + \cdots, \tag{2.171}$$
$$z = z_0 + z_1 + z_2 + \cdots, \tag{2.172}$$

Eq. (2.170) is written for the zeroth order and the first order as

$$m \frac{dv_0}{dt} = 0, \tag{2.173}$$
$$m \frac{dv_1}{dt} = qE \cos(kz_0 - \omega t). \tag{2.174}$$

Solving Eq. (2.173) gives v_0 as

$$v_0 = \text{constant} \tag{2.175}$$

and z_0 as

$$z_0 = v_0 t + z_{\text{ini}}, \tag{2.176}$$

where z_{ini} is the initial position of the particle at $t = 0$. Equation (2.176) is substituted into Eq. (2.174) and a time integration gives

$$v_1 = \frac{qE}{m} \frac{\sin[kz_{\text{ini}} + (kv_0 - \omega)t] - \sin(kz_{\text{ini}})}{kv_0 - \omega}, \tag{2.177}$$

where $v_1 = 0$ at $t = 0$ was used as the initial condition. With $z_1 = 0$ at $t = 0$, a time integration of Eq. (2.177) gives

$$z_1 = \int_0^t v_1 dt = \frac{qE}{m} \left[\frac{-\cos(kz_{\text{ini}} - \alpha t) + \cos(kz_{\text{ini}})}{\alpha^2} - \frac{t \sin(kz_{\text{ini}})}{\alpha} \right], \tag{2.178}$$

where

$$\alpha \equiv kv_0 - \omega. \tag{2.179}$$

The time derivative of the particle kinetic energy is expanded as

$$\frac{d}{dt} \frac{mv^2}{2} = v \frac{d}{dt} mv$$
$$= v_0 \frac{d}{dt} mv_1 + \left(v_1 \frac{d}{dt} mv_1 + v_0 \frac{d}{dt} mv_2 \right) + \cdots. \tag{2.180}$$

67

The first and second terms in Eq. (2.180) are given using Eq. (2.177). The third term is calculated using Eqs. (2.170)–(2.172) as

$$m\frac{d}{dt}\left(v_0 + v_1 + v_2\right) \simeq qE\cos\left[k\left(z_0 + z_1\right) - \omega t\right],$$ (2.181)

which leads to

$$\begin{aligned} m\frac{d}{dt}v_1 + m\frac{d}{dt}v_2 &\simeq qE\cos\left[k\left(z_0 + z_1\right) - \omega t\right] \\ &= qE\cos\left[\left(\alpha t + kz_{\text{ini}}\right) + kz_1\right] \\ &= qE\cos\left(\varphi + kz_1\right), \end{aligned}$$ (2.182)

where Eq. (2.176) was used and $\varphi \equiv \alpha t + kz_{\text{ini}}$. For small kz_1,

$$\begin{aligned} \cos\left(\varphi + kz_1\right) &= \cos\varphi + \left(\frac{d\cos\theta}{d\theta}\right)_{\theta=\varphi}\left(kz_1\right) + \cdots \\ &\simeq \cos\varphi - \sin\varphi \cdot kz_1 \end{aligned}$$ (2.183)

is available and Eq. (2.182) becomes

$$m\frac{d}{dt}v_1 + m\frac{d}{dt}v_2 \simeq qE\cos\left(\alpha t + kz_{\text{ini}}\right) + qEkz_1\sin\left(\alpha t + kz_{\text{ini}}\right).$$ (2.184)

The first terms on both sides of Eq. (2.184) are the same, because from Eqs. (2.174), (2.176), and (2.179),

$$m\frac{dv_1}{dt} = qE\cos\left(kz_0 - \omega t\right) = qE\cos\left[k\left(v_0 t + z_{\text{ini}}\right) - \omega t\right] = qE\cos\left(\alpha t + kz_{\text{ini}}\right).$$ (2.185)

Therefore, from Eq. (2.184),

$$m\frac{dv_2}{dt} \simeq qEkz_1\sin\left(\alpha t + kz_{\text{ini}}\right)$$ (2.186)

is obtained and then Eq. (2.180) can be evaluated.

Averaging over Initial Position and Velocity Distribution Function

Since there is a vast number of particles in space, z_{ini} can take various values. Therefore, Eq. (2.180) must be averaged over z_{ini}. Using Eqs. (2.177), (2.178), (2.186) and trigonometric additive theorems, the result is [51]

$$\left\langle \frac{d}{dt}\frac{mv^2}{2}\right\rangle_{z_{\text{ini}}} = \frac{q^2E^2}{2m}\left(-\frac{\omega\sin\alpha t}{\alpha^2} + t\cos\alpha t + \frac{\omega t\cos\alpha t}{\alpha}\right).$$ (2.187)

Oscillatory terms with respect to z_{ini} vanish. A further averaging of Eq. (2.187) over the velocity distribution function

$$f\left(v_0\right) = f\left(\frac{\alpha + \omega}{k}\right) \equiv g\left(\alpha\right)$$ (2.188)

gives [51]

$$\left\langle \frac{d}{dt}\frac{mv^2}{2}\right\rangle_{z_{\text{ini}},v_0} = -\frac{\omega q^2E^2}{2m|k|}\text{P}\int_{-\infty}^{\infty}d\alpha\frac{g(\alpha)\sin\alpha t}{\alpha^2},$$ (2.189)

where P indicates the principal value. Main contributions to the integral come from the vicinity of $\alpha = 0$ ($v_0 = \frac{\omega}{k} = v_{\text{phase}}$). Therefore, $g(\alpha)$ is expanded around $\alpha = 0$ as

$$g(\alpha) = g(0) + \alpha g'(0) + \frac{\alpha^2}{2}g''(0) + \cdots .$$ (2.190)

Since $\frac{\sin \alpha t}{\alpha^2}$ in the integrand in Eq. (2.189) is an odd function of α, $\alpha g'(0)$ in Eq. (2.190) is retained, yielding [51]

$$
\begin{aligned}
\left\langle \frac{d}{dt} \frac{mv^2}{2} \right\rangle_{z_{\mathrm{ini}}, v_0} &\simeq -\frac{\omega q^2 E^2}{2m|k|} \int_{-\infty}^{\infty} d\alpha \frac{g'(0) \sin \alpha t}{\alpha} \\
&= -\frac{\pi \omega q^2 E^2}{2mk|k|} \left[\frac{df(v_0)}{dv_0} \right]_{v_0 = \frac{\omega}{k}}.
\end{aligned}
\tag{2.191}
$$

Equation (2.191) gives the time derivative of the particle power density [W/m³] due to energy exchange with the wave. For $\left[\frac{df(v_0)}{dv_0} \right]_{v_0 = \frac{\omega}{k}} < 0$, $\left\langle \frac{d}{dt} \frac{mv^2}{2} \right\rangle_{z_{\mathrm{ini}}, v_0}$ is positive. In this case, the number of particles streaming infinitesimally slower than the wave phase velocity $\frac{\omega}{k}$ and being accelerated is greater than the number of particles streaming infinitesimally faster than $\frac{\omega}{k}$ and being decelerated, and the total particle kinetic energy increases, while the total wave energy decreases by the same amount.

2.7.2 Temporal Wave Energy Damping Rate ω_{i}

Since, from Eqs. (2.125) and (2.126), $\left\langle \boldsymbol{E} \cdot \frac{\partial \boldsymbol{D}}{\partial t} \right\rangle_{\mathrm{ave.}}$ and $\left\langle \boldsymbol{H} \cdot \frac{\partial \boldsymbol{B}}{\partial t} \right\rangle_{\mathrm{ave.}}$ are proportional to $\exp\left[2\phi_{\mathrm{i}}(t, \boldsymbol{r})\right]$, the time derivative of wave energy density $\frac{dW}{dt}$ is proportional to $\exp\left[2\phi_{\mathrm{i}}(t, \boldsymbol{r})\right]$. Upon integration

$$
W = W_0 e^{2\phi_{\mathrm{i}}(t, \boldsymbol{r})},
\tag{2.192}
$$

where W_0 is the value of W at $t = 0$. Temporal differentiation of Eq. (2.192) with Eq. (2.119) gives

$$
\frac{dW}{dt} = 2\omega_{\mathrm{i}} W_0 e^{2\phi_{\mathrm{i}}(t, \boldsymbol{r})} = 2\omega_{\mathrm{i}} W,
\tag{2.193}
$$

which can be integrated to give

$$
W = W_0 e^{2\omega_{\mathrm{i}} t}.
\tag{2.194}
$$

Equation (2.194) states that ω_{i} determines the rate of temporal change of the wave energy density.

The power conservation equation

$$
\frac{dW}{dt} + \left\langle \frac{d}{dt} \frac{mv^2}{2} \right\rangle_{z_{\mathrm{ini}}, v_0} = 0
\tag{2.195}
$$

gives ω_{i} using Eqs. (2.191) and (2.193) as

$$
2\omega_{\mathrm{i}} W = \frac{\pi \omega q^2 E_{\parallel}^2}{2mk_{\parallel}|k_{\parallel}|} \left[\frac{df(v_{\parallel})}{dv_{\parallel}} \right]_{v_{\parallel} = \frac{\omega}{k_{\parallel}}} = \frac{\pi \omega q^2 |\phi|^2}{2m} \frac{k_{\parallel}}{|k_{\parallel}|} \left[\frac{df(v_{\parallel})}{dv_{\parallel}} \right]_{v_{\parallel} = \frac{\omega}{k_{\parallel}}},
\tag{2.196}
$$

where E, k, and v_0 in Eq. (2.191) are replaced by $E_{\parallel}$, $k_{\parallel}$, and $v_{\parallel}$ in the presence of magnetic field since the charged particle motion along the magnetic field is not affected. The second equal sign comes from the property of an electrostatic wave,

$$
E_{\parallel}^2 = |E_{\parallel}|^2 = |-i\phi k_{\parallel}|^2 = k_{\parallel}^2 |\phi|^2.
\tag{2.197}
$$

Eqs. (2.165) and (2.196) are combined to give

$$
\omega_{\mathrm{i}} = \frac{\pi \omega q^2}{\epsilon_0 m} \frac{k_{\parallel}}{|k_{\parallel}|} \frac{1}{\frac{\omega^2}{c^2} \frac{k_{\perp}^2 \left[D^2 k^2 + (S-P)^2 k_{\parallel}^2 \right]}{k^4} + \left(F k_{\perp}^2 + H k_{\parallel}^2 \right)} \left[\frac{df(v_{\parallel})}{dv_{\parallel}} \right]_{v_{\parallel} = \frac{\omega}{k_{\parallel}}}.
\tag{2.198}
$$

It should be noted that the velocity distribution function $f(v_\parallel)$ in Eq. (2.198) is one-dimensional, in the direction along the magnetic field. Since Landau damping by electrons is used to drive current, $f(v_\parallel)$ for electrons is considered from now on.

If $f(v_\parallel)$ were a Maxwellian distribution function, $f(v_\parallel)$ takes the form

$$f(v_\parallel) = \frac{n_{\mathrm{e}}}{\sqrt{2\pi}v_{\mathrm{t,e}}}\exp\left(-\frac{v_\parallel^2}{2v_{\mathrm{t,e}}^2}\right), \tag{2.199}$$

where n_{e} is the electron density and $v_{\mathrm{t,e}}$ is the electron thermal velocity. The thermal velocity is defined in Eq. (1.19) and for the present case,

$$v_{\mathrm{t,e}} = \sqrt{\frac{T_{\mathrm{e,\parallel}}}{m_{\mathrm{e}}}} = \sqrt{\frac{\{eT_{\mathrm{e,\parallel}}\,[\mathrm{eV}]\}\,[\mathrm{J}]}{m_{\mathrm{e}}}}, \tag{2.200}$$

where $T_{\mathrm{e,\parallel}}$ is the electron temperature in the direction along the magnetic field. Since the derivative of $f(v_\parallel)$ is calculated as

$$\frac{df(v_\parallel)}{dv_\parallel} = -\frac{n_{\mathrm{e}}}{\sqrt{2\pi}v_{\mathrm{t,e}}^3}v_\parallel\exp\left(-\frac{v_\parallel^2}{2v_{\mathrm{t,e}}^2}\right), \tag{2.201}$$

Eq. (2.198) leads to

$$\begin{aligned}
\omega_{\mathrm{i}} &= \frac{\pi\omega e^2}{\epsilon_0 m_{\mathrm{e}}}\frac{k_\parallel}{|k_\parallel|}\frac{1}{\frac{\omega^2}{c^2}\frac{k_\perp^2\left[D^2k^2+(S-P)^2k_\parallel^2\right]}{k^4}+\left(Fk_\perp^2+Hk_\parallel^2\right)}\cdot\left[-\frac{n_{\mathrm{e}}}{\sqrt{2\pi}v_{\mathrm{t,e}}^3}\frac{\omega}{k_\parallel}\exp\left(-\frac{1}{2v_{\mathrm{t,e}}^2}\frac{\omega^2}{k_\parallel^2}\right)\right] \\
&= -\sqrt{\frac{\pi}{2}}\frac{n_{\mathrm{e}}e^2}{\epsilon_0 m_{\mathrm{e}}}\frac{\omega^2}{|k_\parallel|v_{\mathrm{t,e}}^3}\frac{1}{\frac{\omega^2}{c^2}\frac{k_\perp^2\left[D^2k^2+(S-P)^2k_\parallel^2\right]}{k^4}+\left(Fk_\perp^2+Hk_\parallel^2\right)}\exp\left(-\frac{1}{2v_{\mathrm{t,e}}^2}\frac{\omega^2}{k_\parallel^2}\right) \\
&= -\frac{\sqrt{2\pi}}{2|n_\parallel|}\frac{\omega_{\mathrm{pe}}^2}{\omega}\left(\frac{c}{v_{\mathrm{t,e}}}\right)^3\frac{1}{\frac{n_\perp^2\left[D^2n^2+(S-P)^2n_\parallel^2\right]}{n^4}+\left(Fn_\perp^2+Hn_\parallel^2\right)}\exp\left[-\left(\frac{c}{v_{\mathrm{t,e}}}\right)^2\frac{1}{2n_\parallel^2}\right], \tag{2.202}
\end{aligned}$$

where $\boldsymbol{k}$ is converted to $\boldsymbol{n}$ using $\boldsymbol{k}=\frac{\omega}{c}\boldsymbol{n}$ and

$$\frac{n_{\mathrm{e}}e^2}{\epsilon_0 m_{\mathrm{e}}} = \omega_{\mathrm{pe}}^2$$

is the squared electron plasma angular frequency defined in Eq. (1.32). Although the expression for ω_{i} in Eq. (2.202) was derived using both energy density W evaluated in cold plasma and the temporal rate of change of the particle kinetic energy by Landau damping, which assumes a finite electron temperature, Eq. (2.202) should give a modest approximation for ω_{i} at low plasma temperatures up to about $100\,\mathrm{eV}$.

Chapter 3

Theory of Langmuir Probe Measurement

There are many methods for investigating various properties of the plasma. One powerful method is by an electrostatic probe called the Langmuir probe [56,57]. In this method an electrode is inserted directly into the plasma and the current drawn from the plasma is regarded as an indicator of plasma properties. Electrodes are usually made of metal with high melting point such as tungsten and molybdenum.

3.1   I-V Characteristics

When an electrode is inserted into the plasma, the current I drawn by the electrode depends on the electrode potential relative to the plasma. Denoting the potentials of the electrode and the plasma as V and ϕ_{p}, respectively, different situations are described according to the values of V relative to ϕ_{p}. It is noted that the plasma potential ϕ_{p} is called also the electrostatic potential. The I-V characteristic is obtained by measuring I as V is varied. In this section, the space potential is also introduced and denoted by ϕ.

3.1.1   Electrode Potential Equal to Plasma Potential

If $V = \phi_{\mathrm{p}}$, charged particles in the plasma feel no electric force from the probe electrode, and thus the current drawn from the plasma is determined simply by the thermal motion of the charged particles and the surface area A_{probe} of the electrode. The current carried by the charged particles of species s is given by

$$J_s = q_s A_{\mathrm{probe}} \Gamma_s, \tag{3.1}$$

where Γ_s is the flux density of the particle s and becomes, for the Maxwellian distribution,

$$
\begin{aligned}
\Gamma_s &\equiv \int_0^\infty dv_x \int_{-\infty}^\infty dv_y \int_{-\infty}^\infty dv_z n_s v_x \left(\frac{m_s}{2\pi T_s}\right)^{\frac{3}{2}} \exp\left\{-\frac{m_s \left(v_x^2 + v_y^2 + v_z^2\right)}{2T_s}\right\} \\
&= \frac{1}{2} n_s \sqrt{\frac{2T_s}{\pi m_s}} \\
&= \frac{1}{4} n_s \langle v_s \rangle, \tag{3.2}
\end{aligned}
$$

where the flux density is taken to be in the x direction and $\langle v_s \rangle$ is the averaged particle speed in the isotropic thermal equilibrium

$$
\begin{aligned}
\langle v_s \rangle &\equiv \int_{-\infty}^{\infty} dv_x \int_{-\infty}^{\infty} dv_y \int_{-\infty}^{\infty} dv_z \sqrt{v_x^2 + v_y^2 + v_z^2} \left(\frac{m_s}{2\pi T_s} \right)^{\frac{3}{2}} \exp \left\{ -\frac{m_s \left(v_x^2 + v_y^2 + v_z^2 \right)}{2T_s} \right\} \\
&= \int_0^{\infty} dv \int_0^{\pi} d\theta \int_0^{2\pi} d\phi \, v \left(\frac{m_s}{2\pi T_s} \right)^{\frac{3}{2}} \exp \left(-\frac{mv^2}{2T_s} \right) v^2 \sin \theta \\
&= 2\sqrt{\frac{2T_s}{\pi m_s}}.
\end{aligned}
\tag{3.3}
$$

Here, (v, θ, ϕ) is the velocity in the spherical coordinate system and $v = \sqrt{v_x^2 + v_y^2 + v_z^2}$. If $T_e \simeq T_i$, $\langle v_e \rangle \gg \langle v_i \rangle$ follows because of the large mass separation between ions and electrons, and from Eqs. (3.1) and (3.2), the total current I drawn from the plasma is given as

$$
I = eA_{\text{probe}} \left(\frac{1}{4} n_i \langle v_i \rangle - \frac{1}{4} n_e \langle v_e \rangle \right) \approx -\frac{1}{4} e A n_e \langle v_e \rangle,
\tag{3.4}
$$

meaning that the probe current is negative when $V = \phi_p$.

3.1.2 Electrode Potential Lower than Plasma Potential

If $V < \phi_p$, electrons are decelerated and ions are accelerated when approaching the electrode, and thus the probe current becomes more positive as the electrode potential becomes more negative. In order to deal with this situation quantitatively, one must recall that the effect of the electrode potential is Debye-shielded up to a distance characterized by the Debye length from the probe. The space around the electrode can be divided roughly into two regions; the plasma region and the sheath region. In the plasma region, quasi charge neutrality is satisfied and the space potential is nearly constant. In the sheath region, on the other hand, quasi charge neutrality is violated and the space potential varies in space. This situation is depicted in Fig. 3.1 [58].

A consideration of the Poisson equation

$$
\nabla^2 \phi = -\frac{e}{\epsilon_0} \left(n_i - n_e \right)
\tag{3.5}
$$

in the sheath region near the plasma-sheath boundary leads to an important condition for the boundary between the plasma region and the sheath region to exist. The space potential at this plasma-sheath boundary is denoted by ϕ_{sh} in this thesis (ϕ_{sh} corresponds to V_s in Fig. 3.1). We would like to express the Poisson Eq. (3.5) in terms of ϕ. Before proceeding, it is assumed that ions are stationary far from the electrode and that electrons are in thermal equilibrium. These assumptions are valid in the edge plasma region of experimental fusion devices.

Letting $\phi = 0$ far from the electrode, energy conservation for ions leads to

$$
\frac{1}{2} m_i v_i^2 + e\phi = 0,
\tag{3.6}
$$

where the ion valence is assumed to be unity. This equation can be solved for $\phi \leq 0$,

$$
|v_i| = \sqrt{\frac{2e \left(-\phi \right)}{m_i}}.
\tag{3.7}
$$

Under the condition for the ionization of charge-neutral particles to be negligible, the ion flux is conserved
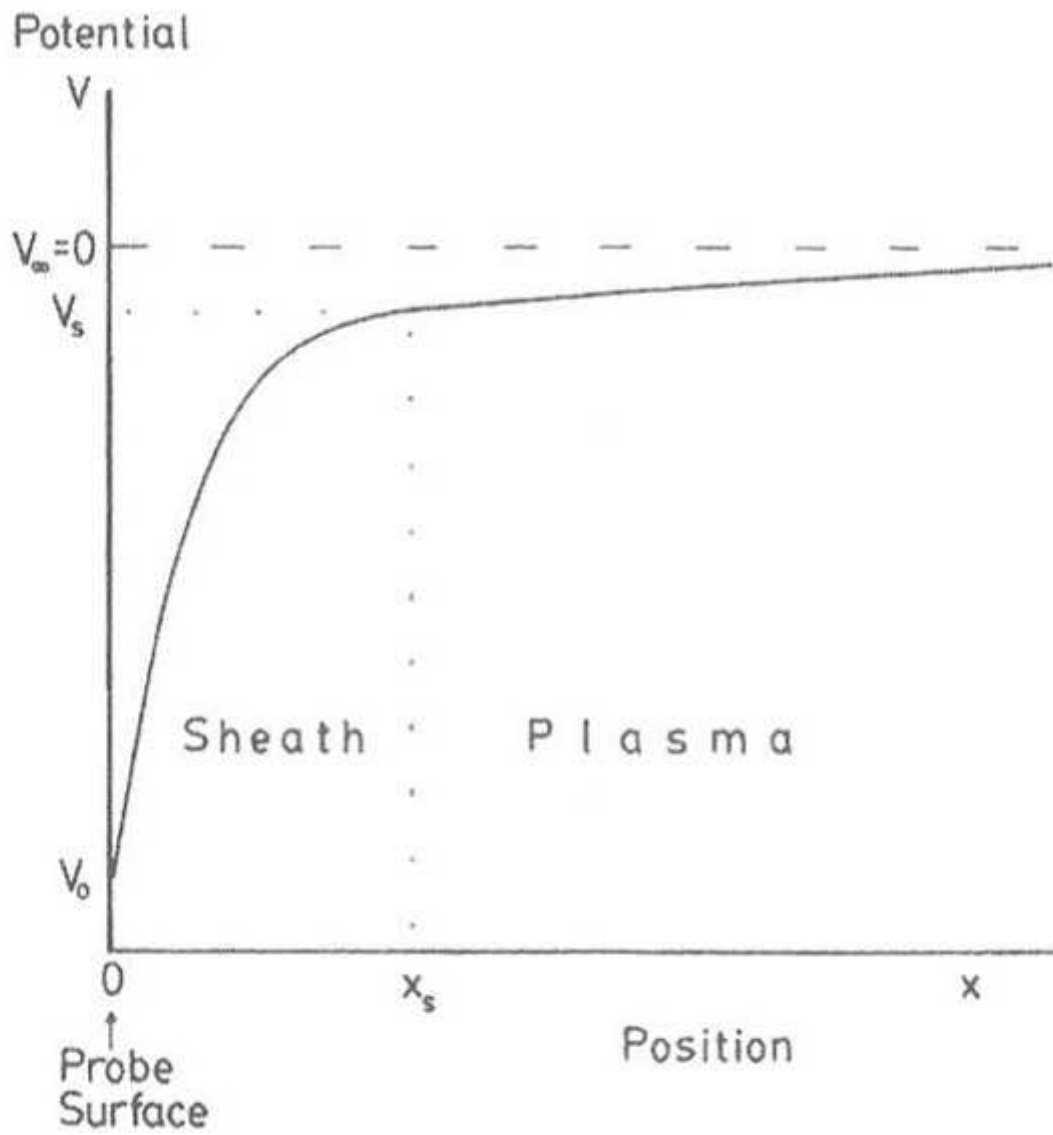
$$
n_i v_i = \text{constant}.
\tag{3.8}
$$

Figure 3.1: Plasma region and sheath region [58]. V_0, V_s, $V_\infty = 0$, and V in this figure correspond to V, ϕ_{sh}, $\phi_\infty = 0$, and ϕ in the text, respectively.

Combining Eqs. (3.7) and (3.8) gives n_i in terms of the ion density at the plasma-sheath boundary $n_{i,sh}$,

$$n_i = n_{i,sh}\sqrt{\frac{\phi_{sh}}{\phi}}.$$ (3.9)

Since electrons are assumed to be in the thermal equilibrium, the electron density at the potential ϕ is given simply using the Boltzmann factor as

$$n_e = n_\infty \exp\left(\frac{e\phi}{T_e}\right) = \left\{n_\infty \exp\left(\frac{e\phi_{sh}}{T_e}\right)\right\}\exp\left\{\frac{e(\phi-\phi_{sh})}{T_e}\right\} = n_{e,sh}\exp\left\{\frac{e(\phi-\phi_{sh})}{T_e}\right\},$$ (3.10)

where n_∞ is the electron density far from the electrode, and the relationship between n_∞ and $n_{e,sh}$,

$$n_{e,sh} = n_\infty \exp\left(\frac{e\phi_{sh}}{T_e}\right)$$ (3.11)

was used in Eq. (3.10). Using n_i and n_e expressed in terms of the values at the plasma-sheath boundary, the Poisson equation becomes

$$\nabla^2\phi = -\frac{e}{\epsilon_0}\left[n_{i,sh}\sqrt{\frac{\phi_{sh}}{\phi}} - n_{e,sh}\exp\left\{\frac{e(\phi-\phi_{sh})}{T_e}\right\}\right].$$ (3.12)

At the plasma-sheath boundary, charge neutrality must be satisfied so that the plasma region and the sheath region are connected smoothly, and this requires

$$n_{i,sh} = n_{e,sh} \equiv n_{sh}.$$ (3.13)

Therefore, the Poisson Eq. (3.12) leads to

$$
\begin{aligned}
\nabla^2\phi &= -\frac{en_{sh}}{\epsilon_0}\left[\sqrt{\frac{\phi_{sh}}{\phi}} - \exp\left\{\frac{e(\phi-\phi_{sh})}{T_e}\right\}\right] \\
&\simeq -\frac{en_{sh}}{\epsilon_0}\left[\sqrt{\phi_{sh}}\left\{\frac{1}{\sqrt{\phi_{sh}}} - \frac{1}{2}\phi_{sh}^{-\frac{3}{2}}(\phi-\phi_{sh})\right\} - \left\{1 + \frac{e(\phi-\phi_{sh})}{T_e}\right\}\right] \\
&= -\frac{en_{sh}}{\epsilon_0}\left[-\frac{1}{2\phi_{sh}} - \frac{e}{T_e}\right](\phi-\phi_{sh}),
\end{aligned}
$$ (3.14)

where the Taylor expansion about $\phi = \phi_{sh}$ to the lowest order was used. If the coefficient $\left[-\frac{1}{2\phi_{sh}} - \frac{e}{T_e}\right]$ is negative, the solution for ϕ in the sheath region is exponential, and this can be connected to the solution in the plasma region. Otherwise, the solution in the sheath becomes sinusoidal, which is unphysical. Thus $\left[-\frac{1}{2\phi_{sh}} - \frac{e}{T_e}\right] \leq 0$, or

$$\phi_{sh} \leq -\frac{T_e}{2e}$$ (3.15)

is required for the sheath to be formed. For the plasma region, the condition of charge neutrality establishes another limit on ϕ_{sh} as [58]

$$\phi_{sh} \geq -\frac{T_e}{2e}.$$ (3.16)

Thus the potential at the plasma-sheath boundary is determined uniquely as

$$\phi_{sh} = -\frac{T_e}{2e}.$$ (3.17)

Now we come back to the problem of current drawn from the plasma by a Langmuir probe. Assuming that the probe potential is sufficiently negative for a sheath to be formed and for all electrons

to be repelled from the probe, the probe current is simply equal to the ion current J_{is} across the sheath surface

$$
\begin{aligned}
J_{\text{is}} &= eA_{\text{sh}}\, n_{\text{i,sh}}\, v_{\text{i,sh}} = eA_{\text{sh}}n_\infty \exp\left(\frac{e\phi_{\text{sh}}}{T_{\text{e}}}\right)\sqrt{\frac{2e\,(-\phi_{\text{sh}})}{m_{\text{i}}}} \\
&= \exp\left(-\frac{1}{2}\right)eA_{\text{sh}}n_\infty\sqrt{\frac{T_{\text{e}}}{m_{\text{i}}}},
\end{aligned}
\tag{3.18}
$$

where A_{sh} denotes the area of the sheath surface and Eqs. (3.11) and (3.13) were used for $n_{\text{i,sh}}$, and Eq. (3.7) for $\phi = \phi_{\text{sh}}$ was used for $v_{\text{i,sh}}$ in the first row. The value given in Eq. (3.18) was given by using Eq. (3.17): $\phi_{\text{sh}} = -\frac{T_{\text{e}}}{2e}$. This J_{is} is called the ion saturation current. For a sufficiently negative probe potential such that all electrons are repelled from the probe, the plasma density n_∞ can be obtained with the knowledge of A_{sh} and T_{e}.

In the intermediate region, not all electrons are repelled from the probe. The electron flux density Γ_{e} near the probe surface, where the potential is V, is given using Eqs. (3.2), (3.3), and (3.10) as

$$
\Gamma_{\text{e}} = \frac{1}{4}n_{\text{e}}\,\langle v_{\text{e}}\rangle = \frac{1}{4}\left\{n_\infty \exp\left(\frac{eV}{T_{\text{e}}}\right)\right\}\cdot 2\sqrt{\frac{2T_{\text{e}}}{\pi m_{\text{e}}}} = \frac{1}{2}n_\infty\sqrt{\frac{2T_{\text{e}}}{\pi m_{\text{e}}}}\exp\left(\frac{eV}{T_{\text{e}}}\right).
\tag{3.19}
$$

Following the convention of adopting the positive sign for the electron current, the total current I_{e} drawn from the plasma is

$$
\begin{aligned}
I_{\text{e}} &= -\left(J_{\text{e}} + J_{\text{is}}\right) \\
&= -\left(-eA_{\text{probe}}\Gamma_{\text{e}}\right) - J_{\text{is}} \\
&= n_\infty eA_{\text{probe}}\sqrt{\frac{T_{\text{e}}}{m_{\text{i}}}}\left[\frac{1}{2}\sqrt{\frac{2m_{\text{i}}}{\pi m_{\text{e}}}}\exp\left(\frac{eV}{T_{\text{e}}}\right) - \frac{A_{\text{sh}}}{A_{\text{probe}}}\exp\left(-\frac{1}{2}\right)\right],
\end{aligned}
\tag{3.20}
$$

where the electron current J_{e} is given using Eq. (3.1) and the area ratio $\frac{A_{\text{sh}}}{A_{\text{probe}}}$ is approximately unity. From Eq. (3.20), the floating potential V_{f} is defined as the probe potential at $I_{\text{e}} = 0$,

$$
V_{\text{f}} = \frac{1}{2}\left[\ln\left(2\pi\frac{m_{\text{e}}}{m_{\text{i}}}\right) - 1\right]\frac{T_{\text{e}}}{e}.
\tag{3.21}
$$

The entire I-V characteristic curve is shown in Fig. 3.2 [58].

The electron temperature T_{e} can be obtained from the slope of the I-V characteristic curve using $J_{\text{e}} = -eA_{\text{probe}}\Gamma_{\text{e}}$ and Eq. (3.19) as

$$
\begin{aligned}
\frac{dI_{\text{e}}}{dV} &= -\frac{dJ_{\text{e}}}{dV} - \frac{dJ_{\text{is}}}{dV} \\
&= -\frac{e}{T_{\text{e}}}J_{\text{e}} - \frac{dJ_{\text{is}}}{dV} \\
&= \frac{e}{T_{\text{e}}}\left(I_{\text{e}} + J_{\text{is}}\right) - \frac{dJ_{\text{is}}}{dV},
\end{aligned}
\tag{3.22}
$$

and in the region where $\frac{dJ_{\text{is}}}{dV}$ is negligible compared to $\frac{dI_{\text{e}}}{dV}$, T_{e} can be obtained as

$$
T_{\text{e}} = \frac{e\left(I_{\text{e}} + J_{\text{is}}\right)}{\frac{dI_{\text{e}}}{dV}}.
\tag{3.23}
$$

Using T_{e} given by Eq. (3.23) and $A_{\text{sh}} \simeq A_{\text{probe}}$, the plasma density n_∞ is derived from Eq. (3.18) as

$$
n_\infty \simeq \frac{J_{\text{is}}}{\exp\left(-\frac{1}{2}\right)eA_{\text{probe}}}\sqrt{\frac{m_{\text{i}}}{T_{\text{e}}}}.
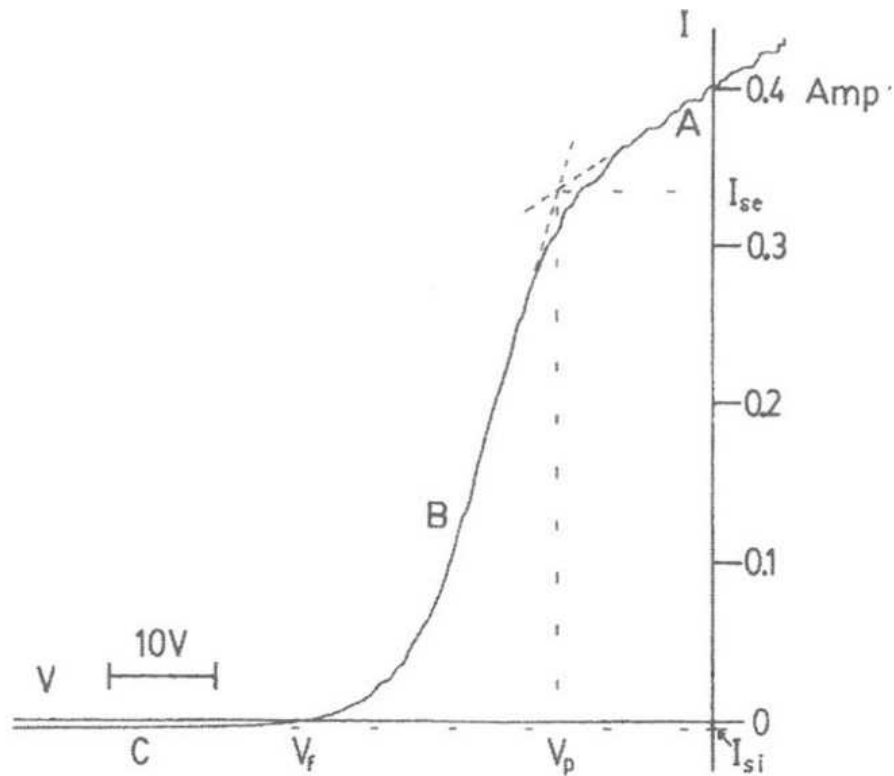\tag{3.24}
$$

Figure 3.2: Typical I-V characteristic curve [58]. A: electron saturation region, B: electron deceleration region, C: ion saturation region. I in this figure corresponds to I_e in the text and I_{si} in this figure corresponds to $-J_{is}$.

3.1.3 Relationship Between Plasma Potential and Floating Potential

In the last subsection, $\phi = 0$ was assumed far from the electrode for simplicity. "Far from the electrode" means that the effect of the probe potential is shielded sufficiently. Since the range of shielding is typically at most an order of magnitude larger than the Debye length given in Eq. (1.42), and in practice it is less than $1\,\text{mm}$ in initial plasmas, the plasma exists in sufficiently shielded regions and the space potential in such regions is equal to the plasma potential ϕ_p. In practice, the potential is measured not with respect to $\phi = 0$ but to $\phi = \phi_\text{p}$. For this case the relationship between V_f and ϕ_p is obtained from Eq. (3.21) by regarding

$$V_\text{f} = V_\text{f} - 0 \quad \rightarrow \quad V_\text{f} - \phi_\text{p}, \tag{3.25}$$

i.e.,

$$V_\text{f} - \phi_\text{p} = \frac{1}{2}\left[\ln\left(2\pi\frac{m_\text{e}}{m_\text{i}}\right) - 1\right]\frac{T_\text{e}}{e},$$

leading to

$$V_\text{f} = \phi_\text{p} + \frac{1}{2}\left[\ln\left(2\pi\frac{m_\text{e}}{m_\text{i}}\right) - 1\right]\frac{T_\text{e}}{e}. \tag{3.26}$$

Equation (3.26) indicates a linear relationship between V_f and ϕ_p. Therefore, the plasma potential or the electrostatic potential ϕ_p, can be estimated from the floating potential V_f. Although there is an additional term that depends on T_e in Eq. (3.26) and this equation holds only in equilibrium, it is expected that V_f reflects ϕ_p even at high frequencies such as $200\,\text{MHz}$. It should be possible to detect the time variation of ϕ_p, which characterizes the LHW, through the time variation of the V_f signal. By definition, V_f is measured when the current drawn from the plasma is zero. This condition is achieved by adding a high impedance resistor to the probe circuit. An attempt to ensure a high impedance on the electrostatic probe at $200\,\text{MHz}$ is discussed in Chapter 5. A flow chart for the determination of the LHW wavenumber from the measurement of V_f is shown in Fig. 3.3.

① Design and fabrication of an electrostatic probe with an embedded high impedance resistor (high impedance Langmuir probe unit) for measuring the floating potential V_f accurately.

↓

② Design and fabrication of a probe assembly consisting of an array of three high impedance Langmuir probe units, one magnetic probe, and one plain Langmuir probe.

↓

③ Sensitivity calibration of the probe assembly to an electromagnetic wave ($|E|=|cB|$) inside a coaxial transmission line.

↓

④ Measurement of the 200 MHz signal using the probe assembly in initial plasmas driven by the LHW at 200 MHz in TST-2.

↓

⑤ Comparison of estimated currents drawn from the plasma by the high impedance Langmuir probe unit and the plain Langmuir probe.

↓

⑥ Identification of the type of the measured wave based on signal amplitudes measured in the plasma (④) and the calibrated sensitivity to the electromagnetic wave (③).

↓

⑦ Calculation of phase differences among signals measured by high impedance Langmuir probe units in the plasma (④), with estimations of their uncertainties using signals measured during RF injection into vacuum.

↓

⑧ Conversion of the phase difference, its error, and its sign to the wavenumber, its error, and its direction.
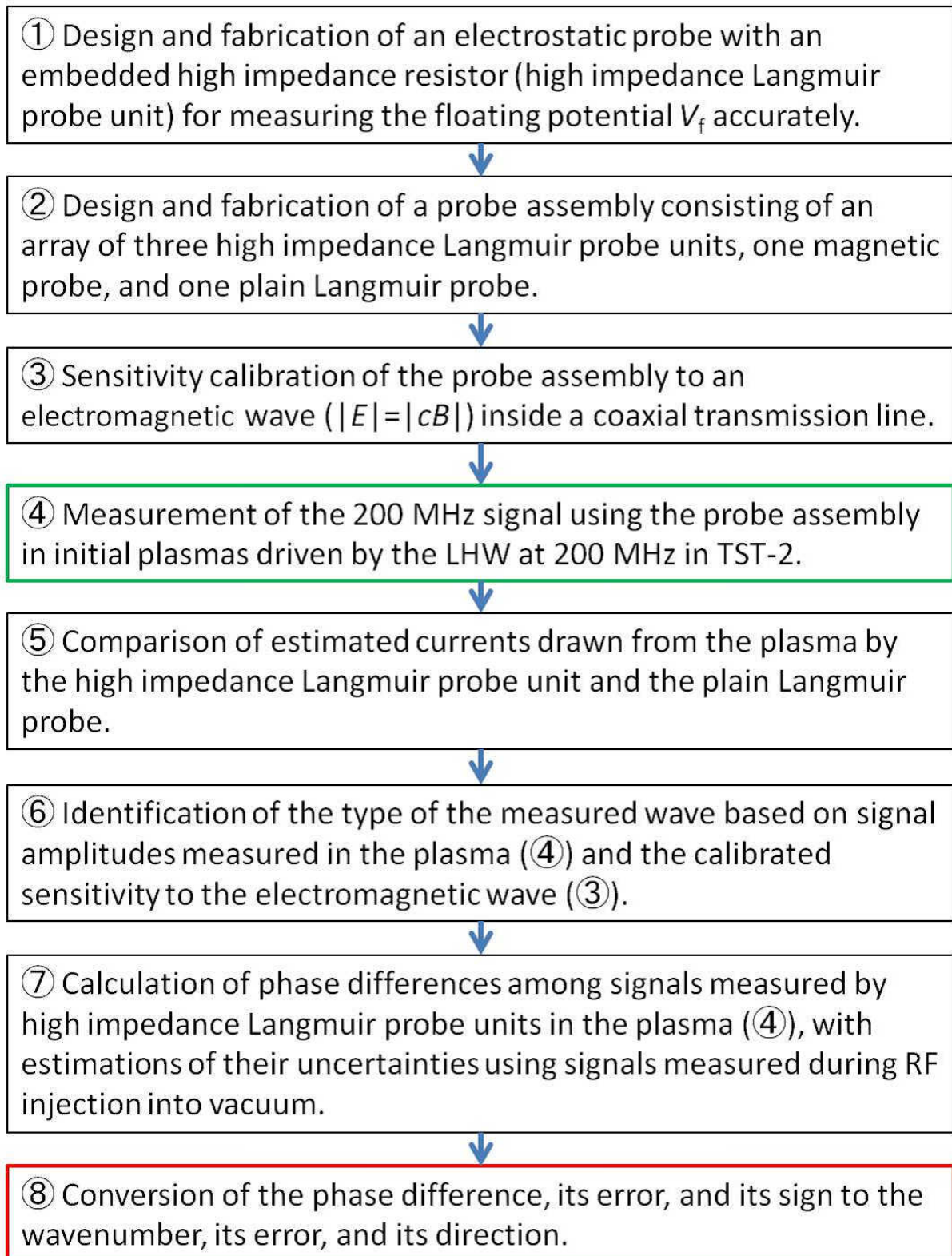
Figure 3.3: Flow chart for the determination of the LHW wavenumber from the measurement of V_f.

Chapter 4

The TST-2 Spherical Tokamak and 200 MHz RF System

4.1 TST-2 Device

TST-2 (Tokyo Spherical Tokamak-2) is a spherical tokamak built in 1999 as an upgrade of the TST-M (Tokyo Spherical Tokamak-Modified) [59,60] and is located in the Kashiwa campus of the university of Tokyo. A photograph of the TST-2 device is shown in Fig. 4.1 and its coil system is shown in Fig. 4.2. The TST-2 has 24 turns of toroidal coils on vertical planes with equal interval in the toroidal direction for making toroidal magnetic field, and 40 turns of poloidal field 3 coils on the two horizontal planes with equal distances from the equatorial plane for making poloidal magnetic field, which is necessary for an equilibrium. The other coils are also used to make additional poloidal magnetic field or adjust a shape of a plasma. The TST-2 has two operation modes using the OH solenoid or the 200 MHz RF wave (the lower hybrid wave). Typical parameters of these operations are listed in Table 4.1. The TST-2 equips many diagnostics to monitor various signals from plasmas. Diagnostics in the TST-2 are summarized in Table 4.2.

Presently, TST-2 has three heating systems. They are an ohmic heating solenoid coil (OH solenoid), a 2.45 GHz magnetron for electron cyclotron heating, and a 200 MHz RF system. The OH solenoid is 1.7 m long and consists of 240 turns of coils inside a center stack of the TST-2. In the case of a charging voltage to be 4 kV, it takes 8 ms for the coil current to reach its maximum of about 23 kA. After a commutation, it takes 21 ms for the current to change from $+23$ kA to -15 kA, which is a maximum

Table 4.1: Typical parameters of TST-2.

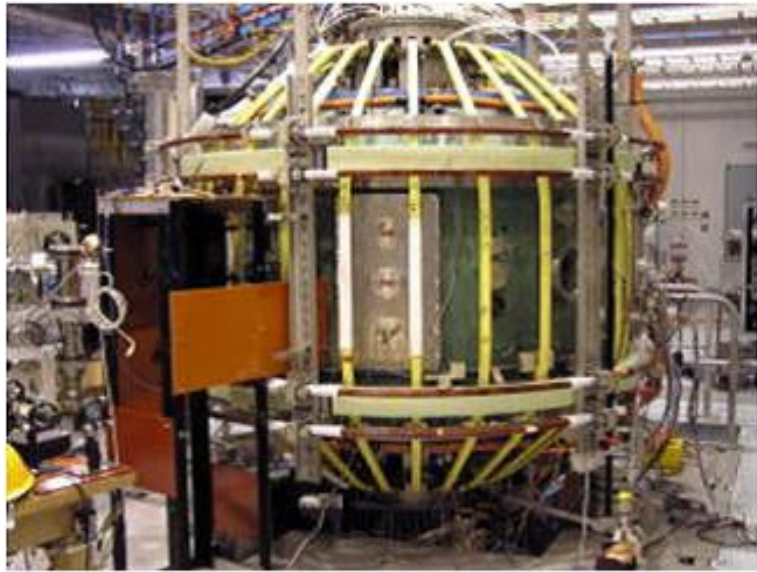|	OH Operation	200 MHz RF Start-up Operation
Major Radius R_0	0.38 m	
Minor Radius a	0.24 m	
Aspect Ratio $A = R_0/a$	< 1.6	
Toroidal Magnetic Field B_t	~ 0.3 T	~ 0.2 T
Plasma Current I_p	< 0.2 MA	< 20 kA
Ion Temperature T_i	$50 \sim 100$ eV	~ 20 eV
Electron Temperature T_e	$100 \sim 400$ eV ($R = 0.38$ m)	~ 20 eV ($R = 0.38$ m, Bulk)
Electron Density n_{e0}	$(1 \sim 2) \times 10^{19}$ m^{-3} ($R = 0.38$ m)	$\sim 5 \times 10^{17}$ m^{-3} ($R = 0.38$ m)
Discharge Duration Time	< 40 ms	< 120 ms

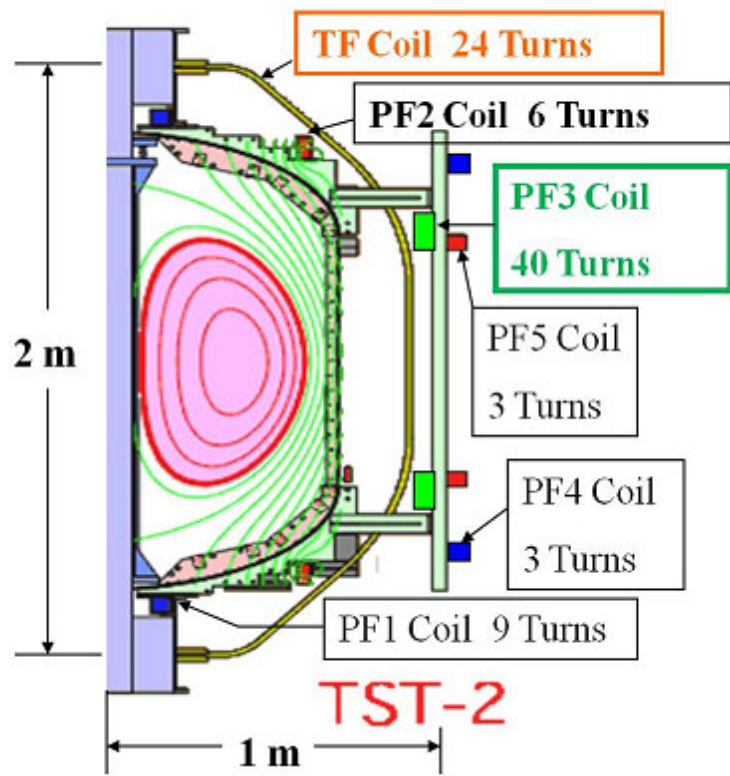Figure 4.1: Tokyo Spherical Tokamak-2 (TST-2).

Figure 4.2: Coil system of TST-2.

Table 4.2: Diagnostics in the TST-2.

Instrument	Measured information
Coils	Magnetic field and plasma current (I_p)
H_{alpha}, H_{beta}	Radiation from hydrogen
AXUV	Total radiation from plasmas
SBD	Hard X ray
Pin-Diode	Soft X ray
CCD-Camera	Visible radiation profile
Visible light spectroscopy	Ion temperature
Thomson scattering	Electron temperature and density
Interferometer	Line integrated density
Electrostatic probes	Electron temperature and density

of a reversed current. In this phase, induced electric field along the toroidal direction accelerates and heats the plasma. An average loop voltage of this phase is estimated as

$$V_{\text{loop,avg}} = \frac{\Delta \Phi}{\Delta t} = \frac{\Delta B \times S}{\Delta t} = \frac{\{4.08 - (-2.66)\}\,[\text{T}] \times 0.0254[\text{m}^2]}{0.021[\text{s}]} = 8.15\,\text{V}, \tag{4.1}$$

where Φ and B are a magnitude of magnetic flux and a magnitude of magnetic flux density inside the OH solenoid, respectively, and S is an area of its cross section.

The magnetron provides 5 kW of microwave at 2.45 GHz, which is the electron cyclotron frequency for the magnetic field of 0.0875 T. This is called ECH and used for electron cyclotron heating and pre-ionization of the plasma. Modes of the wave are selected to O-mode or X-mode by adjusting a polarization in the wave guide. In the ECH plasmas, spherical tokamak start-up experiments have been conducted [61]. The 200 MHz RF system is referred to in detail in the next section.

4.2   200 MHz RF System

4.2.1   High Power Amplifier System

The 200 MHz RF system is utilized for non-inductive plasma start-up and I_p ramp up. Figure 4.3 shows a photograph of the RF system. RF power at 200 MHz was first injected into the TST-2 plasma in February 2010. This system was originally built as the fast wave current drive system for the JFT-2M tokamak at Japan Atomic Energy Agency (JAEA) [37]. The system consists of four identical amplifier chain subsystems with a common RF source. The nominal output power of each subsystem is 100 kW. Therefore, the total output power of up to 400 kW is available. A schematic diagram of this system is shown in Fig. 4.4. The RF source signal is generated by a signal generator, and is amplitude modulated by a pulse modulator to have the desired waveform and pulse width. After amplification, the power is divided into four subsystems and amplified further. Attenuators and phase shifters located after the power divider are used to adjust the relative amplitude and relative phase of waves in each subsystem. The circulator at the output of the final amplifier protects the amplifier from excessive reflected power. The output of each subsystem is fed to each waveguide of the grill antenna, described briefly in the next subsection, and is radiated into the plasma. The transmission line is electrically isolated between the final amplifier and the grill antenna by a DC break. Typical power gains of components in the amplification system are listed in Table 4.3.
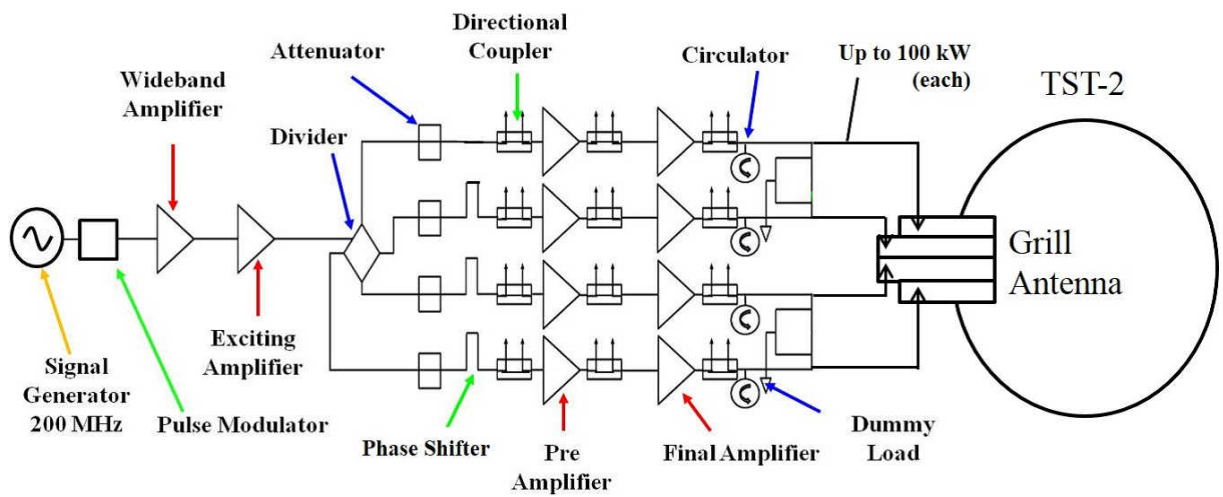
Figure 4.3: 200 MHz RF System.

Figure 4.4: Schematic diagram of the 200 MHz RF system.

Table 4.3: Typical power gains of components in the amplification system.

Component	Power Gain
Wideband Amplifier	$40\,\mathrm{dB}$
Excitation Amplifier	$13\,\mathrm{dB}$
Power Divider	$-6\,\mathrm{dB}$
Attenuator	$-70 \sim 0\,\mathrm{dB}$
Intermediate Amplifier	$10\,\mathrm{dB}$
Final Amplifier	$6\,\mathrm{dB}$

4.2.2 Grill Antenna

A dielectric-loaded waveguide array antenna, called the "Grill antenna" is installed in the TST-2 in order to launch the LHW [36]. This antenna consists of four waveguides filled with alumina ($\epsilon_\mathrm{r} = 10$) to reduce the waveguide size. The launched wavenumber is variable by changing a phase difference between adjacent waveguides by tuning a phase shifter shown in Fig. 4.4. The launched wavenumber is $k_\parallel = 0 \sim 75.4\,\mathrm{m}^{-1}$, or $n_\parallel = 0 \sim 18$. A waveguide size is $285\,\mathrm{mm}$ by $30\,\mathrm{mm}$ and the appearance of the grill antenna is shown in Fig. 4.5.

Figure 4.5: Grill antenna.

Chapter 5

Electrostatic Probe with an Embedded High Impedance Resistor

As stated in Chapter 2, the lower hybrid wave (LHW) can be regarded as an electrostatic wave in the initial plasma, meaning that it is described by an oscillating electrostatic potential ϕ_p. Since ϕ_p can be related to the floating potential V_f, as described in Chapter 3, the measurement of V_f is important. Although Eq. (3.26) is a relationship that holds in equilibrium, a linkage between the oscillating parts of ϕ_p and V_f is expected, and thus it is worth investigating V_f at $200\,\mathrm{MHz}$.

5.1 Floating Potential Measurement at 200 MHz

In order to measure the floating potential, it is necessary to create the condition $I = 0$, where I is the probe current. This is realized by introducing a high impedance to the probe circuit. For low frequencies up to several MHz, the measurement of V_f is easily accomplished by connecting a high impedance resistor at the end of the signal transmission line, as shown schematically in Fig. 5.1. For these frequencies, the wavelength on the transmission line is greater than $100\,\mathrm{m}$ which is usually much longer than the signal transmission line. Therefore, the wave at the left end of the transmission line in Fig. 5.1 sees the high impedance resistor within its wavelength, and the voltage of the wave acts on both the transmission line and the high impedance resistor. This system is called the lumped parameter circuit. In this case, the transmission line is represented by a lumped parameter.

On the other hand, at $200\,\mathrm{MHz}$, the wavelength is only about $1\,\mathrm{m}$ in the transmission line. This wavelength is usually shorter than the transmission line in an experimental system, and thus the wave on the left end of the transmission line in Fig. 5.1 cannot see the high impedance resistor on the right end of the transmission line within its wavelength. In this case, it is necessary to consider how the wave propagates in the transmission line and how the wave behaves when it reaches the high impedance resistor. This system is called the distributed parameter circuit.

In this way, an appropriate model depends on the relative magnitude between the wavelength and the size of circuit elements, including the resistor and the transmission line. Therefore, measuring systems used in this thesis are treated using either lumped parameters or distributed parameters depending on the situation.
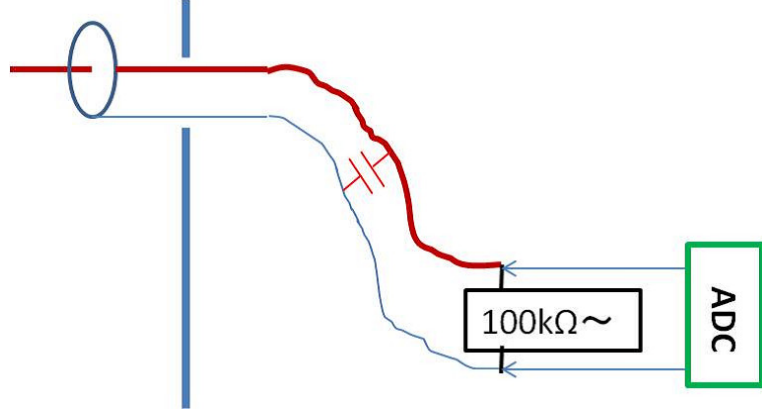
Figure 5.1: Floating potential measurement at low frequencies by a Langmuir probe.

5.2 Loss-less Transmission-Line Theory

5.2.1 Voltage and Current in a Transmission Line

Neglecting the resistive loss and the conductance in the cable, an equivalent circuit for a coaxial cable treated as a distributed parameter element is shown in Fig. 5.2, where L and C are inductance and capacitance per unit length ($1\,\mathrm{m}$), respectively. Considering Kirchhoff's laws, the following equations are derived:

$$\begin{cases} V(z,t) = V(z+\Delta z,t) + (L\Delta z)\dfrac{\partial I(z,t)}{\partial t} \\[2mm] I(z,t) = I(z+\Delta z,t) + (C\Delta z)\dfrac{\partial V(z,t)}{\partial t} \end{cases}$$

or

$$\begin{cases} \dfrac{V(z+\Delta z,t) - V(z,t)}{\Delta z} = -L\dfrac{\partial I(z,t)}{\partial t} \\[2mm] \dfrac{I(z+\Delta z,t) - I(z,t)}{\Delta z} = -C\dfrac{\partial V(z,t)}{\partial t}. \end{cases}$$

In the limit $\Delta z \to 0$,

$$\begin{cases} \dfrac{\partial V(z,t)}{\partial z} = -L\dfrac{\partial I(z,t)}{\partial t} & (5.1) \\[2mm] \dfrac{\partial I(z,t)}{\partial z} = -C\dfrac{\partial V(z,t)}{\partial t}. & (5.2) \end{cases}$$

Upon partial differentiation of Eqs. (5.1) and (5.2) by z and t, the two equations can be combined to give

$$\frac{\partial^2 V(z,t)}{\partial z^2} = LC\frac{\partial^2 V(z,t)}{\partial t^2}. \tag{5.3}$$

For

$$V(z,t) = V_0 \exp\left\{i\left(k_0 z - \omega t\right)\right\}, \tag{5.4}$$

where V_0 is the complex amplitude, k_0 is a constant wavenumber, and $\omega > 0$ is the angular frequency. Substituting Eq. (5.4) into Eq. (5.3) gives
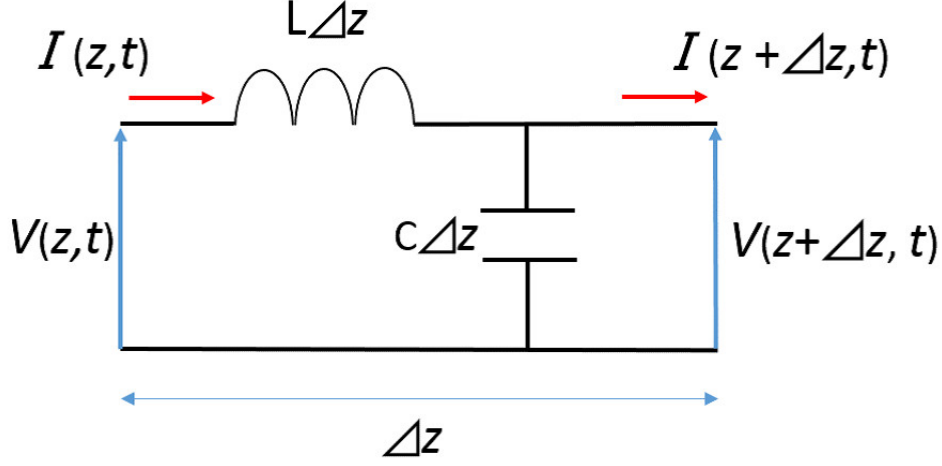
$$k_0 = \pm\omega\sqrt{LC}. \tag{5.5}$$

Figure 5.2: Equivalent circuit diagram for an infinitesimal part of a transmission line.

Defining

$$\omega\sqrt{LC} = k, \tag{5.6}$$

Eq. (5.5) can be written as $k_0 = \pm k$. The solution for Eq. (5.3) is given as

$$V(z,t) = Ae^{i(kz-\omega t)} + Be^{i(-kz-\omega t)}, \tag{5.7}$$

where both A and B are complex amplitudes. Physical meanings of the first term and the second term on the right-hand side of Eq. (5.7) are waves propagating in positive and negative z directions, respectively. This can be understood by considering the position $z = z_0$ of constant phase ϕ_0,

$$\pm kz_0 - \omega t = \phi_0,$$

where the positive and negative signs come from the first term and the second term on the right-hand side of Eq. (5.7). The velocity of the position where the phase is ϕ_0 is

$$\frac{dz_0}{dt} = \pm\frac{\omega}{k}.$$

Since ω and k are both positive, $\frac{dz_0}{dt} > 0$ for the positive sign and $\frac{dz_0}{dt} < 0$ for the negative one. This means that the waves $Ae^{i(kz-\omega t)}$ and $Be^{i(-kz-\omega t)}$ proceed in the positive and negative z directions, respectively. Equation (5.7) can be expressed as a product of the spatially-varying term and the temporally-varying term as

$$\begin{aligned} V(z,t) &= \left(Ae^{ikz} + Be^{-ikz}\right)e^{-i\omega t} \\ &\equiv V(z)e^{-i\omega t}. \end{aligned} \tag{5.8}$$

Assuming the same time dependence $e^{-i\omega t}$ for $I(z,t)$, substituting Eq. (5.7) into Eq. (5.1) gives

$$ik\left(Ae^{ikz} - Be^{-ikz}\right)e^{-i\omega t} = i\omega LI(z,t).$$
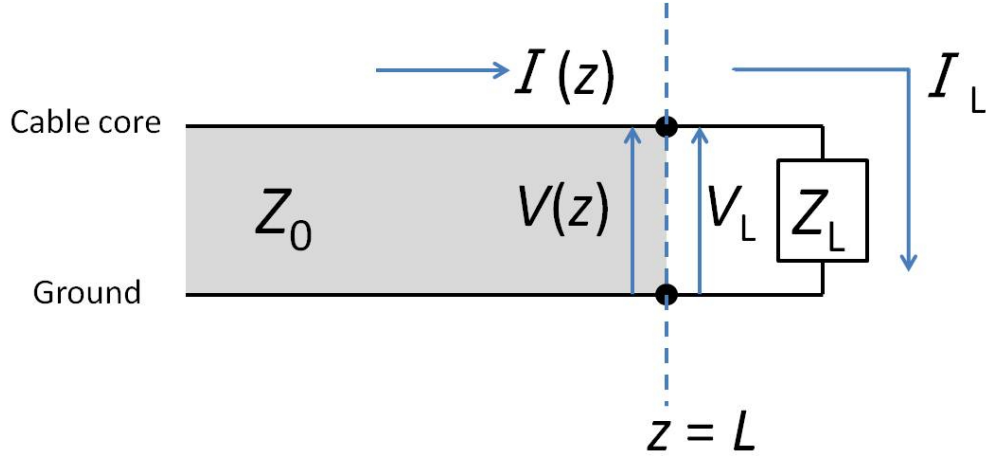
Figure 5.3: Voltage and current on each side of the boundary between a transmission line and a lumped impedance Z_L.

Using Eq. (5.6), this equation reduces to

$$
\begin{aligned}
I(z,t) &= \frac{Ae^{ikz} - Be^{-ikz}}{\sqrt{\frac{L}{C}}} e^{-i\omega t} \\
&\equiv \frac{Ae^{ikz} - Be^{-ikz}}{Z_0} e^{-i\omega t} \\
&\equiv I(z)e^{-i\omega t},
\end{aligned}
\tag{5.9}
$$

where

$$
Z_0 = \sqrt{\frac{L}{C}}
\tag{5.10}
$$

is called the characteristic impedance of the transmission line and is independent of the wave frequency. Equations (5.8) and (5.9) describe the voltage and current in a transmission line.

5.2.2 Reflection and Transmission at a Transmission Line Boundary

In this subsection, wave behavior in a transmission line when it encounters a lumped circuit element is considered. This is the case when the signal propagating in the coaxial cable in Fig. 5.1 reaches the oscilloscope. Taking the z-axis along the coaxial cable and representing the input impedance of the oscilloscope by Z_L, this situation is indicated graphically in Fig. 5.3. The position of Z_L is at $z = L$. Here, $V(z)$ and $I(z)$ are voltage and current in the cable, and are derived from Eqs. (5.8) and (5.9) as

$$
\begin{cases}
V(z) = Ae^{ikz} + Be^{-ikz} & \text{(5.11)} \\
I(z) = \dfrac{Ae^{ikz} - Be^{-ikz}}{Z_0}. & \text{(5.12)}
\end{cases}
$$

V_L in Fig. 5.3 is the voltage across the impedance Z_L, and I_L is the current through the impedance. Continuity of voltage and current at $z = L$ and the definition of the impedance Z_L require

$$\begin{cases} V(L) = Ae^{ikL} + Be^{-ikL} = V_L & (5.13) \\ I(L) = \dfrac{Ae^{ikL} - Be^{-ikL}}{Z_0} = I_L \\ \dfrac{V_L}{I_L} = Z_L. \end{cases}$$

These three equations give

$$\frac{Ae^{ikL} + Be^{-ikL}}{Ae^{ikL} - Be^{-ikL}} = \frac{Z_L}{Z_0}. \tag{5.14}$$

A point of interest is what fraction of the incident wave is reflected back at $z = L$. The voltage reflection coefficient $\Gamma(z)$ is defined as

$$\Gamma(z) \equiv \frac{Be^{-ikz}}{Ae^{ikz}}. \tag{5.15}$$

Equation (5.14) can be expressed in terms of $\Gamma(z = L)$ as

$$\frac{1 + \Gamma(L)}{1 - \Gamma(L)} = \frac{Z_L}{Z_0},$$

or equivalently

$$\Gamma(L) = \frac{Z_L - Z_0}{Z_L + Z_0}. \tag{5.16}$$

From Eq. (5.16), $\Gamma(L) = 0$ when $Z_L = Z_0$, and thus no reflection occurs at $z = L$. When $\Gamma(L) = 0$, $B = 0$ and a wave propagating in the negative z direction no longer exists since

$$\begin{aligned} \Gamma(z) &\equiv \frac{Be^{-ikz}}{Ae^{ikz}} = \frac{Be^{-ik\{L+(z-L)\}}}{Ae^{ik\{L+(z-L)\}}} = \frac{Be^{-ikL}}{Ae^{ikL}} e^{-2ik(z-L)} \\ &= \Gamma(L)e^{-2ik(z-L)} \end{aligned}$$

and thus $\Gamma(L) = 0$ gives $\Gamma(z) = 0$ for any z in the cable. This is called impedance matching, and under this condition the amplitude and the phase of the signal are transferred to subsequent circuit elements without any alteration. Therefore, it is critical to match the input impedance of the instrument to the same value as the characteristic impedance Z_0 of the transmission line.

Another important quantity is the voltage transmission coefficient defined at $z = L$ as

$$T(L) \equiv \frac{V_L}{Ae^{ikL}}. \tag{5.17}$$

Using Eqs. (5.13), (5.15) for $z = L$, and (5.16), $T(L)$ can be expressed as

$$\begin{aligned} T(L) &\equiv \frac{V_L}{Ae^{ikL}} = \frac{Ae^{ikL} + Be^{-ikL}}{Ae^{ikL}} = 1 + \Gamma(L) \\ &= \frac{2Z_L}{Z_L + Z_0}. \end{aligned} \tag{5.18}$$
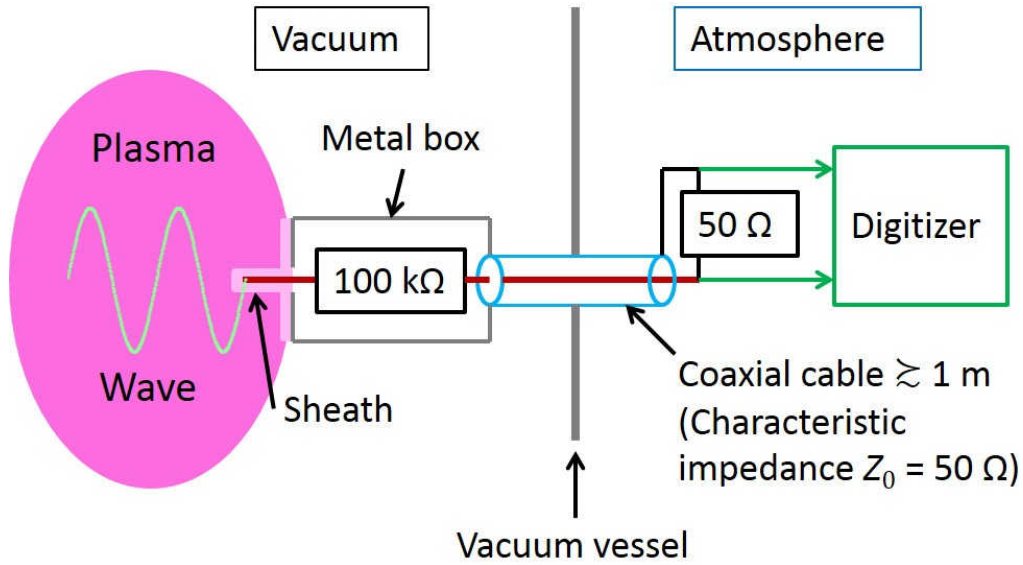
It can be seen that $T(L) = 1$ for $Z_L = Z_0$.

Figure 5.4: Proposed configuration for floating potential measurement at high frequencies, with a high impedance resistor between the probe electrode and the signal transmission cable.

5.3 Electrostatic Probe with an Embedded High Resistance

In the previous section, the requirement for a signal transmission line with a characteristic impedance Z_0 to be terminated by a measurement instrument with the same input impedance was described. Although a sheath that forms in front of a probe electrode adds an impedance of the order of kΩ, the impedance of the probe system is still much smaller than hundreds of kΩ, typical values of resistance used for floating potential measurement at low frequencies.

A new configuration for a floating potential measurement circuit is suggested in which a high impedance resistor is placed before the cable, immediately after the probe electrode, as shown in Fig. 5.4. Under this configuration, even high frequency signals such as 200 MHz can recognize the high impedance resistor within its wavelength at the entrance to the probe circuit, satisfying the condition suitable for measuring V_f. A 100 kΩ non-magnetic chip resistor was used. In order to protect the circuit from the plasma and to shield it from electromagnetic noise, the circuit is enclosed in a stainless steel (SUS304) box. The length of this probe circuit is about 1 cm. The probe unit is shown in Fig. 5.5.

Although inductors can introduce high impedance at high frequency, no such circuit element was used. This is because for the wavenumber measurement, the phase of the probe signal is important and such inductors could alter the phase drastically by creating a resonance in the probe circuit. In order to avoid such a risk and to keep a plain phase response of the probe, only a resistor is used in the probe circuit. In this thesis, the Langmuir probe with an embedded high impedance resistor enclosed in a stainless steel box is called the high impedance Langmuir probe unit, and the high impedance Langmuir probe unit with a transmission cable to the measuring instrument is called the high impedance Langmuir probe system.
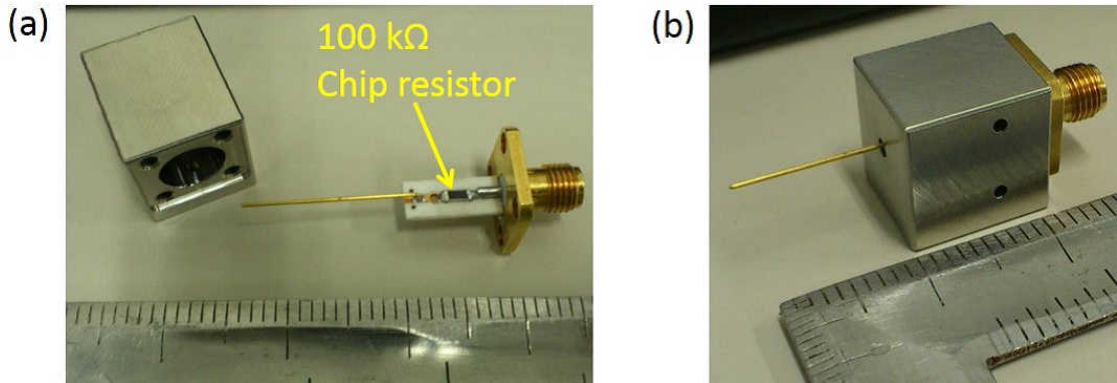
Figure 5.5: Photographs of the probe unit. (a) Probe circuit with a high impedance chip resistor and a stainless steel (SUS304) shield box. (b) Assembled unit.

5.4 Frequency Response of the High Impedance Langmuir Probe System

In this section, the impedance of the high impedance Langmuir probe system is evaluated in air and compared with the impedance of a sheath formed around the probe when the probe is inserted into a plasma. If the absolute value of the impedance of the high impedance Langmuir probe system is larger than the sheath impedance, the $100\,\mathrm{k\Omega}$ chip resistor is effective in presenting a high impedance to the probe circuit.

5.4.1 Equivalent Circuit of the High Impedance Langmuir Probe System

When a signal enters the electrode of the high impedance Langmuir probe unit, it passes through the $100\,\mathrm{k\Omega}$ chip resistor and enters the transmission cable of characteristic impedance Z_0, and is detected by a measuring instrument whose input impedance is matched to Z_0. An equivalent circuit of this high impedance Langmuir probe system is depicted in Fig. 5.6, where Z_{chip}, C_{box}, and Z_0 represent the impedance of the $100\,\mathrm{k\Omega}$ chip resistor, the capacitance formed between the signal line and the stainless steel box, and the transmission cable terminated by its characteristic impedance Z_0, respectively.

It is reasonable to use the lumped parameters Z_{chip} and C_{box} to represent the high impedance Langmuir probe unit because the dimension of the probe unit is no more than $3\,\mathrm{cm}$, much shorter than the wavelength, which is of the order of $1\,\mathrm{m}$ at $200\,\mathrm{MHz}$. A transmission cable longer than $1\,\mathrm{m}$ is usually treated as a distributed parameter element with characteristic impedance Z_0 at $200\,\mathrm{MHz}$, but it can be expressed as a lumped parameter element with impedance Z_0 when it is terminated by the matched impedance Z_0. Under this situation, the energy propagating in the transmission cable will not reflect back to the probe, and can be represented by dissipation by a lumped parameter resistor with $R = Z_0$. In what follows, the impedance of this probe system is discussed.

1. Impedance of the $100\,\mathrm{k\Omega}$ Chip Resistor

Although the nominal impedance of the chip resistor is $100\,\mathrm{k\Omega}$, it also has a parasitic capacitance $C_{\mathrm{parasitic}}$, as shown in Fig. 5.6. This parasitic capacitance can be measured by a network analyzer. The chip resistor was connected to a coaxial cable as shown in Fig. 5.7, with each side of the chip resistor soldered to a plug segment of the coaxial cable, and is inserted into a jack type connector. The RF power is supplied by the output port of the network analyzer through the cable on the left, and the transmitted power goes back to the input port of the network analyzer through the cable on
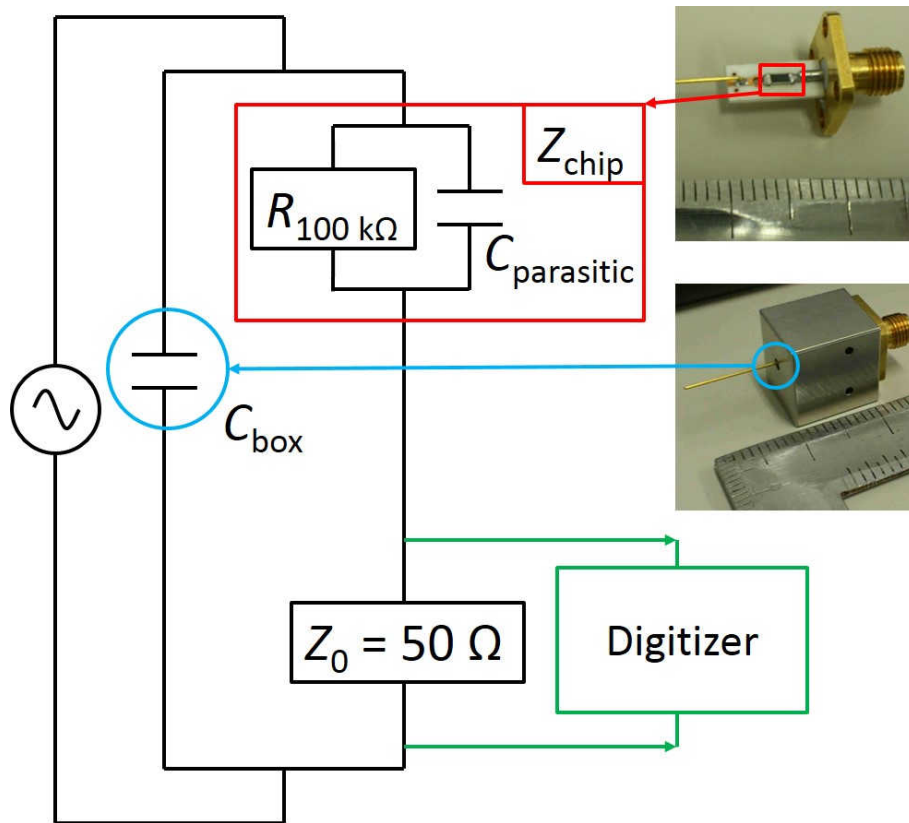
Figure 5.6: Equivalent circuit for the high impedance Langmuir probe system.

Figure 5.7: Chip resistor connection.

the right. The impedance of each port of the network analyzer is $50\,\Omega$. This configuration is modeled as shown in Fig. 5.8, where the chip resistor and the terminated transmission cable are represented by lumped parameters.

The voltage and the current in this model are depicted in Fig. 5.9. In this figure, V and V_{lump} are the voltage in the transmission cable and the voltage on the lumped parameter section. Since the impedance of the lumped parameter section is $Z_{\mathrm{L}} = Z_{\mathrm{chip}} + Z_0$ where Z_{chip} is the impedance of the chip resistor including the parasitic capacitance $C_{\mathrm{parasitic}}$, V_{lump} is given in terms of V using Eq. (5.18) as

$$V_{\mathrm{lump}} = \frac{2Z_{\mathrm{L}}}{Z_{\mathrm{L}} + Z_0} V = \frac{2\left(Z_{\mathrm{chip}} + Z_0\right)}{Z_{\mathrm{chip}} + 2Z_0} V. \tag{5.19}$$

V_{Z_0} and I_{Z_0} in Fig. 5.9 are the voltage across and the current through the network analyzer input port, and are expressed as

$$V_{Z_0} = \frac{Z_0}{Z_{\mathrm{chip}} + Z_0} V_{\mathrm{lump}}, \tag{5.20}$$

$$I_{Z_0} = \frac{V_{\mathrm{lump}}}{Z_{\mathrm{chip}} + Z_0}. \tag{5.21}$$

Thus, the time-averaged power P_{Z_0} into the network analyzer input port is given as

$$\begin{aligned}
P_{Z_0} &= \frac{1}{2}\overline{I_{Z_0}}V_{Z_0} = \frac{1}{2}\frac{Z_0}{|Z_{\mathrm{chip}} + Z_0|^2}|V_{\mathrm{lump}}|^2 \\
&= \frac{2Z_0}{|Z_{\mathrm{chip}} + 2Z_0|^2}|V|^2
\end{aligned} \tag{5.22}$$

where the overline $\overline{I_{Z_0}}$ stands for the complex conjugate of I_{Z_0} and Eq. (5.19) was used. After the effects of the two cables are calibrated out, the network analyzer gives the power ratio of P_{Z_0} to the time-averaged output power provided by the network analyzer $P = \frac{1}{2}\frac{|V|^2}{Z_0}$, i.e.,

$$\frac{P_{Z_0}}{P} = \frac{4Z_0^2}{|Z_{\mathrm{chip}} + 2Z_0|^2}. \tag{5.23}$$
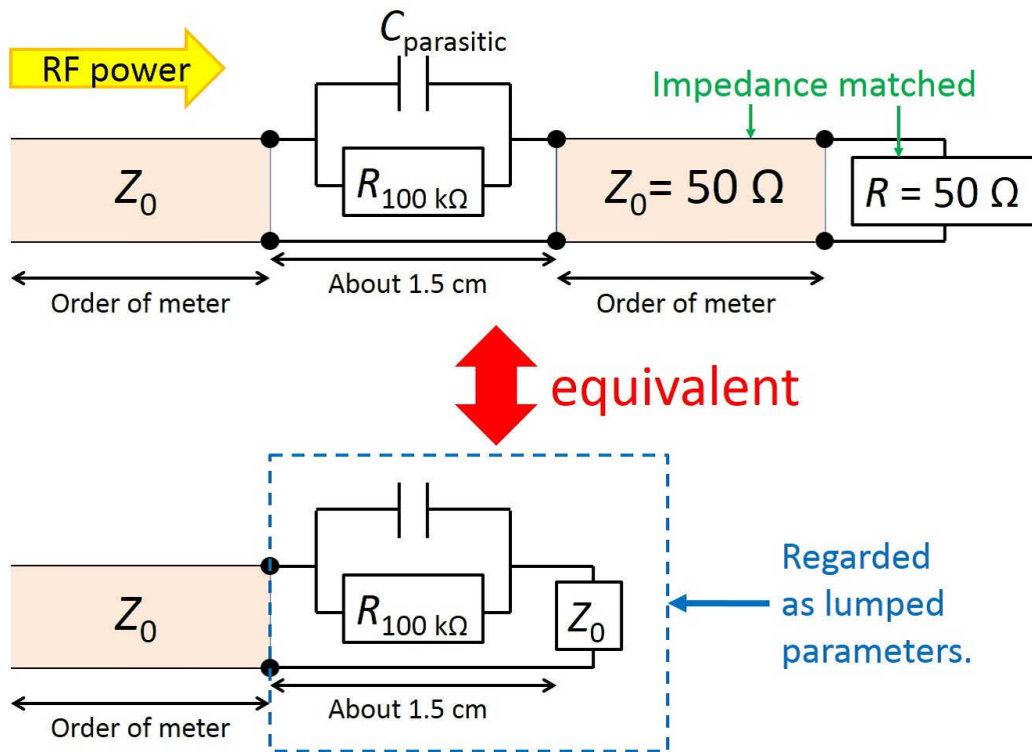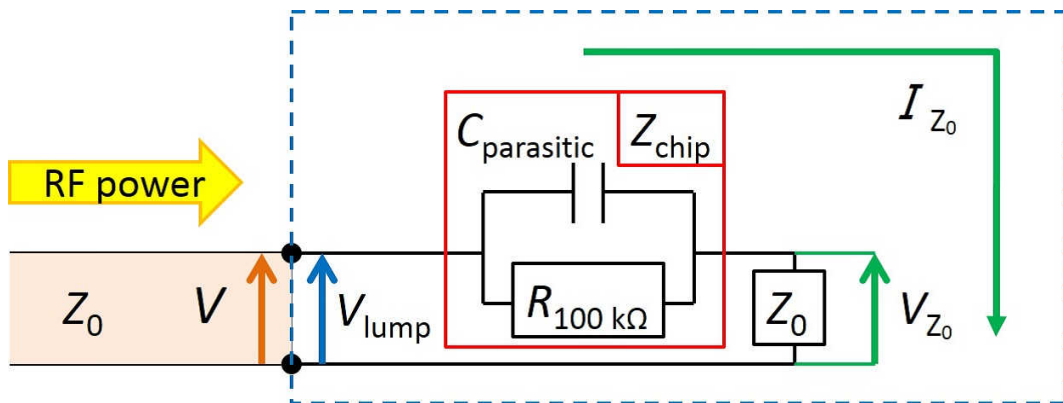
93

Figure 5.8: Circuit model of the chip resistor.

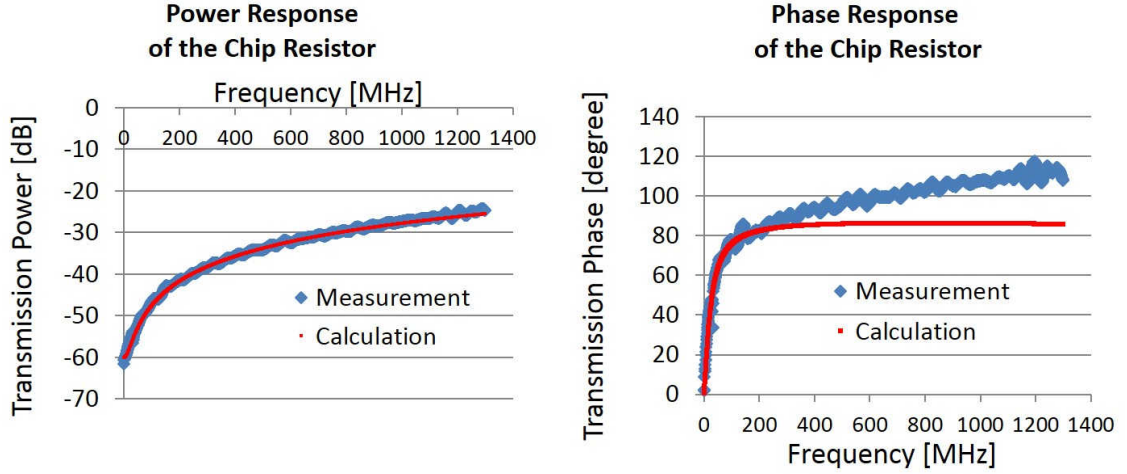Figure 5.9: Voltage and current in the chip resistor circuit model.

Figure 5.10: Measured frequency response of the chip resistor and that calculated by the circuit model using $C_{\mathrm{parasitic}} = 0.065\,\mathrm{pF}$. The blue lines represent the measured response and the red lines represent the model calculation.

Since Z_{chip} is the parallel impedance consisting of $R_{100\,\mathrm{k\Omega}}$ and $C_{\mathrm{parasitic}}$, it is expressed as

$$\frac{1}{Z_{\mathrm{chip}}} = \frac{1}{R_{100\,\mathrm{k\Omega}}} + i\omega C_{\mathrm{parasitic}} = \frac{1 + iK}{R_{100\,\mathrm{k\Omega}}}, \tag{5.24}$$

where a dimensionless constant K is defined as

$$K \equiv \omega C_{\mathrm{parasitic}} R_{100\,\mathrm{k\Omega}}. \tag{5.25}$$

Equation (5.23) can then be expressed including the effect of $C_{\mathrm{parasitic}}$ through K as

$$\frac{P_{Z_0}}{P} = \frac{4\left(1 + K^2\right) Z_0^2}{\left(R_{100\,\mathrm{k\Omega}} + 2Z_0\right)^2 + 4K^2 Z_0^2}. \tag{5.26}$$

The phase shift

$$\arg\left(\frac{V_{Z_0}}{V}\right) = \arg\left(\frac{2Z_0}{Z_{\mathrm{chip}} + 2Z_0}\right) = \arctan\left[\frac{K R_{100\,\mathrm{k\Omega}}}{R_{100\,\mathrm{k\Omega}} + 2\left(1 + K^2\right) Z_0}\right] \tag{5.27}$$

is also measured by the network analyzer.

In order for Eqs. (5.26) and (5.27) to reproduce the measured result, a parasitic capacitance of $0.065\,\mathrm{pF}$ must be included. A comparison between the measured frequency response and that calculated by the circuit model is shown in Fig. 5.10. The discrepancy between the measured and calculated phases is due to the difference in the signal line length for cable calibration and chip resistor measurement, as shown in Fig. 5.11. The length of the signal line is about $5\,\mathrm{mm}$ shorter for chip resistor measurement and thus the same phase reaches to the network analyzer input port at earlier time at measurement than at the calibration. Since the calibration conducts the zero point adjustment, this earlier arrival at measurement gives more positive phase. The length of about $5\,\mathrm{mm}$ shorter at measurement gives the phase $\Delta\theta$ of

$$\begin{aligned} \Delta\theta &= 360° \times \frac{5\,\mathrm{mm}}{\lambda_{\mathrm{in\ cable}}} = 360° \times \left(5 \times 10^{-3}\right) \times \sqrt{2.3}\,\frac{f_{\mathrm{GHz}} \times 10^9}{3 \times 10^8} \\ &= 9° \times f_{\mathrm{GHz}}. \end{aligned} \tag{5.28}$$
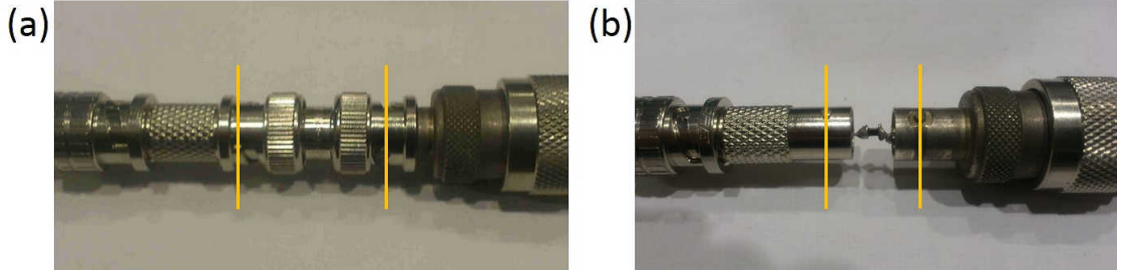
95

Figure 5.11: Difference in the length of signal lines for (a) calibration and (b) chip resistor measurement.

where $\lambda_{\text{in cable}}$ is a wavelength in the transmission cable and f_{GHz} is a frequency in unit of GHz. The $\lambda_{\text{in cable}}$ is given as

$$\lambda_{\text{in cable}} = \frac{\lambda}{\sqrt{\epsilon_r}} \tag{5.29}$$

where λ is the wavelength in vacuum and ϵ_r is the relative permittivity of the transmission cable. The value 2.3 for polyethylene is used for ϵ_r. Equation (5.28) gives $\Delta\theta$ of $+9°$ for $1\,\text{GHz}$. This is about half of $20°$, the difference between the measured and modeled phase in Fig. 5.10 for $1\,\text{GHz}$. Although there is a difference by factor 2, the measured and modeled phases are in the same order and their difference increases linearly as the signal frequency, which is consistent with Eq. (5.28). Therefore it is reasonable to consider $C_{\text{parasitic}} = 0.065\,\text{pF}$.

Using this value, the impedance of the chip resistor Z_{chip} at $200\,\text{MHz}$ is, from Eq. (5.24),

$$Z_{\text{chip}} = \frac{R_{100\,\text{k}\Omega}}{1+K^2} - i\frac{KR_{100\,\text{k}\Omega}}{1+K^2} = 1477 - 12062\,i\ \Omega, \tag{5.30}$$

$$|Z_{\text{chip}}| = 12.2\ \text{k}\Omega. \tag{5.31}$$

The absolute value of the impedance of the chip resistor at $200\,\text{MHz}$ is reduced from $100\,\text{k}\Omega$ to $12.2\,\text{k}\Omega$ by the parasitic capacitance of $0.065\,\text{pF}$.

2. Capacitance between the Signal Line and the Stainless Steel Box

Another capacitance C_{box} shown in Fig. 5.6, the capacitance formed between the signal line and the stainless steel box, must be evaluated. A cross sectional drawing of the high impedance Langmuir probe unit is shown in Fig. 5.12. The space between the signal line and the stainless steel box opening has a coaxial shape. As shown in Fig. 5.12, a ceramic (boron nitride) and a SUS304 board in front of the stainless steel box are used for assembling the high impedance Langmuir probe units, as discussed in Chapter 6. Since the capacitance of a coaxial transmission line C_{coaxial} is given by

$$C_{\text{coaxial}} = \frac{2\pi\epsilon}{\ln\left(\frac{b}{a}\right)} l_{\text{coaxial}}, \tag{5.32}$$

where ϵ, a, b, and l_{coaxial} are the dielectric constant in the coaxial transmission line, the radii of the inner and outer conductors, and the length of the transmission line, respectively. Using this equation and Fig. 5.12, C_{box} is approximately given by

$$C_{\text{box}} \simeq 2\pi\epsilon_0 \times 10^{-3} \times \left\{ \frac{4}{\ln\left(\frac{1.5}{0.25}\right)} + \frac{2}{\ln\left(\frac{1}{0.25}\right)} + \frac{1}{\ln\left(\frac{3.5}{0.25}\right)} + \frac{5.5}{\ln\left(\frac{4}{0.25}\right)} \right\}$$

$$= 3.36 \times 10^{-13}\,\text{F} = 0.336\,\text{pF}, \tag{5.33}$$

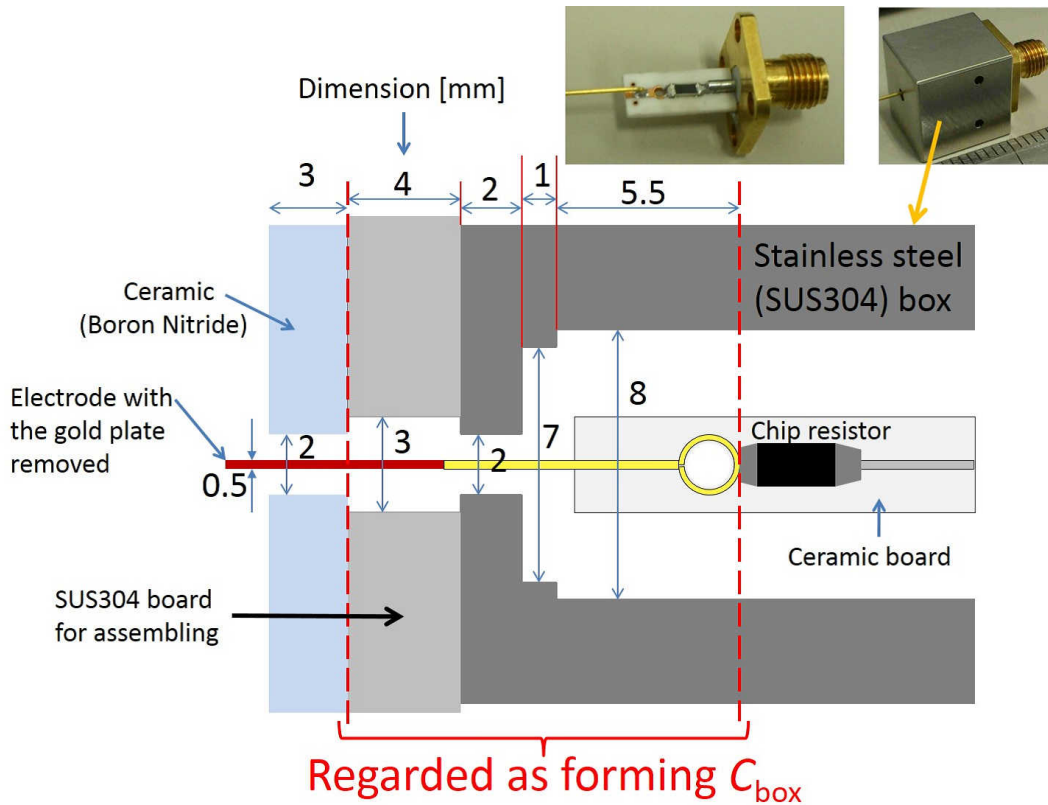Figure 5.12: Cross section of the high impedance Langmuir probe unit.

where ϵ_0 is used for ϵ. The impedance Z_{box} at 200 MHz is

$$Z_{\mathrm{box}} = \frac{1}{i\omega C_{\mathrm{box}}} = -2368\, i\,\Omega \tag{5.34}$$

and its absolute value is about $2.4\,\mathrm{k}\Omega$. Since C_{box} is connected in parallel with the chip resistor as shown in Fig. 5.6, and the absolute value of its impedance is about one fifth of that of the chip resistor $|Z_{\mathrm{chip}}| = 12.2\ \mathrm{k}\Omega$, C_{box} must be included when considering the impedance of the high impedance Langmuir probe system.

3. Impedance of the High Impedance Langmuir Probe System

The impedance of the high impedance Langmuir probe system Z_{system} can be calculated using Eqs. (5.30) and (5.33). According to Fig. 5.6, Z_{system} is given by

$$
\begin{aligned}
\frac{1}{Z_{\mathrm{system}}} &= i\omega C_{\mathrm{box}} + \frac{1}{Z_{\mathrm{chip}} + Z_0} \\
&= i\omega C_{\mathrm{box}} + \frac{1}{\left(\frac{R_{100\,\mathrm{k}\Omega}}{1+K^2} + Z_0\right) - i\frac{KR_{100\,\mathrm{k}\Omega}}{1+K^2}} \\
&= \frac{R_{100\,\mathrm{k}\Omega} + \left(1+K^2\right)Z_0}{\left(R_{100\,\mathrm{k}\Omega} + Z_0\right)^2 + \left(KZ_0\right)^2} + i\left\{ \frac{KR_{100\,\mathrm{k}\Omega}}{\left(R_{100\,\mathrm{k}\Omega} + Z_0\right)^2 + \left(KZ_0\right)^2} + \omega C_{\mathrm{box}} \right\} \\
&\equiv \alpha + i\beta,
\end{aligned}
$$

where K is defined in Eq. (5.25), and α and β are the real and imaginary parts of $\frac{1}{Z_{\mathrm{system}}}$. Z_{system} can be expressed as

$$Z_{\mathrm{system}} = \frac{1}{\alpha + i\beta} = \frac{\alpha - i\beta}{\alpha^2 + \beta^2} \tag{5.35}$$

$$|Z_{\mathrm{system}}| = \frac{1}{\sqrt{\alpha^2 + \beta^2}}. \tag{5.36}$$

The real part, the imaginary part (multiplied by -1), and the absolute value of Z_{system} are plotted in Fig. 5.13 for two cases, with (red solid line) and without (black solid line) C_{box}. From this figure, it can be seen that at 200 MHz, the absolute value of Z_{system} is about $2\,\mathrm{k}\Omega$ with C_{box} included, and $12\,\mathrm{k}\Omega$ without C_{box}. The relative magnitude of the absolute value of Z_{system} at 200 MHz and the sheath impedance at that frequency is of interest.

5.4.2 Probe System Impedance and the Sheath Impedance

Sheath Model

As described in Chapter 3, the sheath is formed around the probe when the electrode is inserted into a plasma. In order to estimate the sheath impedance, the following sheath model is considered. The sheath model for high frequencies around 200 MHz is not well developed. It is noted that the sheath model described here was developed for low frequencies, and may not hold at high frequencies such as 200 MHz. The sheath is regarded as a parallel circuit consisting of the sheath resistance R_{sheath} and the sheath capacitance C_{sheath}. This is shown in the overall circuit diagram of the high impedance Langmuir probe system shown in Fig. 5.14. These quantities are estimated as [63,64]

$$R_{\mathrm{sheath}} \simeq \frac{T_{\mathrm{e}}[\mathrm{eV}]}{J_{\mathrm{is}}[\mathrm{A}]} \tag{5.37}$$

$$C_{\mathrm{sheath}} \approx \frac{\epsilon_0 A_{\mathrm{rea}}}{\lambda_{\mathrm{D}}}, \tag{5.38}$$
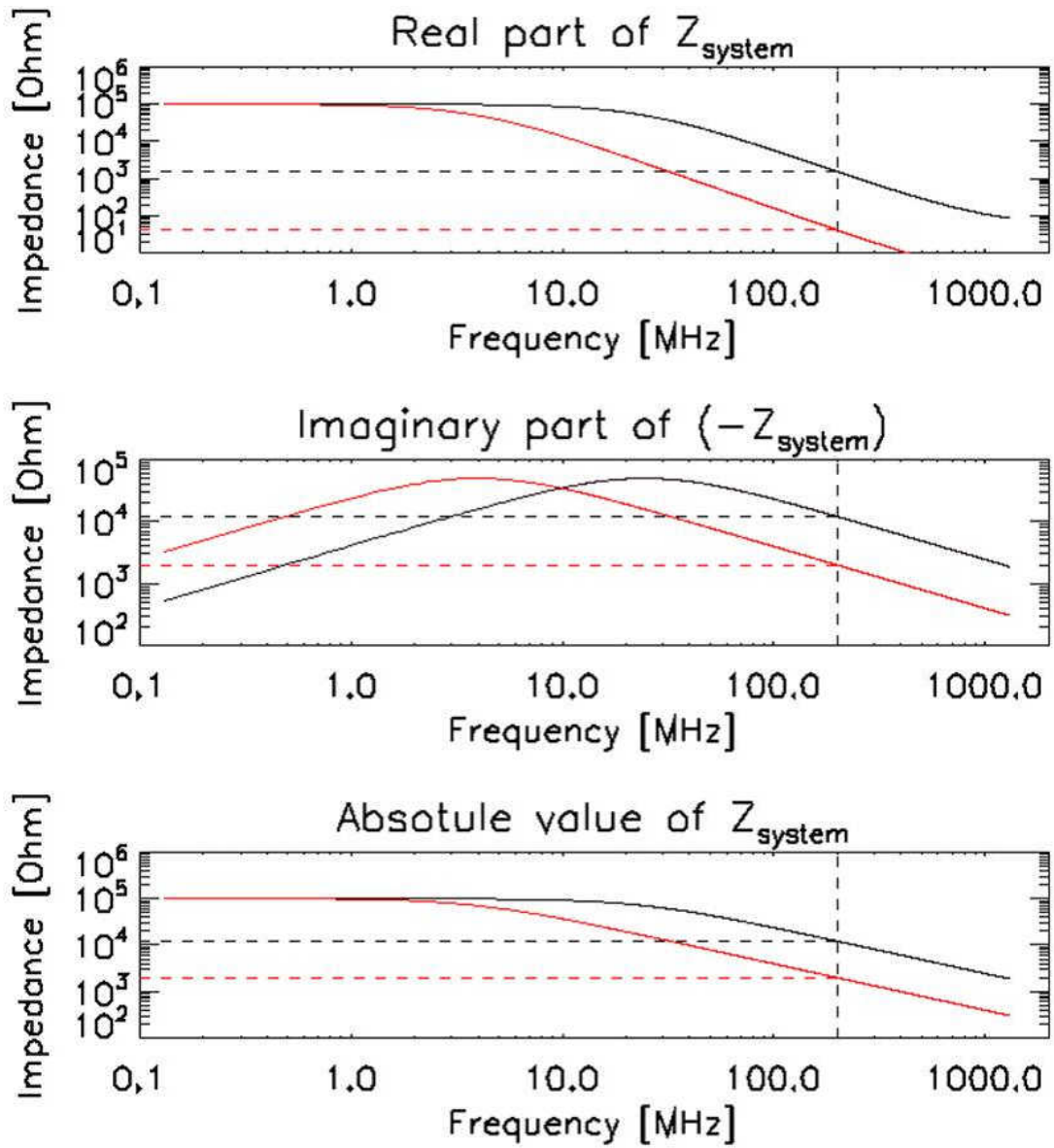
Figure 5.13: Real part, imaginary part, and absolute value of Z_{system} with (red solid line) and without (black solid line) C_{box}.
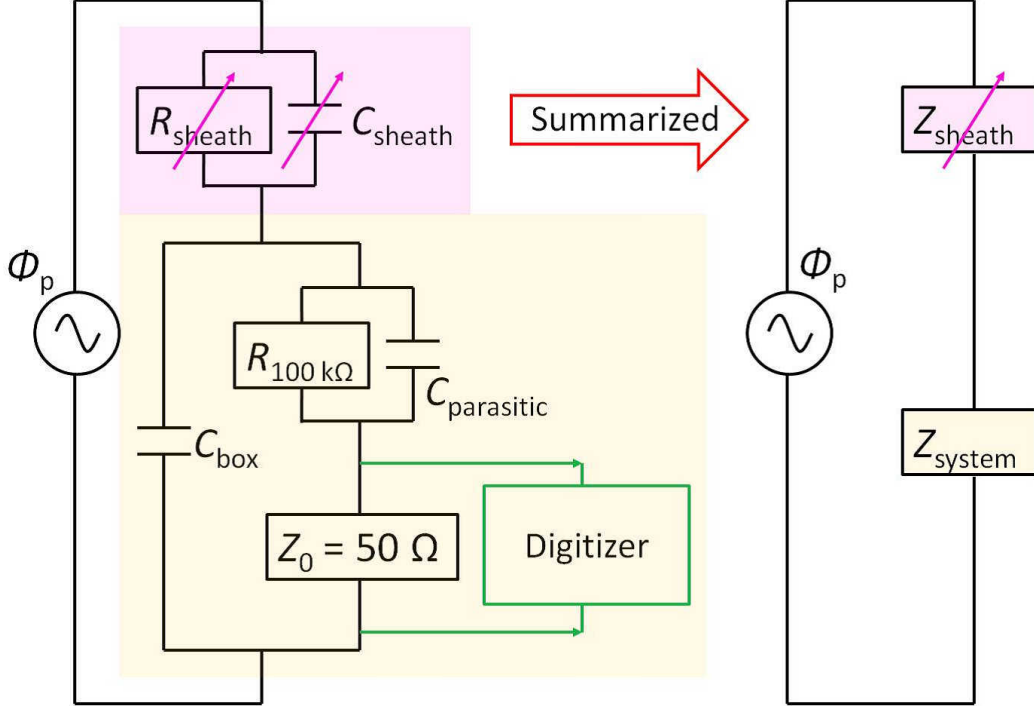
Figure 5.14: Circuit diagram of the high impedance Langmuir probe system including the plasma sheath.

where A_{rea} is the area of the electrode facing the sheath. The sheath impedance Z_{sheath} is expressed in this model as

$$\frac{1}{Z_{\text{sheath}}} = \frac{1}{R_{\text{sheath}}} + i\omega C_{\text{sheath}}. \tag{5.39}$$

For $T_{\text{e}} = 50$ eV, $J_{\text{is}} = 0.5$ mA, and $n_{\text{e}} = 4 \times 10^{16} \text{m}^{-3}$, which are the measured values in the wavenumber measurement experiment described in Chapter 8, and for the electrode length of 1.65 mm and radius 0.25 mm covered by a sheath, $R_{\text{sheath}} \simeq 100\,\text{k}\Omega$ and $C_{\text{sheath}} \approx 0.094$ pF are given (in this case, $A_{\text{rea}} = 2.8\,\text{mm}^2$ and $\lambda_{\text{D}} = 0.26\,\text{mm}$). The frequency characteristics of the absolute values of the impedance of the high impedance Langmuir probe system Z_{system} and the sheath impedance Z_{sheath} are compared in Fig. 5.15. According to this simple sheath model, $|Z_{\text{system}}|$ is smaller than $|Z_{\text{sheath}}|$ in the initial plasma driven by the LHW by an order of magnitude at high frequencies. At 200 MHz, while $|Z_{\text{system}}|$ is evaluated to be $2.0\,\text{k}\Omega$, $|Z_{\text{sheath}}|$ is evaluated to be $8.5\,\text{k}\Omega$. Since Z_{system} is connected in series to Z_{sheath} as shown in Fig. 5.14 and the absolute value of the synthetic impedance $|Z_{\text{sheath}} + Z_{\text{system}}|$ is calculated to be $10.4\,\text{k}\Omega$, this estimation suggests that the effect of the high impedance resistor ($100\,\text{k}\Omega$ nominal) to the wavenumber measurement system including the sheath is limited, and the current drawn from the plasma is reduced by only $\left|\frac{1}{10.4} - \frac{1}{8.5}\right| / \frac{1}{8.5} \times 100 = 18\,\%$ in the peripheral region of initial plasmas driven by the LHW.

Since this estimation was conducted using a simple sheath model developed for low frequencies, this result is not necessarily true for high frequencies such as 200 MHz. In order to validate the effectiveness of using the high impedance resistor in measuring the floating potential V_{f} at 200 MHz, which is expected to contain information on the LHW, the current drawn from the plasma by the probe should be examined experimentally.
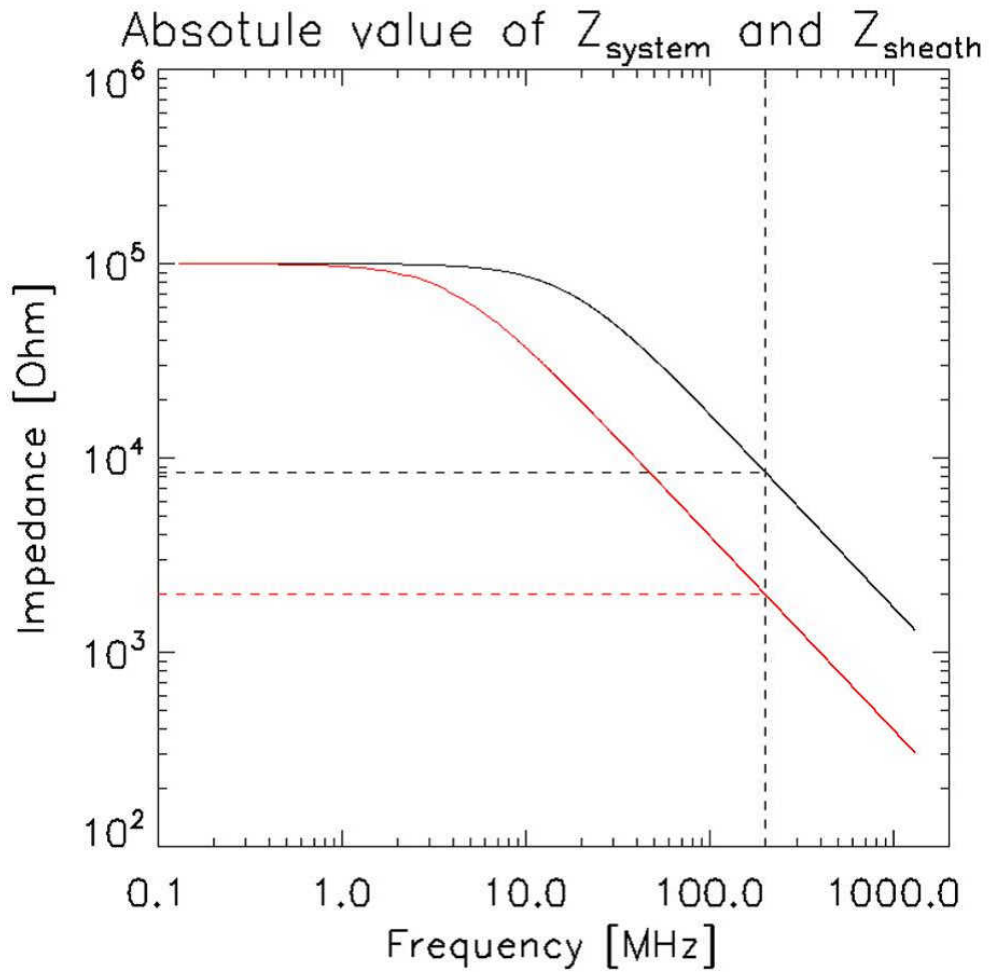
Figure 5.15: Comparison of frequency characteristics of the absolute values of the high impedance Langmuir probe system $|Z_{\text{system}}|$ (red solid line) and the sheath impedance $|Z_{\text{sheath}}|$ (black solid line) using a simple sheath model developed for low frequencies.
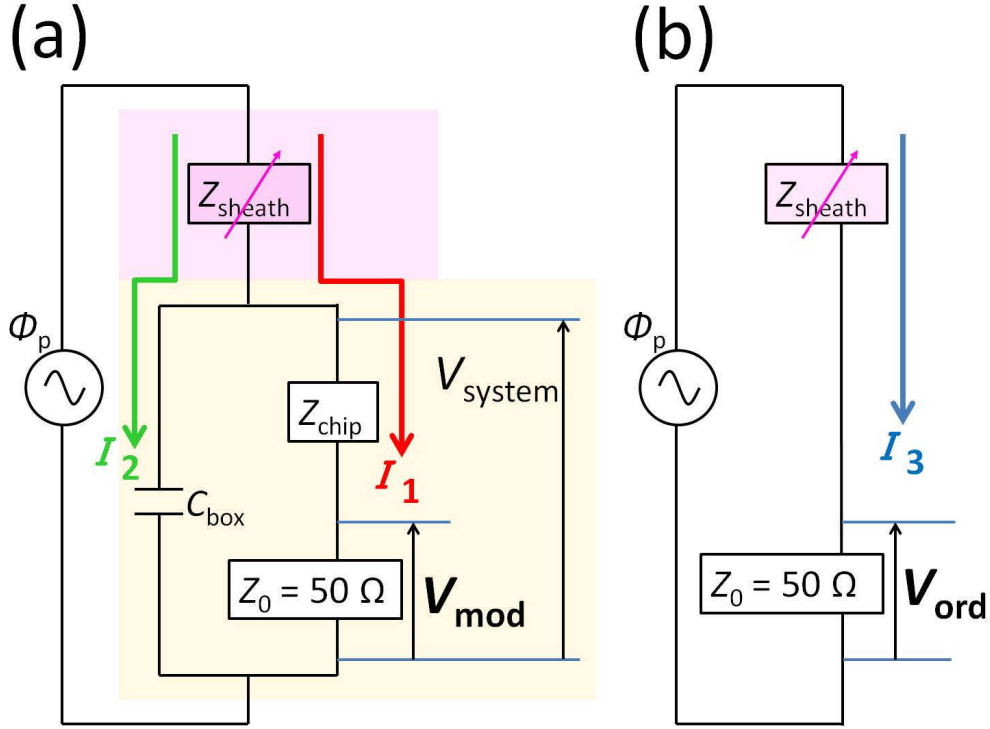
Figure 5.16: Currents drawn from the plasma and voltages at the entrance of the signal transmission line for (a) the high impedance Langmuir probe system and (b) the plain Langmuir probe.

5.5   Evaluation of Current Drawn from the Plasma

The effectiveness of using a high impedance resistor in measuring V_{f} at $200\,\mathrm{MHz}$ is evaluated by comparing the current drawn from the plasma by the high impedance Langmuir probe system with that drawn by the plain Langmuir probe. Figure 5.16 shows the paths of currents and measured voltage signals for (a) the high impedance Langmuir probe system and (b) the plain Langmuir probe. The total current drawn from the plasma is $I_1 + I_2$ for the high impedance Langmuir probe system and I_3 for the plain Langmuir probe. As described in Subsection 5.4.1, the circuit of the high impedance Langmuir probe system can be treated as a lumped parameter circuit. These currents can be evaluated by measuring the voltages V_{mod} and V_{ord} across the characteristic impedance $Z_0 = 50\,\Omega$ of the signal transmission line to the digitizer. Strictly speaking, V_{mod} and V_{ord} shown in Fig. 5.16 are voltages at the entrance of the signal transmission line, different from the voltages measured by the digitizer at the exit of the transmission line. However, since the loss in the transmission line (less than $3\,\mathrm{m}$) is negligibly small, voltages V_{mod} and V_{ord}, and those measured by the digitizer can be considered identical except for the phase.

We can estimate the currents drawn from the plasma using the measured voltages without knowing the sheath impedance, which is assumed to be common to the high impedance Langmuir probe system and the plain Langmuir probe. From Fig. 5.16(a), I_1 is simply given as

$$I_1 = \frac{V_{\mathrm{mod}}}{Z_0}. \tag{5.40}$$

Using V_{system} shown in Fig. 5.16(a):

$$V_{\text{system}} = I_1 \left(Z_{\text{chip}} + Z_0 \right), \tag{5.41}$$

I_2 is evaluated as

$$I_2 = V_{\text{system}} \bigg/ \left(\frac{1}{i\omega C_{\text{box}}} \right) = i\omega C_{\text{box}} \left(Z_{\text{chip}} + Z_0 \right) I_1. \tag{5.42}$$

Combining this equation with Eq. (5.40), the total current $I_1 + I_2$ drawn from the plasma by the high impedance Langmuir probe system is given as

$$I_1 + I_2 = \left[1 + i\omega C_{\text{box}} \left(Z_{\text{chip}} + Z_0 \right) \right] \frac{V_{\text{mod}}}{Z_0}. \tag{5.43}$$

Similarly, the current drawn from the plasma by the plain Langmuir probe is

$$I_3 = \frac{V_{\text{ord}}}{Z_0}. \tag{5.44}$$

Assuming the plasma is identical in front of the high impedance Langmuir probe system and the plain Langmuir probe, which is reasonable for the distance of 10 mm between them, the effectiveness of using the high impedance resistor in measuring V_{f} at 200 MHz is evaluated by comparing $|I_1 + I_2|$ and $|I_3|$, where

$$|I_1 + I_2| \leq \left| 1 + i\omega C_{\text{box}} \left(Z_{\text{chip}} + Z_0 \right) \right| \frac{|V_{\text{mod}}|}{Z_0}, \tag{5.45}$$

in which the triangle inequality was used, and

$$|I_3| = \frac{|V_{\text{ord}}|}{Z_0}. \tag{5.46}$$

C_{box} and Z_{chip} at 200 MHz were already evaluated to be 0.34 pF and $(1477 - 12062i\,\Omega)$ in Subsection 5.4.1, and $|V_{\text{mod}}|$ and $|V_{\text{ord}}|$ can be measured experimentally. The result of this comparison will be discussed in Subsection 8.3.3.

Chapter 6

Probe Assembly for Wavenumber Measurement

A probe assembly consisting of three high impedance Langmuir probe units, a single-loop magnetic probe, and a plain Langmuir probe was made in order to measure the wavenumber of the LHW and to confirm that the measured wave is the LHW. In this chapter, probes necessary for accomplishing these tasks and the process of probe assembly are explained. Calibrations of components forming the signal transmission line and properties of the probe assembly such as the spatial resolution and the rotational functionality are described.

6.1 Quantities Measured by the Probe Assembly

Quantities that can be measured by the probe assembly are listed below:

- Phase difference of 200 MHz signals, used to derive the wavenumber.

- Magnetic component of the wave to be used with the high impedance Langmuir probe unit signal to identify the type of wave being measured. As described in Chapter 2, the amplitude ratio of electric and magnetic fields depends on the type of wave.

- Plasma density needed to identify propagating regions for waves.

The phase difference is measured by an array of three high impedance Langmuir probe units. The high impedance Langmuir probe unit was described in Chapter 5.

The magnetic component of the wave is measured by a single-loop magnetic probe shown in Fig. 6.1. An enameled wire of diameter 1 mm is used to make a single-turn loop. One end of the wire, with enamel removed, is soldered to the inner conductor of a panel-mount type SMA connector and the other end of the wire, with enamel removed, is fastened to the outer conductor (ground) of the SMA connector by a screw and a nut. Enamel between the two ends prevents the loop from any electrical contact. The loop is an ellipse with 15 mm major radius and 9 mm minor radius.

The plasma density is measured by a plain Langmuir probe. A derivation of plasma density was described in Chapter 3.

6.2 Probe Assembly

6.2.1 Probe Head

The probe head consists of three high impedance Langmuir probe units, a single-loop magnetic probe, and a plain Langmuir probe. These probes are enclosed in a stainless steel (SUS304) box to shield
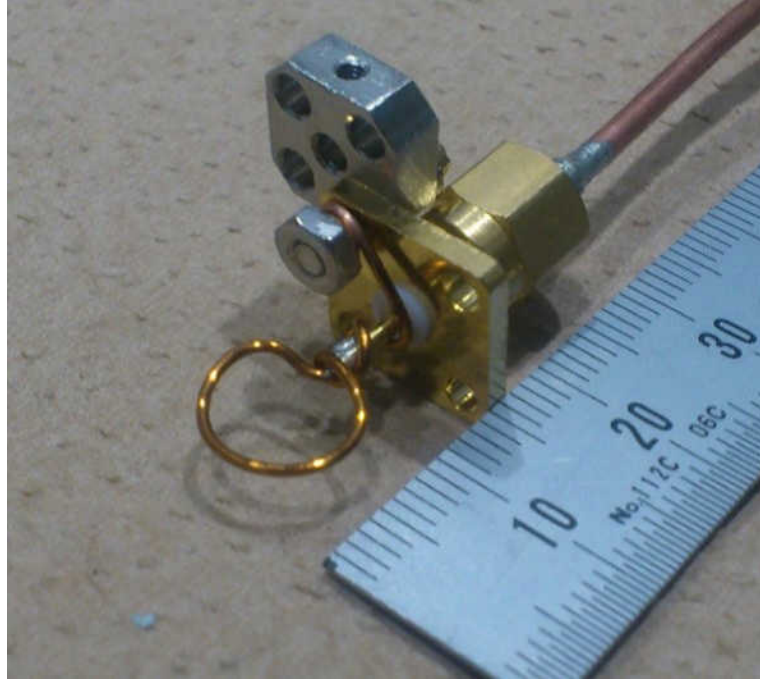
Figure 6.1: A single-loop magnetic probe.

from electromagnetic noise. Figure 6.2 shows the probes and the stainless box. A small space for the plain Langmuir probe is provided at the center.

The three high impedance Langmuir probe units and the magnetic probe are held together by a SUS304 piece with a 2 mm diameter hole, as shown in Fig. 6.3. The plain Langmuir probe passes through this hole and is fixed by a slotted set screw inside the piece.

Figure 6.4 shows the probe assembly without the stainless steel cover and the distances between probe electrodes. Electrode numbers are defined in this figure for the high impedance Langmuir probe units (electrodes 1, 2, and 3), the magnetic probe (electrode 4), and the plain Langmuir probe (electrode 5). Electrodes 1 through 4 form a 14.2 mm square and electrode 5 is placed at the center of the four electrodes.

Gold plating on electrodes 1, 2, and 3 are removed to avoid vaporization by the plasma. Electrodes are cut to proper lengths, as described in the next paragraph, and the stainless square cover is attached as shown in Fig. 6.5. The stainless square cover is 4 mm thick and have four through holes of diameter 3 mm and one slit of 2 mm width and 12 mm length. The slit permits the magnetic field component parallel to the slit to enter the magnetic probe region.

Finally, the probe assembly is covered by 3 mm thick boron nitride (BN) plates as shown in Fig. 6.6 to prevent the plasma particles from entering the stainless steel box and disturbing the ground electrically. The BN plate at the end of the probe has five 2 mm diameter through holes. The length of each electrode from the front surface of the BN plate is 1.70 mm $\pm$ 0.05 mm.

6.2.2   Calibration of Components in the Transmission Line

A full view of the probe assembly is shown in Fig. 6.7. This probe assembly is installed on the TST-2 device as shown in Fig. 6.8. The signal transmission line from the probe head to the oscilloscope consists of four components:

1. Semi-rigid cables of length 90.5 ± 0.5 cm from the probe head to the feed-through flange.
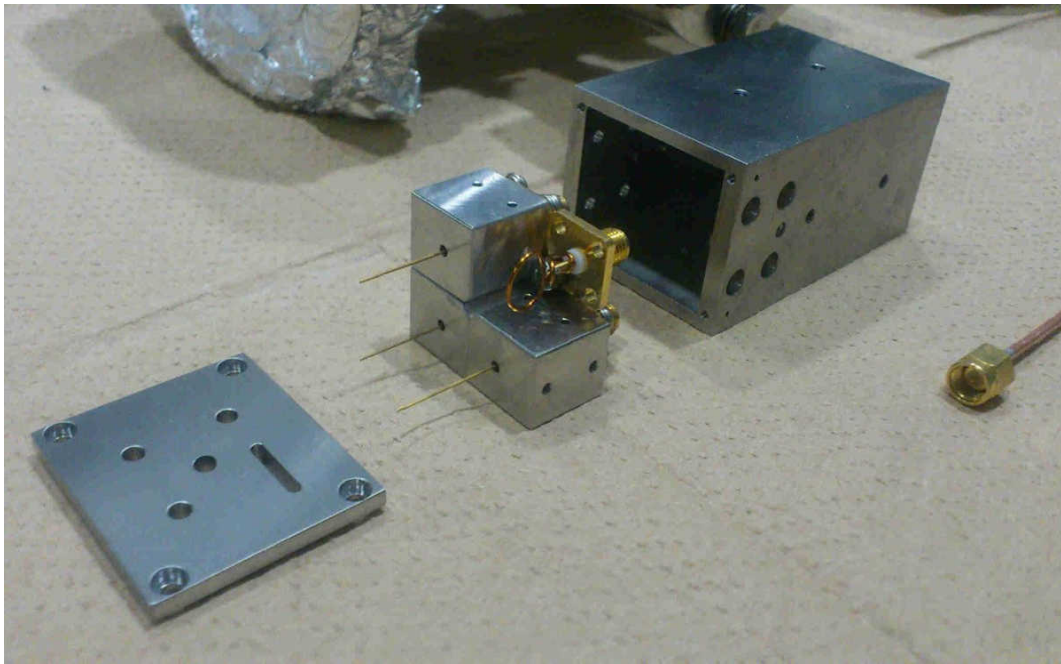
Figure 6.2: Probes with stainless (SUS304) shield box.

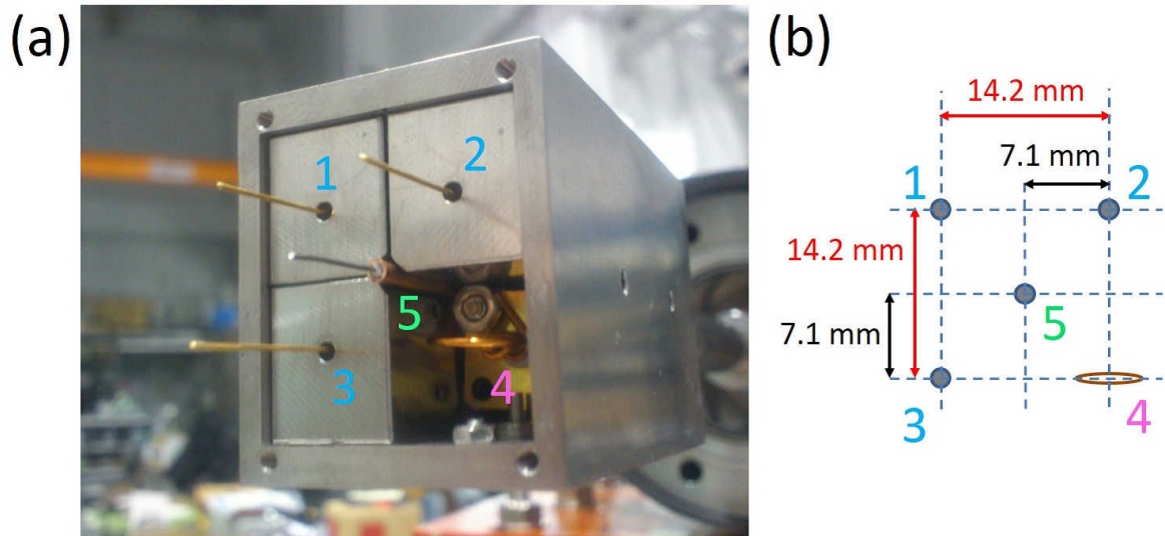Figure 6.3: Back view of the probes held together by a SUS304 piece.

Figure 6.4: Probe assembly. (a) Electrode numbers for the three high impedance Langmuir probes units (electrodes 1, 2, and 3), the magnetic probe (electrode 4), and the plain Langmuir probe (electrode 5). (b) Distances between probe electrodes.
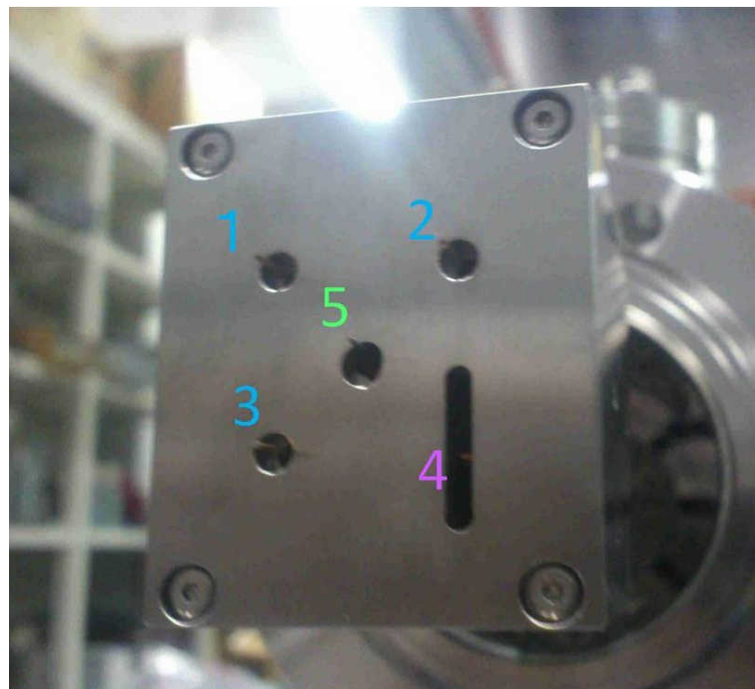

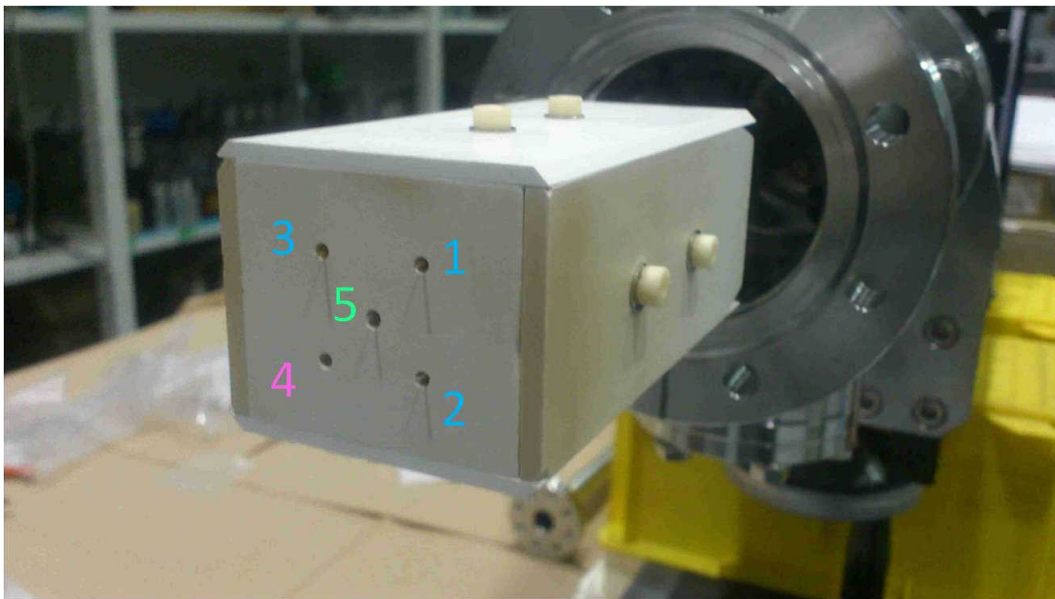Figure 6.5: Probe assembly with the stainless (SUS304) cover attached, showing the holes and the slit.

Figure 6.6: Probe assembly covered by boron nitride plates.
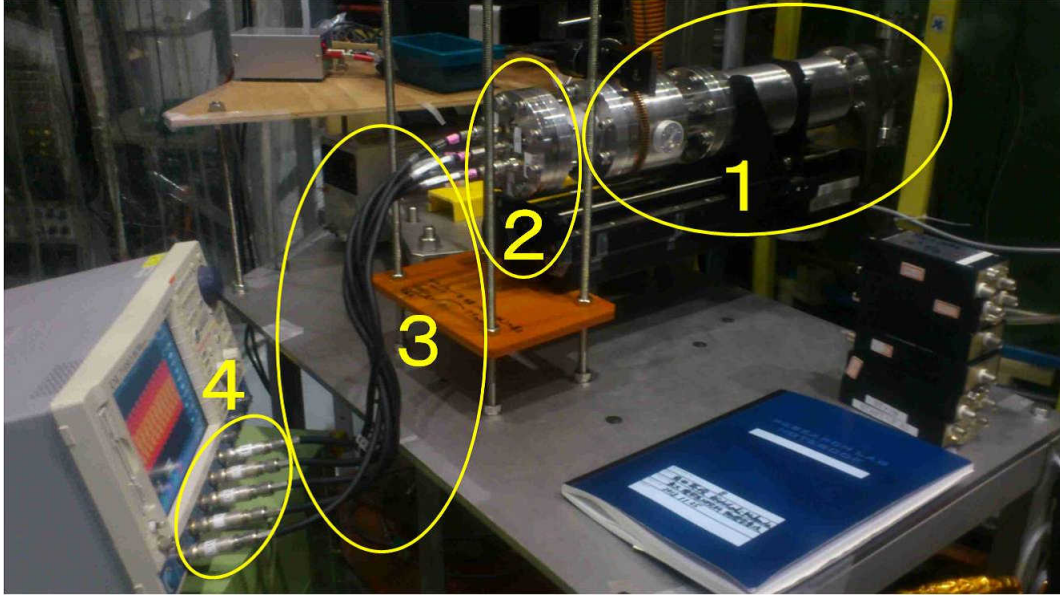

Figure 6.7: Full view of the probe assembly.

Figure 6.8: Four components of the signal transmission line from the probe head to the oscilloscope.

Table 6.1: Attenuation through each component of the transmission line.

Transmitted power [dB]	1. Semi-rigid cables	2. Feed-through flange (non-insulation)	3. 5D-FB cables	4. 50 Ω feed-through terminators	Total [dB]
Electrode 1	-0.70	-0.12	-0.12	$-$	-0.94
Electrode 2	-0.68	-0.14	-0.10	$-$	-0.92
Electrode 3	-0.69	-0.14	-0.10	$-$	-0.93
Electrode 4	-0.69	-0.11	-0.17	$-$	-0.97
Electrode 5	-0.73	-0.10	-0.10	$-$	-0.93

2. Feed-through flange (uninsulated type).

3. 5D-FB coaxial cables of length 55.0 ± 0.5 cm.

4. $50\,\Omega$ feed-through type terminators.

When measuring the power and phase of the signal transmitted through the transmission line, effects of these components must be taken into account. Power attenuation and phase shift through each component are summarized in Tables 6.1 and 6.2. The difference in the phase shift among cables attached to different electrodes is less than 4 degrees. For cables used for electrodes 1, 2, and 3, the difference in the phase shift is less than 2 degrees.

6.3 Properties of the Probe Assembly

6.3.1 Spatial Resolution

The probe assembly is envisioned to be used in a configuration shown in Fig. 6.9. This probe must ensure a finer spatial resolution than the wavelengths of waves in the plasma at 200 MHz. The di-

Table 6.2: Phase shift through each component of the transmission line.

Transmitted phase [degrees]	1. Semi-rigid cables	2. Feed-through flange (non-insulation)	3. 5D-FB cables	4. 50 Ω feed-through terminators	Total [degrees]
Electrode 1	−17.6	−2	−167.6	−11.1	−198.3
Electrode 2	−16.4	−2	−167.5	−11.5	−197.4
Electrode 3	−16.8	−2	−167.5	−10.7	−197.0
Electrode 4	−17.6	−2	−169.2	−12.0	−200.8
Electrode 5	−17.1	−2	−167.2	−10.9	−197.2
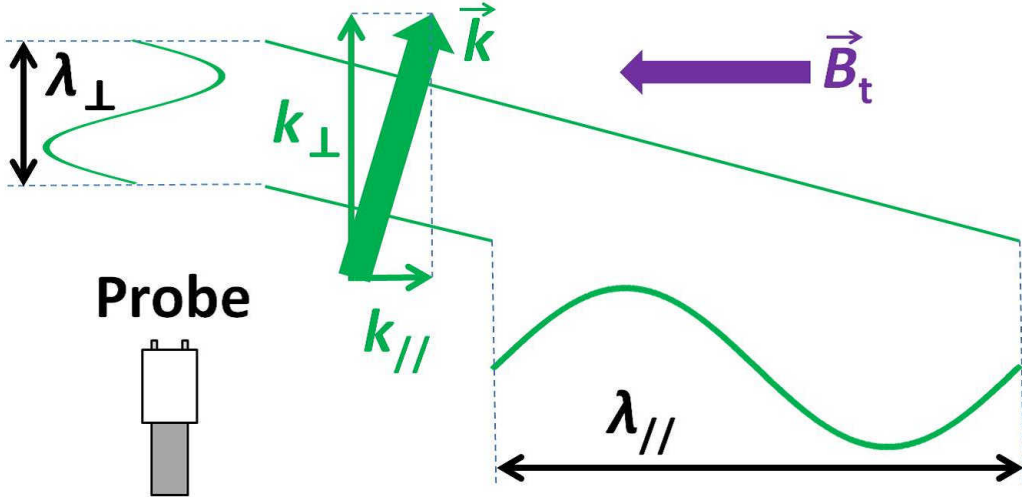
Figure 6.9: Configuration intended for probe usage.

mensions of the probe are discussed for both parallel and perpendicular directions with respect to the toroidal magnetic field.

Direction Parallel to the Toroidal Magnetic Field

The probe electrodes are arranged on a vertical plane which includes the toroidal magnetic field. The parallel wavelength $\lambda_{//}$ itself or its projection along the electrode array, λ_{p}, can be derived from the phase differences of signals measured by different high impedance Langmuir probe units, as depicted in Fig. 6.10. Here, λ_{p}, d, and $\Delta\phi$ denote the projected wavelength along the electrode array, the distance between the two electrodes, and the phase difference between the two signals measured by the two electrodes. The relationship among them is given by

$$\lambda_{\mathrm{p}} = d \times \frac{360°}{\Delta\phi_{\mathrm{degree}}},\tag{6.1}$$

where $\Delta\phi_{\mathrm{degree}}$ is the phase difference in degrees. The projected wavenumber k_{p} is given as

$$k_{\mathrm{p}} = \frac{2\pi}{\lambda_{\mathrm{p}}} = \frac{2\pi}{d} \cdot \frac{\Delta\phi_{\mathrm{degree}}}{360°}.\tag{6.2}$$

By the Nyquist Theorem, the inter-electrode distance $d = 14.2\,\mathrm{mm}$ gives the maximum measurable wavenumber of $223\,\mathrm{m}^{-1}$, which covers the wavenumber from $0\,\mathrm{m}^{-1}$ to $75.4\,\mathrm{m}^{-1}$ launched by the grill
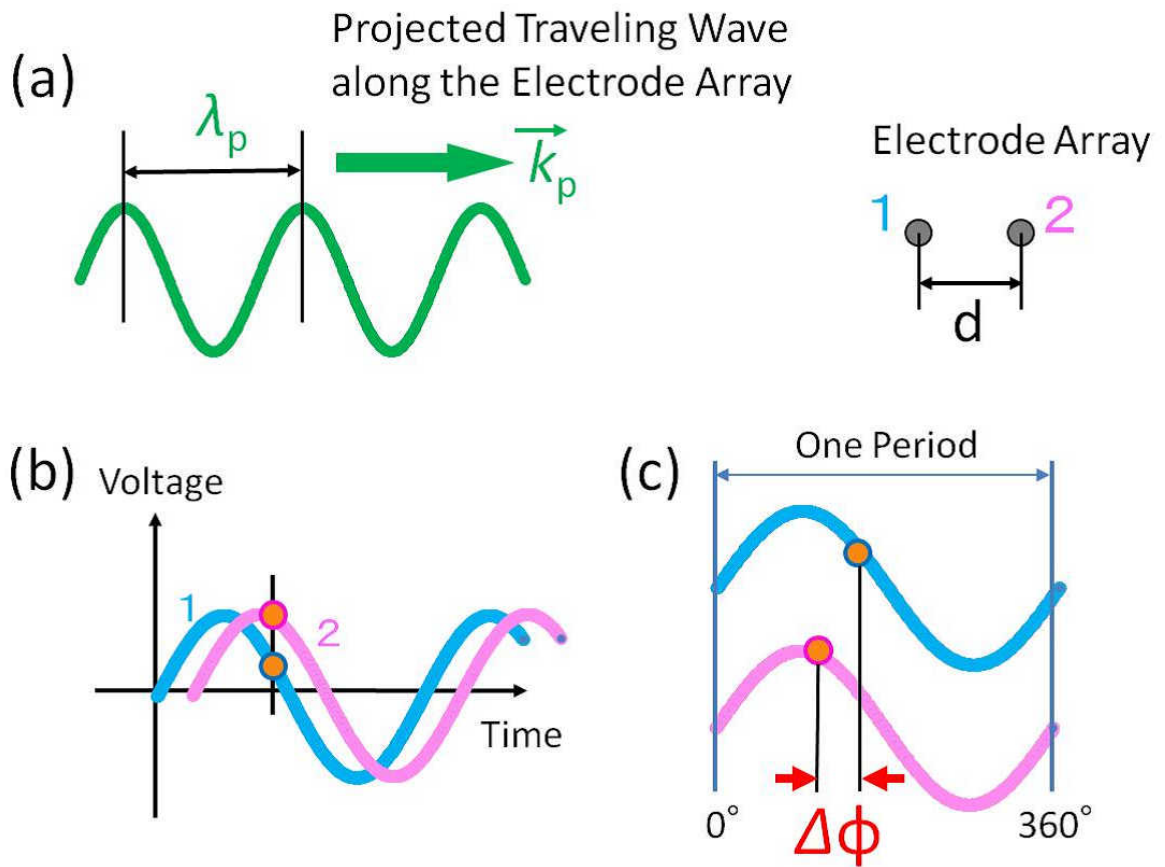
Figure 6.10: Concept of measuring the projected wavelength λ_p. (a) Traveling wave projected along a two-electrode array. (b) Signals at the same time. (c) Phase difference $\Delta\phi$.
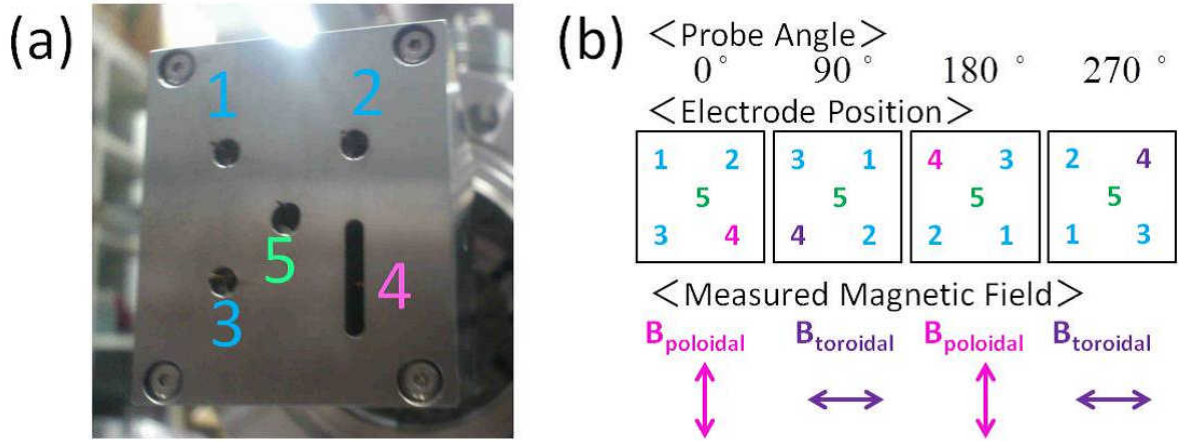
Figure 6.11: Rotation of the probe head. (a) Probe head without BN plates at the probe angle of 0 degree. (b) Electrode positions and measured magnetic field components at different probe angles.

antenna.

Direction Perpendicular to the Toroidal Magnetic Field

The length of the electrodes, which is in the perpendicular (radial) direction, must be shorter than the perpendicular wavelength $\lambda_\perp$ of waves in the plasma, because otherwise the signal is averaged out over a wavelength in that direction and the wave information could be lost. The length of each electrode exposed beyond the surface of the BN plate is 1.70 mm $\pm$ 0.05 mm. In the peripheral region of start-up plasmas with the toroidal magnetic field of about 0.05 T, the plasma density is around $10^{17}\,\mathrm{m}^{-3}$ or less, so the wavelength along the electrode is more than 20 mm from Fig. 2.4. Therefore, the electrode length of 1.70 mm $\pm$ 0.05 mm is short enough and the spatial resolution in the radial direction is secured.

6.3.2   Rotation of the Probe Head about its Axis

The probe head can be rotated about the axis of the probe head, which is collinear with electrode 5. Rotation of the probe enables measurement of different components of the magnetic field, and also measurement of the same wave with different electrodes when the probe assembly is rotated by 90 degrees as described in Fig. 6.11, which is useful for validating the wavenumber measurement. The positive direction of the probe rotation angle is defined to be in the clockwise direction as seen from the front of the probe assembly.

Chapter 7

Electromagnetic Sensitivity of the Probe

As described in Chapter 2, the amplitude ratio of the electric field $\boldsymbol{E}$ and the magnetic field $\boldsymbol{B}$ is different between the fast wave and the slow wave (LHW). Therefore, it would be helpful for identifying the wave type if $|\boldsymbol{E}|$ and $|c\boldsymbol{B}|$ could be measured using the high impedance Langmuir probe unit and the magnetic probe. In this chapter, the measured electric and magnetic fields of the electromagnetic wave propagating in a coaxial transmission line, for which $|\boldsymbol{E}| = |c\boldsymbol{B}|$ holds, are discussed.

7.1 Electromagnetic Wave in a Coaxial Transmission Line

A coaxial transmission line with inner and outer conductor radii a and b is considered. A cylindrical coordinate system (r, θ, z) with the z-axis along the axis of the coaxial transmission line is used. According to Appendix A, waves with $E_z = 0$ and $B_z = 0$, which are called the Transverse Electro-Magnetic (TEM) wave, are dominant in a coaxial transmission line. From Eqs. (A.39) and (A.40) in Appendix A, this condition places restrictions on the electric field $\boldsymbol{E}_{\mathrm{t}}$ perpendicular to the z-axis as

$$\begin{cases} \nabla_t \cdot \boldsymbol{E}_t = 0 & \text{(7.1)} \\ \nabla_t \times \boldsymbol{E}_t = \boldsymbol{0} & \text{(7.2)} \end{cases}$$

and on the wavenumber k_z in the z direction as

$$k_z = \omega\sqrt{\mu\epsilon}, \tag{7.3}$$

where ∇_t is the spatial differential operator in the r-θ plane [65]. From Eqs. (7.1) and (7.2), the spatial distribution of $\boldsymbol{E}_{\mathrm{t}}$ in a coaxial transmission line is the same as that in a 2-dimensional electrostatic problem. Therefore, an electrostatic situation shown in Fig. 7.1 in which line charge densities $\sigma\,[\mathrm{C/m}]$ and $-\sigma\,[\mathrm{C/m}]$ are given to the inner and outer conductors, respectively, can be used. Since the coaxial transmission line is symmetric about the z-axis, σ is distributed uniformly on the inner conductor and $\boldsymbol{E}_{\mathrm{t}}$ has only the radial (r) component E_r. For $a < r < b$, Gauss's law on the coaxial transmission line of unit length gives

$$\epsilon_0 \cdot E_r(r) \cdot 2\pi r \cdot 1 = \sigma,$$

yielding

$$E_r(r) = \frac{\sigma}{2\pi\epsilon_0}\frac{1}{r} \qquad (a < r < b)\,. \tag{7.4}$$

From Eq. (7,3), it is found that both the phase velocity and the group velocity of TEM waves are $\frac{1}{\sqrt{\mu_0\epsilon_0}} = c$ in air. This means that E_r propagates in z direction at speed c, which can be seen as the
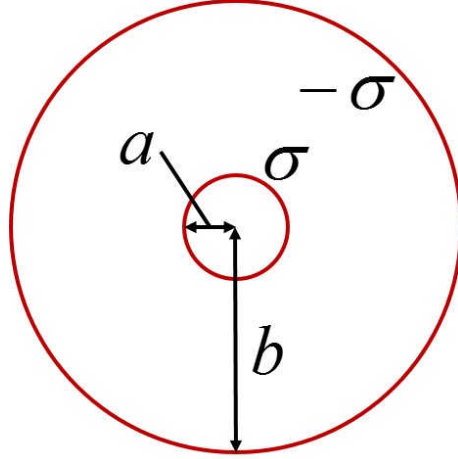
Figure 7.1: Line charge densities σ and $-\sigma$ distributed uniformly on the inner and outer coaxial cylinders of radii a and b, respectively, used for the analysis of a coaxial transmission line.

line charge density σ traveling in the z direction at speed c, indicating that a current $c\sigma$ flows in the z direction because the charge distributed over the length $c\,[\text{m}]$, $c\sigma\,[\text{C}]$, passes through a cross section in the coaxial transmission line per unit time. Therefore, a magnetic field in the θ direction B_θ is induced by Ampere's law as

$$B_\theta(r) = \mu_0 \frac{c\sigma}{2\pi} \frac{1}{r} \qquad (a < r < b). \tag{7.5}$$

Using Eqs. (7.4) and (7.5), the relationship between $E_r(r)$ and $B_\theta(r)$ is obtained as

$$E_r(r) = \frac{\sigma}{2\pi\epsilon_0} \frac{1}{r} = \frac{1}{\mu_0\epsilon_0} \left(\mu_0 \frac{\sigma}{2\pi} \frac{1}{r} \right) = c^2 \left\{ \frac{1}{c} B_\theta(r) \right\} = cB_\theta(r), \tag{7.6}$$

which satisfies Eq. (A.38) in Appendix A. Therefore, the electric and magnetic fields of TEM waves in a coaxial transmission line satisfy $|\boldsymbol{E}| = |c\boldsymbol{B}|$ and their spatial distributions are as shown in Fig. 7.2.

7.2   Coaxial Transmission Line as a Calibrator

Sensitivities of the probes against the electromagnetic wave with $|\boldsymbol{E}| = |c\boldsymbol{B}|$ were measured inside a coaxial transmission line of length $1\,\text{m}$ length and radii $a = 26\,\text{mm}$ and $b = 60\,\text{mm}$, with a characteristic impedance of $50\,\Omega$. A hole of about $90\,\text{mm}$ diameter is opened on the outer conductor of the transmission line and a copper cylinder of length $125\,\text{mm}$ is attached as shown in Fig. 7.3. After the horizontal position of the probe with respect to the coaxial transmission line calibrator is adjusted as shown in Fig. 7.4, the probe assembly is inserted into the calibrator. Figure 7.5 shows the configuration of electromagnetic sensitivity calibration of the probe assembly. The RF power is supplied from the output port of the network analyzer to the left end of the calibrator and the transmitted power returns to the input port of the network analyzer through each probe. The right end of the calibrator is terminated by a $50\,\Omega$ terminator. Therefore, no power is reflected back from the right end of the calibrator and only the rightward traveling wave exists in the coaxial calibrator.

The actual electric and magnetic fields measured by the probe assembly are those at positions of electrodes 1 through 4, $E_r(s)\cos\alpha$ and $B_\theta(s)\cos\alpha$ as shown in Fig. 7.6 where $s \equiv \sqrt{r^2 + h^2}$ and $h = 7.1\,\text{mm}$. $E_r(s)\cos\alpha$ is parallel to electrodes 1 through 3 and $B_\theta(s)\cos\alpha$ is perpendicular to the magnetic probe. Using Eqs. (7.4) and (7.5), the ratio of $E_r(s)\cos\alpha$ to $cB_\theta(s)\cos\alpha$ is
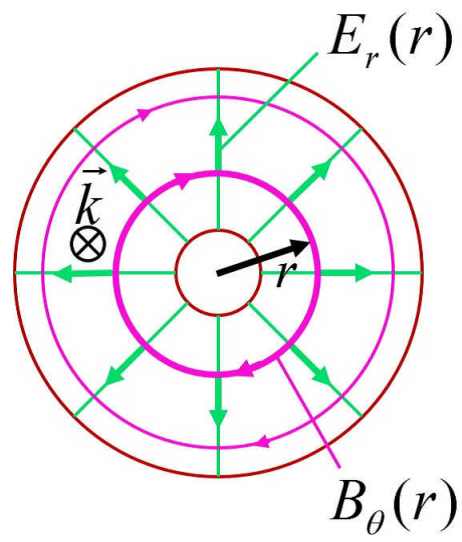
Figure 7.2: Electric and magnetic fields in a coaxial transmission line.

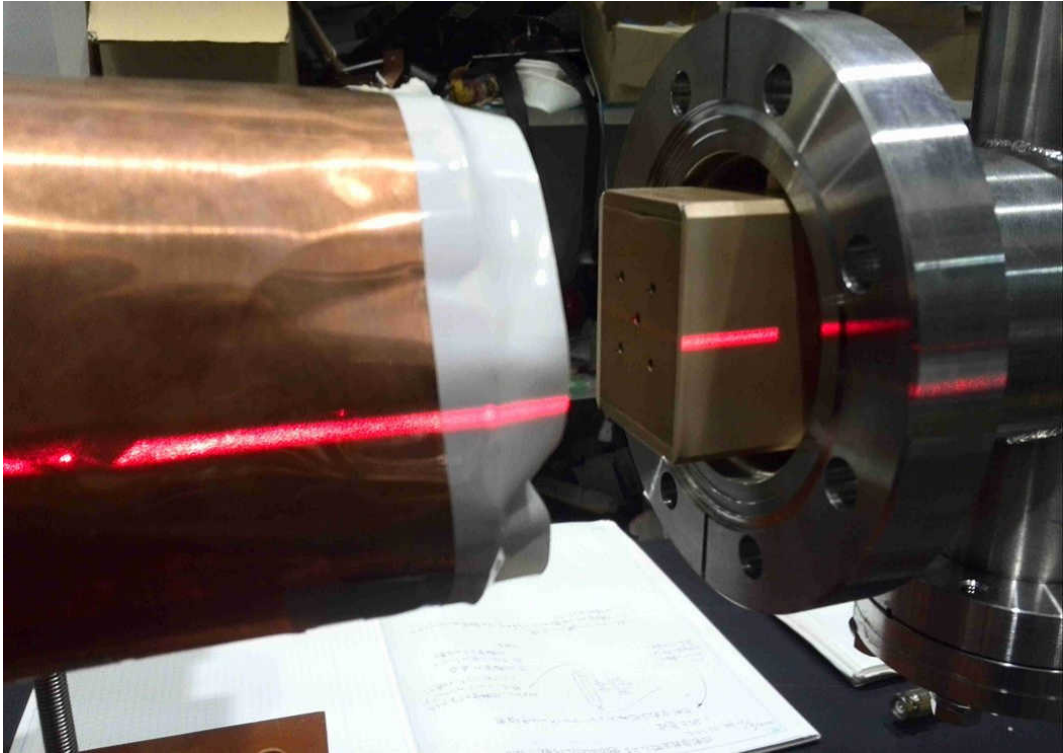Figure 7.3: Coaxial transmission line calibrator.

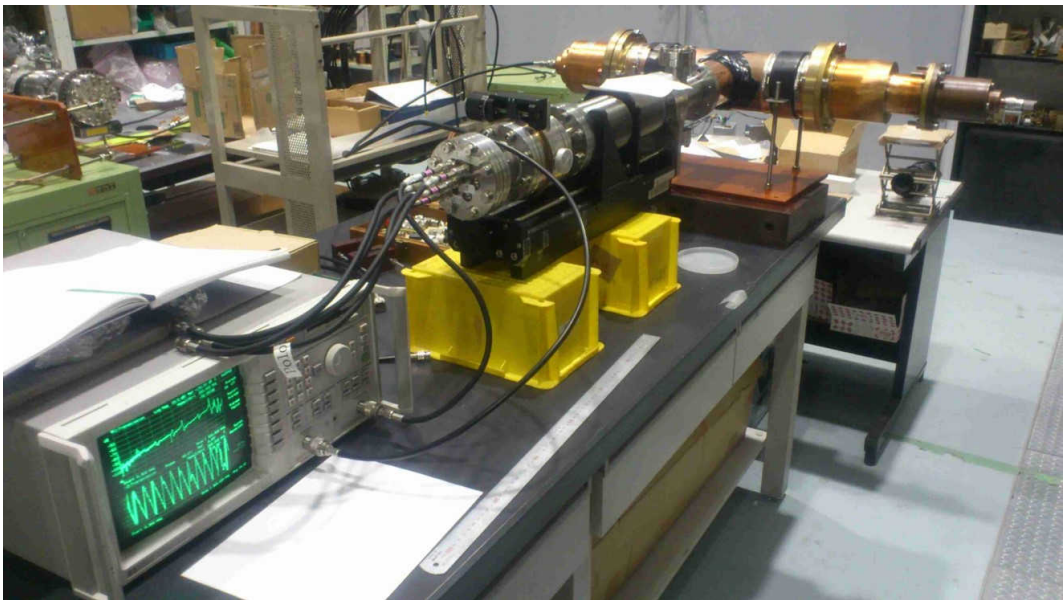Figure 7.4: Horizontal position adjustment.

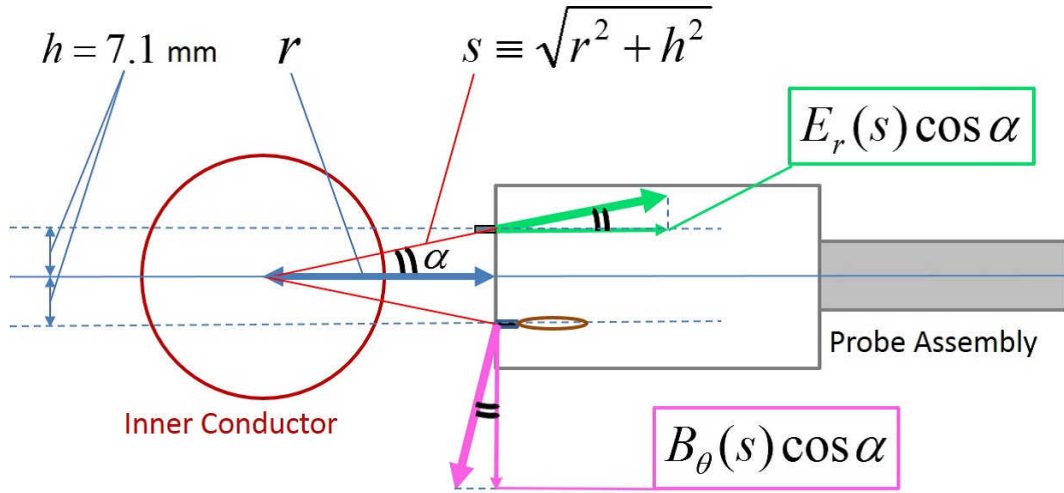Figure 7.5: Configuration of the electromagnetic sensitivity calibration.

Figure 7.6: Actual electric and magnetic fields measured by probes.

$$\frac{E_r(s)\cos\alpha}{cB_\theta(s)\cos\alpha} = \frac{1}{\mu_0\epsilon_0 c^2}\frac{\sqrt{r^2+h^2}}{\sqrt{r^2+h^2}} = 1, \tag{7.7}$$

giving $E_r(s)\cos\alpha = cB_\theta(s)\cos\alpha$. In addition, from Fig. 7.6, the measured components $E_r(s)\cos\alpha$ and $B_\theta(s)\cos\alpha$ are perpendicular to each other. Under this situation the probe assembly can be considered to measure the electromagnetic wave with $|\boldsymbol{E}| = |c\boldsymbol{B}|$.

7.3 Angular Dependence of Probe Response

The angular dependence of the probe response was measured with the front surface of the probe head located at $r = 40\,\mathrm{mm}$, which is within the region $26\,\mathrm{mm} \leq r \leq 60\,\mathrm{mm}$ where the electromagnetic wave propagates inside the coaxial transmission line calibrator. Since the position and the angle of each probe change as the probe head is rotated about its axis, the probe response can be checked by scanning the probe angle. In this section, the frequency response to the electromagnetic wave up to 500 MHz measured at probe angles of 0 degree and 90 degrees are presented first. Then the angular dependence of the electromagnetic sensitivity at 200 MHz is investigated. The transmitted power and phase are measured for the signal path from the entrance of the coaxial calibrator, through probes to the input port of the network analyzer.

7.3.1 Frequency Response Up to 500 MHz

Figures 7.7 and 7.8, and Figs. 7.9 and 7.10 show the frequency responses of the transmitted power and phase for probe angles of 0 degree and 90 degrees, respectively, up to 500 MHz. While no significant difference is seen for electrostatic electrodes 1, 2, 3, and 5 between the probe angles of 0 degree and 90 degrees, electrode 4 (magnetic probe) for the probe angle of 90 degrees shows a drastic reduction in the transmitted power by 20 to 30 dB compared to the probe angle of 0 degree, and the transmitted phase for the probe angle of 90 degrees has large uncertainties because of the small transmitted power. This is because for the probe angle of 90 degrees, the plane of the magnetic loop becomes parallel to the magnetic field in the coaxial calibrator and the detection efficiency reduces to nearly zero.

At both probe angles, no resonance appears at 200 MHz for any electrode. Considering rotational symmetry of the probe head by 180 degrees, it is reasonable to conclude that no resonance appears at
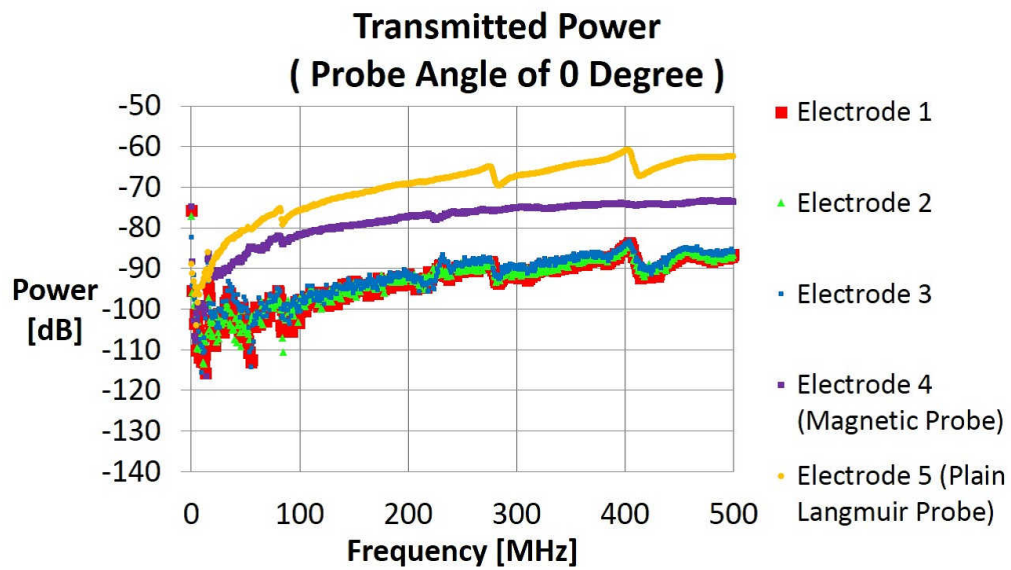
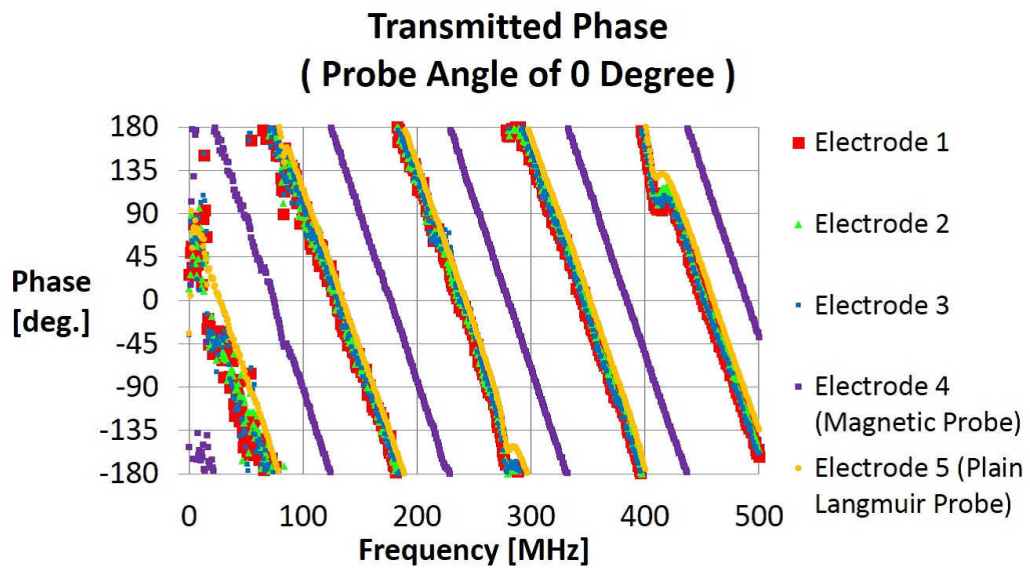Figure 7.7: Frequency response of the transmitted power for the probe angle of 0 degree.

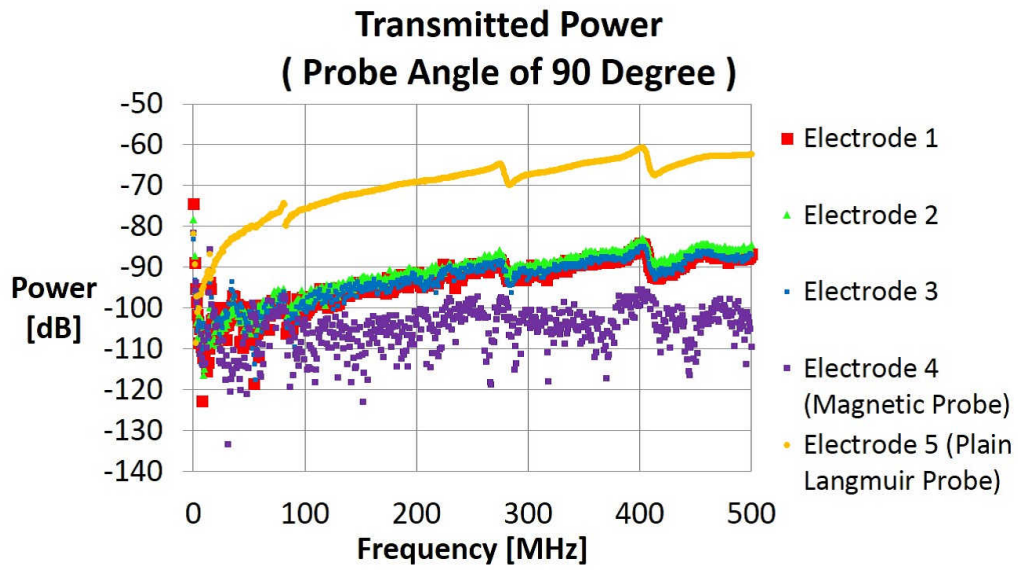Figure 7.8: Frequency response of the transmitted phase for the probe angle of 0 degree.

Figure 7.9: Frequency response of the transmitted power for the probe angle of 90 degrees.
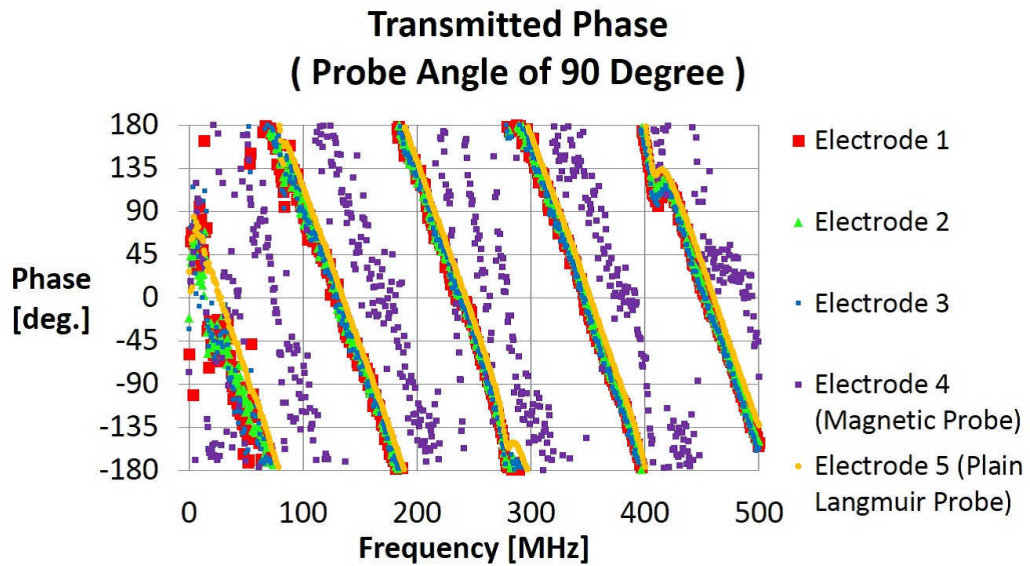

Figure 7.10: Frequency response of the transmitted phase for the probe angle of 90 degrees.
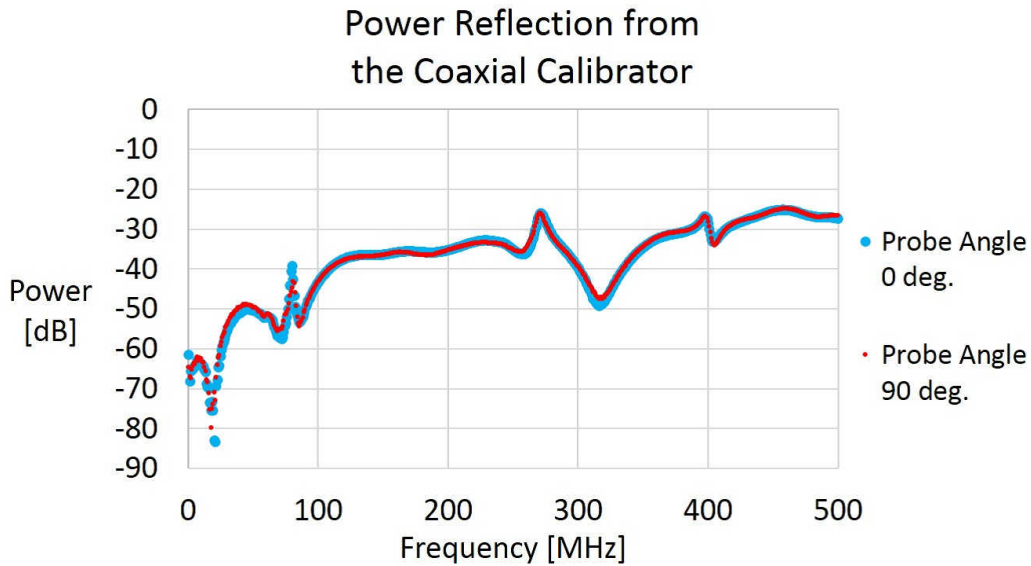
119

Figure 7.11: Reflected power from the calibrator for probe angles 0 degree and 90 degrees.

200 MHz for any other probe angle.

Figure 7.11 shows the reflected power from the coaxial calibrator for the probe angles of 0 degree and 90 degrees up to 500 MHz. At 200 MHz, the reflected power is only -35 dB at both probe angles and is negligible compared to the forward traveling wave in the calibrator.

7.3.2 Angular Dependence of Probe Response at 200 MHz

The angular dependence of probe sensitivities to the electromagnetic wave at 200 MHz was measured. Figures 7.12 and 7.13 show the transmitted power and phase at 200 MHz for various probe angles. From these figures, it is evident that electrostatic electrodes 1, 2, 3, and 5 show no significant change as the probe head rotates about its axis. Although a phase difference of 3.4 degrees, which corresponds to a phase difference of the 200 MHz wave over a distance of 14.2 mm (inter-electrode distance) in air, should be detected, the phase output measured by the network analyzer varies by about 5 degrees due to small signal levels. This gives the uncertainty in the phase measurement.

The magnetic probe (electrode 4), on the other hand, shows a drastic change as the probe head is rotated. Its sensitivity to the electromagnetic wave in the calibrator changes by about 30 dB at 200 MHz between the cases with the magnetic field parallel and perpendicular to the loop. The transmitted power measured by the magnetic probe has a 180 degree periodicity and takes the maximum values at probe angles 0 degree and 180 degrees, and minimum values at 90 degrees and 270 degrees, consistent with the magnetic field orientation in a coaxial transmission line.

As for the phase measured by the magnetic probe, it is constant from 90 degrees to 270 degrees and from 270 degrees (or -90 degrees) to 90 degrees, with a phase jump by 180 degrees at 90 degrees and 270 degrees. The phase jumps occur when the plane of the magnetic loop crosses the angle of the magnetic field. Thus, the magnetic probe behaves as expected, and it can be concluded that the magnetic probe measures the magnetic field correctly even in the presence of a radial electric field E_r.
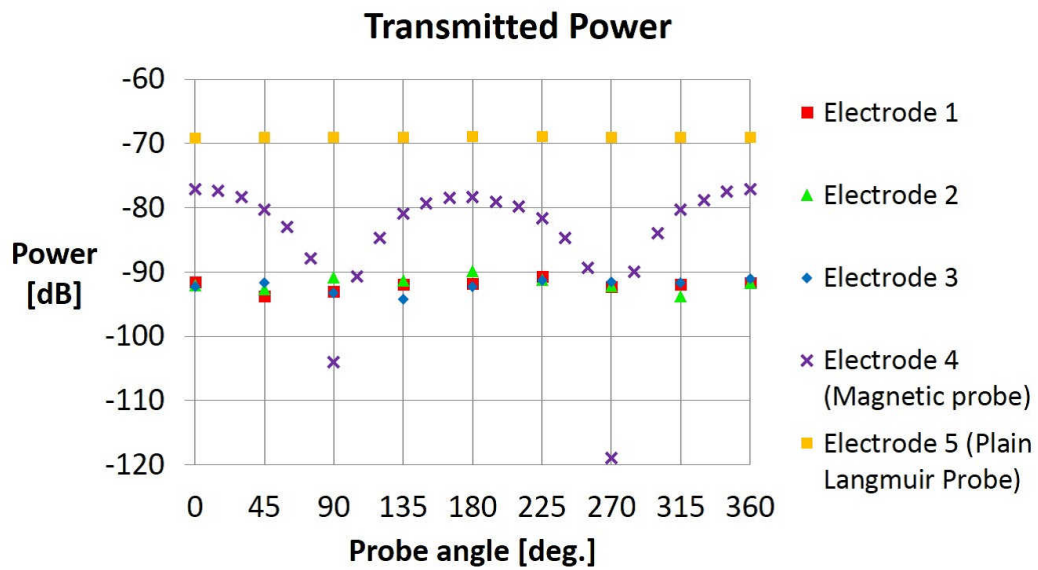
120

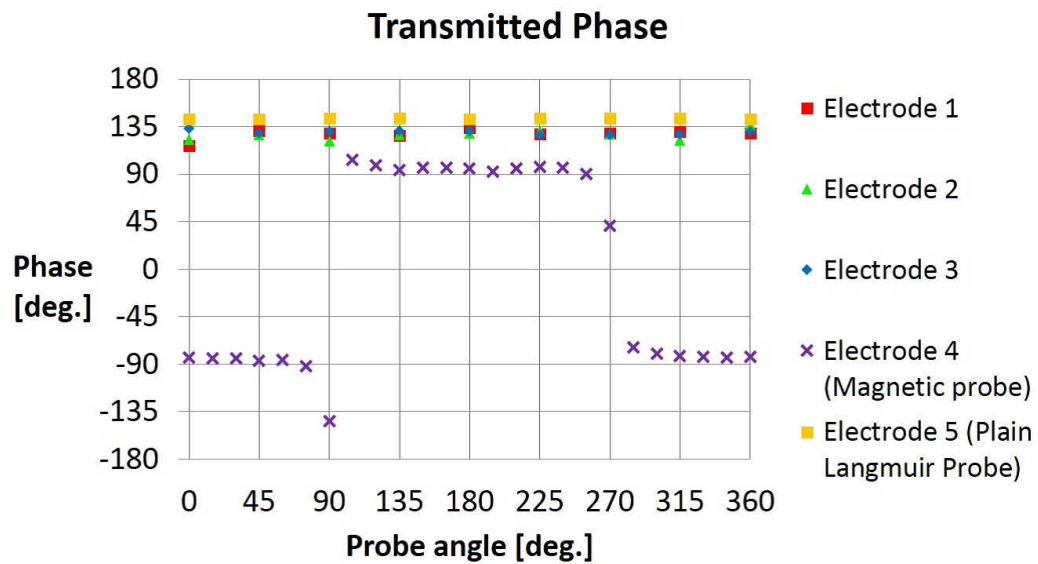Figure 7.12: Dependence of the transmitted power at 200 MHz on the probe angle.

Figure 7.13: Dependence of the transmitted phase at 200 MHz on the probe angle.
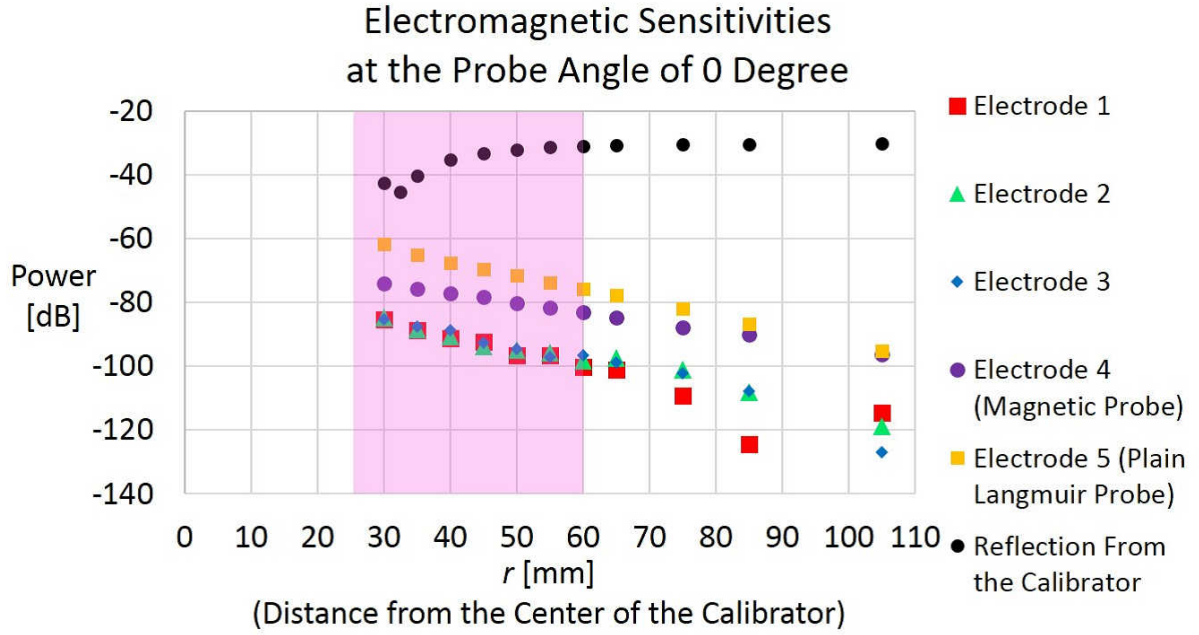
Figure 7.14: Dependence of the electromagnetic sensitivities of probes at 200 MHz on the radial position. Reflected power from the calibrator is also shown.

7.4 Dependence of Probe Response on Radial Position

The purpose of this section is to derive the signal amplitude ratios of electrodes 1 through 3 to the magnetic probe signal at 200 MHz. The probe angle is set to 0 degree since the magnetic loop gives the maximum signal amplitude at this angle.

7.4.1 Transmitted Power and Phase

Figures 7.14 and 7.15 show the dependence of the transmitted power and phase at 200 MHz on the radial position. The hatched region indicates the region between the inner and outer cylinders of the coaxial transmission line calibrator. Throughout the radial scan, the reflected power from the calibrator is about 30 dB or less, so only a forward traveling wave exists in the calibrator. Phases measured by electrode 1 through 5 are nearly constant, consistent with the TEM wave in a coaxial transmission line which has no radial wavenumber.

7.4.2 Amplitude Ratios of Electrostatic and Magnetic Probes

The RF power supplied by the network analyzer output port (P_{RF}) is 10 dBm. From Fig. 7.14, this power gives the signal amplitudes ($V_{0-\mathrm{peak}}$) measured by electrodes 1 through 4 by the relationship $P_{\mathrm{RF}} = \frac{V_{0-\mathrm{peak}}^2}{2Z_0}$, as shown in Fig. 7.16. The amplitude ratios of signals measured by electrodes 1 through 3 to the magnetic probe signal are given in Fig. 7.17. These ratios are less than 0.3. The value 0.3 is used as the signal amplitude ratio for the wave with $|\boldsymbol{E}| = |c\boldsymbol{B}|$ to identify the type of wave measured in the plasma.
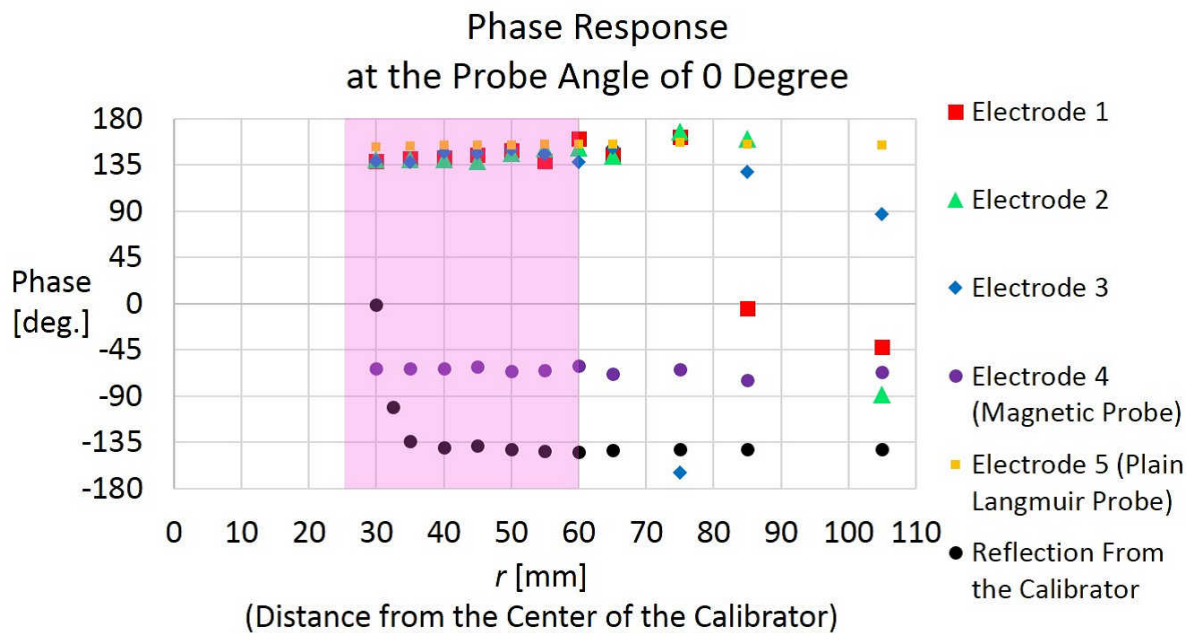
Figure 7.15: Dependence of the probe phase responses to the electromagnetic wave at 200 MHz on the radial position. Phase of the reflected power from the calibrator is also shown.
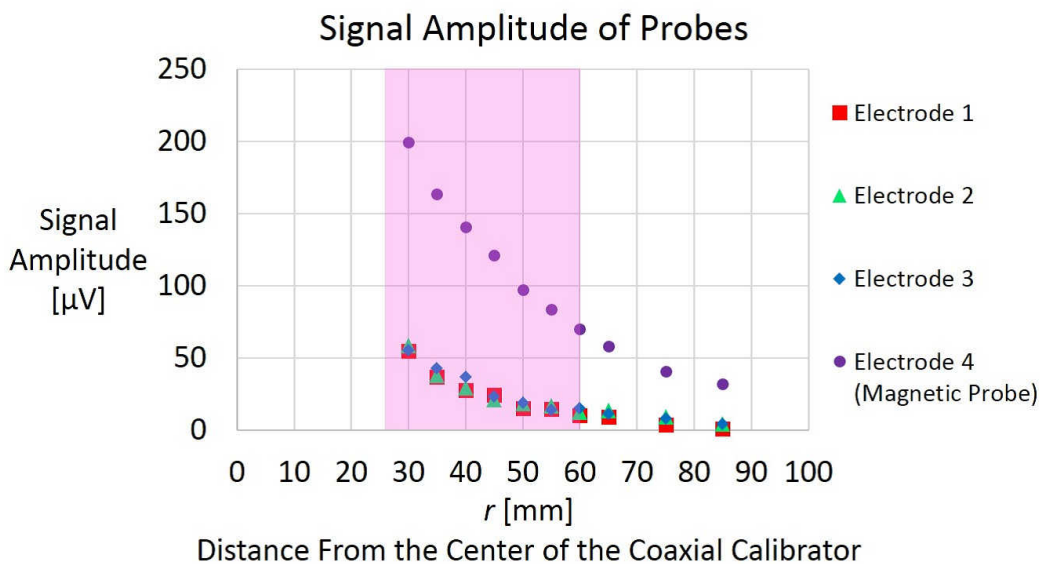

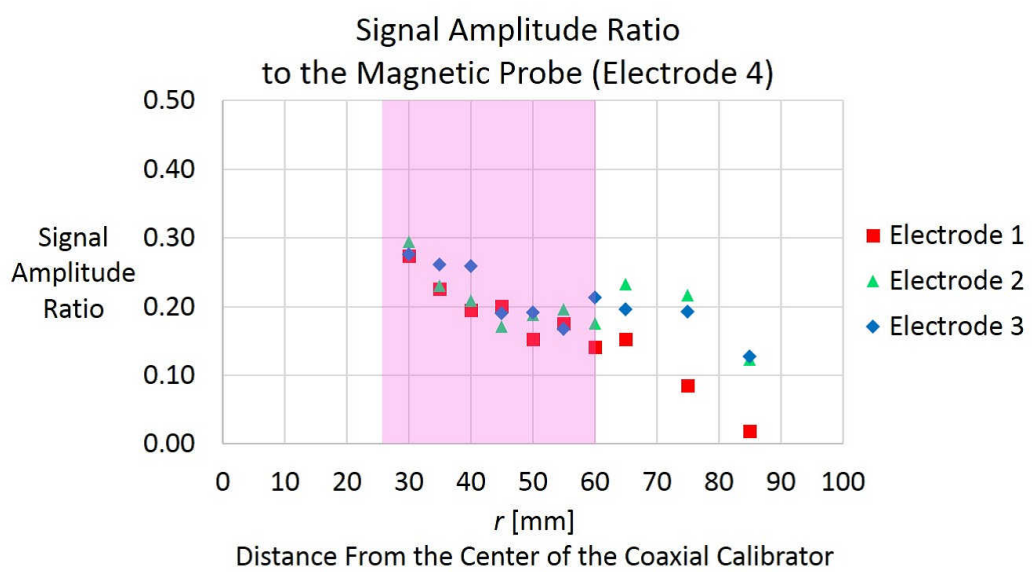Figure 7.16: Radial position dependence of probe signal amplitudes at 200 MHz.

Figure 7.17: Amplitude ratios of signals measured by electrodes 1 through 3 to the magnetic probe (electrode 4) signal at 200 MHz.

Chapter 8

Wavenumber Measurement of the Lower Hybrid Wave

The probe assembly, which consists of three high impedance Langmuir probe units, one magnetic probe, and one plain Langmuir probe was installed on TST-2 and wavenumber measurements were conducted in RF start-up plasmas. In this chapter, the experimental configuration is described, and an overview of the plasma discharge and probe signals are given. Using the measured signals, the effect of using a high impedance resistor on an electrostatic probe is investigated, and phase differences among the high impedance Langmuir probe signals are extracted and converted to the wavenumber, its error, and the direction of phase propagation. Identification of the type of the measured wave is also conducted based on the measured signal amplitudes in a plasma and the calibrated sensitivity of probes to the electromagnetic wave.

8.1 Experimental Configuration

Top view of the experimental configuration is shown in Fig. 8.1. The toroidal magnetic field and the plasma current are in the clockwise direction and the RF wave is launched into the plasma from the grill antenna in the counter-clockwise direction to accelerate electrons in that direction (i.e., to drive the plasma current in the clockwise direction). The radial, poloidal, and toroidal directions are defined in terms of the Cartesian x, y, and z-axes, respectively. The radial direction R from the center of the TST-2 device is also defined. The front surface of the probe assembly is placed at $R = 590\,\mathrm{mm}$ and the position of the front surface of the grill antenna is at $R = 650\,\mathrm{mm}$. They are displaced in the toroidal direction by 120 degrees. The plasma is physically limited in radial direction by a structure called the limiter at $R = 607\,\mathrm{mm}$, and thus the probe surface is inside the plasma and the grill antenna is behind the limiter.

Signals of the high impedance Langmuir probe units (electrodes 1, 2, and 3) and the magnetic probe (electrode 4) were digitized by a digital oscilloscope (DL7480, Yokogawa Electric Corporation) with a sampling rate of 1 GHz. The signal from the directional coupler which samples a fraction of the forward power to waveguide #1 of the grill antenna is also digitized by the same oscilloscope. The plain Langmuir probe (electrode 5) signal is digitized by this oscilloscope for the RF signal, or by a digitizer (HIOKI 8861-50 MEMORY HiCORDER and HIOKI 8956 ANALOG UNIT, HIOKI E. E. CORPORATION) for measuring the low frequency V_f or the plasma density.
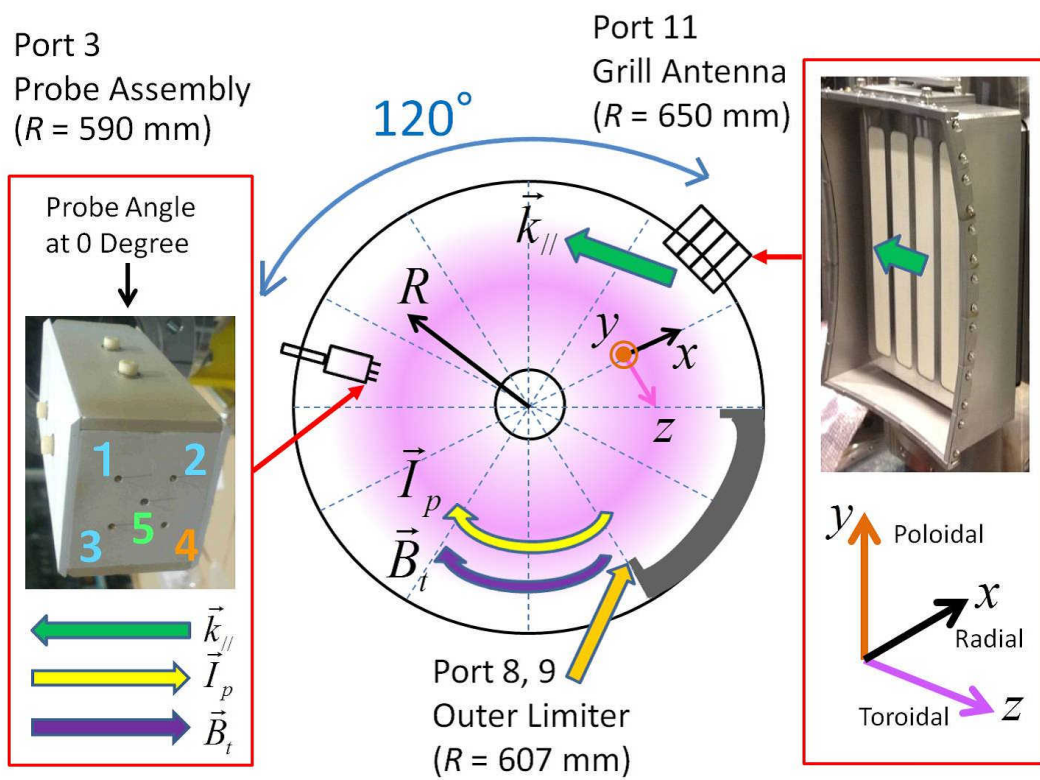
Figure 8.1: Cross sectional view of the experimental configuration as seen from the top.

8.2   Plasma Discharge

In this section, an overview of a representative plasma discharge is given. The plasma density is needed to identify regions where waves can propagate, and is measured by the plain Langmuir probe (electrode 5). The wavenumber of the wave launched by the grill antenna is also evaluated.

8.2.1   Typical Plasma Discharge

A representative discharge used in this experiment is shown in Fig. 8.2. The shot number is 105498. This is a deuterium plasma created by RF wave at 2.45 GHz injected from 5 ms to 45 ms. In TST-2, this wave is used for pre-ionization of the deuterium gas. The incident (or forward) and reflected powers are shown by black and red lines, respectively, in the "ECH Forward and Reflected Power" frame. Subsequently, the plasma current (I_p) is driven by RF wave at 200 MHz. The toroidal magnetic field (TF) is shown by black and green lines for the major radial positions $R = 380$ mm (approximate center of the plasma center) and $R = 590$ mm, respectively. In order to maintain the plasma in equilibrium (major radial force balance), the vertical field must be applied to prevent the toroidal plasma current from expanding outward. The time evolution of the vertical field is shown in the "Poloidal Field Coil Current" frame as the current flowing in the poloidal field coil. The low frequency floating potential is plotted in the "Floating potential (Vf)" frame. The soft x-ray radiation over a broad range of energy is also plotted. The trace plotted in the "Rout [m]" frame represents the approximate major radial position of the outermost closed flux surface which defines the boundary of confined plasma.

The power of the RF wave at 200 MHz is shown in the "Total RF Forward and Reflected Power" frame where the black and red lines represent the total forward and reflected powers summed over the four waveguides of the grill antenna.

The front surface of the probe assembly is located on the mid-plane (equatorial plane) of TST-2, and is inserted to the radial position $R = 590$ mm, slightly outboard of "Rout", so that the probe does not disturb the confined plasma. Although the probe position is outside the last closed flux surface, it is located farther in than the limiter, which is located at $R = 607$ mm and physically limits the outboard side of the plasma. The peripheral region of the plasma is measured in this way. RF signals from the probe assembly were analyzed for the time interval from 55 ms to 63 ms, which marked by black vertical solid lines in Fig. 8.2.

8.2.2   Plasma Density

The plasma density is important for identifying the regions where waves can propagate, and is measured by the plain Langmuir probe, electrode 5. The plasma density and temperature can be derived from the response of the probe current to the varying applied bias voltage on the probe electrode, as described in Chapter 3. In this experiment, a sinusoidal sweep of the bias voltage from -250 V to 50 V at 1 kHz is used, and the probe current is measured by the voltage drop across a $100\,\Omega$ resistor. Figure 8.3 shows an expanded view of the plasma current, the bias voltage, and the probe current during the RF signal analysis period from 55 ms to 63 ms for shot number 105562. The plasma condition is the same as shot number 105498. The probe current is examined for seven half sweep periods, each of which is shown as an interval between vertical lines of the same color in Fig. 8.3.

Figure 8.4 shows the seven traces of the probe current for the seven intervals indicated in Fig. 8.3 and the averaged probe current. At sufficiently negative bias voltage, the probe current is slightly positive. This is the ion saturation region. From Fig. 8.4, the ion saturation current is 0.48 mA. For this measurement, the surface of the probe assembly was located at $R = 570$ mm, 20 mm farther in than $R = 590$ mm, because at $R = 590$ mm the probe current did not reach the ion saturation region due to low plasma density.

The electron current is derived by subtracting the ion saturation current of 0.48 mA from the probe current. Figure 8.5 shows the electron current (with positive sign for electron current). The electron deceleration region is fitted by the red curve shown in Fig. 8.5, from which T_e is estimated to be 55 eV.
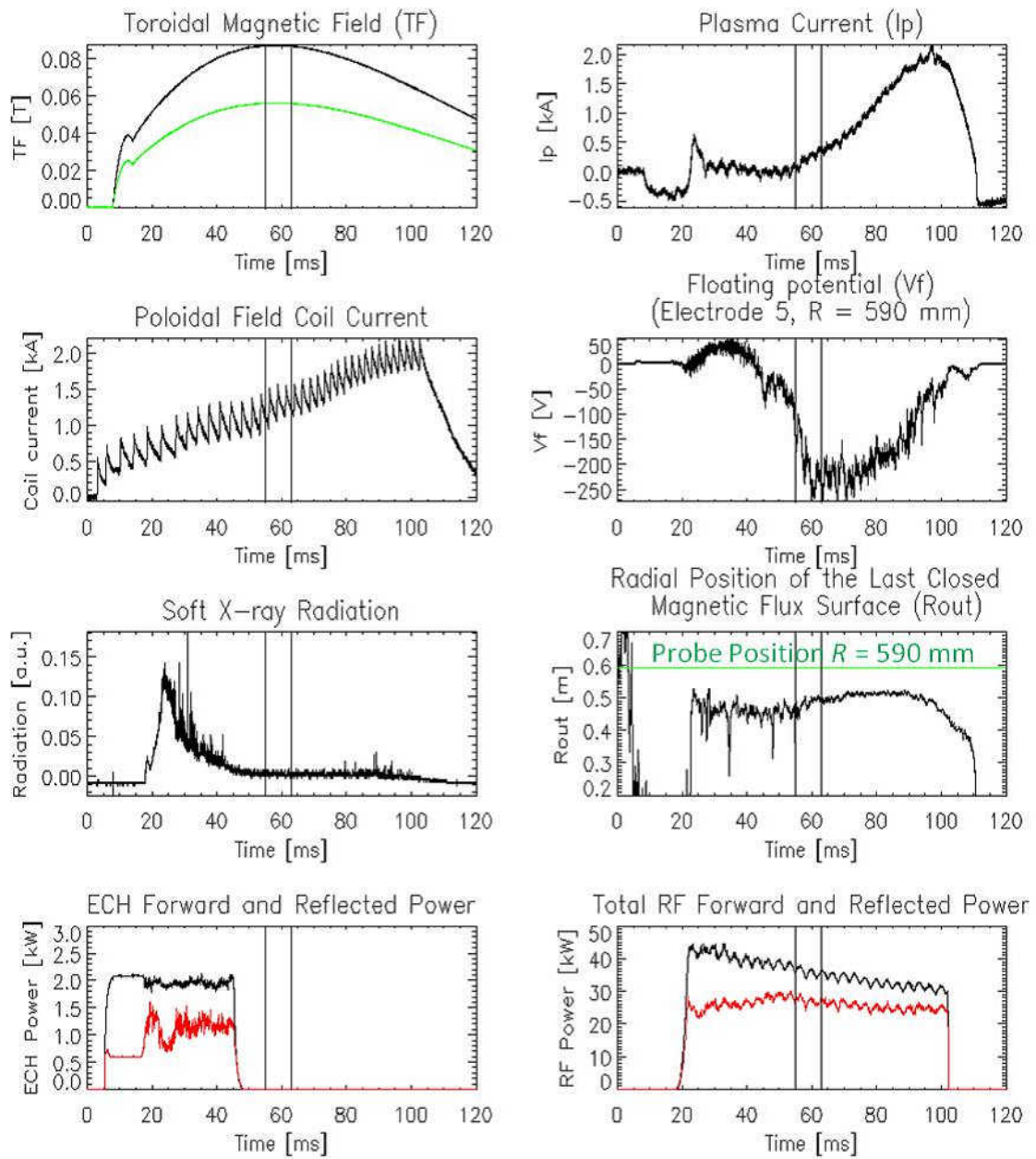
Figure 8.2: Discharge waveforms of a representative discharge used in this experiment (shot number 105498). The probe is located at $R = 590\,\mathrm{mm}$.
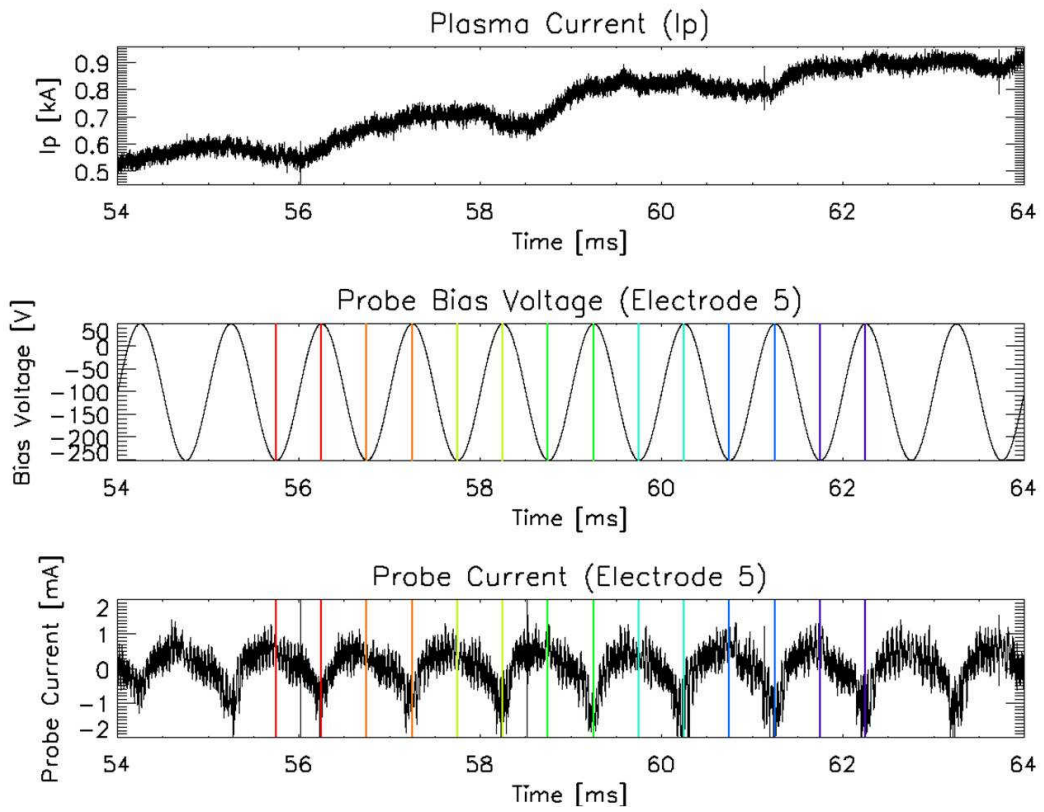
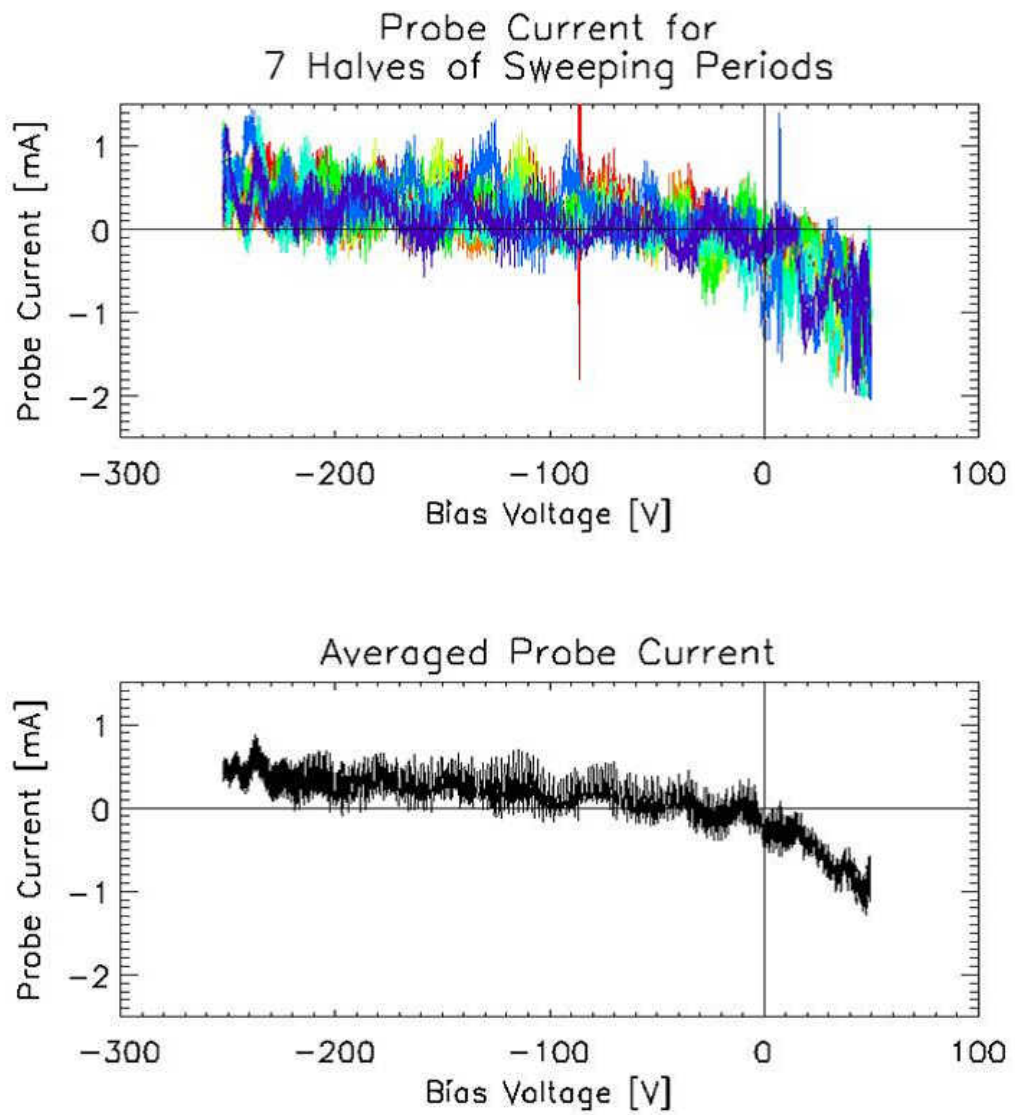Figure 8.3: Expanded view of discharge waveforms for shot number 105562. The probe is located at $R = 570\,\text{mm}$.

Figure 8.4: Probe current for seven half sweep periods and the averaged probe current.
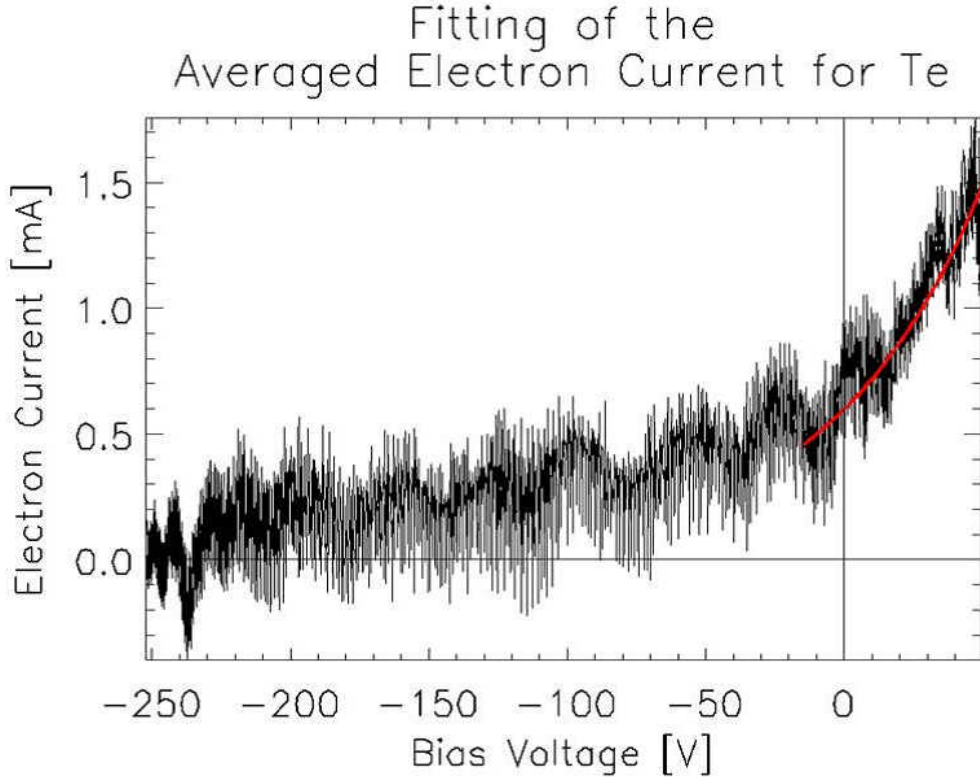
Figure 8.5: Electron current used for deriving T_{e}.

For the probe surface area of the plain Langmuir probe of $0.4\,\mathrm{mm}$ diameter and $1.65\,\mathrm{mm}$ length is $2.2\,\mathrm{mm}^2$, using which the plasma density n_{e} of

$$n_{\mathrm{e}} = 4 \times 10^{16}\,\mathrm{m}^{-3} \tag{8.1}$$

is derived. The plasma density derived from the plain Langmuir probe data is only an estimate because the probe I-V characteristic curve is distorted in the presence of RF waves [66].

8.2.3 Launched Wavenumber from the Grill Antenna

The RF power and phase data for the grill antenna is shown in Fig. 8.6 for the representative discharge (shot number 105498). The black and red lines in frames #1 through #4 are the forward and reflected powers measured for the four waveguides. The blue solid line in the "Total power" frame is the total power radiated into the plasma from the antenna. The "Phase" frame shows the phases measured for the four waveguides. The phase differences between adjacent waveguides determine the toroidal wavenumber (synonymous to the component of wavenumber parallel to the magnetic field in this experiment) of the wave excited in the plasma. In this experiment, the phase difference between adjacent waveguides was fixed to 90 degrees. From these data, the parallel wavenumber spectrum of the wave excited by this antenna is derived as follows.

Figure 8.7 is the equatorial cross sectional view of the TST-2 device and the grill antenna. The RF field is specified at the front surface of the grill antenna located at $R \equiv R_{\mathrm{antenna}} = 650\,\mathrm{mm}$. The toroidal extent of the antenna ranges in toroidal angle from 0 degree to 13.2 degrees. The toroidal circumference is $L = 2\pi R_{\mathrm{antenna}}$. The amplitude and phase of this RF field is given by the time
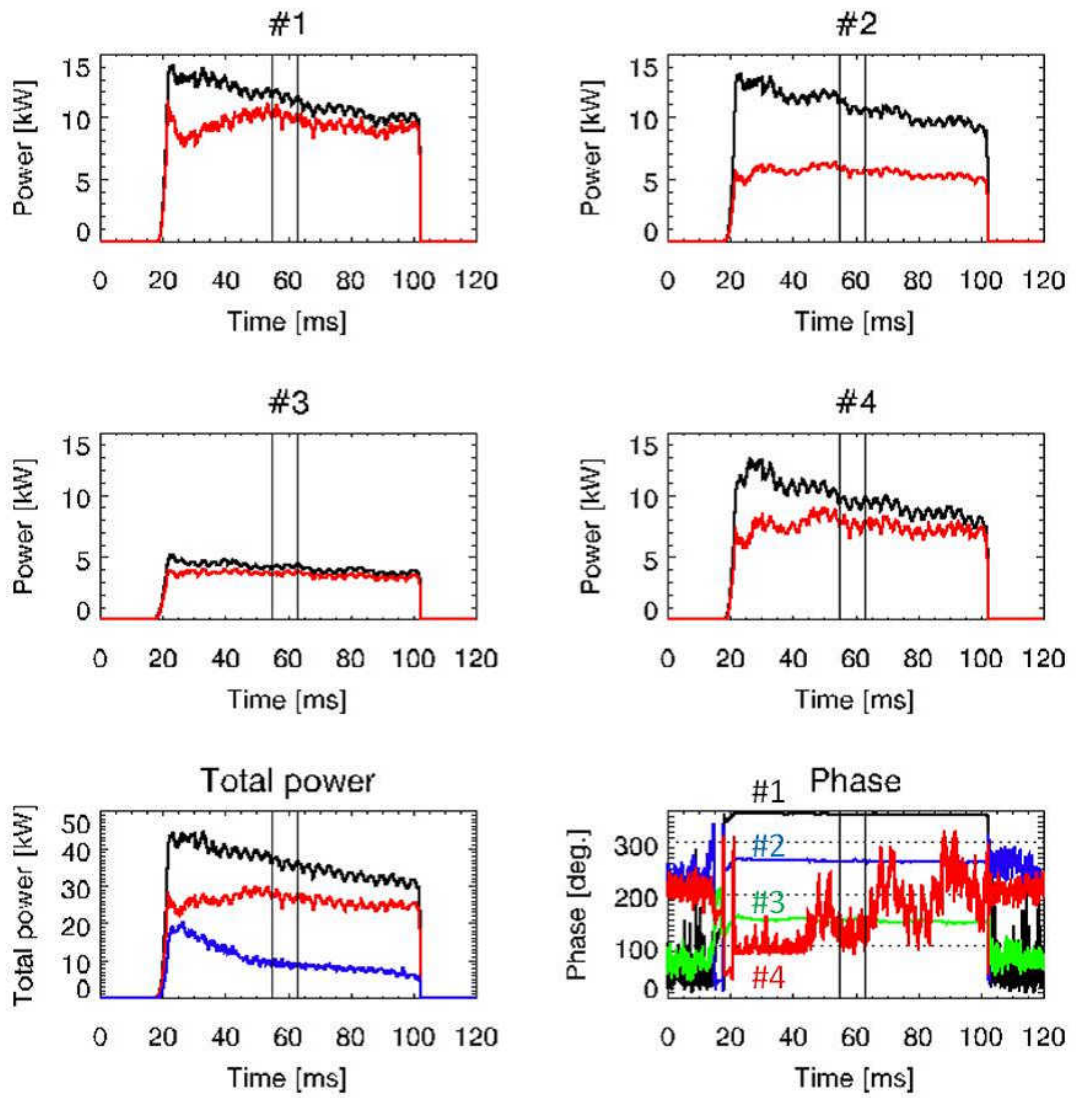
131

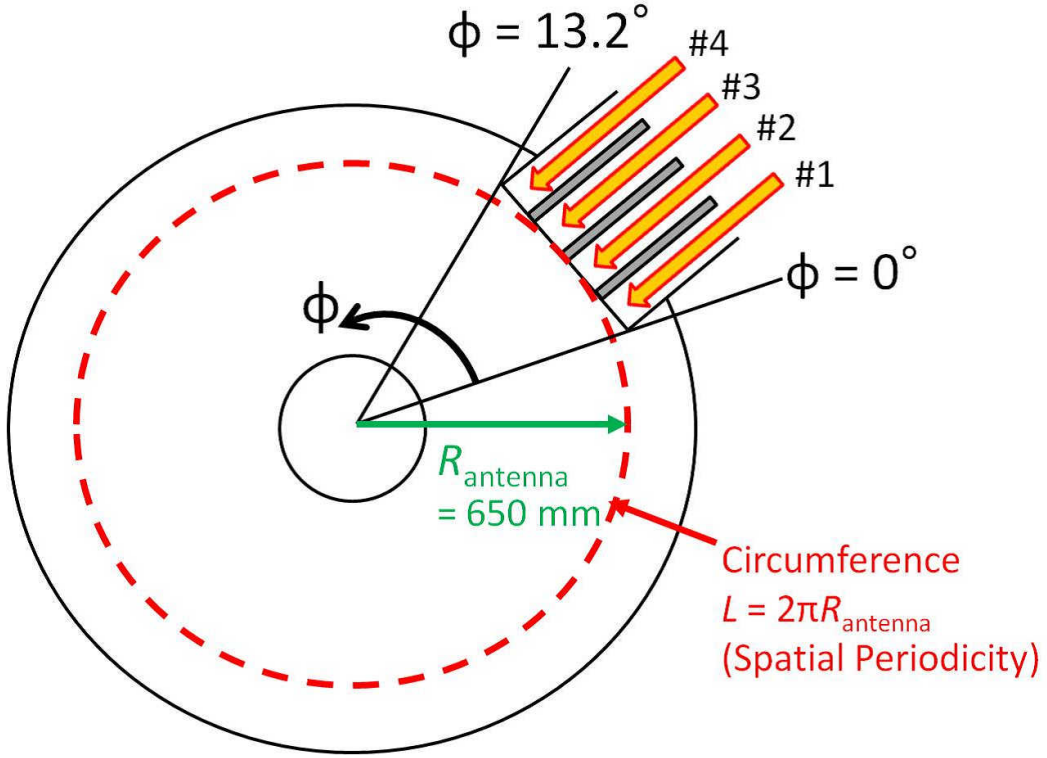Figure 8.6: RF waveforms for shot number 105498.

Figure 8.7: Cross sectional view of the grill antenna placement as seen from the top.

average from 55 ms to 63 ms as shown in Fig. 8.8 and is expanded in terms of k_n, which are multiples of the fundamental wavenumber k_f.

k_f is given as

$$k_f = \frac{2\pi}{L} = \frac{1}{R_{\text{antenna}}} \tag{8.2}$$

and k_n is given by

$$k_n = n k_f = \frac{n}{R_{\text{antenna}}}, \tag{8.3}$$

where n is an integer, called the toroidal mode number and is denoted by n_{tor}.

A situation is considered in which the circumference of length L is equally divided by $N+1$ points, where N is a positive even number and a positive number m is defined as $m = \frac{N}{2}$. Defining the coordinate z along the circumference of length L, the time averaged RF field $V(z)$ is expressed by inverse discrete Fourier transform as

$$V(z) = \sum_{n=-m}^{m-1} \left(A_n e^{i k_n z} \right), \tag{8.4}$$

where A_n is the complex amplitude for spatial wavelength k_n and is calculated as

$$A_n = \frac{1}{N} \sum_{l=0}^{N-1} V\left(\frac{L}{N}l\right) e^{-i \frac{2\pi n}{N} l}. \tag{8.5}$$

According to Eq. (8.4), the parallel wavenumber spectrum is given by plotting

$$\{|A_{-m}|^2, |A_{-m+1}|^2, \cdots, |A_{-1}|^2, |A_0|^2, |A_1|^2, \cdots |A_{m-1}|^2\}$$
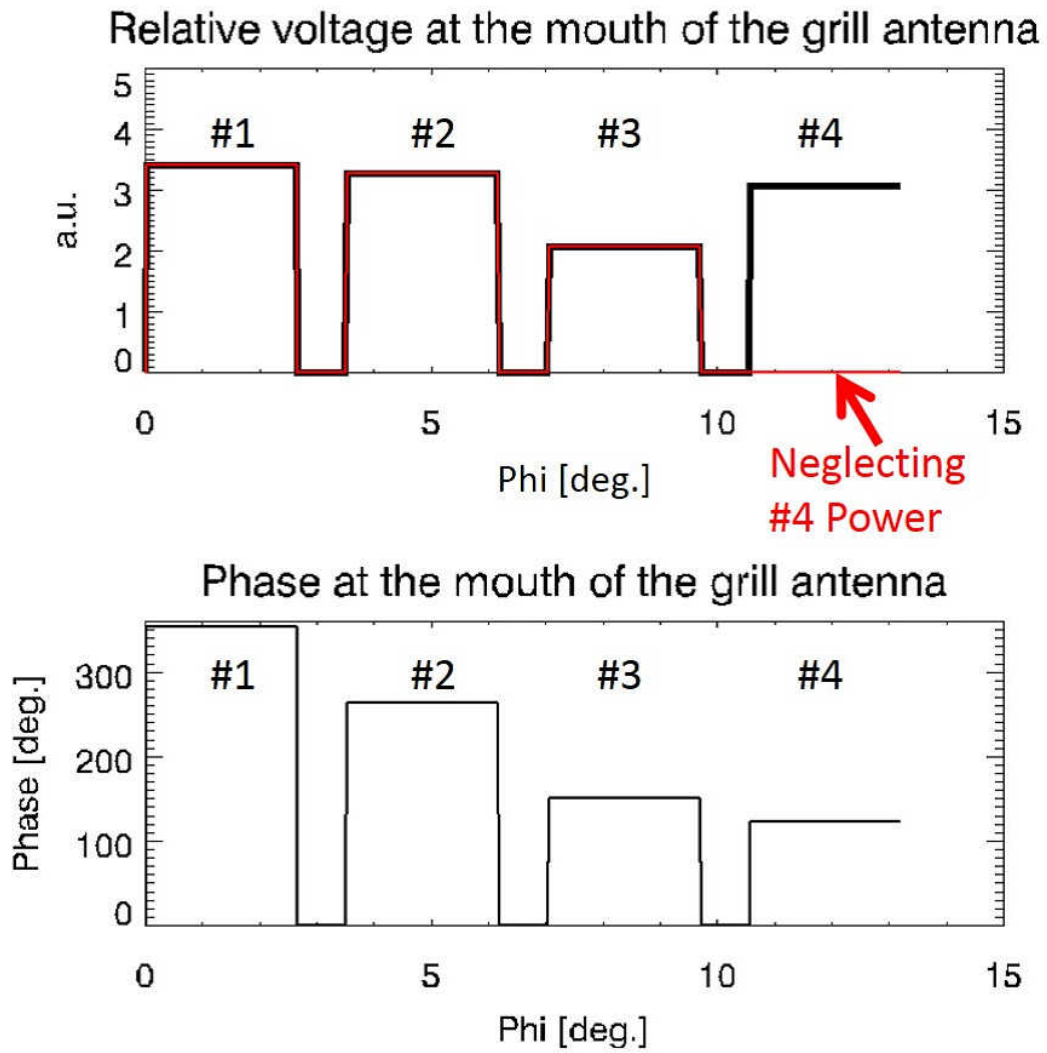
133

Figure 8.8: Relative voltage and phase at the front surface of the grill antenna.

against
$$\{k_{-m}, k_{-m+1} \cdots , k_{-1}, k_0, k_1, \cdots .k_{m-1}\}.$$

Although the phase difference between adjacent waveguides is fixed at 90 degrees, the phase measured at waveguide #4 in Fig. 8.6 was not constant. The cause of this phase variation at #4 is not clear. An external source of noise could affect the phase measurement. The parallel wavenumber spectrum is calculated in two ways, with the RF power #4 included or not included in $V(z)$, as shown in Fig. 8.8. Figure 8.9 shows the calculated parallel wavenumber spectra for the two cases. Overall features of the wavenumber spectra are similar. Considering the possibility that the phase signal of waveguide #4 is spoiled by noise, the parallel wavenumber spectrum without waveguide #4 data is used. As described in Chapter 9, this choice does not affect the physics consideration.

8.3 Wavenumber Derivation from Probe Assembly Signals

The wavenumber of the 200 MHz RF wave is derived from the phase difference of signals measured by the probe assembly, in particular by the three high impedance Langmuir probes. A discrete Fourier transform is performed on measured signals and the resultant Fourier complex amplitudes are used to give phase differences between signals. The wavenumber and its direction are derived from the phase difference with its sign considered. An overview of these processes are given in this section.

8.3.1 Raw Waveforms of Probe Assembly Signals

RF signals were measured with a sampling rate of 1 GHz by a digital oscilloscope (DL7480, Yokogawa Electric Corporation) as shown in Fig 8.10. RF noise suppression is achieved by bundling cables from the vacuum feedthrough to the oscilloscope with cable ties to reduce eliminate loops, and by covering the feedthrough flange by aluminum foil to prevent the electromagnetic noise from entering signal lines. In this section, shot number 105590, with the same conditions for the representative discharge 105498, is used for explanation. Figure 8.11 shows the plasma discharge (shot number 105590) by black lines and a vacuum shot (105591) with RF injection only by red lines. The RF forward power (solid line) is almost the same between the two shots, whereas the reflected power (dashed line) is smaller for the plasma because the RF power is absorbed by the plasma. R_{out} does not work in the absence of plasma. RF signals were sampled over the time interval 55 ms to 63 ms, shown as the region between two solid black lines.

As in the representative plasma discharge (shot number 105498), the magnetic field is nearly purely toroidal (horizontal) in the shot number 105590. The probe assembly was inclined at 15 degrees from the horizontal direction to prevent shadowing of the probe electrode from plasma flow along the magnetic field by a neighboring probe electrode. Figures 8.12, 8.13, and 8.14 show raw signals over the whole time interval of 8 ms for electrodes 1 through 3, for electrode 4 and 5, and for the RF reference signal and the noise reference signal, respectively, with expanded views of the waveforms. Zero on the time axis of windows for signals over the time interval of 8 ms corresponds to 55 ms. Expanded views of signals are shown at 59 ms for 20 nano seconds. The expanded view of raw signals shows that the period is about 5 ns, which corresponds to the period of 200 MHz. For the same RF forward power (shown in the first and the second rows in Fig. 8.14), all signal magnitudes of the probe assembly are obviously larger for the plasma shot (black lines) than in a vacuum shot (red lines). DC components of electrodes 1 through 3 are negative, whereas that of electrode 4 (magnetic probe) is nearly zero.

8.3.2 Amplitude Spectra of Probe Assembly Signals

A discrete Fourier transform is performed on raw signals to extract the amplitude and phase of 200 MHz frequency. As in Subsection 8.2.3, the situation in which the data time interval T is equally divided by $N + 1$ points is considered. N is a positive even number and a positive number m is defined as
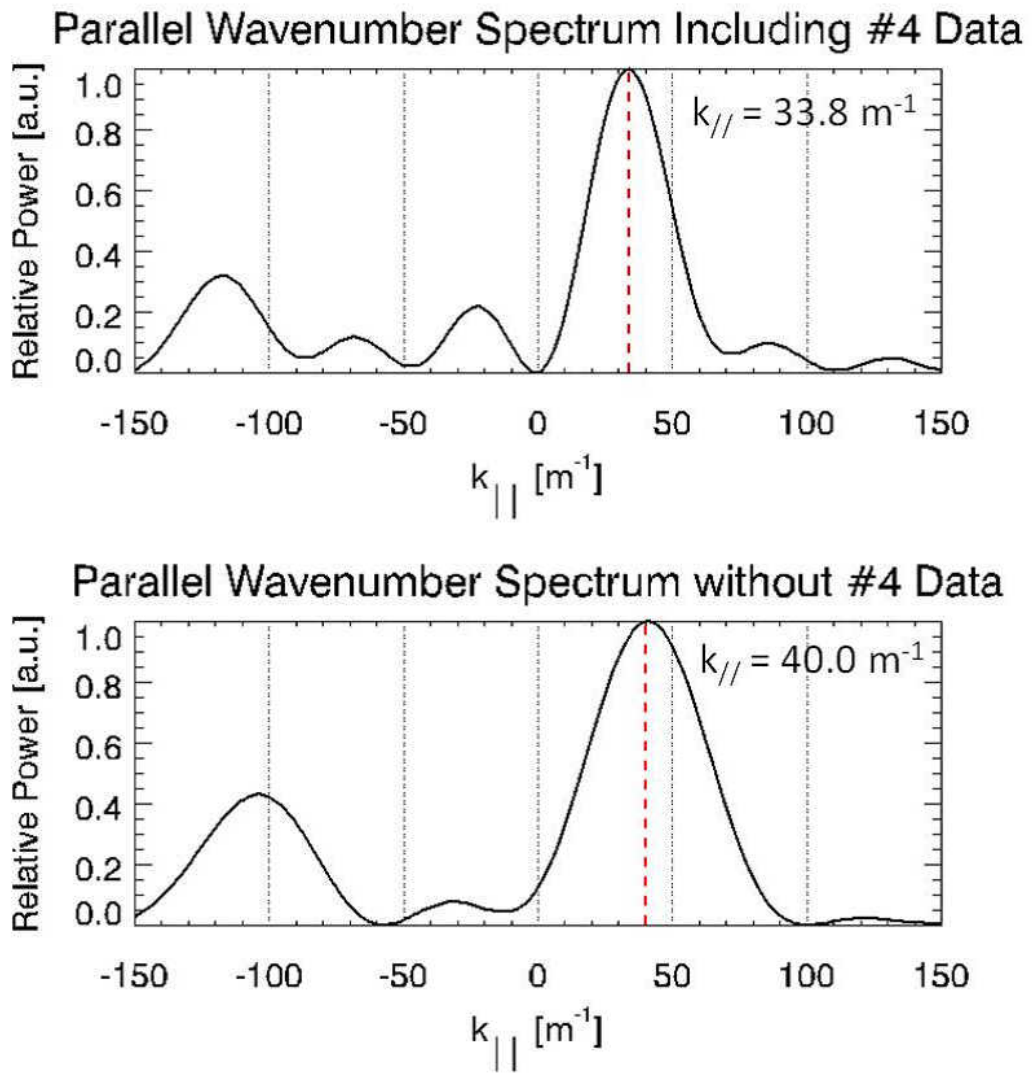
Figure 8.9: Parallel wavenumber spectra of the wave launched by the grill antenna with and without waveguide #4 data.

Figure 8.10: Provision for noise suppression.
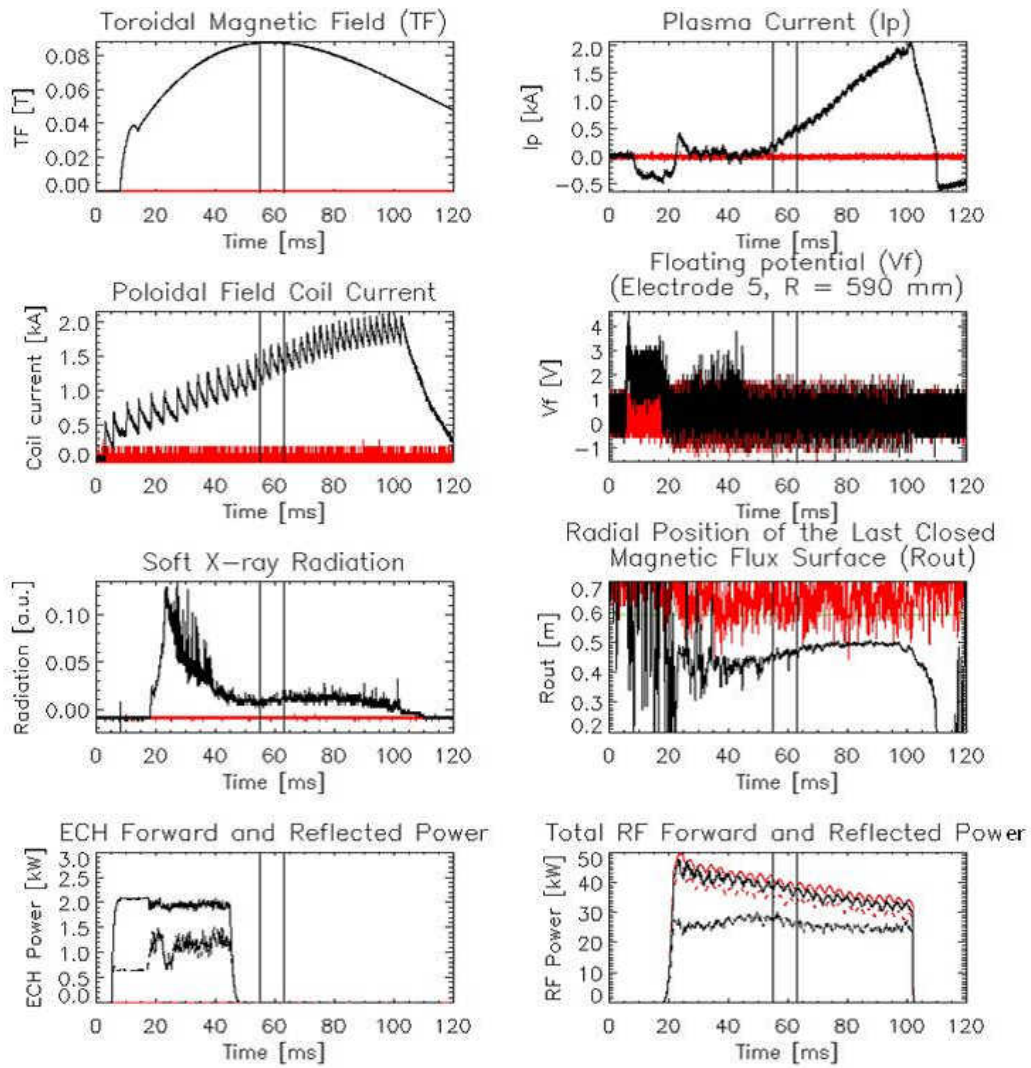
Figure 8.11: Comparison of the plasma discharge of the shot number 105590 (black) with the vacuum shot number 105591 (red).
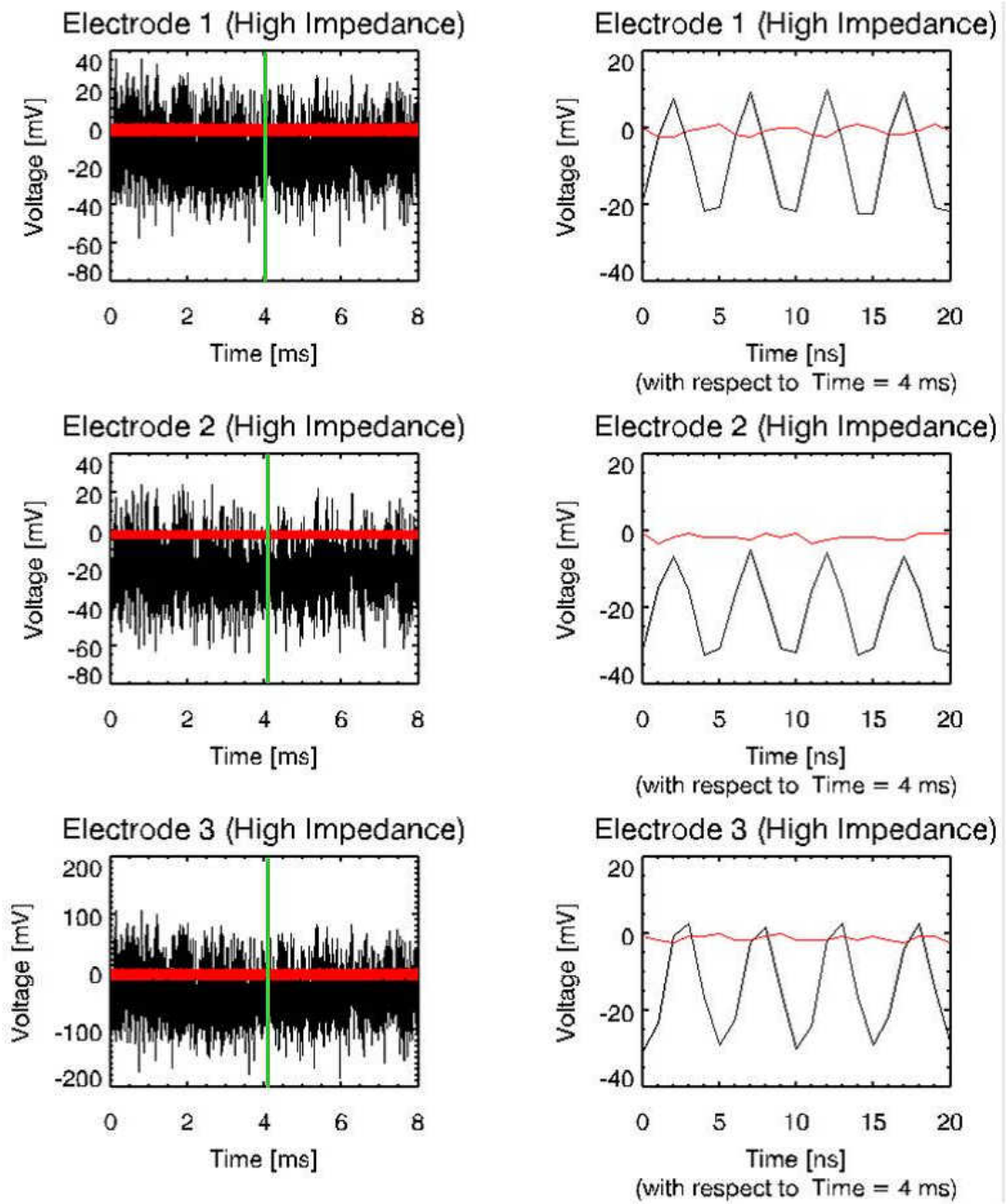
Figure 8.12: Raw waveforms of the whole time interval of 8 ms and expanded views of the waveforms of signals from electrodes 1 through 3 for the plasma shot number 105590 (black) and the vacuum shot number 105591 (red).

Figure 8.13: Raw waveforms of the whole time interval of 8 ms and expanded views of the waveforms of signals from electrodes 4 and 5 for the plasma shot number 105590 (black) and the vacuum shot number 105591 (red).

Figure 8.14: Raw waveforms of the whole time interval of 8 ms and expanded views of the waveforms of the RF reference signal and the noise reference signal for the plasma shot number 105590 (black) and the vacuum shot number 105591 (red).
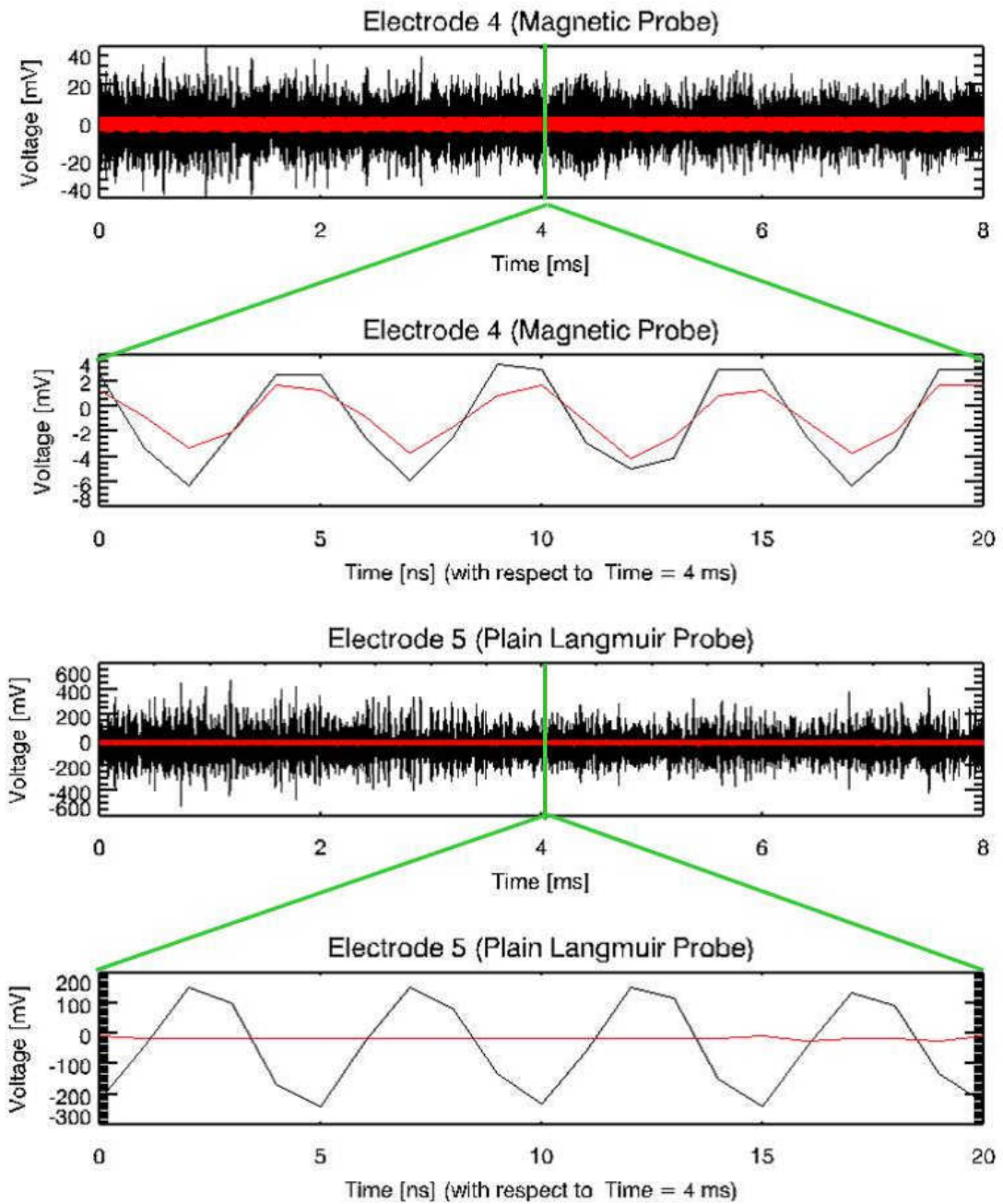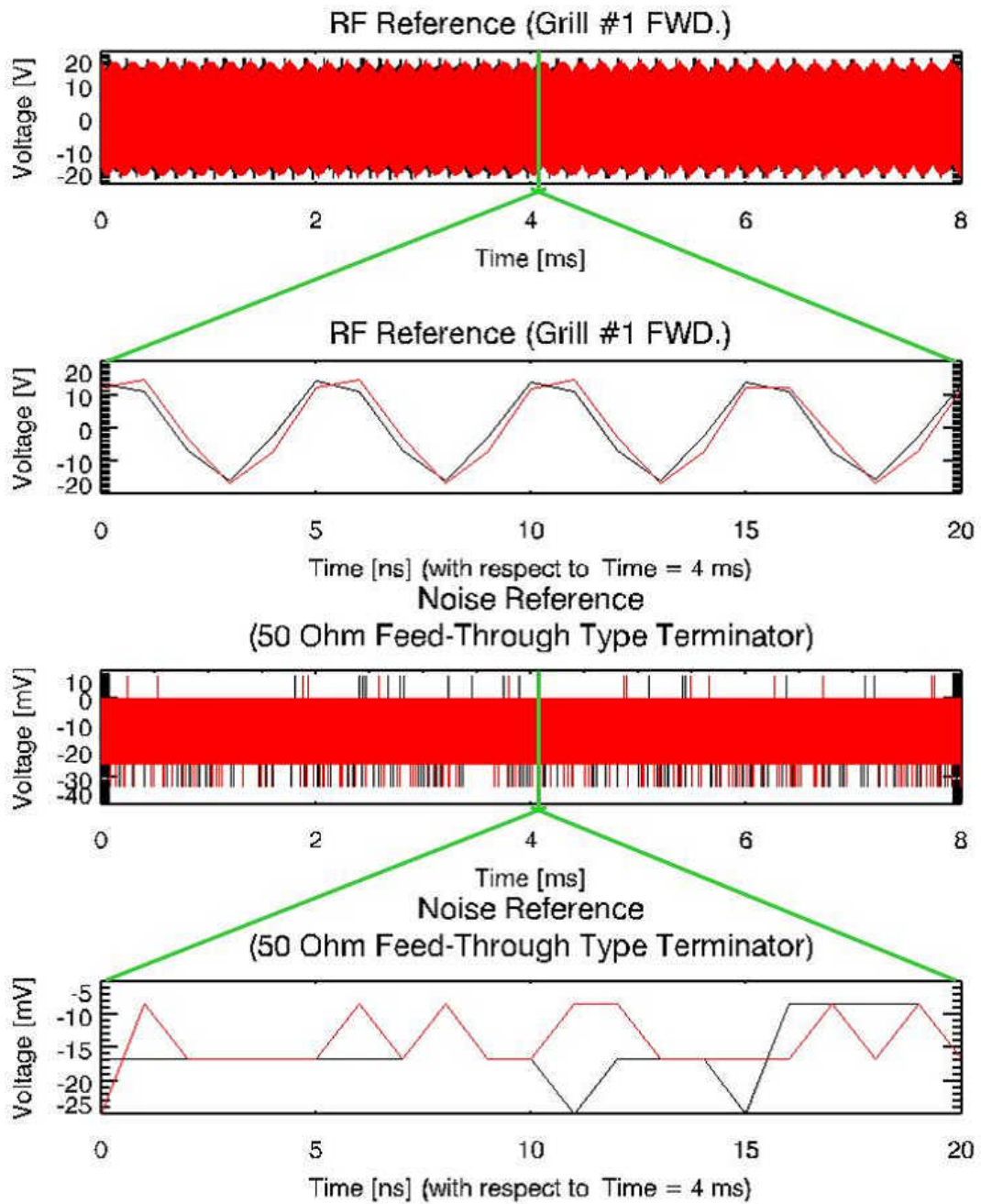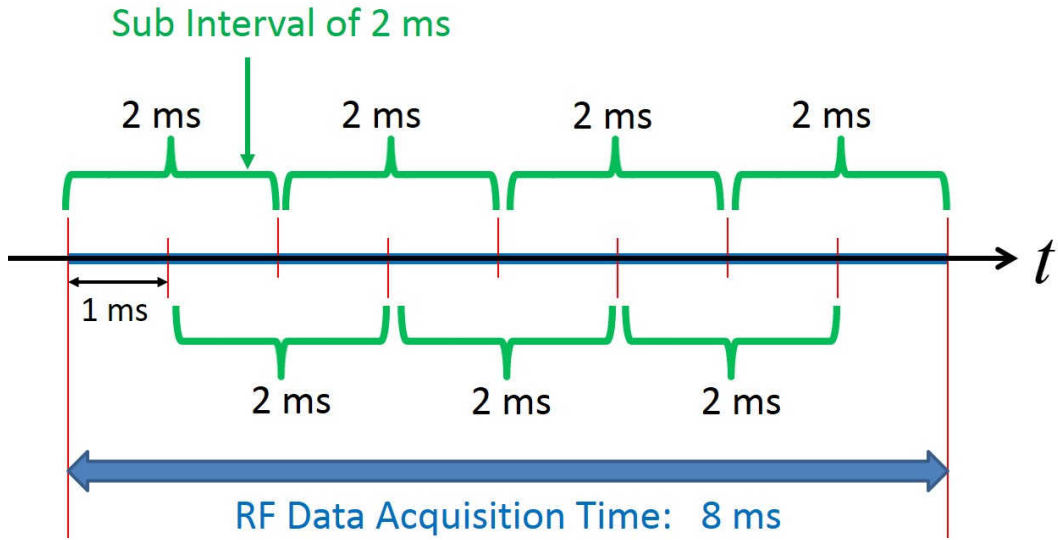
Figure 8.15: RF data acquisition time interval of 8 ms and seven 2 ms sub-intervals.

$m = \frac{N}{2}$. From Appendix B, the time-dependent voltage $V(t)$ is expressed as

$$V(t) = C_0 + \sum_{n=1}^{m-1} \{2|C_n| \cos(\omega_n t + \arg C_n)\}, \tag{8.6}$$

where C_n is the complex Fourier amplitude

$$C_n = \frac{1}{N} \sum_{l=0}^{N-1} V\left(\frac{T}{N}l\right) e^{-i\frac{2\pi n}{N}l} \tag{8.7}$$

and ω_n is defined as

$$\omega_n = \frac{2\pi}{T}n. \tag{8.8}$$

From Eq. (8.6), it is found that the amplitude and phase of the signal component for the angular frequency ω_n are given by $2|C_n|$ and $\arg C_n$, respectively. Since Fourier analysis assumes stationarity of the analyzed signal in time, the sampled time interval of 8 ms is divided into "sub-intervals" to check whether the complex Fourier amplitudes derived from each sub-interval are stationary in time or not. In this thesis, the 8 ms time interval is divided into 2 ms sub-intervals (the first sub-interval is 55 ms to 57 ms, the second sub-interval is 56 ms to 58 ms, and so on), as shown in Fig. 8.15. For the sub-interval of $T = 2$ ms with a data sampling rate of 1 GHz, $N = 2 \times 10^6$. In performing discrete Fourier transform, the data in a sub-interval was windowed by a hanning window $w(t)$, which is defined for the time interval $[0, T]$ as

$$w(t) = \begin{cases} 1 & \frac{1}{10}T \leq t \leq \frac{9}{10}T, \\ \frac{1}{2}\{1 - \cos(2\pi\frac{5}{T}t)\} & 0 \leq t \leq \frac{1}{10}T, \ \frac{9}{10}T \leq t \leq T. \end{cases} \tag{8.9}$$

Figure. 8.16 shows $w(t)$ with the abscissa expressed by the data point number for a 2 ms sub-interval. Using $w(t)$, the signal $w(t)V(t)$ is used instead of $V(t)$ in Eq. (8.7) and the complex Fourier
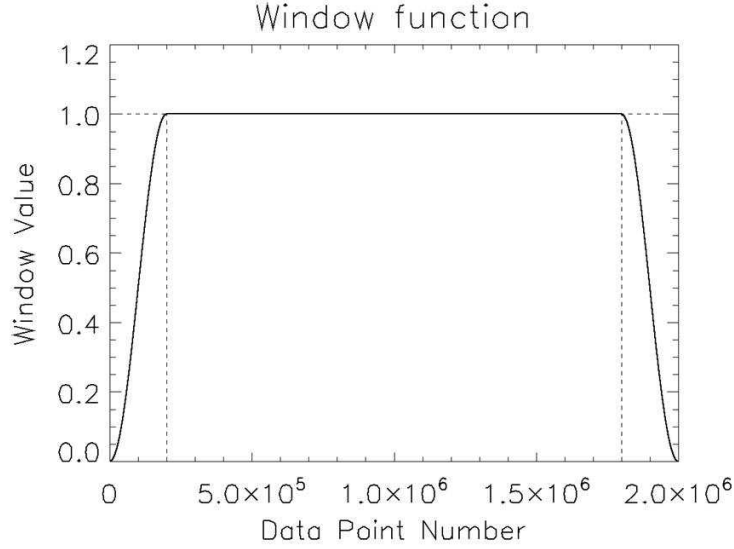
Figure 8.16: Window function.

amplitude C_n' for the windowed data $w(t)V(t)$ is calculated as

$$C_n' = \frac{1}{N} \sum_{l=0}^{N-1} w\left(\frac{T}{N}l\right) V\left(\frac{T}{N}l\right) e^{-i\frac{2\pi n}{N}l}.$$

In order for C_n' to take a correct signal amplitude, C_n' should be corrected by dividing by a factor

$$\frac{\sum_{l=0}^{N-1} w\left(\frac{T}{N}l\right)}{\sum_{l=0}^{N-1} 1} = 0.9\,,$$

which is the ratio of the window area to the area not windowed. This amplitude correction was confirmed to be valid using virtual test signals. From now on, the corrected complex Fourier amplitude $C_n'/0.9$ is used as C_n:

$$\frac{C_n'}{0.9} \to C_n. \tag{8.10}$$

It should be noted that $2|C_n|$ given in Eq. (8.10) reflects the correct signal amplitude for angular frequency ω_n.

Figure 8.17 shows the averaged $2|C_n|$ of measured signals over the seven sub-intervals for plasma shot number 105590 (black line) and vacuum shot number 105591 (red line). All amplitudes take the maximum value at 200.001 MHz. For the same RF reference signal amplitude, the amplitudes of all probe assembly electrodes are larger for plasma discharge at this frequency than for vacuum. The noise reference signal amplitude is slightly smaller for plasma discharge than for vacuum. This is presumably because the amplitude of RF wave in a plasma discharge is reduced from that in vacuum due to absorption of RF wave power by the plasma.

Figure 8.18 shows the double corrected complex Fourier amplitudes $2C_n$ at 200.001 MHz for each sub-interval for plasma shot number 105590. Colors of data points begin with red for the first sub-interval and the colors for subsequent sub-intervals progress in the same order as the rainbow. The distance between each data point and the origin represents the amplitude of the real signal. The argument changes by similar values because the sub-interval is not an exact integral multiple of the
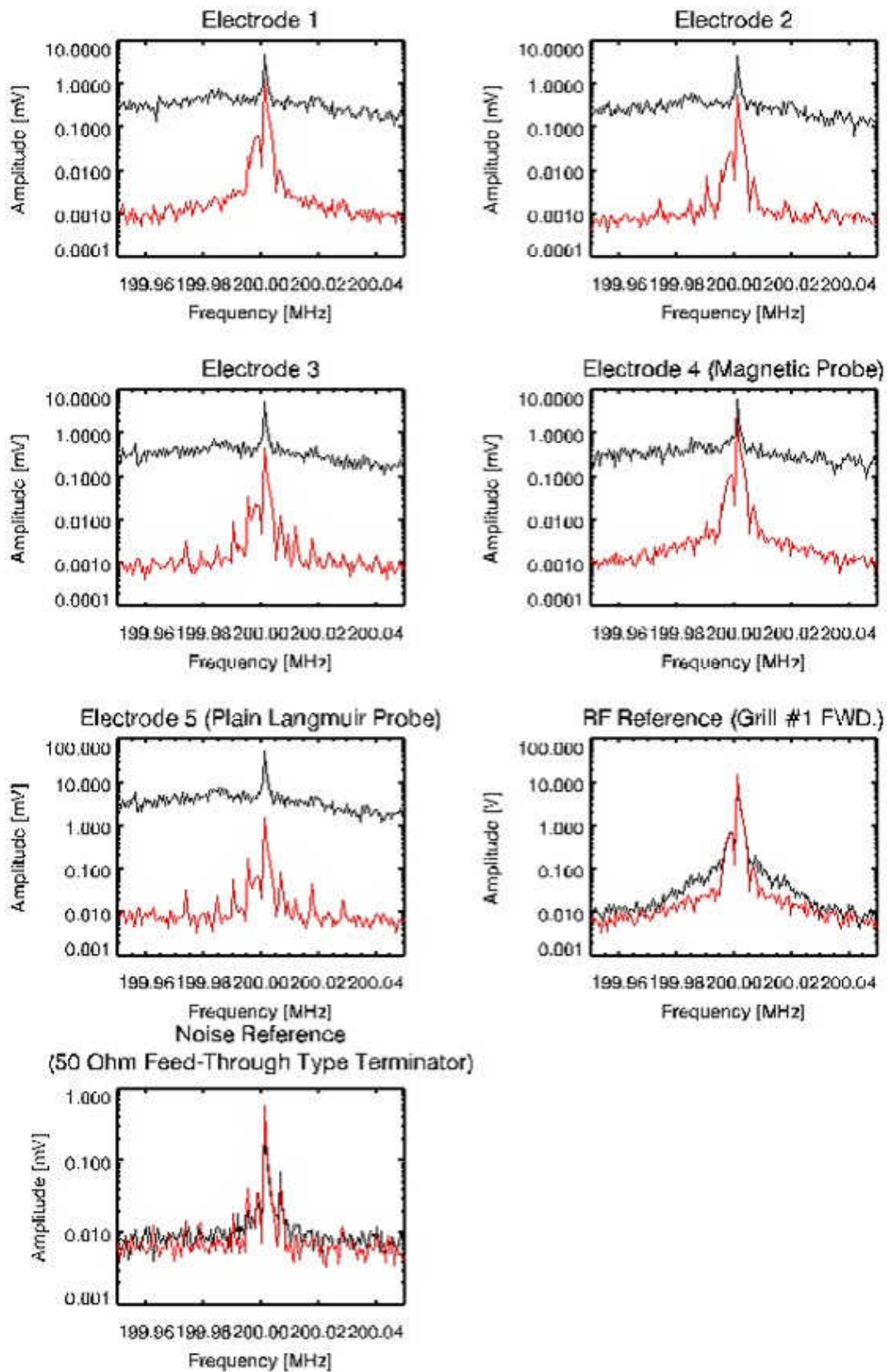
143

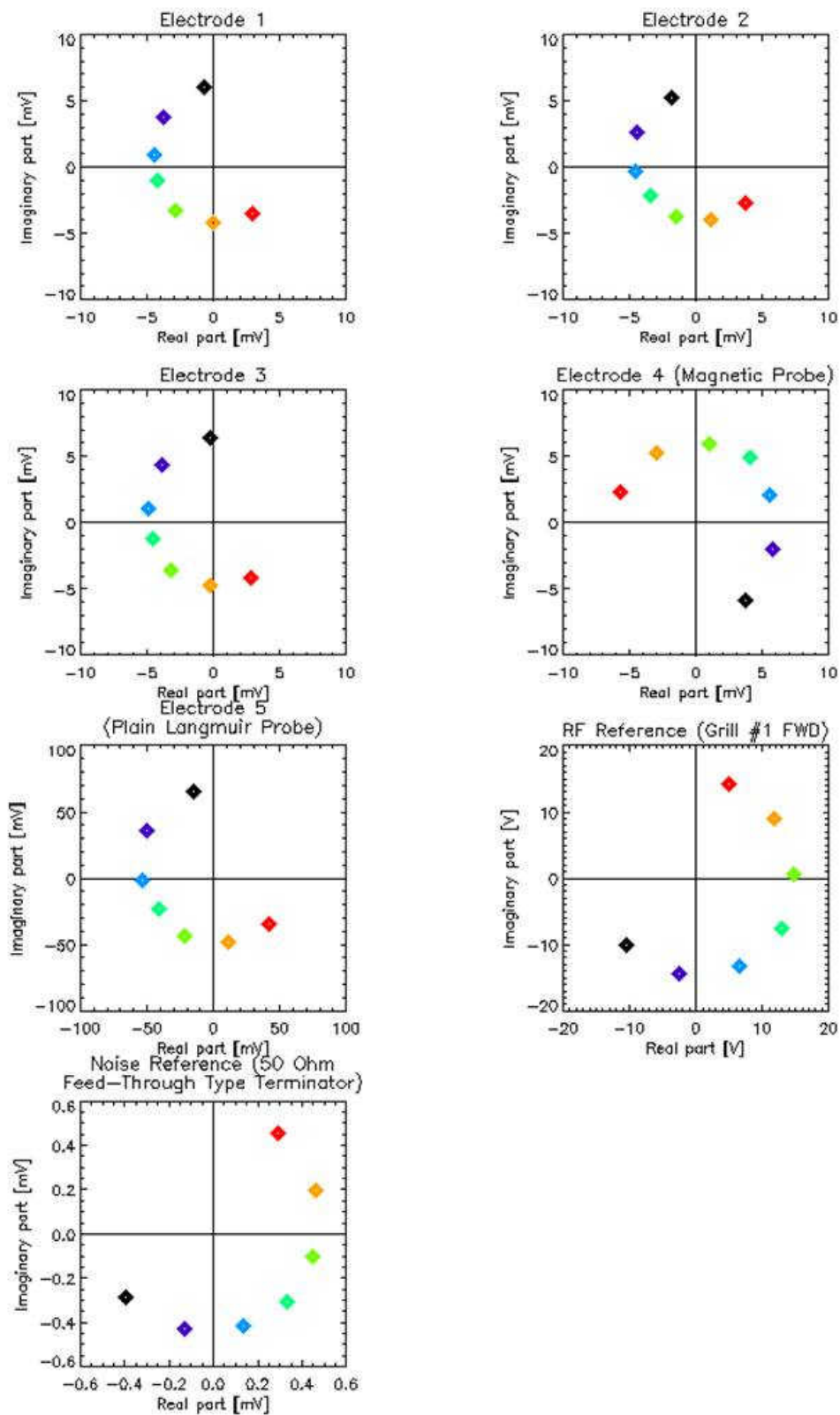Figure 8.17: Signal amplitudes averaged over the seven sub-intervals.

Figure 8.18: Fourier components $2C_n$ for each sub-interval for the frequency of 200.001 MHz for plasma shot number 105590.
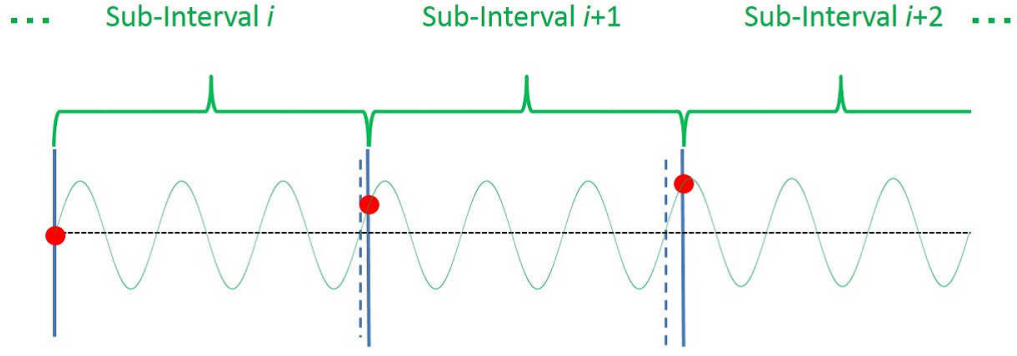
145

Figure 8.19: Phase shift between sub-intervals.

period corresponding to 200.001 MHz, and thus each sub-interval perceive the signal with different phase, as depicted in Fig. 8.19. As long as the wave frequency is constant, this effect is irrelevant to the phase difference, which is calculated for each sub-interval, because the phase increment is cancelled out by subtracting one phase from another phase in the same sub-interval. With this effect taken into account, it is reasonable to conclude from Fig. 8.18 that signals are nearly stationary during the data acquisition time of 55 ms to 63 ms.

8.3.3 Effect of Using a High Impedance Resistor for Measuring the Floating Potential at 200 MHz

In this Subsection, the effect of using a high impedance resistor ($100\,\mathrm{k\Omega}$ nominal) on the floating potential measurement at 200 MHz is considered using amplitudes of voltage signals measured by the high impedance Langmuir probe systems and the plain Langmuir probe, as described in Section 5.5. Table 8.1 shows the average signal amplitudes and errors measured by electrodes 1 through 3 (high impedance Langmuir probes) and electrode 5 (plain Langmuir probe) over seven sub-intervals for the plasma shot 105590 and the vacuum shot 105591, and Table 8.2 shows those of electrode 4 (magnetic probe), RF reference signal, and noise reference signal. It should be noted that the rows for "Plasma Shot 105590" in Tables 8.1 and 8.2 come from the absolute values of Fourier components (signal amplitudes) shown in Fig. 8.18. The error is taken from the standard deviation over seven sub-intervals.

From Eqs. (5.45) and (5.46), the absolute values of currents drawn from the plasma by the high impedance Langmuir probe system and the plain Langmuir probe are:

$$|I_1 + I_2| \leq |1 + i\omega C_{\mathrm{box}}(Z_{\mathrm{chip}} + Z_0)| \frac{|V_{\mathrm{mod}}|}{Z_0}$$

Table 8.1: Average signal amplitudes of electrodes 1 through 3 (high impedance Langmuir probes) and electrode 5 (plain Langmuir probe) over seven sub-intervals for the plasma shot 105590 and the vacuum shot 105591.

Signal Amplitude (mV)	1 High Impedance Langmuir Probe	2 High Impedance Langmuir Probe	3 High Impedance Langmuir Probe	5 Plain Langmuir Probe
Plasma Shot 105590	4.77 ± 0.68	4.57 ± 0.58	5.23 ± 0.63	54.56 ± 7.45
Vacuum Shot 105591	1.40 ± 0.01	0.61 ± 0.03	0.49 ± 0.02	1.56 ± 0.16

146

Table 8.2: Average signal amplitudes of electrode 4 (magnetic probe), RF reference, and noise reference over seven sub-intervals for the plasma shot 105590 and the vacuum shot 105591.

Signal Amplitude (mV) ((V) for CH. 6)	4 Magnetic Probe	6 RF Reference	7 Noise Reference
Plasma Shot 105590	6.24 $\pm\,0.48$	14.78 $\pm\,0.19$	0.48 $\pm\,0.04$
Vacuum Shot 105591	2.39 $\pm\,0.03$	15.43 $\pm\,0.20$	0.59 $\pm\,0.03$

and

$$|I_3| = \frac{|V_{\mathrm{ord}}|}{Z_0},$$

respectively. $C_{\mathrm{box}} = 0.34\,\mathrm{pF}$ and $Z_{\mathrm{chip}} = 1477 - 12062i\,\Omega$ for $200\,\mathrm{MHz}$ were given in Subsection 5.4.1. From Table 8.1, signal amplitudes measured measured by the high impedance Langmuir probe system $|V_{\mathrm{mod}}|$ and by the plain Langmuir probe $|V_{\mathrm{ord}}|$ take the values of

$$
\begin{aligned}
|V_{\mathrm{mod}}| &= 5.2\,\mathrm{mV}, \\
|V_{\mathrm{ord}}| &= 54.6\,\mathrm{mV},
\end{aligned}
$$

where the signal amplitude measured by electrode 3, the highest among the three high impedance Langmuir probe systems, was chosen for $|V_{\mathrm{mod}}|$. Using these values, $|I_1 + I_2|$ and $|I_3|$ are calculated as

$$
\begin{aligned}
|I_1 + I_2| &\leq \left|1 + i\left(2\pi \times 2 \times 10^8\right) \times \left(3.4 \times 10^{-13}\right) \times [(1477 + 50) - 12062\,i]\right| \times \frac{5.2 \times 10^{-3}}{50} \\
&\cong 6.4 \times 10^{-4}\,\mathrm{A} = 0.64\,\mathrm{mA}
\end{aligned}
$$

and

$$|I_3| = \frac{54.6 \times 10^{-3}}{50} \cong 1.1 \times 10^{-3}\,\mathrm{A} = 1.1\,\mathrm{mA},$$

leading to

$$|I_1 + I_2| < 0.6 \times |I_3|.$$

This result signifies that at $200\,\mathrm{MHz}$ the total current drawn from the plasma by the high impedance Langmuir probe system is less than that drawn by the plain Langmuir probe by at least $40\,\%$, showing that using a high impedance resistor of $100\,\mathrm{k\Omega}$ just after the electrode of the Langmuir probe is effective for floating potential measurement at $200\,\mathrm{MHz}$. Although the signal level is smaller than that measured by the plain Langmuir probe, the measurement using the high impedance Langmuir probe system is less perturbative. The high impedance Langmuir probe system detects the signal closer to the floating potential than that measured by the plain Langmuir probe. It is expected that the signal measured by the high impedance Langmuir probe system is closer to that originating from the LHW.

The reduction of the current drawn from the plasma by at least $40\,\%$ is more than twice larger than $18\,\%$ estimated using the low frequency sheath model in Subsection 5.4.2, suggesting that the sheath at $200\,\mathrm{MHz}$ is not described correctly by the low frequency sheath model.

8.3.4 Phase Difference and Coherence for Plasma Discharge

The quantity needed is the phase difference between signals measured by the high impedance Langmuir probe units. From Eq. (8.6), $\arg C_n$ can be regarded as the phase for angular frequency ω_n. If the two complex Fourier amplitudes $C_{n,1}$ and $C_{n,2}$ are given for the two signals $V_1(t)$ and $V_2(t)$, they can be written as

$$
\begin{aligned}
C_{n,1} &= |C_{n,1}|e^{i(\arg C_{n,1})} & (8.11) \\
C_{n,2} &= |C_{n,2}|e^{i(\arg C_{n,2})}, & (8.12)
\end{aligned}
$$

since they are complex numbers. Defining the phase difference $\Delta\phi_{2,1}$ of signal 2 with respect to signal 1 for a common n as

$$\Delta\phi_{2,1} \equiv \arg C_{n,2} - \arg C_{n,1}, \tag{8.13}$$

$\Delta\phi_{2,1}$ is given from Eqs. (8.11) and (8.12) by the argument of the quantity

$$\overline{C_{n,1}}C_{n,2} = |C_{n,1}||C_{n,2}|e^{i(\arg C_{n,2} - \arg C_{n,1})} = |C_{n,1}||C_{n,2}|e^{i\Delta\phi_{2,1}}. \tag{8.14}$$

The quantity $\overline{C_{n,1}}C_{n,2}$ has the information of $\Delta\phi_{2,1}$ weighted by the absolute values of complex Fourier amplitudes. In this sense, the argument of the ensemble average of $\overline{C_{n,1}}C_{n,2}$ over the seven sub-intervals is considered to be a good estimate of the phase difference during the entire 8 ms time interval. In the field of spectrum analysis, the cross-spectrum $S_{xy}(\omega)$ is calculated using the complex Fourier amplitudes of $X(\omega)$ and $Y(\omega)$ of signals $x(t)$ and $y(t)$, respectively, as

$$S_{xy}(\omega) = \lim_{T\to\infty}\left[\frac{2\pi}{T}\overline{X(\omega)}Y(\omega)\right] = \mathrm{E}\left[\frac{2\pi}{T}\overline{X(\omega)}Y(\omega)\right], \tag{8.15}$$

where "E[ ]" stands for ensemble average and the second equal sign holds for Ergodic signals, for which the time average of the signal over a long time interval is equal to its ensemble average. A derivation of Eq. (8.15) is given in Appendix B. For the measured signals with modest time-stationarity, the corresponding notation to Eq. (8.15) for the cross-spectrum for signal 2 with respect to signal 1 is given as

$$S_{n,21} = \mathrm{E}\left[\frac{2\pi}{T}\overline{C_{n,1}}C_{n,2}\right], \tag{8.16}$$

where the ensemble average is taken over the seven sub-intervals and $T = 2\,\mathrm{ms}$ for the sub-interval. The average phase difference $\Delta\theta_{n,21}$ during the entire 8 ms time interval, or over the seven sub-intervals, is given by

$$\Delta\theta_{n,21} = \arg\left(S_{n,21}\right). \tag{8.17}$$

The squared coherence $\mathrm{coh}^2_{n,21}$, which evaluates the linearity of signal 2 with respect to signal 1, is defined as

$$\mathrm{coh}^2_{n,21} \equiv \frac{|S_{n,21}|^2}{S_{n,11}S_{n,22}}. \tag{8.18}$$

The phase differences and the squared coherence of signals with respect to the electrode 1 signal are shown in Figs. 8.20 and 8.21.

Each squared coherence is larger than 0.97 at 200.001 MHz. Therefore, the phase differences of the electrode 2 signal to the electrode 1 signal, and of the electrode 3 signal to the electrode 1 signal of 15.1 degrees and -2.9 degrees at this frequency, respectively, are reliable as median values.

8.3.5 Relationship between the Sign of Phase Difference and the Wavenumber Direction

The phase differences of RF signals detected by different high impedance Langmuir probes are related to the wavenumber of the measured wave. As described by Eq. (5.7), the phase factor including both space and time coordinates is taken as $(\boldsymbol{k} \cdot \boldsymbol{r} - \omega t)$ instead of $(\omega t - \boldsymbol{k} \cdot \boldsymbol{r})$ because in the former notation $\boldsymbol{k} \cdot \boldsymbol{r} > 0$ means that $\boldsymbol{k}$ has a component in the positive direction of $\boldsymbol{r}$ and it is easier to imagine the direction of wave propagation. Adopting the phase factor θ as

$$\theta_n = \boldsymbol{k}_n \cdot \boldsymbol{r} - \omega_n t, \tag{8.19}$$

Eq (8.6) is rewritten as

$$
\begin{aligned}
V(t) &= C_0 + \sum_{n=1}^{m-1}\{2|C_n|\cos\left(\omega_n t + \arg C_n\right)\} \\
&= C_0 + \sum_{n=1}^{m-1}\{2|C_n|\cos\left(-\arg C_n - \omega_n t\right)\}.
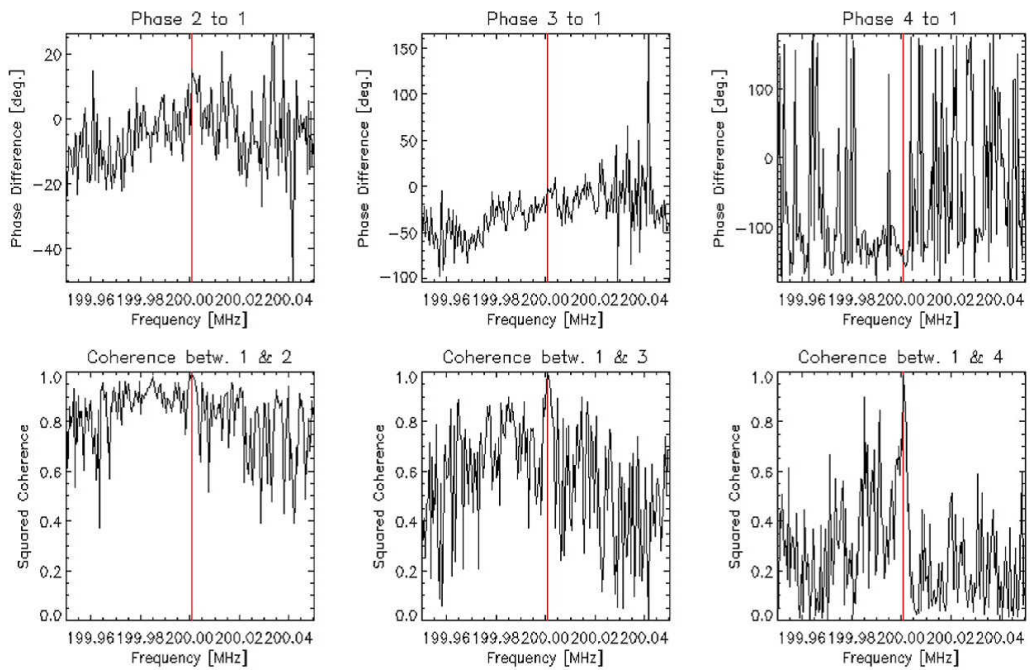\end{aligned} \tag{8.20}
$$

Figure 8.20: Phase difference and squared coherence of electrodes 2 through 4 with respect to the electrode 1 signal.
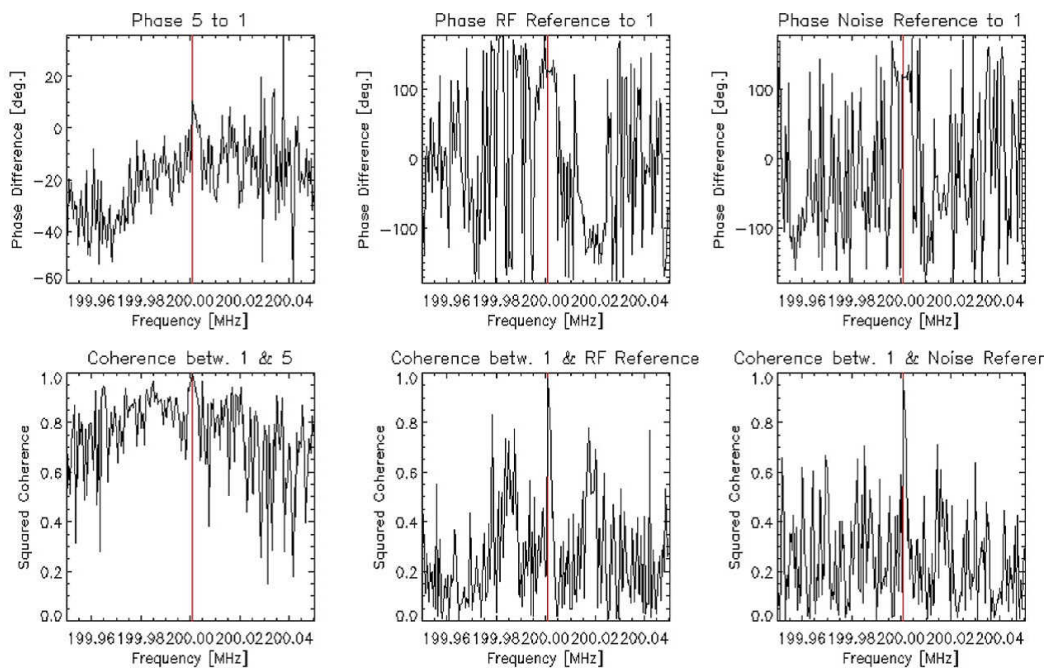

Figure 8.21: Phase difference and squared coherence of the electrode 5 signal, the RF reference signal, and the noise reference signal, with respect to the electrode 1 signal.
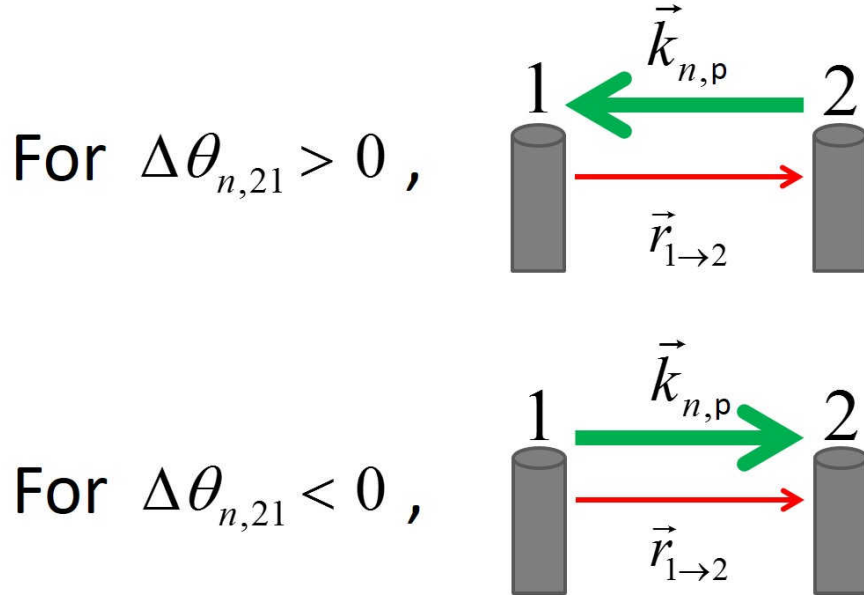
Figure 8.22: Correspondence between the wavenumber direction and the sign of phase difference.

The phase factor $(-\arg C_n - \omega_n t)$ in Eq. (8.20) can be regarded equal to θ_n in Eq. (8.19). Denoting the phase factors of signals of electrodes 1 and 2 as $\theta_{n,1}$ and $\theta_{n,2}$, they are given as

$$\theta_{n,1} = \boldsymbol{k}_n \cdot \boldsymbol{r}_1 - \omega_n t = -\arg C_{n,1} - \omega_n t \qquad (8.21)$$
$$\theta_{n,2} = \boldsymbol{k}_n \cdot \boldsymbol{r}_2 - \omega_n t = -\arg C_{n,2} - \omega_n t, \qquad (8.22)$$

where $\boldsymbol{r}_1$ and $\boldsymbol{r}_2$ are the position vectors of electrodes 1 and 2, and $\boldsymbol{k}$ and $\omega_n t$ are assumed to be the same for the two electrodes. Eqs. (8.21) and (8.22) give

$$\boldsymbol{k}_n \cdot (\boldsymbol{r}_2 - \boldsymbol{r}_1) = -\left\{\arg C_{n,2} - \arg C_{n,1}\right\}, \qquad (8.23)$$

which leads to

$$\boldsymbol{k}_n \cdot \boldsymbol{r}_{1\to2} = -\Delta\phi_{n,21} \qquad (8.24)$$

where $\boldsymbol{r}_{1\to2}$ is the vector from electrode 1 to electrode 2 and $\Delta\phi_{n,21}$ is defined in Eq. (8.13). Using the phase difference $\Delta\theta_{n,21} = \arg(S_{n,21})$ calculated in Eq. (8.17) by ensemble average, $\Delta\phi_{n,21}$ is replaced by $\Delta\theta_{n,21}$ and the averaged wavenumber over the seven sub-intervals $<\boldsymbol{k}_n>$ is given as

$$<\boldsymbol{k}_n> \cdot \boldsymbol{r}_{1\to2} = -\Delta\theta_{n,21}, \qquad (8.25)$$

where $<>$ stands for the ensemble average over the seven sub-intervals. Equation (8.25) indicates that the projected wavenumber $<\boldsymbol{k}_{n,\mathrm{p}}>$ along the electrode array is in the direction from electrode 2 to electrode 1 for a positive $\Delta\theta_{n,21}$ and vice versa, as shown in Fig. 8.22.

Following Fig. 8.22, the measured phase difference $\Delta\theta_{n,21} = 15.1°$ and $\Delta\theta_{n,31} = -2.9°$ at the probe angle of 15 degrees are translated using Eq. (6.2):

$$|<\boldsymbol{k}_{n,\mathrm{p}}>| = \frac{2\pi}{d} \cdot \frac{|\Delta\theta_n|}{360°},$$

where k_p and ϕ_degree are replaced by $|<\boldsymbol{k}_{n,\mathrm{p}}>|$ and $|\Delta\theta_n|$, respectively, to the absolute value of the projected wavenumbers of $|<\boldsymbol{k}_{n,\mathrm{p},21}>| = 18.6\,\mathrm{m}^{-1}$ and $|<\boldsymbol{k}_{n,\mathrm{p},31}>| = 3.6\,\mathrm{m}^{-1}$, respectively.
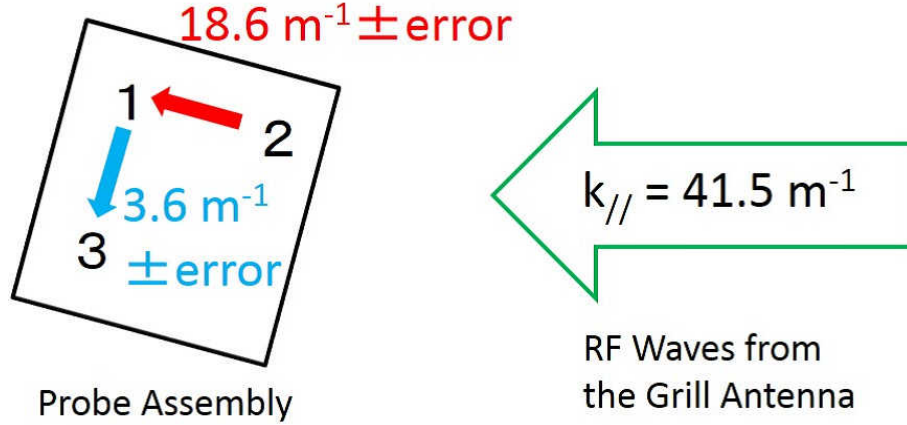
Figure 8.23: Median values and directions of measured wavenumbers for plasma shot number 105590.

These wavenumbers are shown in Fig. 8.23, including the directions of wavenumbers. Since two arrays formed between electrodes 1 and 2, and that formed between electrodes 1 and 3 are diagonal, the measured horizontal (parallel) wavenumber $k_{\parallel,\text{mea.}}$ is given as

$$k_{\parallel,\text{mea.}} = \sqrt{(18.6 \cos 15°)^2 + (3.6 \cos 75°)^2} \cong 18.0\,\text{m}^{-1},$$

which is smaller than the launched parallel wavenumber for shot number 105590 of $k_{\parallel} = 41.5\,\text{m}^{-1}$ by a factor of about 2. The value of $k_{\parallel} = 41.5\,\text{m}^{-1}$ here is derived by the same process described in Subsection 8.2.3 (excluding the RF data of the waveguide #4) using the RF data for shot number 105590. Although the wavenumber directions are consistent with the launched RF waves from the grill antenna, an evaluation of errors in the wavenumber measurement is needed.

8.3.6 Error of the Phase Difference

Supposing that the measured signal $V(t)$ consists of signals of interest $V_{\text{s}}(t)$ and noise $V_{\text{noise}}(t)$ as

$$V(t) = V_{\text{s}}(t) + V_{\text{noise}}(t), \tag{8.26}$$

the linearity of the discrete Fourier transformation leads to

$$
\begin{aligned}
C_n &= \frac{1}{N} \sum_{l=0}^{N-1} V\left(\frac{T}{N}l\right) e^{-i\frac{2\pi n}{N}l} \\
&= \frac{1}{N} \sum_{l=0}^{N-1} \left\{ V_{\text{s}}\left(\frac{T}{N}l\right) + V_{\text{noise}}\left(\frac{T}{N}l\right) \right\} e^{-i\frac{2\pi n}{N}l} \\
&= C_{n,\text{s}} + C_{n,\text{noise}}.
\end{aligned}
\tag{8.27}
$$

Equation (8.27) states

$$C_{n,\text{s}} = C_n - C_{n,\text{noise}}, \tag{8.28}$$

meaning that the objective Fourier complex amplitude $C_{n,\text{s}}$ is given by subtracting the noise Fourier complex amplitude $C_{n,\text{noise}}$ from the measured C_n. Although Eq. (8.28) requires both C_n and $C_{n,\text{noise}}$ must be known in one discharge to calculate $C_{n,\text{s}}$, this is difficult because they are mixed each other.
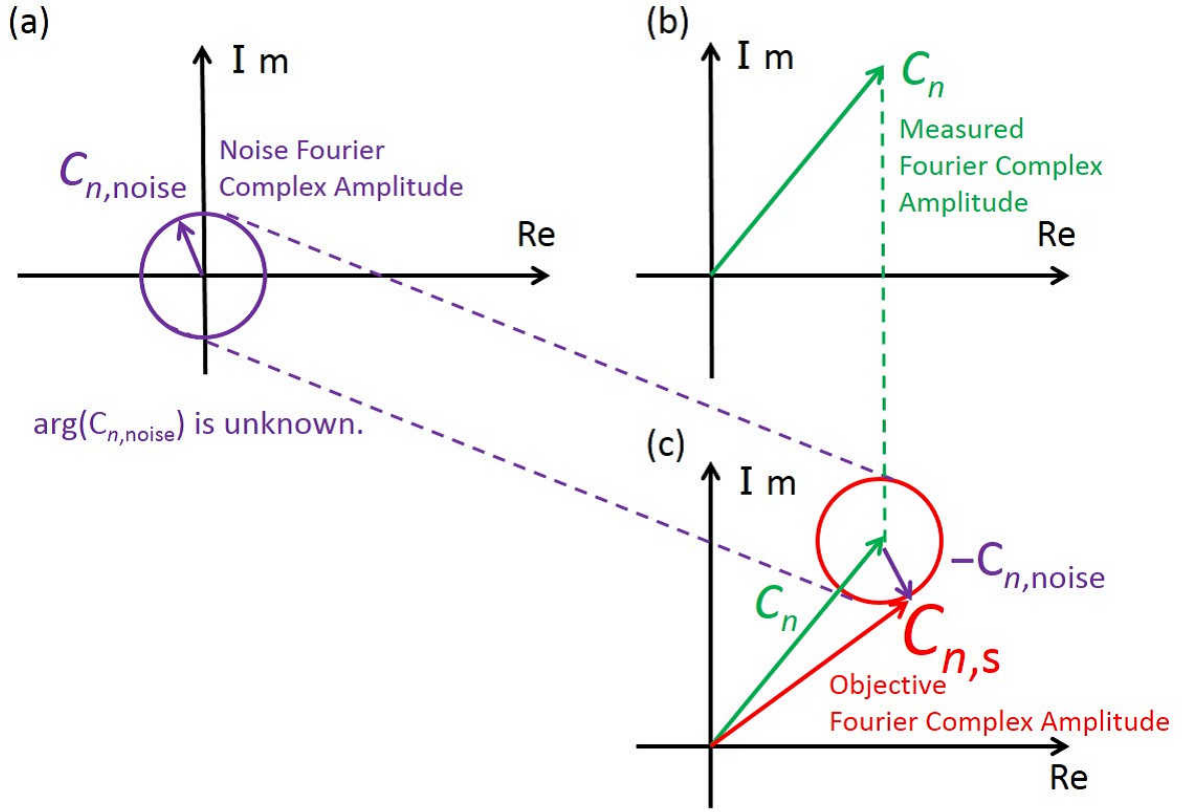
Figure 8.24: Evaluation of the objective Fourier complex amplitude $C_{n,\mathrm{s}}$. (a) Noise Fourier complex amplitude $C_{n,\mathrm{noise}}$. (b) Measured Fourier complex amplitude C_n. (c) Objective Fourier complex amplitude $C_{n,\mathrm{s}}$.

If $|C_{n,\mathrm{noise}}|$ is similar to or less in a plasma discharge than that in other discharges, for example in vacuum shots, it is possible to evaluate $C_{n,\mathrm{s}}$ by using C_n from a plasma discharge and $C_{n,\mathrm{noise}}$ from another shot. This situation is shown schematically in Fig. 8.24 for a situation with known $|C_{n,\mathrm{noise}}|$ and unknown $\arg(C_{n,\mathrm{noise}})$.

The phase information of $C_{n,\mathrm{noise}}$ is lost by being applied to another shot and only the absolute amplitude information $|C_{n,\mathrm{noise}}|$ is available. In this sense, $C_{n,\mathrm{noise}}$ is represented by a purple circle in Fig. 8.24 (a). This purple circle is subtracted by vector operation from the measured Fourier complex amplitude C_n in (b) and the resultant figure of $C_{n,\mathrm{s}}$ becomes also a circle shown as a red circle in (c). For the fixed C_n, the argument of $C_{n,\mathrm{s}}$ is evaluated by the absolute amplitude of $C_{n,\mathrm{noise}}$. Denoting the argument between the $C_{n,\mathrm{s}}$ and C_n by δ, which gives an error of the $\arg(C_{n,\mathrm{s}})$, $\tan\delta$ is derived according to Fig. 8.25 as

$$\tan\delta = \frac{|C_{n,\mathrm{noise}}|\sin\theta}{|C_n| + |C_{n,\mathrm{noise}}|\cos\theta} \equiv \gamma(\theta) \tag{8.29}$$

and δ is given as

$$\delta(\theta) = \arctan\left\{\gamma(\theta)\right\}. \tag{8.30}$$

Since $\arg(C_{n,\mathrm{noise}})$ is unknown, θ in Fig. 8.25 is assumed to be random and the mean value of δ is evaluated by a standard deviation σ_δ instead of a mean value over θ because the mean value of δ over
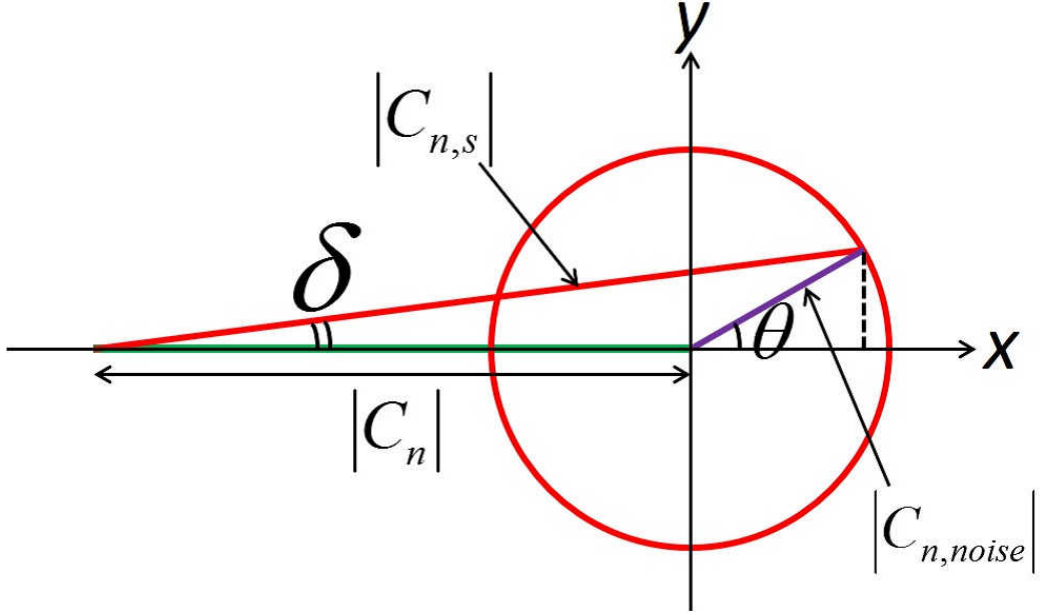
Figure 8.25: Argument δ between $C_{n,\mathrm{s}}$ and C_n.

θ is zero. The variance V_δ of δ is given and numerically calculated as

$$
\begin{aligned}
V_\delta &= \frac{1}{2\pi} \int_0^{2\pi} \{\delta(\theta)\}^2 \, d\theta = \frac{1}{2\pi} \sum_{l=0}^{N-1} \left\{ \delta\left(\frac{2\pi}{N}l\right) \right\}^2 \cdot \frac{2\pi}{N} \\
&= \frac{1}{N} \sum_{l=0}^{N-1} \left\{ \arctan\left[\gamma\left(\frac{2\pi}{N}l\right)\right] \right\}^2
\end{aligned}
\tag{8.31}
$$

and σ_δ is then calculated as

$$
\sigma_\delta = \sqrt{V_\delta} = \sqrt{\frac{1}{N} \sum_{l=0}^{N-1} \left\{ \arctan\left[\gamma\left(\frac{2\pi}{N}l\right)\right] \right\}^2}.
\tag{8.32}
$$

For example, for $|C_n| : |C_{n,\mathrm{noise}}| = 4 : 1$ and $N = 1000$, $\sigma_\delta = 10.2°$ is calculated. This value is about 70 % of the maximum value $\delta_{\max} = \arcsin\left(\frac{|C_{n,\mathrm{noise}}|}{|C_n|}\right) = 14.5°$.

Using σ_δ, arguments of objective signals of electrode 1 and 2 are evaluated as

$$
\begin{aligned}
\arg C_{n,\mathrm{s},1} &= \arg C_{n,1} \pm \sigma_{\delta,1} \\
\arg C_{n,\mathrm{s},2} &= \arg C_{n,2} \pm \sigma_{\delta,2},
\end{aligned}
\tag{8.33}
\tag{8.34}
$$

and the objective wavenumber $\boldsymbol{k}_\mathrm{s}$ is evaluated using $\sigma_{\delta,1}$ and $\sigma_{\delta,2}$ according to Eq. (8.23) as

$$
\begin{aligned}
\boldsymbol{k}_{n,\mathrm{s}} \cdot \boldsymbol{r}_{1\to2} &= -(\arg C_{n,\mathrm{s},2} - \arg C_{n,\mathrm{s},1}) \\
&= -(\arg C_{n,2} - \arg C_{n,1}) \pm \sqrt{\sigma_{\delta,1}^2 + \sigma_{\delta,2}^2} \\
&= -\Delta\phi_{n,21} \pm \sqrt{\sigma_{\delta,1}^2 + \sigma_{\delta,2}^2},
\end{aligned}
\tag{8.35}
$$

153

where no correlation between $\sigma_{\delta,1}$ and $\sigma_{\delta,2}$ is assumed and Eq. (8.13) is used. As in the derivation of Eq. (8.25) from Eq. (8.24) in the ensemble averaging, Eq. (8.35) is rewritten by replacing $\Delta\phi_{n,21}$ to $\Delta\theta_{n,21} = \arg\left(S_{n,21}\right)$ and the objective wavenumber $< \boldsymbol{k}_{n,\mathrm{s}} >$ is given as

$$< \boldsymbol{k}_{n,\mathrm{s}} > \cdot \boldsymbol{r}_{1\to 2} = -\Delta\theta_{n,21} \pm \sqrt{< \sigma_{\delta,1} >^2 + < \sigma_{\delta,2} >^2}, \tag{8.36}$$

where $< \sigma_{\delta,1} >$ and $< \sigma_{\delta,2} >$ are ensemble averaged $\sigma_{\delta,1}$ and $\sigma_{\delta,2}$ over the seven sub-intervals.

In this thesis, the slow wave (LHW) signal is the objective one and the fast wave and the electromagnetic wave are treated as noise signals. Whether the way of evaluating the phase error described above is applicable or not depends on types of propagating waves in the plasma discharge.

8.4   Wavenumber Measurement

Wavenumber measurements were performed by a shot-to-shot angular scan of the probe assembly in reproducible plasmas represented by shot number 105498. From rotational symmetry, the phase difference of electrode 2 relative to electrode 1 at the probe angle of 0 degree should be the same as the phase difference of electrode 1 relative to electrode 3 at the probe angle of 90 degrees in reproducible plasmas. This can be used to validate the wavenumber measurement. The magnetic field amplitude and polarization can also be determined from an angular scan of the probe assembly using the magnetic probe (electrode 4), which can be used to identify the wave type of the measured wave. The wave type identification is accomplished by comparing the maximum amplitude of the magnetic probe signal with the signal amplitudes measured by the high impedance Langmuir probe units (electrodes 1 through 3). The ratio of $|\boldsymbol{E}|$ to $|c\boldsymbol{B}|$ can be compared to that obtained for the electromagnetic wave using the coaxial calibrator, shown in Fig. 7.17.

In the representative plasma discharge (shot number 105498), the magnetic field is nearly purely toroidal (horizontal). The probe assembly was inclined at 15 degrees from the horizontal direction to prevent shadowing of the probe electrode from plasma flow along the magnetic field by a neighboring probe electrode. The angular scan consisted of probe angles 15 degrees, 105 degrees, 195 degrees, 285 degrees, and an intermediate probe angle of 60 degrees as shown in Fig. 8.26, in which positions of electrodes and the magnetic probe orientation are also shown.

At each probe angle, measurements were conducted for one vacuum shot and three plasma shots. The plasma discharges were highly reproducible. The measured signals were processed as described in Section 8.3.

8.4.1   Magnetic Probe Signal Amplitude and Polarization

The amplitude and the polarization of the RF magnetic field can be determined from an angular scan of the magnetic probe. Figure 8.27 shows the coordinate system for the magnetic probe, with definitions of the magnetic field $\boldsymbol{B}$ and the unit vector $\boldsymbol{n}$ normal to the loop surface of the magnetic probe. The angle θ in Fig. 8.27 is the same as the orientation angle of the probe assembly, and the angle δ is the phase difference between the y- and z-components of the magnetic field, which determines the polarization of the magnetic field in the y-z plane. Using the vector $\boldsymbol{S} = S\boldsymbol{n}$, in which S is the area of the magnetic loop, the magnetic flux Φ threading the magnetic loop is expressed as

$$\Phi \equiv \boldsymbol{B} \cdot \boldsymbol{S} = S\left\{-B_{z0} \sin\theta \cos\left(\omega t\right) + B_{y0} \cos\theta \cos\left(\omega t + \delta\right)\right\}. \tag{8.37}$$

Note that the radial component of the magnetic field B_x is not measured by the magnetic probe. The induced voltage V on the magnetic loop is given by

$$
\begin{aligned}
V = -\frac{d\Phi}{dt} &= -\omega S\left\{B_{z0} \sin\theta \sin\left(\omega t\right) - B_{y0} \cos\theta \sin\left(\omega t + \delta\right)\right\} \\
&= -\omega S\left\{\left[B_{z0} \sin\theta - B_{y0} \cos\theta \cos\delta\right] \sin\left(\omega t\right) - \left[B_{y0} \cos\theta \sin\delta\right] \cos\left(\omega t\right)\right\} \\
&= -\omega S\sqrt{B_{z0}^2 \sin^2\theta - B_{z0}B_{y0} \cos\delta \sin 2\theta + B_{y0}^2 \cos^2\theta} \sin\left(\omega t + \alpha\right), \tag{8.38}
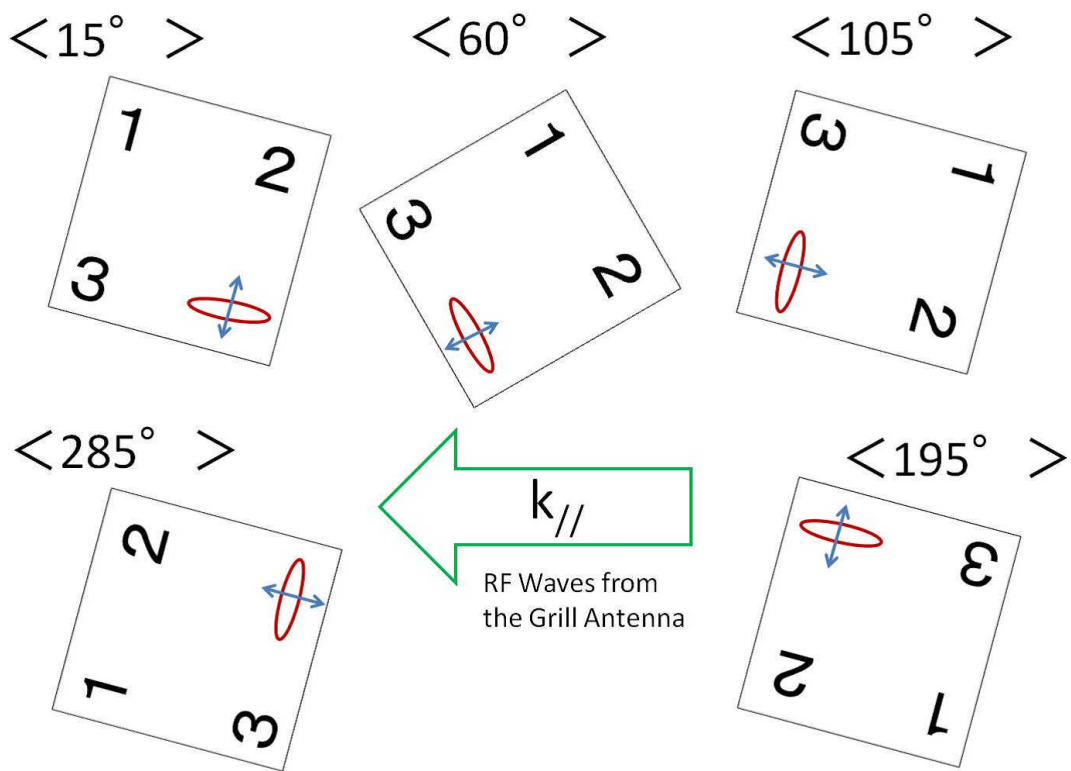\end{aligned}
$$

154

Figure 8.26: Probe angles, positions of electrodes, and the magnetic probe orientation.
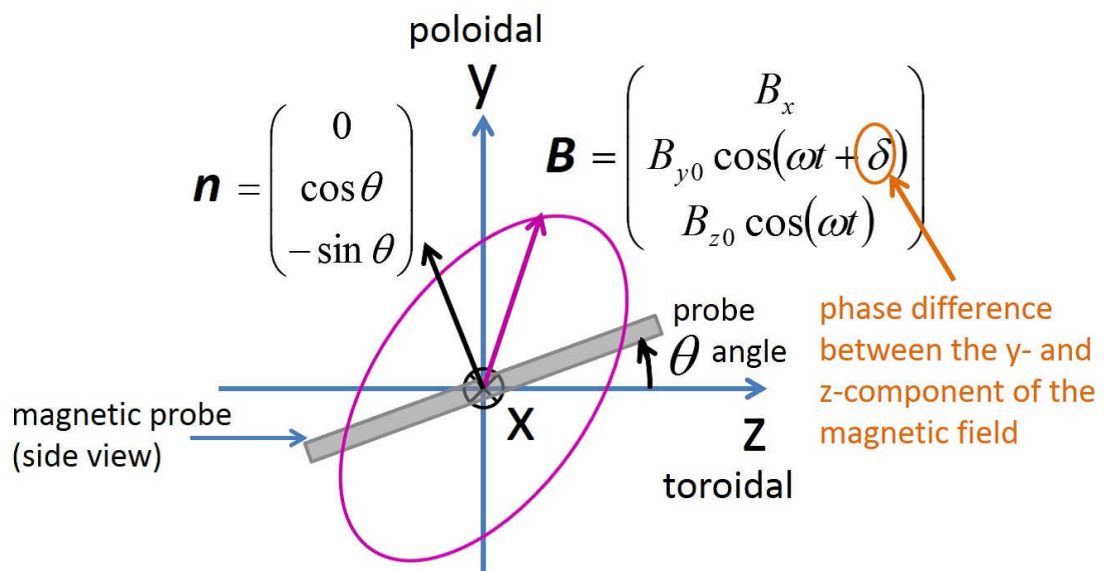

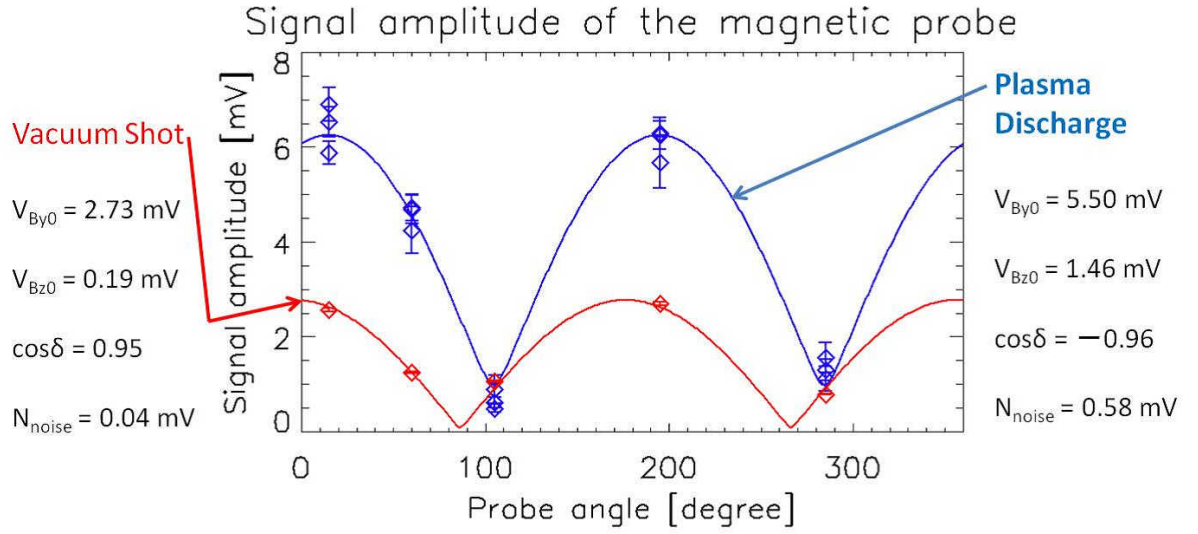Figure 8.27: Coordinate system for magnetic probe signal analysis.

Figure 8.28: Angular dependences of magnetic probe signals and fitted curves for plasma shots (blue points and solid line) and vacuum shots (red points and solid line).

where α is a constant which depends on both θ and δ. Since $\omega S B_{z0}$ and $\omega S B_{y0}$ have the dimension of voltage, they are denoted by $\omega S B_{z0} = V_{B_{z0}}$ and $\omega S B_{y0} = V_{B_{y0}}$. Using the noise amplitude N_{noise}, the absolute value of the output voltage of the magnetic probe is expressed as

$$|V| = \sqrt{V_{B_{z0}}^2 \sin^2 \theta - V_{B_{z0}} V_{B_{y0}} \cos \delta \sin 2\theta + V_{B_{y0}}^2 \cos^2 \theta} + N_{\mathrm{noise}} \tag{8.39}$$

and this equation is used to fit the angular dependence of the magnetic probe signal to derive the amplitude of the RF magnetic field for discharges represented by shot number 105498.

Figure 8.28 shows the angular dependence of the magnetic probe signal. The data points in blue and red represent data for plasma shots and vacuum shots, respectively. Error bars represent the standard deviation of the signal amplitude over seven sub-intervals for each shot. It is obvious that the RF magnetic field amplitude is larger for plasma shots than for vacuum shots. The blue and red curves are fits to data points by Eq. (8.39). The fitted value of $\cos \delta$ for plasma shots is -0.96, which is nearly -1. When $\cos \delta = -1$ holds, $\delta = \pi + 2n\pi$ where n is an integer, and the y- and z-components of the magnetic field B_y and B_z become

$$\begin{cases} B_y = B_{y0} \cos (\omega t + \delta) = -B_{y0} \cos (\omega t) \\ B_z = B_{z0} \cos (\omega t), \end{cases}$$

yielding

$$B_y = -\frac{B_{y0}}{B_{z0}} B_z. \tag{8.40}$$

Equation (8.40) means that the magnetic field is linearly polarized in the y-z plane. Defining the polarization angle from the z-axis to be β and using the fitted values $V_{B_{y0}} = 5.50\,\mathrm{mV}$ and $V_{B_{z0}} = 1.46\,\mathrm{mV}$, β is given as

$$\begin{aligned} \beta &= \arctan \left(-\frac{B_{y0}}{B_{z0}} \right) = \arctan \left(-\frac{V_{B_{y0}}}{V_{B_{z0}}} \right) = \arctan (-3.77) \\ &= 104.9^\circ. \end{aligned} \tag{8.41}$$
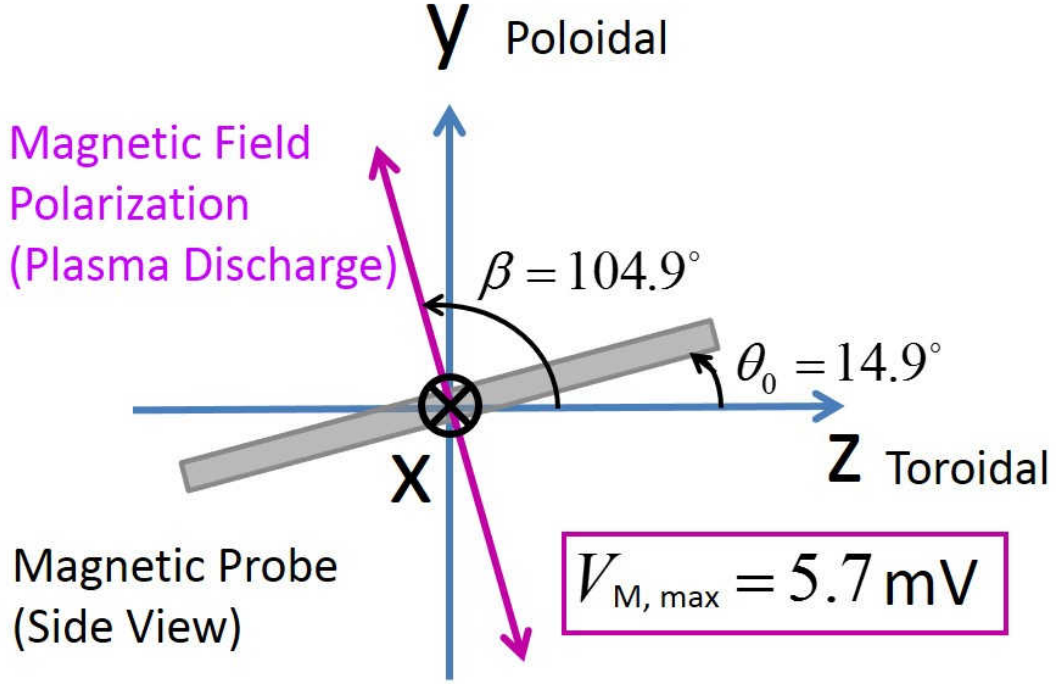
Figure 8.29: Magnetic field polarization and the magnetic probe orientation at the maximum signal amplitude.

$|V|$ is calculated for $\cos \delta = -1$ to be

$$
\begin{aligned}
|V| &= \sqrt{V_{B_{z0}}^2 \sin^2 \theta - V_{B_{z0}} V_{B_{y0}} \cos \delta \sin 2\theta + V_{B_{y0}}^2 \cos^2 \theta} + N_{\text{noise}} \\
&= \sqrt{V_{B_{z0}}^2 \sin^2 \theta + 2 V_{B_{z0}} V_{B_{y0}} \sin \theta \cos \theta + V_{B_{y0}}^2 \cos^2 \theta} + N_{\text{noise}} \\
&= |V_{B_{z0}} \sin \theta + V_{B_{y0}} \cos \theta| + N_{\text{noise}} \\
&= \sqrt{V_{B_{z0}}^2 + V_{B_{y0}}^2} |\cos(\theta - \theta_0)| + N_{\text{noise}},
\end{aligned}
\tag{8.42}
$$

where

$$
\begin{aligned}
\theta_0 &= \arctan\left(\frac{V_{B_{z0}}}{V_{B_{y0}}}\right) = \arctan(0.265) \\
&= 14.9°
\end{aligned}
\tag{8.43}
$$

and the maximum amplitude of the magnetic probe signal $V_{\text{M,max}}$ is given as

$$
V_{\text{M,max}} = \sqrt{V_{B_{z0}}^2 + V_{B_{y0}}^2} = \sqrt{1.46^2 + 5.50^2} = 5.7 \, \text{mV}.
\tag{8.44}
$$

Figure 8.29 summarizes the result of angular scan. The polarization of the magnetic field is linear and is nearly in the poloidal (y) direction due to the dominance of the poloidal magnetic field, which is consistent with the dominance of cB_y in the field amplitude calculation for plasma densities of $4 \times 10^{16} \, \text{m}^{-3}$ or less in Fig. 2.3. The estimated maximum amplitude of the magnetic probe signal $V_{\text{M,max}} = 5.7 \, \text{mV}$ in the plasma is used to identify the type of wave measured by the probe assembly.

157

8.4.2 Wave Type Identification

There are three types of wave that can be detected by the probe assembly inside the TST-2 vacuum vessel: The slow wave (the lower hybrid wave), the fast wave, and the electromagnetic wave. This is because the slow wave and the fast wave can exist in start-up plasmas (seen as cold plasmas) as propagative waves as two real solutions of the cold plasma dispersion relation. Solutions of the cold plasma dispersion relation are limited to the slow wave and the fast wave. The electromagnetic wave can also exist inside the TST-2 vacuum vessel because the wave launched from the grill antenna initially takes the form of the electromagnetic wave, and not all of the launched wave are absorbed by the plasma. This thesis aims at measuring the lower hybrid wave. The signal amplitudes measured by the high impedance Langmuir probe units (electrodes 1 through 3) are compared with the signal amplitude measured by the magnetic probe (electrode 4) to identify which type of wave is measured by the probe assembly.

Since the signal amplitudes measured by electrodes 1 through 3 were at most 0.3 times that measured by electrode 4 for the electromagnetic wave as shown in Fig. 7.17, the maximum amplitude of the magnetic probe signal $V_{\mathrm{M,max}} = 5.7 \, \mathrm{mV}$ measured in the plasma should give signal amplitudes due to the electromagnetic wave on electrodes 1 through 3 of equal to or less than the maximum value $V_{\mathrm{EM,max}}$ defined as

$$V_{\mathrm{EM,max}} \equiv 0.3 \times V_{\mathrm{M,max}} = 0.3 \times 5.7 \, \mathrm{mV} = 1.71 \, \mathrm{mV}. \tag{8.45}$$

Figure 8.30 shows the signal amplitudes measured by electrodes 1 through 4 for the five probe angles. For each graph, signal amplitudes measured for one vacuum shot and three plasma shots are plotted, with the maximum EM amplitude $V_{\mathrm{EM,max}}$ level shown by the orange line. The error bars for each plot represent the standard deviation of signal amplitude over seven sub-intervals for each shot.

It is found that the signal amplitudes measured by electrodes 1 through 3, in the yellow shaded regions in Fig. 8.30, exceeds the maximum EM amplitude $V_{\mathrm{EM,max}} = 1.71 \, \mathrm{mV}$ by a factor of two or larger at all probe angles. This means that the signal amplitudes measured by electrodes 1 through 3 cannot be explained by the electromagnetic wave.

The fast wave cannot explain the signal amplitudes measured by electrodes 1 through 3 either because the fast wave has a even weaker electric field amplitude for a given magnetic field amplitude than the electromagnetic wave, according to Table 2.1. Since the plasma density is measured to be $4 \times 10^{16} \, \mathrm{m}^{-3}$ at $R = 570 \, \mathrm{mm}$ and is even lower at the probe surface position $R = 590 \, \mathrm{mm}$, the fast wave is evanescent at the probe surface according to Fig. 2.2. Figure 8.31 shows $n_\perp^2$ for the fast wave in the upper frame and the imaginary part of the perpendicular wavenumber for the fast wave in the lower frame for $B_{\mathrm{toroidal}} = 0.06 \, \mathrm{T}$, which is the toroidal magnetic field strength at the probe surface. The perpendicular wavenumber $k_\perp$ is expressed as

$$k_\perp = k_{\perp,\mathrm{r}} + i k_{\perp,\mathrm{i}}, \tag{8.46}$$

where $k_{\perp,\mathrm{r}}$ and $k_{\perp,\mathrm{i}}$ are real, and $k_{\perp,\mathrm{i}} > 0$ at the plasma density of $4 \times 10^{16} \, \mathrm{m}^{-3}$ or lower. The wave amplitude varies as $\exp(i k_\perp r)$ in the perpendicular direction,

$$\exp(i k_\perp r) = \exp(-k_{\perp,\mathrm{i}} r) \cdot \exp(i k_{\perp,\mathrm{r}} r) \tag{8.47}$$

and the spatial decay length L_{d} is given as

$$L_{\mathrm{d}} = \frac{1}{k_{\perp,\mathrm{i}}}. \tag{8.48}$$

From Fig. 8.31, $k_{\perp,\mathrm{i}}$ is $37.5 \, \mathrm{m}^{-1}$ at plasma densities of $4 \times 10^{16} \, \mathrm{m}^{-3}$ or lower, giving $L_{\mathrm{d}} = 26.7 \, \mathrm{mm}$. This is small compared to the distance of order $100 \, \mathrm{mm}$ or longer from the probe surface to the high density region where the density is of order $10^{18} \, \mathrm{m}^{-3}$ and the fast wave can propagate. Thus, the fast wave is negligible around the probe location.

Neither the electromagnetic wave nor the fast wave can explain the measured signal amplitudes of electrodes 1 through 3 for the measured amplitude of electrode 4 and therefore it is concluded that the signals measured by the probe assembly are dominated by the slow wave.
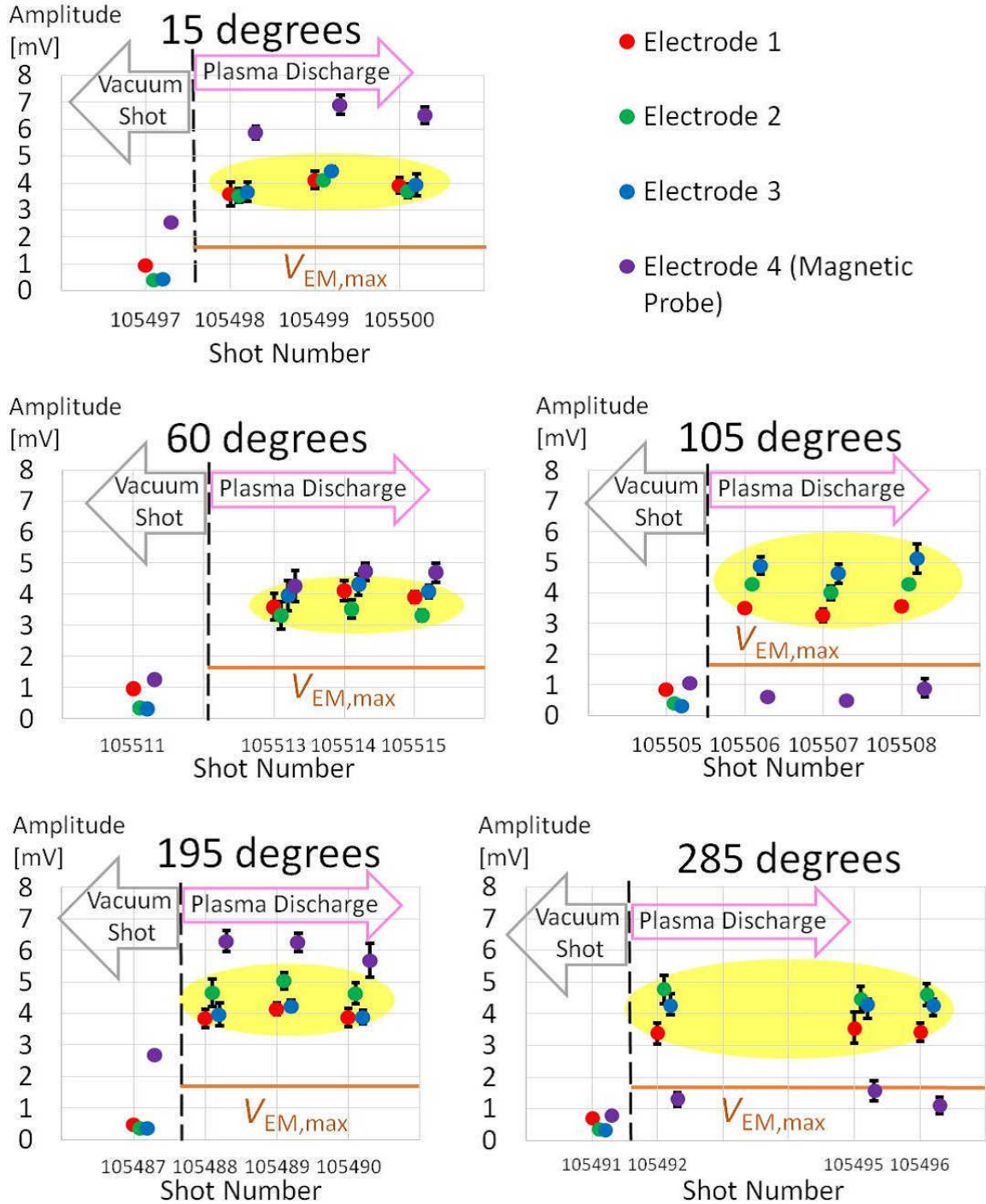
Figure 8.30: Signal amplitudes measured by electrodes 1 through 4 for one vacuum shot and three plasma shots for the five probe angles, compared with $V_{\text{EM,max}} = 1.71\,\text{mV}$.
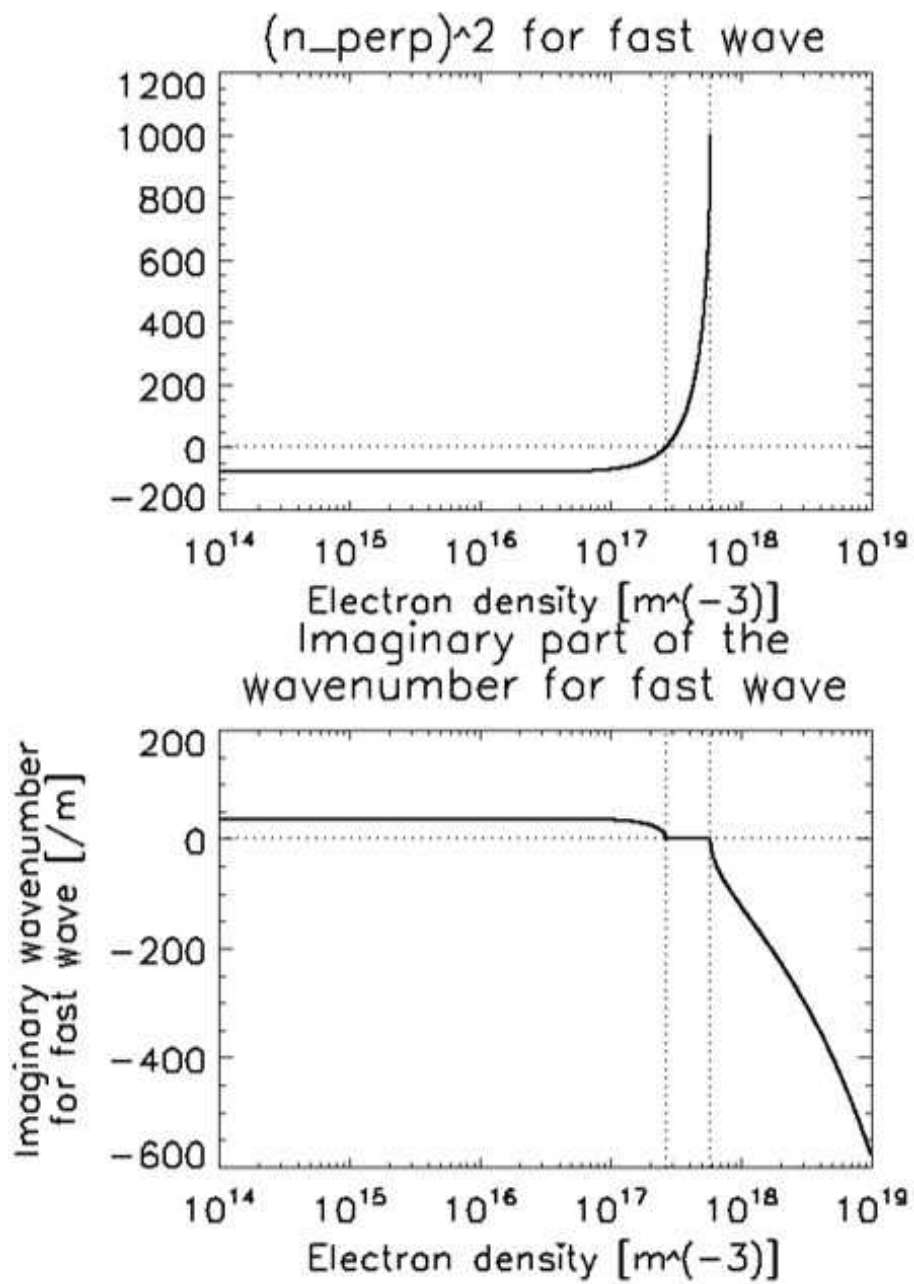
159

Figure 8.31: $n_\perp^2$ and the imaginary part of the perpendicular wavenumber of the fast wave.

8.4.3 Phase Difference and Wavenumber Measured by the Probe Assembly

Since the signals measured by the probe assembly are dominated by the slow wave, the phase difference between different electrodes is considered to reflect the wavelength of the slow wave. Figure 8.32 shows the phase differences of electrodes 2 and 3 with respect to electrode 1 for one vacuum shot and three plasma shots for five probe angles (signal amplitudes are shown in Fig. 8.30).

Estimation of Error in the Phase Difference

Error bars in Fig. 8.32 are determined according to the procedure described in Subsection 8.3.5 using the signal amplitudes shown in Fig. 8.30. As an estimate of the noise signal $V_{\mathrm{noise}}(t)$ for plasma shots, signals measured in vacuum shots, which reflect electromagnetic waves both inside and outside the TST-2 vacuum vessel, are used. Although the fast wave is also a candidate for $V_{\mathrm{noise}}(t)$, it is not included in $V_{\mathrm{noise}}(t)$ since it is negligible around the probe location as shown in Subsection 8.4.2. The electromagnetic wave strength inside the TST-2 vacuum vessel in plasma shots is unknown but it is reasonable to assume that it is smaller than in vacuum shots, because some of the electromagnetic wave energy is absorbed by the plasma, and the wave energy is distributed in the slow wave and the fast wave in addition to the electromagnetic wave. The electromagnetic wave strength outside the TST-2 vacuum vessel in plasma shots is also the same as or smaller than in vacuum shots (see the "Noise Reference" in Fig. 8.17). In this way, the noise signals $V_{\mathrm{noise}}(t)$ for electrodes 1 through 3 in plasma shots are smaller than the noise signals measured in vacuum shots. Therefore, the error in the phase difference for plasma shots is limited by that evaluated using signals measured in vacuum shots for $V_{\mathrm{noise}}(t)$.

For example, the error in the phase difference of electrode 2 with respect to electrode 1 for shot number 105498 is calculated as follows. The phase error is given by $\sqrt{<\sigma_{\delta,1}>^2 + <\sigma_{\delta,2}>^2}$ in Eq. (8.36). Here, $<\sigma_{\delta,1}>$ and $<\sigma_{\delta,2}>$ are $\langle\sigma_\delta\rangle$ for signals measured by electrodes 1 and 2, respectively. Although $\langle\sigma_\delta\rangle$ is the ensemble averaged σ_δ over seven sub-intervals, it is approximated to be given from Eqs. (8.32) and (8.29) using the ensemble averaged signal amplitudes $\langle 2|C_n|\rangle$ and $\langle 2|C_{n,\mathrm{noise}}|\rangle$ as

$$\langle\sigma_\delta\rangle = \left\langle\sqrt{V_\delta}\right\rangle = \left\langle\sqrt{\frac{1}{N}\sum_{l=0}^{N-1}\left\{\arctan\left[\gamma\left(\frac{2\pi}{N}l\right)\right]\right\}^2}\right\rangle \approx \sqrt{\frac{1}{N}\sum_{l=0}^{N-1}\left\{\arctan\left[\left\langle\gamma\left(\frac{2\pi}{N}l\right)\right\rangle\right]\right\}^2}, \quad (8.49)$$

where $\left\langle\gamma\left(\frac{2\pi}{N}l\right)\right\rangle = \langle\gamma(\theta)\rangle$ is defined using the ensemble averaged Fourier amplitudes $\langle|C_n|\rangle$ and $\langle|C_{n,\mathrm{noise}}|\rangle$ as

$$\langle\gamma(\theta)\rangle \equiv \frac{\langle|C_{n,\mathrm{noise}}|\rangle\sin\theta}{\langle|C_n|\rangle + \langle|C_{n,\mathrm{noise}}|\rangle\cos\theta} = \frac{\langle 2|C_{n,\mathrm{noise}}|\rangle\sin\theta}{\langle 2|C_n|\rangle + \langle 2|C_{n,\mathrm{noise}}|\rangle\cos\theta}. \quad (8.50)$$

This approximation for $\langle\sigma_\delta\rangle$ is valid due to the modest stationarity of signals during the data acquisition time interval of $55\,\mathrm{ms}$ to $63\,\mathrm{ms}$ as shown representatively in Fig. 8.18. In Eq. (8.50), $\langle 2|C_n|\rangle$ is the ensemble averaged signal amplitude over seven sub-intervals and is taken from the plasma shot number 105498. $\langle 2|C_{n,\mathrm{noise}}|\rangle$ represents the ensemble averaged noise signal amplitude over seven sub-intervals and is taken from the vacuum shot number 105497. Explicitly, the values of $\langle 2|C_n|\rangle$ and $\langle 2|C_{n,\mathrm{noise}}|\rangle$ for electrode 1, denoted by $\langle 2|C_{n,1}|\rangle$ and $\langle 2|C_{n,\mathrm{noise},1}|\rangle$, are obtained from Fig. 8.30 as

$$\begin{cases} \langle 2|C_{n,1}|\rangle = 3.59\,\mathrm{mV}, \\ \langle 2|C_{n,\mathrm{noise},1}|\rangle = 0.95\,\mathrm{mV}, \end{cases}$$

which lead to $<\sigma_{\delta,1}>$ using Eqs. (8.49) and (8.50) with $N = 1000$ as

$$\langle\sigma_{\delta,1}\rangle = 11.0\,\mathrm{degrees}.$$

For electrode 2,

$$\begin{cases} \langle 2|C_{n,2}|\rangle = 3.53\,\mathrm{mV}, \\ \langle 2|C_{n,\mathrm{noise},2}|\rangle = 0.40\,\mathrm{mV}, \end{cases}$$
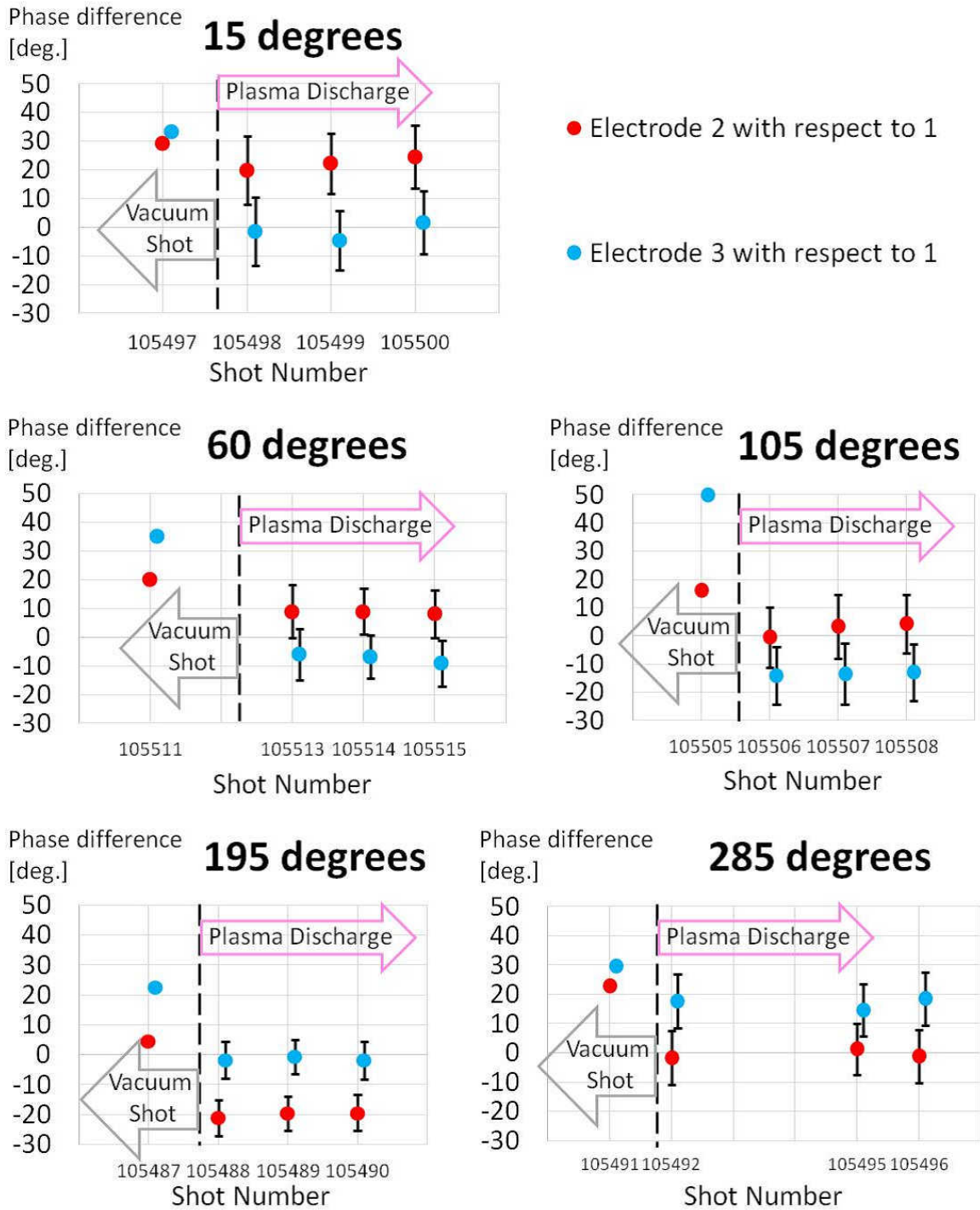
Figure 8.32: Phase differences of electrodes 2 and 3 with respect to electrode 1 for one vacuum shot and three plasma shots for five probe angles.

and
$$\langle \sigma_{\delta,2} \rangle = 4.6 \,\text{degrees}.$$

$\langle \sigma_{\delta,1} \rangle$ and $\langle \sigma_{\delta,2} \rangle$ are combined to give the error in the phase difference of electrode 2 with respect to 1 as

$$\sqrt{<\sigma_{\delta,1}>^2 + <\sigma_{\delta,2}>^2} = \sqrt{11.0^2 + 4.6^2} = 11.9 \,\text{degrees}. \tag{8.51}$$

This value is used for the error bar for the phase difference of electrode 2 with respect to electrode 1 plotted by the red dot for shot number 105498 in Fig. 8.32.

Determination of the Wavenumber along the Electrode Array

The phase difference and its error are translated into the wavenumber and its error. Since the ensemble averaged phase difference over seven sub-intervals is calculated to be $\Delta\theta_{n,21} = 19.8$ degrees for the plasma shot number 105498, Eqs. (8.36) and (8.51) yield

$$< \boldsymbol{k}_{n,\text{s}} > \cdot \boldsymbol{r}_{1\to 2} = -19.8 \pm 11.9 \,\text{degrees}. \tag{8.52}$$

Defining the projected wavenumber component along the line from electrode 1 to electrode 2 as $\langle k_{n,\text{n},\text{p}} \rangle_{1\to 2}$,

$$< \boldsymbol{k}_{n,\text{s}} > \cdot \boldsymbol{r}_{1\to 2} = \langle k_{n,\text{n},\text{p}} \rangle_{1\to 2} |\boldsymbol{r}_{1\to 2}|. \tag{8.53}$$

Numerically, using Eq. (8.52) gives

$$< k_{n,\text{n},\text{p}} >_{1\to 2} = \frac{-19.8 \pm 11.9}{|\boldsymbol{r}_{1\to 2}|} \times \frac{\pi}{180} = -24.3 \pm 14.6 \,\text{m}^{-1}, \tag{8.54}$$

where $|\boldsymbol{r}_{1\to 2}| = 14.2 \,\text{mm} = 1.42 \times 10^{-2} \,\text{m}$. Since $\langle k_{n,\text{n},\text{p}} \rangle_{1\to 2}$ is negative, the projected component of $< \boldsymbol{k}_{n,\text{s}} >$ is in the direction from electrode 2 to electrode 1.

In this way, phase differences of electrode 2 with respect to electrode 1 (red), and of electrode 3 with respect to electrode 1 (blue) shown in Fig. 8.32 are translated into wavenumber components and their directions as shown in Fig. 8.33. The wavenumber and its error for each probe angle are averaged over three plasma shots.

Toroidal Wavenumber and Poloidal Wavenumber

The toroidal wavenumber k_{tor} and the poloidal wavenumber k_{pol} are derived by vector operation from Fig. 8.33. The positive toroidal direction is defined leftward and the positive poloidal direction is defined upward in Fig. 8.33. For the probe angle of 15 degrees, for example, k_{tor} and k_{pol} are calculated as

$$\begin{aligned} k_{\text{tor}} &= -\{(27.3 \pm 13.6)\cos 165° + (1.8 \pm 13.6)\cos 255°\} \simeq 26.8 \pm \sqrt{(13.6\cos 165°)^2 + (13.6\cos 255°)^2} \\ &= 26.8 \pm 13.6 \,\text{m}^{-1} \end{aligned} \tag{8.55}$$

and

$$\begin{aligned} k_{\text{pol}} &= (27.3 \pm 13.6)\sin 165° + (1.8 \pm 13.6)\sin 255° \simeq 5.3 \pm \sqrt{(13.6\sin 165°)^2 + (13.6\sin 255°)^2} \\ &= 5.3 \pm 13.6 \,\text{m}^{-1}. \end{aligned} \tag{8.56}$$

It is assumed that the errors in wavenumbers in the two directions defined by electrodes 1 and 2, and by electrodes 1 and 3 are uncorrelated. Similar calculations for other probe angles give independent measurements of k_{tor} and k_{pol}, as summarized in Fig 8.34.

The measured values of the toroidal wavenumber vary from $12.8 \pm 10.3 \,\text{m}^{-1}$ to $26.8 \pm 13.6 \,\text{m}^{-1}$, and its direction is consistent with that of the main lobe of the wave launched from the grill antenna. The
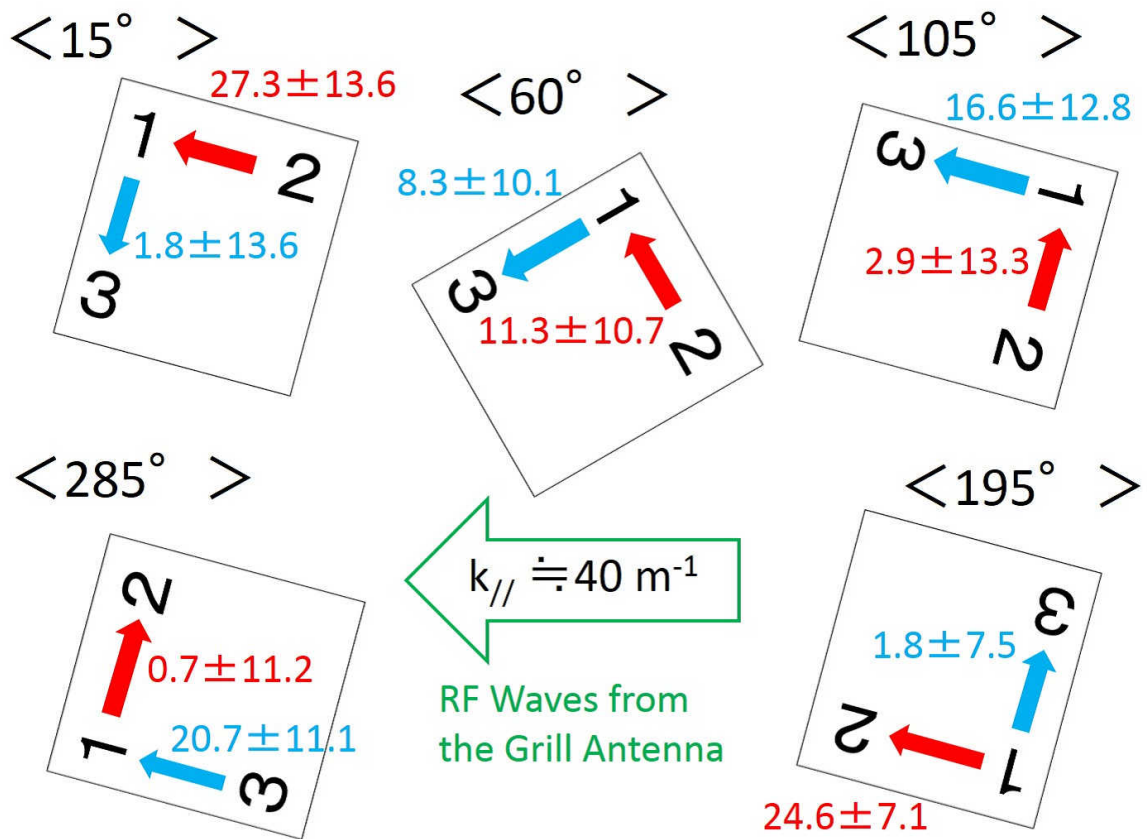
Figure 8.33: Measured wavenumber and direction along the high impedance Langmuir probe array. Units are m^{-1}.
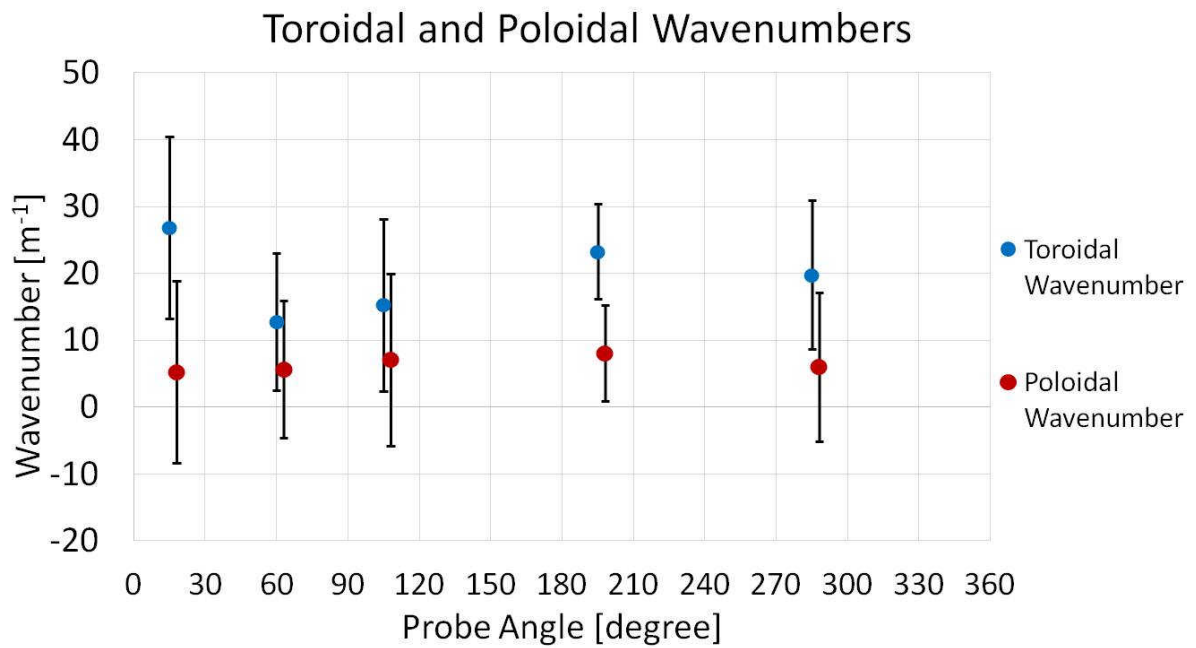
Figure 8.34: Measured toroidal and poloidal wavenumbers at 200 MHz.

average toroidal wavenumber and its error over the five probe angles are $19.6 \pm 11.0\,\mathrm{m}^{-1}$. This value is smaller than the main lobe of the launched wavenumber, $40\,\mathrm{m}^{-1}$. The average poloidal wavenumber and its error are $6.4 \pm 11.0\,\mathrm{m}^{-1}$. Although the error encompasses both positive and negative regions, the median value is positive. This direction is the direction of the magnetic field created by the plasma current.

Chapter 9

Discussion

The measured toroidal wavenumber $k_\parallel = 19.6 \pm 11.0\,\text{m}^{-1}$ is smaller by a factor of two compared to the main wavenumber component of the wave launched by the grill antenna, $k_\parallel = 40\,\text{m}^{-1}$. This chapter is devoted to the discussion of physical mechanisms which might be responsible for this experimental result. The discussion consists of three parts. In the first part, for wave energy damping during propagation inside the plasma is discussed. The simplest case of a spatially uniform cold plasma with a Maxwellian electron distribution function is treated as an analytically tractable case and is used as a basis for considering more complicated effects such as a non-Maxwellian electron distribution function. In the second part, $k_\parallel$ 'upshift' and 'downshift' due to the effect of propagation in toroidal geometry are discussed. In the third part, the apparent phase difference measured by the probe assembly in the presence of two different wavenumbers is discussed.

From now on and throughout Chapter 9, the sign of $k_\parallel$ is defined with respect to the direction of the toroidal magnetic field (z-axis). With this definition, and referring to Fig. 8.1, the measured toroidal wavenumber of $k_\parallel = 19.6 \pm 11.0\,\text{m}^{-1}$ and the launched wavenumber of $k_\parallel = 40\,\text{m}^{-1}$ are labeled $k_\parallel = -19.6 \pm 11.0\,\text{m}^{-1}$ and $k_\parallel = -40\,\text{m}^{-1}$, respectively.

9.1 Group Velocity and Wave Energy Damping for Maxwellian Distribution Function

If a wave were damped before reaching the probe assembly, the wave would not be measured. Only surviving waves reaching the probe are detected. Figure 9.1 shows the launched parallel wavenumber ($k_\parallel$) spectrum for a representative shot number 105498 (already shown in Fig. 8.9), and the parallel refractive index ($n_\parallel$) spectrum converted from the $k_\parallel$ spectrum using the relationship $n_\parallel = \frac{c}{\omega}k_\parallel$. Because of the definition of the sign of $k_\parallel$ ($n_\parallel$) introduced in this chapter, the sign for the abscissa is opposite to that in Fig. 8.9. In this section, wave propagation and damping are treated under two assumptions, the plasma is cold and spatially uniform, and the electron velocity distribution function is Maxwellian. These assumptions enable analytic calculation of the group velocity and wave energy damping.

9.1.1 Group Velocity

The group velocity is calculated using Eq. (2.167) as

$$\boldsymbol{v}_{\text{g}} = -\frac{2c}{\frac{n_\perp^2\left[D^2 n^2 + (S-P)^2 n_\parallel^2\right]}{n^4} + \left(F n_\perp^2 + H n_\parallel^2\right)} \begin{pmatrix} S n_\perp \\ 0 \\ P n_\parallel \end{pmatrix}. \tag{9.1}$$
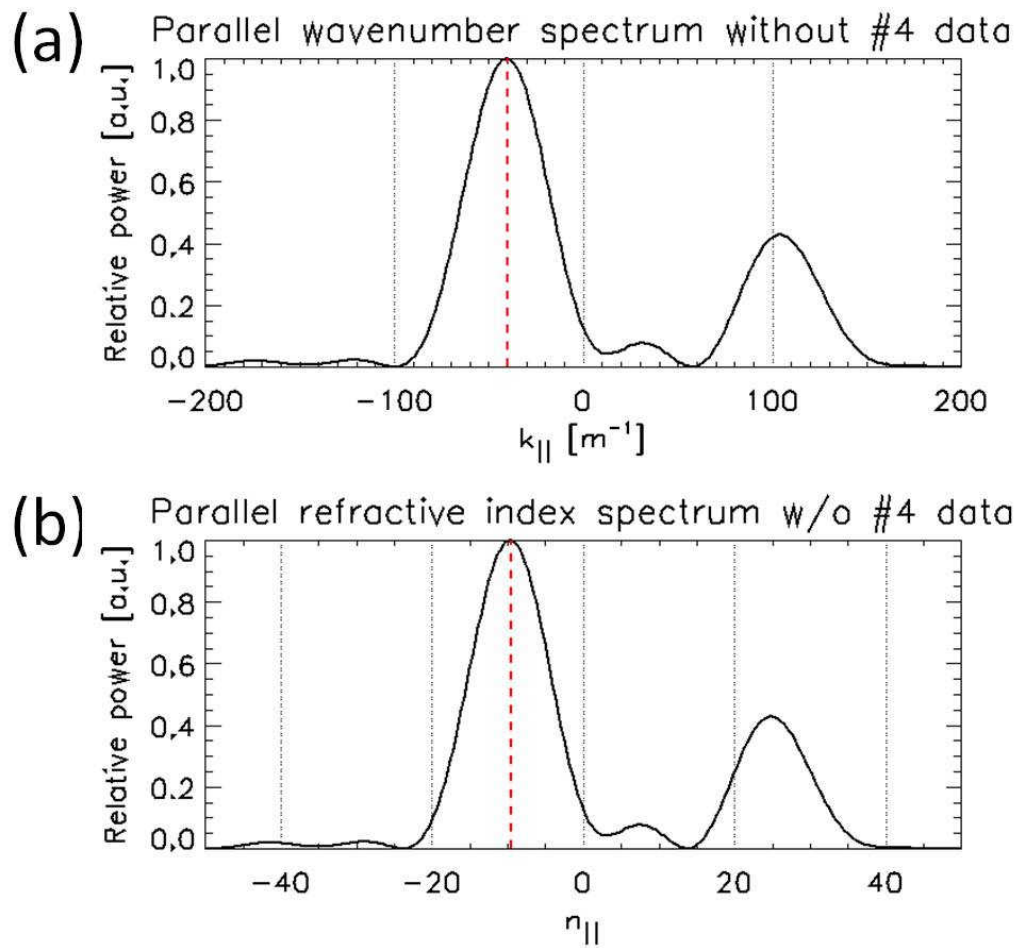
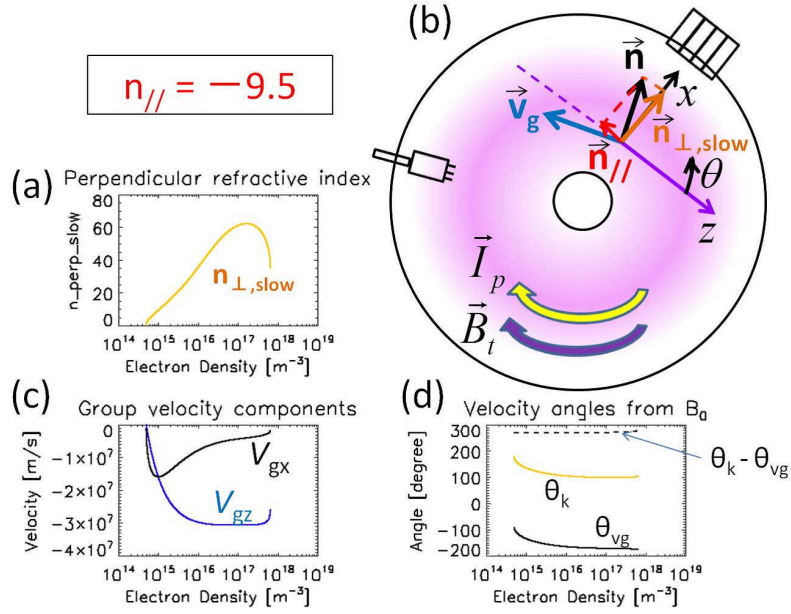Figure 9.1: Launched parallel wavenumber and refractive index spectra for a representative shot number 105498.

Figure 9.2: Wave propagation calculated for $n_\parallel = -9.5$. (a) Perpendicular refractive index for the slow wave ($n_{\perp,\text{slow}}$), (b) vector configuration, (c) group velocity components, and (d) angles from the toroidal magnetic field direction.

The magnetic field of $B_0 = 0.055\,\text{T}$ at $R = 590\,\text{mm}$, where the wavenumber measurement was conducted, was used. Figures 9.2 and 9.3 show (a) $n_{\perp,\text{slow}}$, (b) directions of various vectors, (c) group velocity components, and (d) angles of vectors $\boldsymbol{k}$ and $\boldsymbol{v}_\text{g}$ from the direction of the toroidal magnetic field $\boldsymbol{B}_\text{t} = B_0\hat{\boldsymbol{z}}$, for the two peaks in the refractive index spectrum $n_\parallel = -9.5$ and 25, plotted as functions of the electron density. For both $n_\parallel = -9.5$ and 25, the group velocity in the toroidal direction ($v_{\text{g}z}$) is of order $10^7\,\text{m/s}$ for the electron density of $10^{16}\,\text{m}^{-3}$ where the wavenumber measurement was conducted. Denoting the angles of the refractive index vector $\boldsymbol{n}$ (or the wavenumber vector $\boldsymbol{k}$) and the group velocity $\boldsymbol{v}_\text{g}$ from the toroidal magnetic field direction as θ_k and θ_{v_g}, respectively, $\theta_k - \theta_{v_\text{g}}$ is nearly 270 degrees (or 90 degrees), meaning that $\boldsymbol{v}_\text{g}$ is nearly perpendicular to $\boldsymbol{n}$. From Figs. 9.2 and 9.3, it can be seen that the group velocity $\boldsymbol{v}_\text{g}$ is nearly in the same (opposite) direction to the toroidal magnetic field for positive (negative) $n_\parallel$.

9.1.2 Wave Damping

In order to grasp the overall picture of wave energy transport as the wave propagates, the amount of wave energy damped during the time interval for the launched wave to reach the probe assembly for the first time is estimated. This time interval τ is estimated as the time required for the wave to propagate from the grill antenna to the probe assembly at a major radius of $R = 600\,\text{mm}$ at speed $v_{\text{g}z}$, the z component of the group velocity. The reason for choosing $R = 600\,\text{mm}$ is that the probe assembly is located at $R = 590\,\text{mm}$ and the front end of the grill antenna is located at $R = 650\,\text{mm}$. The relative locations of the grill antenna and the probe assembly are shown in Fig. 9.4. Since τ
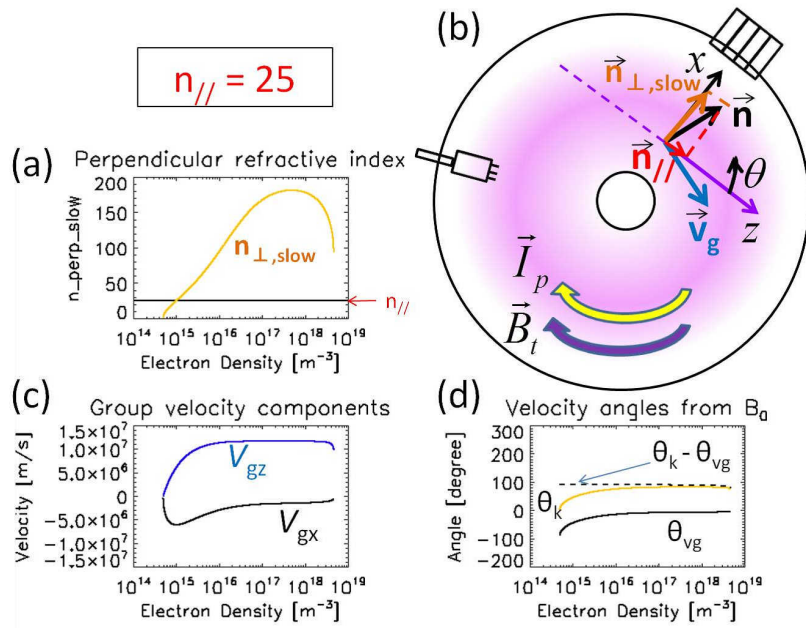
Figure 9.3: Wave propagation calculated for $n_\parallel = 25$. (a) Perpendicular refractive index for the slow wave ($n_{\perp,\text{slow}}$), (b) vector configuration, (c) group velocity components, and (d) angles from the toroidal magnetic field direction.
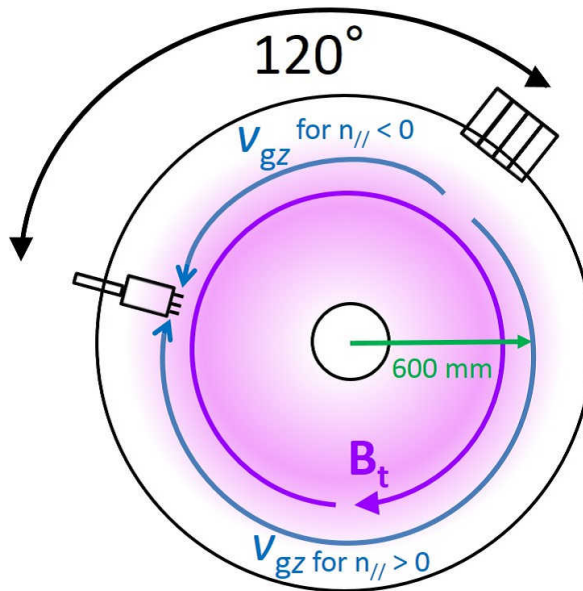

Figure 9.4: Geometry for wave propagation (mid-plane cross section of TST-2).
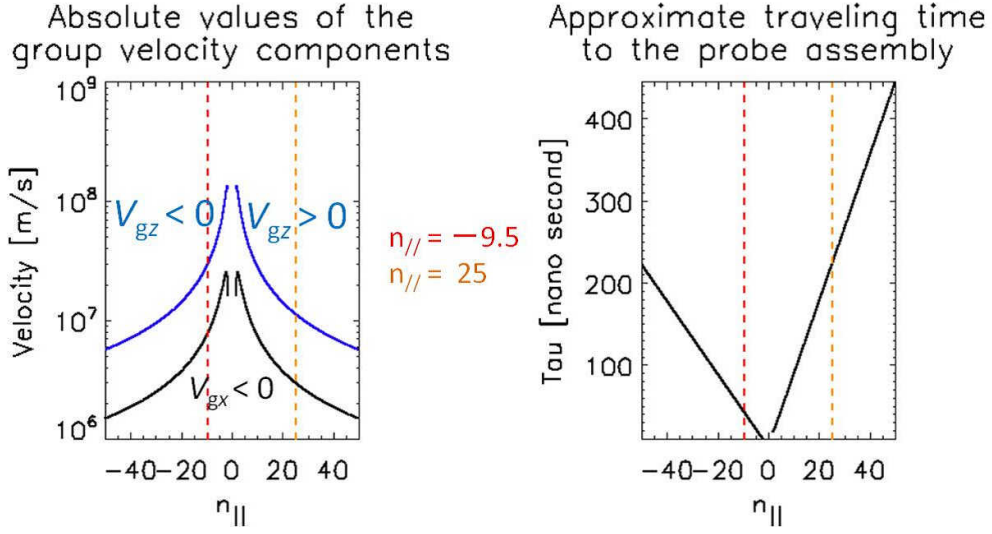
Figure 9.5: Group velocity components and τ for $n_\parallel$ from -50 to 50 for $B_0 = 0.055\,\text{T}$ and $n_\text{e} = 10^{16}\,\text{m}^{-3}$.

depends on the sign of $n_\parallel$, τ_+ and τ_- are defined for positive and negative $n_\parallel$, respectively,

$$\tau_+ = \left(2\pi \times 0.6 \times \frac{240°}{360°}\right)/v_{\text{g}z}(n_\parallel > 0), \tag{9.2}$$

$$\tau_- = \left(2\pi \times 0.6 \times \frac{120°}{360°}\right)/v_{\text{g}z}(n_\parallel < 0). \tag{9.3}$$

The z-component of the group velocity $v_{\text{g}z}$ is calculated using Eq. (9.1) using the toroidal magnetic field $B_0 = 0.055\,\text{T}$ and electron density $n_\text{e} = 10^{16}\,\text{m}^{-3}$. Figure 9.5 shows the x and z-components of the group velocity ($v_{\text{g}x}$ and $v_{\text{g}z}$), and τ (τ_+ and τ_-) for $n_\parallel$ from -50 to 50. Using τ_+ and τ_-, the temporal wave energy damping factor is given by $e^{2\omega_\text{i}\tau_+}$ for $n_\parallel > 0$ and $e^{2\omega_\text{i}\tau_-}$ for $n_\parallel < 0$, where ω_i is

$$\omega_\text{i} = -\frac{\sqrt{2\pi}}{2|n_\parallel|}\frac{\omega_{\text{p}e}^2}{\omega}\left(\frac{c}{v_{\text{t,e}}}\right)^3 \frac{1}{\frac{n_\perp^2\left[D^2 n^2 + (S-P)^2 n_\parallel^2\right]}{n^4} + \left(Fn_\perp^2 + Hn_\parallel^2\right)} \exp\left[-\left(\frac{c}{v_{\text{t,e}}}\right)^2 \frac{1}{2n_\parallel^2}\right] \tag{9.4}$$

from Eq. (2.202). Figure 9.6 shows the absolute value of the temporal energy damping rate $-\omega_\text{i}$ and $2\omega_\text{i}\tau$ for $T_\text{e} = 10\,\text{eV}$, $50\,\text{eV}$, and $100\,\text{eV}$, for $B_0 = 0.055\,\text{T}$ and $n_\text{e} = 10^{16}\,\text{m}^{-3}$. The energy damping factor $e^{2\omega_\text{i}\tau}$ is plotted in Fig. 9.7. From Fig. 9.7, $e^{2\omega_\text{i}\tau_-}$ is almost unity for $n_\parallel = -9.5$ up to $T_\text{e} = 100\,\text{eV}$, so no significant wave damping is expected within time τ_-. On the other hand, $e^{2\omega_\text{i}\tau_+}$ is nearly zero for $n_\parallel = 25$ for T_e of $50\,\text{eV}$ or greater. Therefore, using the cold plasma group velocity and a low temperature Maxwellian electron distribution function in a simple propagation geometry wave components with $n_\parallel$ from -15 to 0 ($n_\parallel$ components from 0 to 15 in the lower graph of Fig. 9.1) survive for T_e of $50\,\text{eV}$ or greater. The surviving $n_\parallel$ components will circulate toroidally inside the vacuum vessel many times and can experience a modification of $n_\parallel$ (upshift/downshift), as described in the next section.

9.2 $k_\parallel$ Upshift/Downshift in Toroidal Geometry

The parallel wavenumber $k_\parallel$ (or $n_\parallel$) can change during propagation in a toroidal plasma. In this section, the physical picture of $k_\parallel$ upshift/downshift is described and the magnitude of $k_\parallel$ change is
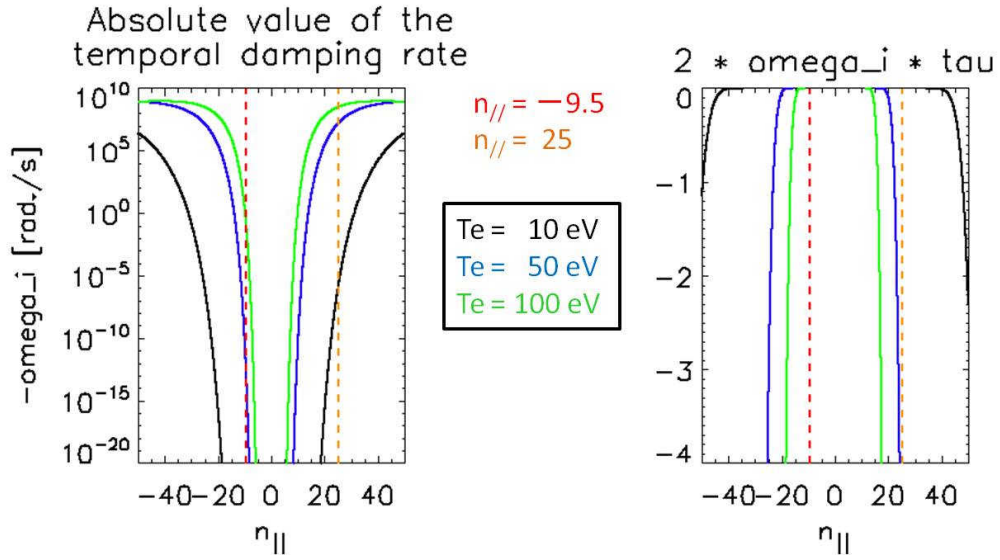
Figure 9.6: Absolute value of the temporal energy damping rate $-\omega_i$ and $2\omega_i\tau$ for $T_e = 10\,\text{eV}$ (black), $50\,\text{eV}$ (blue) and $100\,\text{eV}$ (green), for $B_0 = 0.055\,\text{T}$ and $n_e = 10^{16}\,\text{m}^{-3}$.
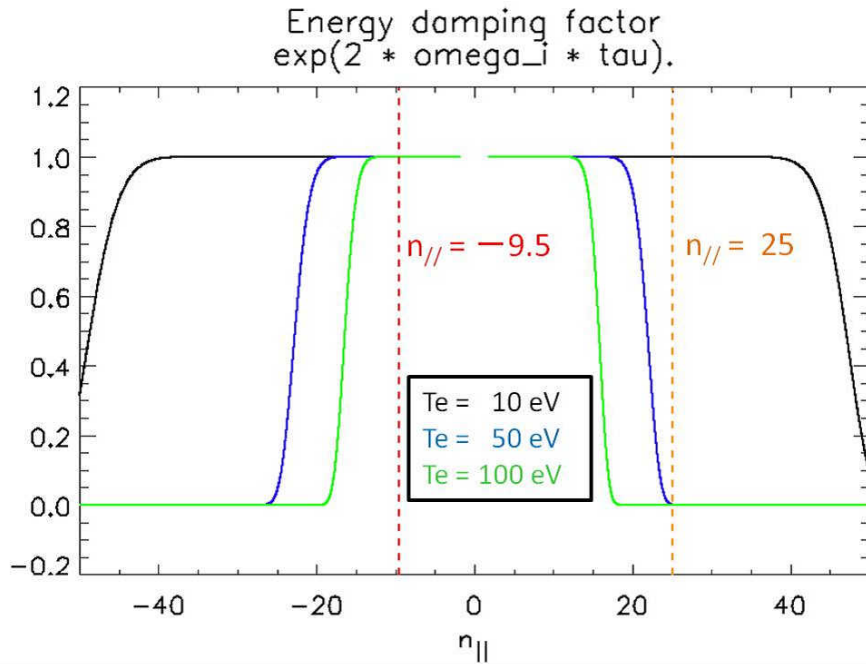
Figure 9.7: Energy damping factor $e^{2\omega_i\tau}$ for $T_e = 10\,\text{eV}$ (black), $50\,\text{eV}$ (blue) and $100\,\text{eV}$ (green), for $B_0 = 0.055\,\text{T}$ and $n_e = 10^{16}\,\text{m}^{-3}$.

estimated.

9.2.1 Decomposition of $k_\parallel$ into Toroidal and Poloidal Components

The parallel wavenumber $k_\parallel$ is defined as

$$k_\parallel = \frac{\boldsymbol{k} \cdot \boldsymbol{B}}{|\boldsymbol{B}|}. \tag{9.5}$$

Decomposing the magnetic field $\boldsymbol{B}$ into the toroidal (z-) component $\boldsymbol{B}_{\text{tor}} = B_0\hat{\boldsymbol{z}}$ and the poloidal (θ-) component $\boldsymbol{B}_{\text{pol}} = B_{\text{pol}}\hat{\boldsymbol{\theta}}$, where $\hat{\boldsymbol{\theta}}$ is the unit vector in the poloidal direction, $\boldsymbol{B}$ is written as

$$\boldsymbol{B} = \boldsymbol{B}_{\text{tor}} + \boldsymbol{B}_{\text{pol}} = B_0\hat{\boldsymbol{z}} + B_{\text{pol}}\hat{\boldsymbol{\theta}}. \tag{9.6}$$

Denoting the wavenumber components along $\boldsymbol{B}_{\text{tor}}$ and $\boldsymbol{B}_{\text{pol}}$ by k_{tor} and k_{pol}, $k_\parallel$ is expressed using Eqs. (9.5) and (9.6) as

$$k_\parallel = k_{\text{tor}}\frac{B_0}{|\boldsymbol{B}|} + k_{\text{pol}}\frac{B_{\text{pol}}}{|\boldsymbol{B}|}. \tag{9.7}$$

Since k_{tor} is the wavenumber component in the toroidal direction, k_{tor} can be regarded as k_n in Eq. (8.3):

$$k_n = \frac{n}{R_{\text{antenna}}}$$

and is written as

$$k_{\text{tor}} = \frac{n_{\text{tor}}}{R}, \tag{9.8}$$

where R_{antenna} is replaced by a general R because the wave propagates over various positions. n_{tor} is an integer called the toroidal mode number. Using Eq. (9.8), Eq. (9.7) gives $k_\parallel$ as

$$k_\parallel = \frac{n_{\text{tor}}}{R}\frac{B_0}{|\boldsymbol{B}|} + k_{\text{pol}}\frac{B_{\text{pol}}}{|\boldsymbol{B}|}. \tag{9.9}$$

9.2.2 $k_\parallel$ Variation in a Low Current Plasma

$k_\parallel$ variation from the toroidal effect

At $R = R_{\text{probe}} = 590\,\text{mm}$ where the wavenumber measurement was conducted, the toroidal magnetic field strength B_0 is 0.055 T. The poloidal magnetic field strength, $|\boldsymbol{B}_{\text{pol}}|$, at R_{probe} can be estimated using the plasma current of $I_{\text{p}} = 0.5\,\text{kA}$ and the major radial position of the plasma center $R = R_{\text{center}} = 380\,\text{mm}$ as

$$|\boldsymbol{B}_{\text{pol}}| \simeq \mu_0\frac{I_{\text{p}}}{2\pi\left(R_{\text{probe}} - R_{\text{center}}\right)} = \frac{4\pi}{10^7} \cdot \frac{0.5 \times 10^3}{2\pi \times (0.59 - 0.38)} = 0.47 \times 10^{-3}\,\text{T}, \tag{9.10}$$

resulting in

$$|\boldsymbol{B}_{\text{pol}}| \ll B_0 \tag{9.11}$$

at the position of the probe assembly. Since $B_0 \propto \frac{1}{R}$ and the total amount of I_{p} which contributes to $|\boldsymbol{B}_{\text{pol}}|$ decreases inside the plasma, the relationship Eq. (9.11) holds for any R inside the vacuum vessel for a series of shots represented by shot number 105498. Since $|\boldsymbol{B}| = \sqrt{B_0^2 + |\boldsymbol{B}_{\text{pol}}|^2}$ from Eq. (9.6), under Eq. (9.11),

$$\frac{B_0}{|\boldsymbol{B}|} \simeq 1 \tag{9.12}$$

and

$$\frac{|\boldsymbol{B}_{\text{pol}}|}{|\boldsymbol{B}|} \ll 1 \tag{9.13}$$

are satisfied. Unless $k_{\rm pol}$ is large, Eq. (9.9) is combined with Eqs. (9.12) and (9.13) to give

$$k_\parallel \simeq \frac{n_{\rm tor}}{R}. \tag{9.14}$$

Denoting $k_\parallel$ at the position of the grill antenna $R = R_{\rm probe} = 650\,{\rm mm}$ by $k_{\parallel,{\rm antenna}}$,

$$k_{\parallel,{\rm antenna}} \simeq \frac{n_{\rm tor}}{R_{\rm antenna}}. \tag{9.15}$$

If the plasma were symmetric in the toroidal direction, $n_{\rm tor}$ is conserved [68], so $|k_\parallel| > |k_{\parallel,{\rm antenna}}|$ for $R < R_{\rm antenna}$. This is called the toroidal upshift of $k_\parallel$. If the antenna for plasma heating and/or current drive is installed on the outboard side of the torus, $R < R_{\rm antenna}$ inside the plasma. In this case, and with Eq. (9.11), $k_\parallel$ is upshifted as the wave propagates inside the plasma, and becomes more likely to be absorbed by the plasma as shown in Fig. 9.7.

$k_\parallel$ variation from the poloidal effect

Another mechanism of $k_\parallel$ variation comes from the second term on the right-hand side of Eq. (9.9), i.e., $k_{\rm pol}\frac{B_{\rm pol}}{|\boldsymbol{B}|}$. For a constant R, for example for $R = R_{\rm probe}$, only the term $k_{\rm pol}\frac{B_{\rm pol}}{|\boldsymbol{B}|}$ determines the variation of $k_\parallel$. Denoting

$$\Delta k_\parallel \equiv k_{\rm pol}\frac{B_{\rm pol}}{|\boldsymbol{B}|}, \tag{9.16}$$

the sign of $\Delta k_\parallel$ depends on the sign of $k_{\rm pol}B_{\rm pol}$, and $k_\parallel$ can experience not only upshift but also downshift. The absolute value of $\Delta k_\parallel$ is evaluated as

$$|\Delta k_\parallel| = \frac{|k_{\rm pol}B_{\rm pol}|}{|\boldsymbol{B}|} \leq |k_{\rm pol}|\frac{|\boldsymbol{B}_{\rm pol}|}{|\boldsymbol{B}|}. \tag{9.17}$$

Since $k_y \simeq 0$ for an electrostatic wave in the present geometry,

$$|k_{\rm pol}| \simeq |k_\perp| = 149\,{\rm m}^{-1} \tag{9.18}$$

for $B_0 = 0.055\,{\rm T}$ and $n_{\rm e} = 10^{16}\,{\rm m}^{-3}$ from Fig. 2.2. Using Eqs. (9.10), (9.12), and (9.17), $|\Delta k_\parallel|$ is evaluated as

$$|\Delta k_\parallel| \leq |k_{\rm pol}|\frac{|\boldsymbol{B}_{\rm pol}|}{|\boldsymbol{B}|} \simeq 149 \times \frac{0.47 \times 10^{-3}}{0.055} = 1.3\,{\rm m}^{-1}. \tag{9.19}$$

From this estimation of $|\Delta k_\parallel|$, the downshift of $k_\parallel$ is at most $1.3\,{\rm m}^{-1}$, which is too small to explain the difference between the launched value of $k_\parallel = 40\,{\rm m}^{-1}$ and the measured value of $k_\parallel = 19.6 \pm 11.0\,{\rm m}^{-1}$.

9.3   Behavior of the Measured Phase Difference in the Presence of Two Wavenumbers

The velocity distribution function was assumed to be Maxwellian in Section 9.1. However, it could be different from Maxwellian and both $k_\parallel = -40\,{\rm m}^{-1}$ and $k_\parallel = 105\,{\rm m}^{-1}$ might survive. In this section, the phase difference between probe electrodes in the presence of waves with wavenumbers in exactly opposite directions is investigated.

9.3.1   Coordinate System and Model

Taking the x-axis in the direction of two wavenumbers $k_{\rm f}$ and $k_{\rm b}$, the two dimensional coordinate system is defined as shown in Fig. 9.8. There are three electrodes 1 through 3 with electrode numbers corresponding to those of the probe assembly used in the wavenumber experiment. Taking the angle
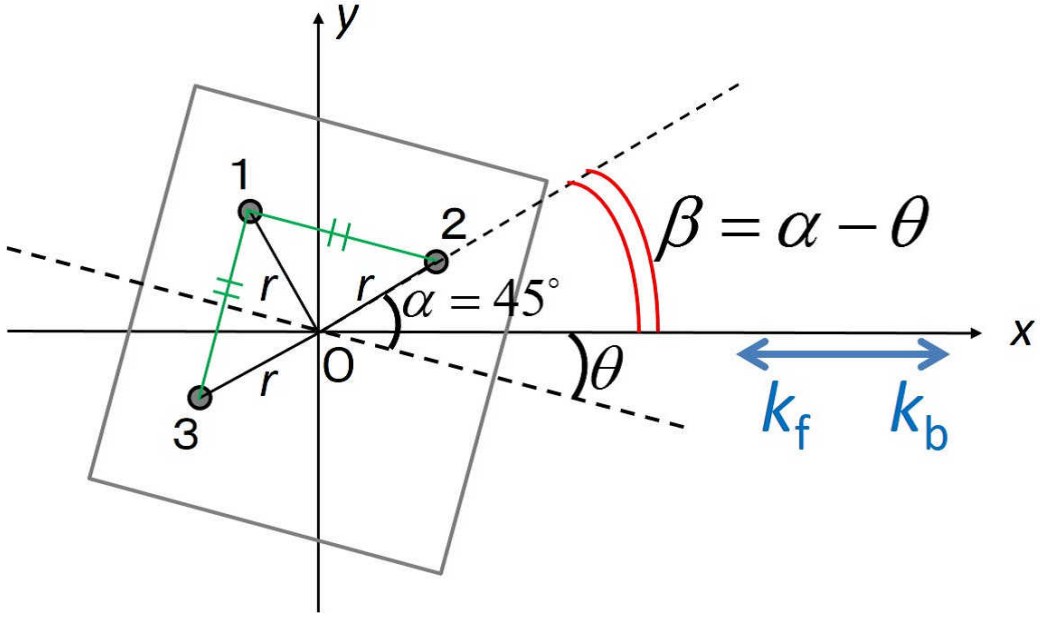
Figure 9.8: Coordinate system for the three point measurement.

of the thick broken line, which passes through the origin and is parallel to the line segment formed by electrodes 1 and 2, from the x-axis as θ, β is defined as

$$\beta = \alpha - \theta, \tag{9.20}$$

where $\alpha = 45°$, and the distance from the origin to each electrode is

$$r = \frac{14.2 \times 10^{-3}}{\sqrt{2}} = 0.01 \, \text{m}. \tag{9.21}$$

Using this coordinate system and assuming that the phase is constant in the y-direction over the distance of several times r, The measured signal at electrode i ($i = 1, 2, 3$), $\psi(x_i, t)$, is expressed as

$$\psi(x_i, t) = A_{\mathrm{f}} e^{i(k_{\mathrm{f}} x_i - \omega t + \phi_{\mathrm{f}})} + A_{\mathrm{b}} e^{i(k_{\mathrm{b}} x_i - \omega t + \phi_{\mathrm{b}})} \tag{9.22}$$

$$\equiv \Psi_i e^{i(-\omega t + \Theta_i)}, \tag{9.23}$$

where A_{f}, A_{b}, and Ψ_i are real amplitudes, and ϕ_{f} and ϕ_{b} are phases of each wave. The case with $k_{\mathrm{b}} = -k_{\mathrm{f}}$ for three electrode in a linear arrangement with equal intervals is studied in [69]. The notations of Eqs. (9.22) and (9.23) are adopted from [69]. x_i is given in terms of β as

$$\begin{cases} x_1 = -r \sin \beta, & (9.24) \\ x_2 = r \cos \beta, & (9.25) \\ x_3 = -r \cos \beta. & (9.26) \end{cases}$$

9.3.2 Derivation of Cosine of Phase Difference and $A_f^2 + A_b^2$

Since the phase difference $\Delta\Theta_{ji} \equiv \Theta_j - \Theta_i$ is of interest, taking the real part of $\overline{\psi(x_i,t)}\psi(x_j,t)$ gives

$$\Psi_i \Psi_j \cos \Delta\Theta_{ji}$$

$$
\begin{aligned}
= \ & A_f^2 \cos\left[k_f\left(x_j - x_i\right)\right] + A_b^2 \cos\left[k_b\left(x_j - x_i\right)\right] \\
& + A_f A_b \left\{\cos\left[k_f x_i - k_b x_j + (\phi_f - \phi_b)\right] + \cos\left[k_f x_j - k_b x_i + (\phi_f - \phi_b)\right]\right\}
\end{aligned}
$$

$$
\begin{aligned}
= \ & A_f^2 \cos\left[k_f\left(x_j - x_i\right)\right] + A_b^2 \cos\left[k_b\left(x_j - x_i\right)\right] \\
& + 2 A_f A_b \cos\left[\frac{k_f + k_b}{2}\left(x_j - x_i\right)\right] \cos\left[\frac{k_f - k_b}{2}\left(x_j + x_i\right) + (\phi_f - \phi_b)\right]
\end{aligned}
$$

$$
\begin{aligned}
= \ & A_f^2 \cos\left[k_f\left(x_j - x_i\right)\right] + A_b^2 \cos\left[k_b\left(x_j - x_i\right)\right] \\
& + 2 A_f A_b \cos\left[\frac{k_f + k_b}{2}\left(x_j - x_i\right)\right] \\
& \times \left\{\cos\left[\frac{k_f - k_b}{2}\left(x_j + x_i\right)\right] \cos(\phi_f - \phi_b) - \sin\left[\frac{k_f - k_b}{2}\left(x_j + x_i\right)\right] \sin(\phi_f - \phi_b)\right\},
\end{aligned}
$$

$$\tag{9.27}$$

and $\overline{\psi(x_i,t)}\psi(x_i,t)$ leads to

$$\Psi_i^2 = A_f^2 + A_b^2 + 2 A_f A_b \cos\left[(k_f - k_b) x_i + (\phi_f - \phi_b)\right]. \tag{9.28}$$

In order to eliminate $(\phi_f - \phi_b)$ from Eq. (9.27), $\cos(\phi_f - \phi_b)$ and $\sin(\phi_f - \phi_b)$ are calculated as follows. Using Eq. (9.28) for $x_2 = r\cos\beta$ and $x_3 = -r\cos\beta$, and defining

$$\theta_c \equiv (k_f - k_b)\, r\cos\beta, \tag{9.29}$$

$$
\begin{aligned}
\Psi_2^2 \ = \ & A_f^2 + A_b^2 \\
& + 2 A_f A_b \left\{\cos\left[(k_f - k_b)\, r\cos\beta\right] \cos(\phi_f - \phi_b) - \sin\left[(k_f - k_b)\, r\cos\beta\right] \sin(\phi_f - \phi_b)\right\}
\end{aligned}
$$

$$
= \ A_f^2 + A_b^2 + 2 A_f A_b \left[\cos\theta_c \cos(\phi_f - \phi_b) - \sin\theta_c \sin(\phi_f - \phi_b)\right] \tag{9.30}
$$

and

$$
\begin{aligned}
\Psi_3^2 \ = \ & A_f^2 + A_b^2 \\
& + 2 A_f A_b \left\{\cos\left[(k_f - k_b)\, r\cos\beta\right] \cos(\phi_f - \phi_b) + \sin\left[(k_f - k_b)\, r\cos\beta\right] \sin(\phi_f - \phi_b)\right\}
\end{aligned}
$$

$$
= \ A_f^2 + A_b^2 + 2 A_f A_b \left[\cos\theta_c \cos(\phi_f - \phi_b) + \sin\theta_c \sin(\phi_f - \phi_b)\right] \tag{9.31}
$$

are derived. Summing and subtracting Eqs. (9.29) and (9.30) yield

$$\Psi_3^2 + \Psi_2^2 = 2 A_f^2 + 2 A_b^2 + 4 A_f A_b \cos\theta_c \cos(\phi_f - \phi_b), \tag{9.32}$$

$$\Psi_3^2 - \Psi_2^2 = 4 A_f A_b \sin\theta_c \sin(\phi_f - \phi_b), \tag{9.33}$$

leading to

$$\cos(\phi_f - \phi_b) = \frac{\Psi_3^2 + \Psi_2^2 - 2\left(A_f^2 + A_b^2\right)}{4 A_f A_b \cos\theta_c}, \tag{9.34}$$

$$\sin(\phi_f - \phi_b) = \frac{\Psi_3^2 - \Psi_2^2}{4 A_f A_b \sin\theta_c}, \tag{9.35}$$

where $\cos\theta_c \neq 0$ and $\sin\theta_c \neq 0$.

Substituting Eqs. (9.34) and (9.35) into Eq. (9.27) gives

$$\Psi_i\Psi_j\cos\Delta\Theta_{ji}$$

$$
\begin{aligned}
= \quad & A_f^2\cos\left[k_f\left(x_j-x_i\right)\right] + A_b^2\cos\left[k_b\left(x_j-x_i\right)\right] \\
& +\frac{1}{2}\cos\left[\frac{k_f+k_b}{2}\left(x_j-x_i\right)\right] \\
& \times\left\{\cos\left[\frac{k_f-k_b}{2}\left(x_j+x_i\right)\right]\frac{\Psi_3^2+\Psi_2^2-2\left(A_f^2+A_b^2\right)}{\cos\theta_c} - \sin\left[\frac{k_f-k_b}{2}\left(x_j+x_i\right)\right]\frac{\Psi_3^2-\Psi_2^2}{\sin\theta_c}\right\}.
\end{aligned}
$$

(9.36)

From Eq. (9.36), the cosine of phase difference of electrode 2 with respect to electrode 1, $\Delta\Theta_{21} = \Theta_2 - \Theta_1$, is given by setting $x_j = x_2 = r\cos\beta$ and $x_i = x_1 = -r\sin\beta$ as

$$\Psi_1\Psi_2\cos\Delta\Theta_{21}$$

$$
\begin{aligned}
= \quad & A_f^2\cos\left[k_f r\left(\cos\beta+\sin\beta\right)\right] + A_b^2\cos\left[k_b r\left(\cos\beta+\sin\beta\right)\right] \\
& +\frac{1}{2}\cos\left[\frac{k_f+k_b}{2}r\left(\cos\beta+\sin\beta\right)\right] \\
& \times\left\{\cos\left[\frac{k_f-k_b}{2}r\left(\cos\beta-\sin\beta\right)\right]\frac{\Psi_3^2+\Psi_2^2-2\left(A_f^2+A_b^2\right)}{\cos\theta_c} - \sin\left[\frac{k_f-k_b}{2}r\left(\cos\beta-\sin\beta\right)\right]\frac{\Psi_3^2-\Psi_2^2}{\sin\theta_c}\right\}.
\end{aligned}
$$

(9.37)

Equation (9.37) states that $\cos\Delta\Theta_{21}$ is calculated in terms of r, β, Ψ_1 Ψ_2, Ψ_3, k_f, k_b, A_f, and A_b. Variables r, β, Ψ_1 Ψ_2, and Ψ_3 are determined by the probe configuration or measured signal amplitudes. k_f and k_b are wavenumbers in opposite directions and can be taken as the two peaks in the launched spectrum of the grill antenna. The wave amplitudes A_f and A_b should be set according to r, β, Ψ_1 Ψ_2, Ψ_3, k_f and k_b.

Actually a constraint is applied on the quantity $A_f^2 + A_b^2$. Defining

$$\theta_s \equiv \left(k_f-k_b\right)r\sin\beta, \tag{9.38}$$

Eq. (9.28) for $x_i = x_1 = -r\sin\beta$ reduces to

$$
\begin{aligned}
\Psi_1^2 = \quad & A_f^2+A_b^2 \\
& +2A_fA_b\left\{\cos\left[\left(k_f-k_b\right)r\sin\beta\right]\cos\left(\phi_f-\phi_b\right) + \sin\left[\left(k_f-k_b\right)r\sin\beta\right]\sin\left(\phi_f-\phi_b\right)\right\} \\
= \quad & A_f^2+A_b^2 + \cos\theta_s\frac{\Psi_3^2+\Psi_2^2-2\left(A_f^2+A_b^2\right)}{2\cos\theta_c} + \sin\theta_s\frac{\Psi_3^2-\Psi_2^2}{2\sin\theta_c},
\end{aligned}
\tag{9.39}
$$

where Eqs. (9.34), (9.35), and (9.38) were used. Equation (9.39) is solved for $A_f^2 + A_b^2$ as

$$\Psi_1^2 = \left(1-\frac{\cos\theta_s}{\cos\theta_c}\right)\left(A_f^2+A_b^2\right) + \frac{1}{2}\cdot\frac{\cos\theta_s}{\cos\theta_c}\left(\Psi_3^2+\Psi_2^2\right) + \frac{1}{2}\cdot\frac{\sin\theta_s}{\sin\theta_c}\left(\Psi_3^2-\Psi_2^2\right), \tag{9.40}$$

giving

$$A_f^2 + A_b^2 = \frac{\cos\theta_c}{\cos\theta_c-\cos\theta_s}\left[\Psi_1^2 - \frac{1}{2}\left(\frac{\cos\theta_s}{\cos\theta_c}-\frac{\sin\theta_s}{\sin\theta_c}\right)\Psi_2^2 - \frac{1}{2}\left(\frac{\cos\theta_s}{\cos\theta_c}+\frac{\sin\theta_s}{\sin\theta_c}\right)\Psi_3^2\right] \tag{9.41}$$

for $\cos\theta_c \neq \cos\theta_s$ and $\cos\theta_c\sin\theta_s \neq 0$.

From Eq. (9.41), if A_f is given, A_b is calculated using r, β, Ψ_1 Ψ_2, Ψ_3, k_f, k_b and A_f. Substituting A_f and A_b into Eq. (9.37) together with r, β, Ψ_1 Ψ_2, Ψ_3, k_f, and k_b, $\cos\Delta\Theta_{21}$ and therefore $\Delta\Theta_{21}$ can be calculated explicitly.

9.3.3 Calculation of Phase Difference $\Delta\Theta_{21}$ for the Condition of Wavenumber Measurement

$A_{\rm b}$ and $\Delta\Theta_{21}$ are calculated using Eqs. (9.41) and (9.37) for given $A_{\rm f}$. Variables r, β, Ψ_1 Ψ_2, Ψ_3, $k_{\rm f}$, and $k_{\rm b}$, are set as follows: $r = 0.01\,{\rm m}$ from Eq. (9.21),

$$\theta = 10^\circ,\ 15^\circ,\ 30^\circ,\ 45^\circ,\ 60^\circ,\ 75^\circ,\ 85^\circ,\ 100^\circ, \tag{9.42}$$

and thus

$$\begin{aligned}
\beta &= \alpha - \theta = 45^\circ - \theta \\
&= 35^\circ,\ 30^\circ,\ 15^\circ,\ 0^\circ,\ -15^\circ,\ -30^\circ,\ -40^\circ,\ -55^\circ.
\end{aligned} \tag{9.43}$$

Signal amplitudes Ψ_1 Ψ_2, and Ψ_3 are set with reference to the experimental signal amplitudes shown in Fig. (8.30) as

$$\left\{ \begin{aligned}
&\Psi_1 = 3.5\,{\rm mV} && (9.44)\\
&\Psi_2 = 4.0\,{\rm mV} && (9.45)\\
&\Psi_3 = 4.5\,{\rm mV}. && (9.46)
\end{aligned} \right.$$

$k_{\rm f}$ and $k_{\rm b}$ are set to

$$\left\{ \begin{aligned}
&k_{\rm f} = -40\,{\rm m}^{-1} && (9.47)\\
&k_{\rm b} = 105\,{\rm m}^{-1}. && (9.48)
\end{aligned} \right.$$

according to Fig. 9.1 (a). The signs are inverted to correspond to the definition with respect to the direction of the toroidal magnetic field. Scanning $A_{\rm f}$ up to $5\,{\rm mV}$, $A_{\rm b}$ and $\Delta\Theta_{21}$ are calculated as shown in Fig. 9.9. As θ increases, the line segment between electrodes 1 and 2 changes from parallel to perpendicular to the wavenumber vector (x-axis), and the phase difference $\Delta\Theta_{21}$ should decrease, consistent with the behavior of $\Delta\Theta_{21}$ shown in Fig. 9.9.

Assuming that $k_\parallel$ is in the horizontal plane in the wavenumber measurement, the probe angle of 15 degrees in the experiment corresponds to the case of $\theta = 15^\circ$ in Fig. 9.8. In Fig. 9.9, however, the calculated phase difference is from 70 degrees to 150 degrees, far larger than the measured phase difference of about 20 degrees at the probe angle of 15 degrees. For this reason, the model of two wavenumbers opposite to each other cannot explain the experimental result.

9.4 Evaluation of Wave Damping for Non-Maxwellian Electron Velocity Distribution Function

The experimental results cannot be explained if the electron velocity distribution function were assumed to be Maxwellian. In this section, the wave energy damping factor $\exp\left(2\omega_{\rm i}\tau\right)$ is considered for non-Maxwellian distribution functions. The one-dimensional electron velocity distribution function in the direction of the magnetic field can be expressed as

$$f(v_\parallel) = n_{\rm e} P(v_\parallel), \tag{9.49}$$

where P is the probability distribution function and $n_{\rm e}$ is the electron density. From Eq. (2.199), P for the Maxwellian distribution function, $P_{\rm M}$, is written as

$$P_{\rm M}(v_\parallel) = \frac{1}{\sqrt{2\pi}v_{\rm t,e}}\exp\left(-\frac{v_\parallel^2}{2v_{\rm t,e}^2}\right) = \frac{1}{\sqrt{2\pi}v_{\rm t,e}}\exp\left[-\left(\frac{v_\parallel}{\sqrt{2}v_{\rm t,e}}\right)^2\right]. \tag{9.50}$$
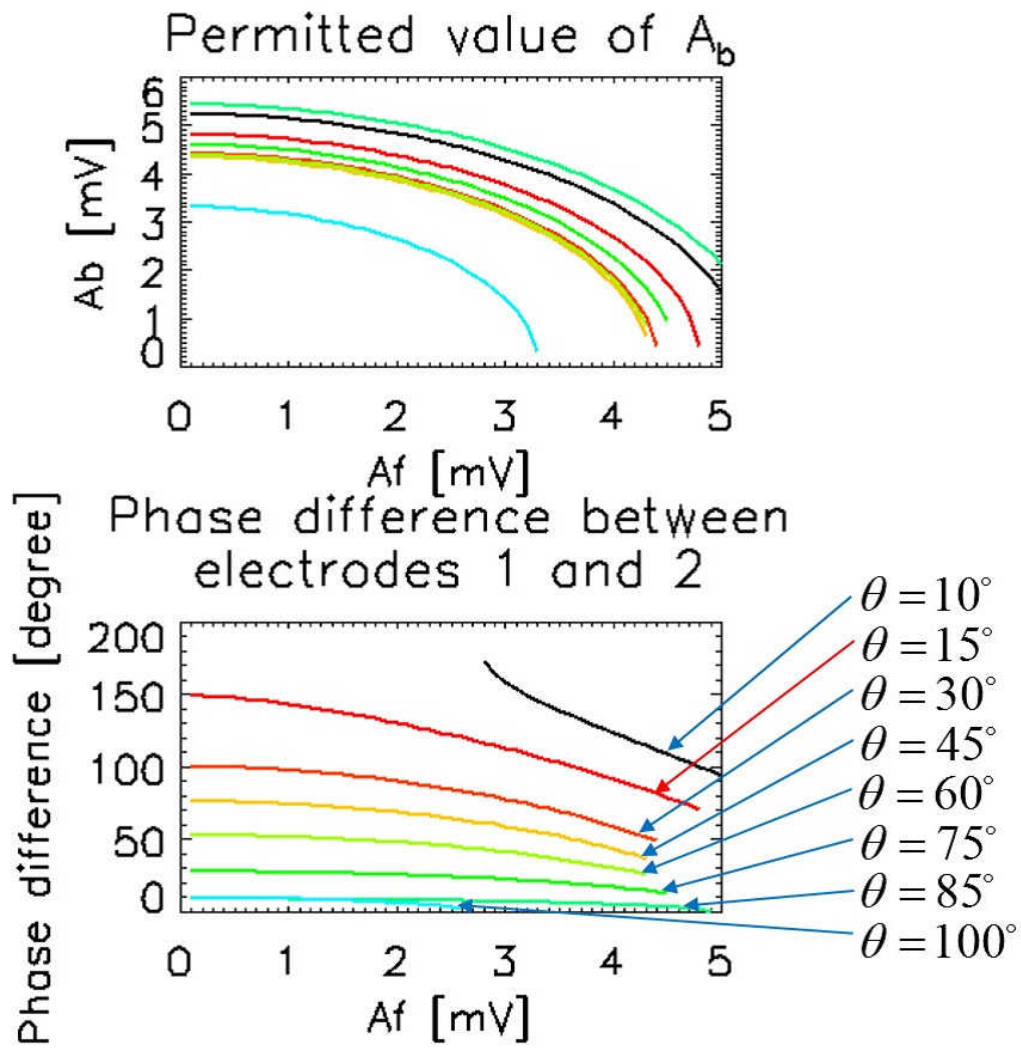
Figure 9.9: A_{b} and $\Delta\Theta_{21}$ plotted as functions of A_{b} for eight angles, and $k_{\mathrm{f}} = -40\,\mathrm{m}^{-1}$ and $k_{\mathrm{b}} = 105\,\mathrm{m}^{-1}$. Colors in both plots correspond to each other.

Since the main lobe of the $k_\parallel$ spectrum of the LHW launched from the grill antenna is in the negative region of $k_\parallel$ ($n_\parallel$) as shown in Fig. 9.1, it is expected that electrons with $v_\parallel < 0$ are dominantly accelerated. A simple non-Maxwellian probability distribution function $P_{\text{hybrid}}(v_\parallel)$ is considered:

$$P_{\text{hybrid}}(v_\parallel \geq 0) \quad \equiv \quad P_{\text{M}}(v_\parallel) = \frac{1}{\sqrt{2\pi}v_{\text{t,e}}} \exp\left(-\frac{v_\parallel^2}{2v_{\text{t,e}}^2}\right) \tag{9.51}$$

$$P_{\text{hybrid}}(v_\parallel < 0) \quad \equiv \quad P_{\text{non}-\text{M}}(v_\parallel) \equiv \frac{1}{2\sqrt{2}v_{\text{t,e}}} \exp\left(-\frac{|v_\parallel|}{\sqrt{2}v_{\text{t,e}}}\right), \tag{9.52}$$

where $P_{\text{non}-\text{M}}$ is a non-Maxwellian (exponential) probability distribution function. Figure 9.10 shows $P_{\text{hybrid}}(v_\parallel \geq 0)$ in black line and $P_{\text{hybrid}}(v_\parallel < 0)$ in red line, with $P_{\text{M}}(v_\parallel < 0)$ in black dashed line for comparison, for $T_{\text{e}} = 10$, 50, and 100 eV. It can be seen that $P_{\text{hybrid}}(v_\parallel < 0)$ (shown in red) has more high energy electrons and fewer low energy electrons than $P_{\text{M}}(v_\parallel < 0)$. It should be noted that T_{e} is the electron temperature only for the Maxwellian distribution. For example, the effective temperatures for $P_{\text{hybrid}}(v_\parallel < 0)$ shown in the top frame in Fig. 9.10 is larger than 10 eV, it is labeled $T_{\text{e}} = 10$ eV in the present discussion.

Using Eqs. (9.49), (9.51), and (9.52), the electron velocity distribution function $f_{\text{hybrid}}(v_\parallel)$ is defined as

$$f_{\text{hybrid}}(v_\parallel \geq 0) \quad \equiv \quad n_{\text{e}}P_{\text{hybrid}}(v_\parallel \geq 0) = \frac{n_{\text{e}}}{\sqrt{2\pi}v_{\text{t,e}}} \exp\left(-\frac{v_\parallel^2}{2v_{\text{t,e}}^2}\right), \tag{9.53}$$

$$f_{\text{hybrid}}(v_\parallel < 0) \quad \equiv \quad n_{\text{e}}P_{\text{hybrid}}(v_\parallel < 0) = \frac{n_{\text{e}}}{2\sqrt{2}v_{\text{t,e}}} \exp\left(-\frac{|v_\parallel|}{\sqrt{2}v_{\text{t,e}}}\right). \tag{9.54}$$

This will be referred to as the "hybrid" distribution. Although $f_{\text{hybrid}}(v_\parallel)$ is discontinuous at $v_\parallel = 0$ and is unphysical, this discontinuity does not affect the evaluation of wave damping below because there is no wave component which can interact with electrons with $v_\parallel = 0$ ($|n_\parallel| = \infty$). Although the hybrid distribution $f_{\text{hybrid}}(v_\parallel)$ used here does not represent the true distribution function, it is a convenient model to evaluating the effect of high energy electrons on wave damping analytically.

Since the derivatives of $f_{\text{hybrid}}(v_\parallel)$ are given for $v_\parallel \neq 0$ as

$$\frac{df_{\text{hybrid}}(v_\parallel > 0)}{dv_\parallel} \quad = \quad -\frac{n_{\text{e}}}{\sqrt{2\pi}v_{\text{t,e}}^3}v_\parallel \exp\left(-\frac{v_\parallel^2}{2v_{\text{t,e}}^2}\right), \tag{9.55}$$

$$\frac{df_{\text{hybrid}}(v_\parallel < 0)}{dv_\parallel} \quad = \quad -\frac{n_{\text{e}}}{4v_{\text{t,e}}^2} \exp\left(-\frac{|v_\parallel|}{\sqrt{2}v_{\text{t,e}}}\right), \tag{9.56}$$

the values at $v_\parallel = \omega/k_\parallel = c/n_\parallel$ are given as

$$\left[\frac{df_{\text{hybrid}}(v_\parallel > 0)}{dv_\parallel}\right]_{v_\parallel = \frac{\omega}{k_\parallel} = \frac{c}{n_\parallel}} \quad = \quad -\frac{n_{\text{e}}}{\sqrt{2\pi}v_{\text{t,e}}^3}\frac{c}{n_\parallel} \exp\left[-\left(\frac{c}{v_{\text{t,e}}}\right)^2 \cdot \frac{1}{2n_\parallel}\right], \tag{9.57}$$

$$\left[\frac{df_{\text{hybrid}}(v_\parallel < 0)}{dv_\parallel}\right]_{v_\parallel = \frac{\omega}{k_\parallel} = \frac{c}{n_\parallel}} \quad = \quad -\frac{n_{\text{e}}}{4v_{\text{t,e}}^2} \exp\left(-\frac{c}{v_{\text{t,e}}} \cdot \frac{1}{\sqrt{2}|n_\parallel|}\right). \tag{9.58}$$

Equation (2.198) for the wave damping rate ω_i is expressed in terms of $n_\parallel$ as

$$\omega_i = \frac{\pi c^2}{\omega}\frac{e^2}{\epsilon_0 m_{\text{e}}}\frac{n_\parallel}{|n_\parallel|}\frac{1}{\frac{n_\perp^2\left[D^2 n^2 + (S-P)^2 n_\parallel^2\right]}{n^4} + \left(Fn_\perp^2 + Hn_\parallel^2\right)}\left[\frac{df(v_\parallel)}{dv_\parallel}\right]_{v_\parallel = \frac{\omega}{k_\parallel} = \frac{c}{n_\parallel}}. \tag{9.59}$$
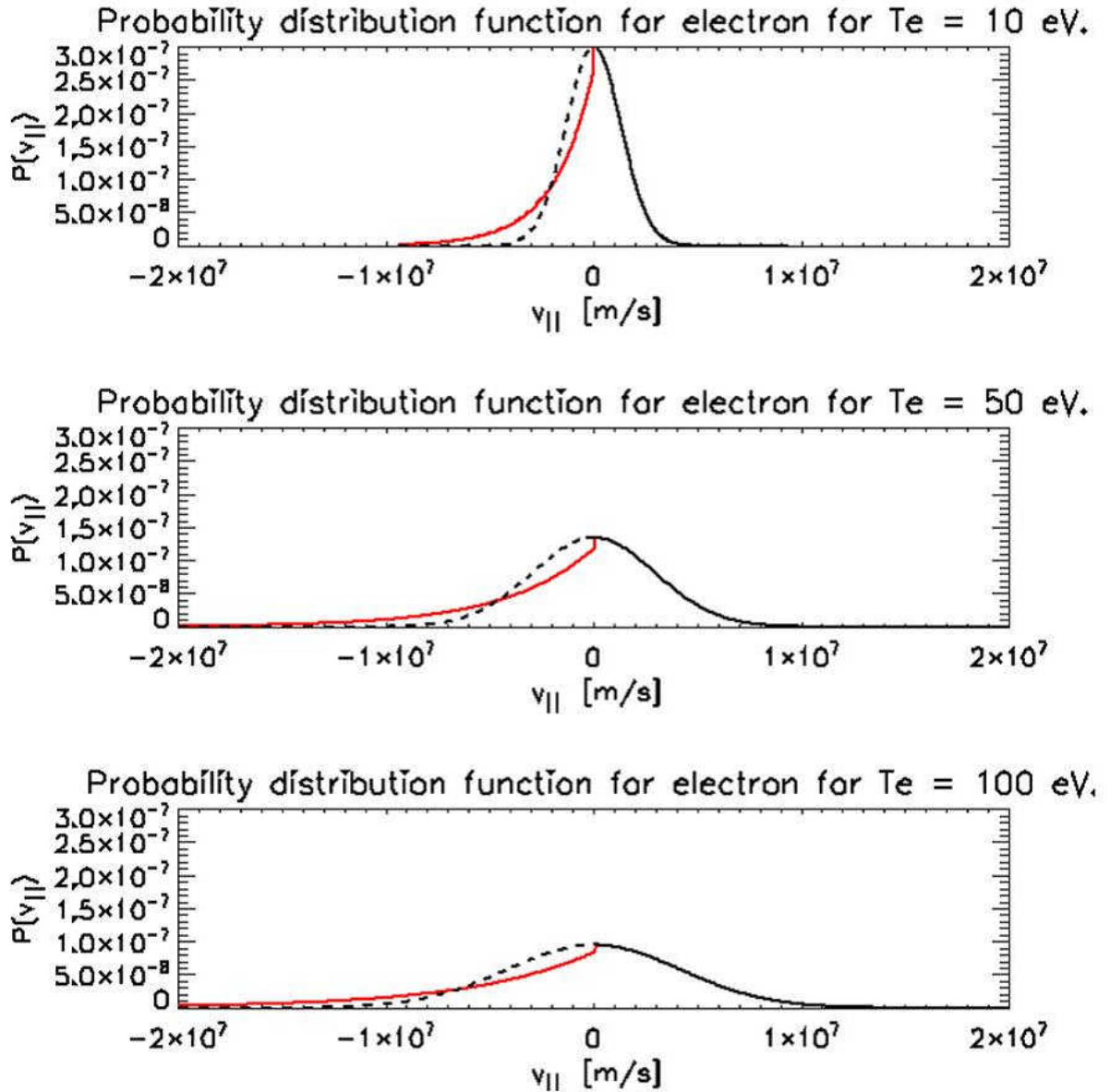
Figure 9.10: Probability distribution functions $P_{\mathrm{hybrid}}(v_\parallel \geq 0) = P_{\mathrm{M}}(v_\parallel \geq 0)$ (black line) and $P_{\mathrm{hybrid}}(v_\parallel < 0) = P_{\mathrm{non-M}}(v_\parallel < 0)$ (red line), with $P_{\mathrm{M}}(v_\parallel < 0)$ (black dashed line) shown for comparison, for $T_{\mathrm{e}} = 10$, 50, and $100\,\mathrm{eV}$.

Substituting Eqs. (9.57) and (9.58) into Eq. (9.59) gives the wave damping rate $\omega_{\text{i,hybrid}}$ as

$$\omega_{\text{i,hybrid}}(n_\parallel > 0) \quad = \quad -\frac{\sqrt{2\pi}}{2|n_\parallel|}\frac{\omega_{\text{pe}}^2}{\omega}\left(\frac{c}{v_{\text{t,e}}}\right)^3 \frac{1}{\frac{n_\perp^2\left[D^2 n^2 + (S-P)^2 n_\parallel^2\right]}{n^4} + \left(F n_\perp^2 + H n_\parallel^2\right)} \exp\left[-\left(\frac{c}{v_{\text{t,e}}}\right)^2 \frac{1}{2n_\parallel^2}\right],$$

(9.60)

$$\omega_{\text{i,hybrid}}(n_\parallel < 0) \quad = \quad -\frac{\pi}{4}\frac{\omega_{\text{pe}}^2}{\omega}\left(\frac{c}{v_{\text{t,e}}}\right)^2 \frac{1}{\frac{n_\perp^2\left[D^2 n^2 + (S-P)^2 n_\parallel^2\right]}{n^4} + \left(F n_\perp^2 + H n_\parallel^2\right)} \exp\left(-\frac{c}{v_{\text{t,e}}}\cdot\frac{1}{\sqrt{2}|n_\parallel|}\right).$$

(9.61)

The wave energy damping factor $\exp\left(2\omega_{\text{i,hybrid}}\tau\right)$ for the hybrid distribution is calculated and compared with $\exp\left(2\omega_{\text{i}}\tau\right)$ for the Maxwellian case in Fig. 9.11. For τ, values in the right column of Fig. 9.5 were used. From Fig. 9.11, it can be seen that the highest surviving $|n_\parallel|$ decreases as the population of higher energy electrons increases. It is noted that for the hybrid distributions with $T_{\text{e}} = 50\,\text{eV}$ and $100\,\text{eV}$, almost no wave energy survives for $|n_\parallel| > 10$, showing the possibility of explaining the measured wavenumber of $-19.6 \pm 11.0\,\text{m}^{-1}$ (corresponding to $n_\parallel = -9.5 \pm 2.6$). The wavenumber component around $k_\parallel = 105\,\text{m}^{-1}$ also vanishes for $T_{\text{e}} = 100\,\text{eV}$.

The surviving wave power spectrum at the probe assembly is calculated by multiplying the wavenumber spectrum of the LHW launched by the grill antenna (shown in Fig. 9.1) by the energy damping factor $\exp\left(2\omega_{\text{i,hybrid}}\tau\right)$ for the hybrid distribution shown in Fig. 9.11(b). The result is shown in Fig 9.12. From Fig. 9.12, the peak of the surviving power spectrum for $100\,\text{eV}$ (red solid line) is consistent with the measured wavenumber of $k_\parallel = -19.6 \pm 11.0\,\text{m}^{-1}$. From the comparison between the hybrid distribution and the Maxwellian distribution, it can be inferred that the same peak of the surviving spectrum at the probe assembly can be obtained even at lower electron temperatures than $100\,\text{eV}$ if a larger population of high energy electrons than the hybrid distribution with $100\,\text{eV}$ was present. Such a scenario could explain the experimentally measured wavenumber of $k_\parallel = -19.6 \pm 11.0\,\text{m}^{-1}$.

9.5   Summary of Discussion

In Section 9.1, the simplest case of a spatially uniform cold plasma with Maxwellian electron distribution function was treated. For low electron temperatures of up to $100\,\text{eV}$, two cases were examined:

- For T_{e} of $50\,\text{eV}$ or greater, the wave component with $n_\parallel = 25$ is expected to be damped before reaching the probe assembly, whereas the wave component with $n_\parallel = -9.5$ will survive and could be detected by the probe assembly.

- For T_{e} lower than $50\,\text{eV}$, both $n_\parallel = -9.5$ and 25 components survive and could be detected by the probe assembly.

For the first case, the down shift of $k_\parallel$ by the poloidal effect was discussed in Section 9.2. The expected downshift of $k_\parallel$ is at most $1.3\,\text{m}^{-1}$, which is too small to explain the difference between the launched value of $k_\parallel = 40\,\text{m}^{-1}$ and the measured value of $k_\parallel = 19.6 \pm 11.0\,\text{m}^{-1}$. For the second case, the apparent phase difference measured by the probe assembly in the presence of two different wavenumbers in exactly opposite directions was considered in Section 9.3. For typical signal amplitudes measured by electrodes 1 through 3, the calculated phase difference between electrodes 1 and 2 at the probe angle of 15 degrees was estimated to be in the range 70 degrees to 150 degrees, which is too large to explain the measured phase difference of about 20 degrees at the probe angle of 15 degrees.

In both cases, the difference between the launched value of $k_\parallel = -40\,\text{m}^{-1}$ and the measured value of $k_\parallel = -19.6 \pm 11.0\,\text{m}^{-1}$ cannot be explained. There are at least two possibilities:
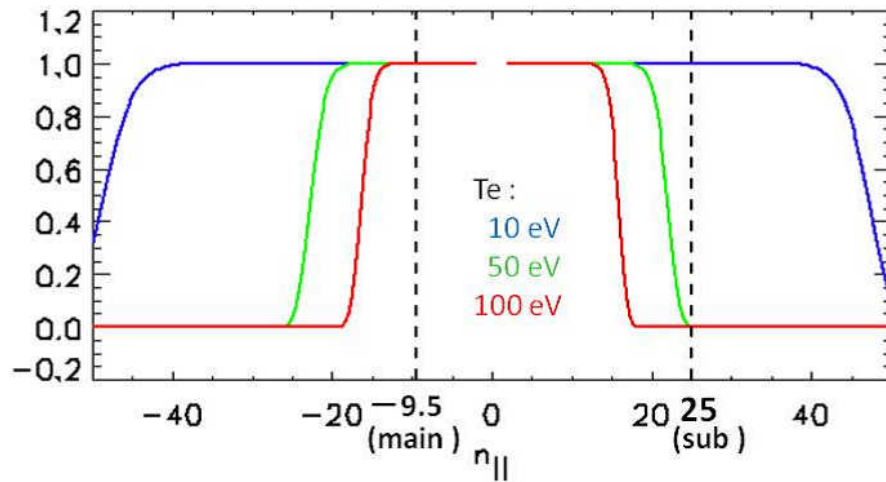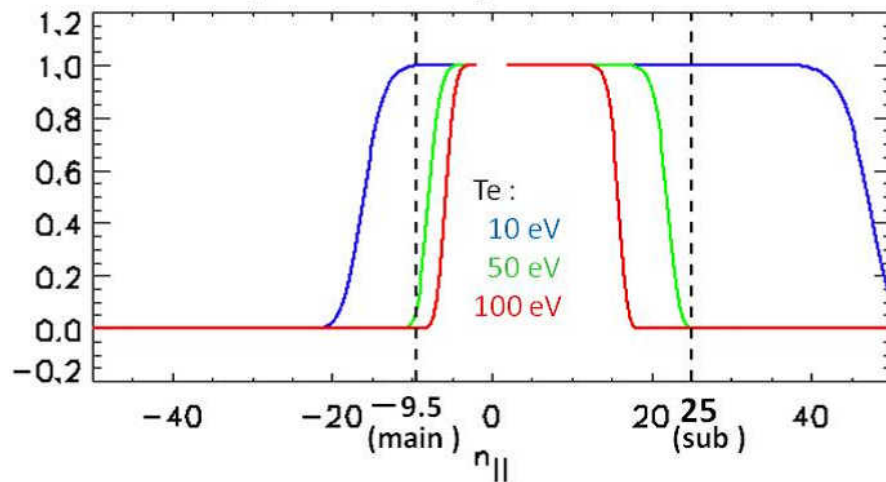
Figure 9.11: Wave energy damping factors for $T_e = 10\,\text{eV}$ (blue), $50\,\text{eV}$ (green), and $100\,\text{eV}$ (red) for (a) Maxwellian distribution and (b) hybrid distribution.
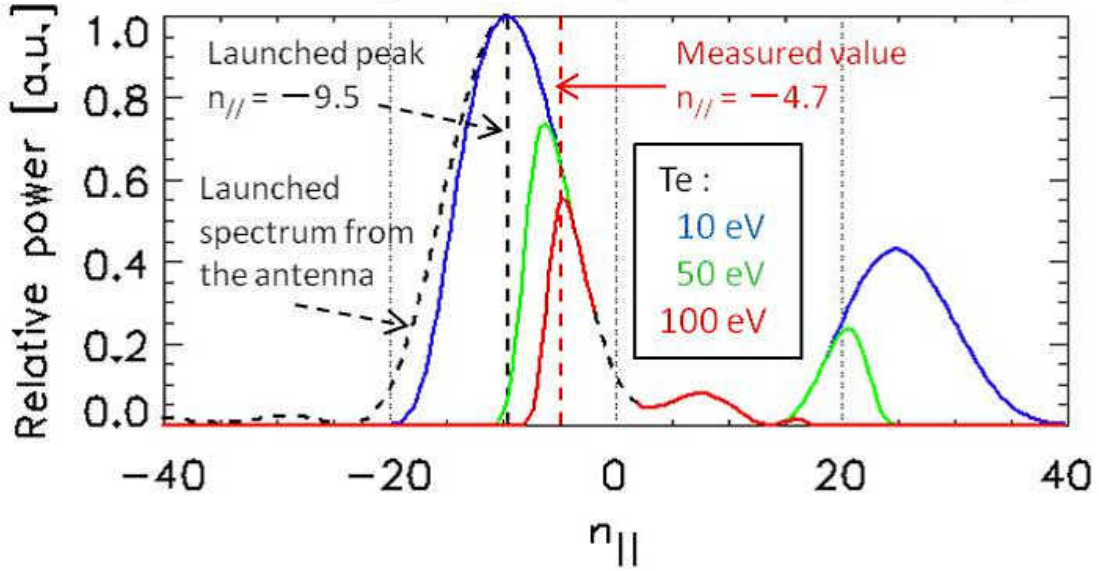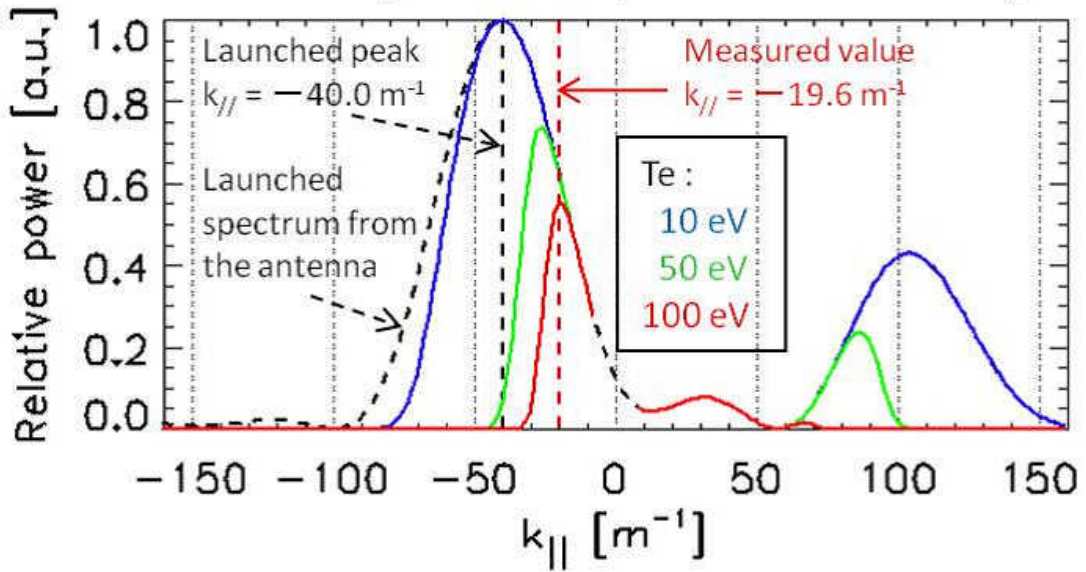
Figure 9.12: Calculated surviving refractive index spectrum and the wavenumber spectrum at the probe assembly for $T_e = 10$ (blue), 50 (green), and 100 eV (red) using the energy damping factor $\exp\left(2\omega_{i,\mathrm{hybrid}}\tau\right)$ for the hybrid distribution, shown in Fig. 9.11(b). The black dashed line shows the spectrum of the wave launched from the grill antenna.

183

- Electron velocity distribution function is not Maxwellian and fast electrons with energies of a few keV or grater exist in the plasma.

- Waves with different wavenumbers reach the probe assembly from different directions.

In Section 9.4, a "hybrid" distribution $f_{\text{hybrid}}(v_\parallel)$, with a larger population of fast electrons moving in the direction of the main lobe of the launched wave compared to the Maxwellian distribution, was used to evaluate wave damping analytically. A possible scenario to explain the experimentally measured wavenumber of $k_\parallel = -19.6 \pm 11.0\,\text{m}^{-1}$ (a factor of two smaller than the launched $k_\parallel = -40\,\text{m}^{-1}$) was given, indicating that the contribution of fast electrons to wave damping is important. Although this scenario was given for the "hybrid" distribution with $T_\text{e} = 100\,\text{eV}$, this distribution does not represent the real velocity distribution accurately. Wave damping depends sensitively on the slope of the distribution function at the wave phase velocity, which is difficult to determine experimentally. An improvement beyond the present analysis would involve a consistent use of a Fokker-Planck code to model the deformation of the velocity distribution function and a wave code (either full-wave or ray-tracing) to evaluate the spatial distribution of the wave fields.

The energy of electrons that interact with the launched wave can be estimated as follows. Electrons with velocity $v_\parallel$ can interact with the wave and absorb energy from the wave if

$$v_\parallel = \frac{\omega}{k_\parallel}, \tag{9.62}$$

where $\frac{\omega}{k_\parallel}$ is the parallel phase velocity of the wave. This is a literal expression of Eq. (2.196). Electrons with $v_\parallel$ have energies of at least

$$E_{\min} = \frac{1}{2} m_\text{e} v_\parallel^2, \tag{9.63}$$

where m_e is the electron mass. In order for waves at 200 MHz with $k_\parallel$ in the range $-40\,\text{m}^{-1}$ to $-20\,\text{m}^{-1}$ to be absorbed by the plasma, the minimum energy $E_{\min}$ of fast electrons is 2.8 keV for $k_\parallel = -40\,\text{m}^{-1}$ and 11.2 keV for $k_\parallel = -20\,\text{m}^{-1}$. From the measured value of $k_\parallel = -19.6 \pm 11.0\,\text{m}^{-1}$, electrons with energies in this range should exist during the initial phase of RF driven plasmas in TST-2.

For further considerations, there is a numerical code for simulating the development of the electron velocity distribution function in the presence of RF wave fields, called CQL3D [70]. This code is usually used with an RF wave code (ray-tracing or full-wave) and iterated until a self-consistent solution is obtained. In order to obtain simulation results which can be compared directly with experimental results, detailed measurements of the density profile, temperature profile, and hard x-ray profile (including the energy spectrum) are necessary. These quantities can be measured by a multichord interferometry, Thomson scattering, and hard x-ray tomography, but these diagnostic systems are still under development in TST-2. Such detailed comparisons remain a subject of future work.

Chapter 10

Conclusions and Future Works

10.1 Conclusions

Wavenumber measurements were performed during plasma start-up experiments on TST-2 using RF power at 200 MHz. Plasmas with plasma current of up to 2 kA were diagnosed using a probe assembly consisting of three high impedance Langmuir probe units, one single-loop magnetic probe, and one plain Langmuir probe. The high impedance Langmuir probe unit has a high impedance (100 kΩ) non-magnetic resistor placed immediately behind the probe electrode. From the results of wavenumber measurements using this probe assembly, the following conclusions are drawn:

1. Measurements of the identical wave performed using different pairs of electrodes by rotating the probe assembly gave the same phase difference, confirming the validity of wavenumber measurement. The direction of the measured wavenumber was nearly along the toroidal direction and counter-clockwise, consistent with the direction of the main component of the $k_\parallel$ spectrum of the wave launched from the grill antenna.

2. The polarization of the RF magnetic field was dominantly in the poloidal direction, consistent with the calculated polarization of the slow wave (LHW).

3. The fast wave is evanescent for the measured density of order $10^{16} \, \mathrm{m}^{-3}$.

4. The sensitivity of the probe assembly to electromagnetic waves was measured using a coaxial transmission line calibrator. Using the measured sensitivity to electromagnetic waves, neither the fast wave nor the electromagnetic wave can explain the ratio of the measured signal amplitudes of the high impedance Langmuir probe system (electrostatic probe) and the magnetic probe, whose typical amplitudes are about 4 mV and 6 mV, respectively. Since the waves which can exist inside the TST-2 vacuum vessel in the presence of a plasma are limited to the slow wave, the fast wave, and the electromagnetic wave, this result indicates that the contribution to the measured signal from the slow wave (LHW) is dominant.

5. Even though the absolute value of impedance of the high impedance Langmuir probe unit decreases from 100 kΩ to 2 kΩ due to capacitances $C_{\mathrm{box}} = 0.34 \, \mathrm{pF}$ formed between the probe electrode and the stainless steel shield box and $C_{\mathrm{parasitic}} = 0.065 \, \mathrm{pF}$ in the 100 kΩ non-magnetic resistor, the measured voltage signal amplitudes of 5.3 mV for the high impedance Langmuir probe unit and 54.6 mV for the plain Langmuir probe at 200 MHz showed that the total current drawn from the plasma is reduced by at least 40 % compared to the plain Langmuir probe by placing a high impedance resistor immediately behind the probe electrode. This reduction of the current drawn from the plasma indicates that the high impedance Langmuir probe unit detects the signal closer to the floating potential than a plain Langmuir probe. Therefore, the signal

measured by the high impedance Langmuir probe unit is closer to that originating from the LHW. This is consistent with the detection of the LHW-dominant signal mentioned in item 4.

6. Considering the five items 1 through 5 altogether, it can be concluded that the wavenumber of the slow wave (LHW) was measured successfully.

7. The measured toroidal wavenumber $k_\parallel = 19.6 \pm 11.0\,\mathrm{m}^{-1}$ is smaller by a factor of two compared to the main wavenumber component of the wave launched by the grill antenna, $k_\parallel = 40\,\mathrm{m}^{-1}$. This difference cannot be explained by a spatially uniform cold plasma model with Maxwellian electron velocity distribution function, even with the inclusion of $k_\parallel$ upshift/downshift and the presence of two different wavenumbers.

8. A possible scenario that can explain the measured toroidal wavenumber of $k_\parallel = 19.6 \pm 11.0\,\mathrm{m}^{-1}$ was given by a non-Maxwellian electron velocity distribution function with a larger population of fast electrons moving in the direction of the main lobe of the launched wave compared to the Maxwellian distribution, indicating that the contribution of fast electrons to wave damping is important. This scenario suggests that the main component of the launched wavenumber around $k_\parallel = 40\,\mathrm{m}^{-1}$ is absorbed by such fast electrons before reaching the probe assembly, and the wavenumber component not absorbed by the plasma reached the probe assembly, and was detected as $k_\parallel = 19.6 \pm 11.0\,\mathrm{m}^{-1}$.

9. From the Landau damping condition, the measured value of $k_\parallel = 19.6 \pm 11.0\,\mathrm{m}^{-1}$ requires fast electrons with energies in the range $2.8\,\mathrm{keV}$ (for $k_\parallel = 40\,\mathrm{m}^{-1}$) to $11.2\,\mathrm{keV}$ (for $k_\parallel = 20\,\mathrm{m}^{-1}$) during the initial phase of RF driven plasma in TST-2.

10. More detailed analysis of wave propagation and wave energy damping with proper inclusion of the electron distribution function evolution using sophisticated codes such as CQL3D, which makes quantitative comparison between experimental results and simulation results possible, remains a subject of future work. Such work will require more detailed information of the plasma including the density profile, the electron temperature profile, and hard x-ray profile (including the energy spectrum).

11. The work reported in this thesis provides experimentally measured toroidal and poloidal wavenumbers of the LHW at 200 MHz. These measured wavenumbers can be used as reference data for checking the validity of numerical codes such as CQL3D coupled with wave codes (GENRAY, TORLH, etc.). From the point of view of nuclear fusion research, this work makes important contributions needed for proper validation of such numerical codes which are widely used to analyze existing data and to make predictions for planned reactor-grade devices such as ITER and DEMO.

12. The measured wavenumbers provide information on wave excitation and propagation, as well as evidence of wave absorption by the plasma. These data can be used to characterize the initial plasmas driven by the LHW, and extract information such as the lower bound for the energy of fast electrons. Such information is useful for optimizing the plasma formation and plasma current ramp-up for ST plasmas, and for improving the design of the LHW antenna for the ST. Through such processes, the work reported in this thesis contributes to the realization of a more compact and economical magnetic fusion power plant.

10.2 Future Work

The following items are unanswered or unexplored, and remain subjects of future study:

1. In order to reduce the error for the measured phase difference, a reduction of RF noise is necessary. For example, in Fig. 8.10, there is room for improving the wavenumber measurement by reducing

the area of loops at the entrance of the oscilloscope. Enclosing the whole measurement system by metal completely might reduce RF noise. By reducing the RF noise, it is expected that in addition to the toroidal wavenumber, the poloidal wavenumber could also be specified.

2. In order to measure signals even closer to the floating potential, the impedance of the high impedance Langmuir probe unit should be increased. Since the reduction of the impedance is caused primarily by the capacitance C_{box}, it is suggested that C_{box} is reduced by decreasing the thickness of the stainless steel shield box to increase the distance of the stainless steel shield box from the probe electrode.

3. For a more direct proof of the detection of the LHW, the LHW dispersion relation should be confirmed. This is possible, as described in Ref. [48], by measuring the radial wavenumber component by scanning the position of the probe assembly radially and measuring the phase shift with respect to a reference signal sampled from the incident wave to the antenna. It should be noted that by scanning the radial position of the probe assembly, the sheath in front of the electrostatic probe changes, leading to the possibility for the frequency response of the electrostatic probe to depend on the radial position, thus breaking the simple relationship between the signal measured by the electrostatic probe and the reference signal. If this were the case, it may be necessary to use a magnetic probe, which is considered to be less sensitive to the effect of the sheath than the electrostatic probe.

4. In order to expand the range of application of the electrostatic probe, such as measuring the phase difference of high frequency signals by scanning the radial position of the probe mentioned in item 3, the establishment of the high frequency sheath model is important. This should be possible by accumulating data obtained by electrostatic probes with various impedances to plasmas with various densities and temperatures at high frequencies such as 200 MHz.

5. Wavenumber measurements of the LHW at different positions and times, using arrays of probe assemblies distributed in space, will reveal the spatio-temporal change of the wavenumber and the RF field strength, providing further information on start-up plasmas driven by the LHW.

6. Effects of secondary electron emission from the probe electrode by collisions with fast electrons are necessary to measure the LHW wavenumber in RF start-up plasmas with larger plasma currents, in which larger numbers of fast electrons are present.

7. As stated in the conclusions, the result of wavenumber measurements should be compared with the analysis of wave propagation and wave energy damping with proper inclusion of the electron distribution function evolution using sophisticated codes such as CQL3D, which will require more detailed information of the plasma including the electron density profile, the electron temperature profile, and the hard x-ray emission profile (including the energy spectrum).

Acknowledgements

Appendix A

Theory of Electromagnetic Waves in a Coaxial Transmission Line

In order to calibrate the sensitivities of the electrostatic probe and the magnetic probe to the electromagnetic wave in a coaxial transmission line, it is necessary to understand how the wave propagates in the coaxial transmission line. A wave propagating in a waveguide which satisfies the following three conditions is considered [65]:

- Made by a perfect conductor.

- Filled with a non-dissipative material uniformly whose permittivity and permeability are ϵ and μ, respectively.

- The axis of the waveguide is straight and the shape of the cross-section is identical along the axis of the waveguide.

A.1 Expression of Transverse Field Components in Terms of Longitudinal Field Components

In this analysis, the z-axis is taken along the axis of the waveguide. In the absence of external charge or current, Maxwell's equations take the form

$$
\left\{
\begin{aligned}
& \nabla \cdot \boldsymbol{E} = 0, && \text{(A.1)} \\
& \nabla \times \boldsymbol{E} = -\frac{\partial \boldsymbol{B}}{\partial t}, && \text{(A.2)} \\
& \nabla \cdot \boldsymbol{B} = 0, && \text{(A.3)} \\
& \nabla \times \boldsymbol{B} = \mu\epsilon\frac{\partial \boldsymbol{E}}{\partial t}. && \text{(A.4)}
\end{aligned}
\right.
$$

These equations yield

$$
\left\{
\begin{aligned}
& \nabla^2 \boldsymbol{E} = \mu\epsilon\frac{\partial^2 \boldsymbol{E}}{\partial t^2}, && \text{(A.5)} \\
& \nabla^2 \boldsymbol{B} = \mu\epsilon\frac{\partial^2 \boldsymbol{B}}{\partial t^2}. && \text{(A.6)}
\end{aligned}
\right.
$$

These two differential equations are symmetric for $\boldsymbol{E}$ and $\boldsymbol{B}$. Taking the waveguide geometry into account, $\boldsymbol{E}$ and $\boldsymbol{B}$ can be expressed as

$$
\begin{cases}
\boldsymbol{E}(x,y,z,t) = \boldsymbol{E}(x,y)e^{i(kz-\omega t)}, & \text{(A.7)} \\
\boldsymbol{B}(x,y,z,t) = \boldsymbol{B}(x,y)e^{i(kz-\omega t)}. & \text{(A.8)}
\end{cases}
$$

where the x-y plane is perpendicular to the z-axis and k is the wavenumber for a wave propagating in the z direction. Using Eq. (A.7), Eq. (A.5) gives

$$
\left\{ \left(\frac{\partial^2}{\partial x^2} + \frac{\partial^2}{\partial y^2} - k^2 \right) \boldsymbol{E}(x,y) \right\} e^{i(kz-\omega t)} = \mu\epsilon \left(-\omega^2 \right) \boldsymbol{E}(x,y)e^{i(kz-\omega t)},
$$

from which

$$
\left[\nabla_t{}^2 + \left(\mu\epsilon\omega^2 - k^2 \right) \right] \boldsymbol{E}(x,y,z,t) = 0 \tag{A.9}
$$

is obtained where $\nabla_t{}^2$ is defined as

$$
\nabla_t{}^2 \equiv \frac{\partial^2}{\partial x^2} + \frac{\partial^2}{\partial y^2} = \nabla^2 - \frac{\partial^2}{\partial z^2} \, . \tag{A.10}
$$

The differentiation in Eq. (A.9) is two dimensional. It is convenient to separate $\boldsymbol{E}(x,y,z,t)$ into components parallel and perpendicular to the z-axis:

$$
\boldsymbol{E}(x,y,z,t) = \boldsymbol{E}_z(x,y,z,t) + \boldsymbol{E}_t(x,y,z,t) = \hat{\boldsymbol{z}}E_z + \boldsymbol{E}_t \tag{A.11}
$$

where $\hat{\boldsymbol{z}}$ is the unit vector along the z-axis and

$$
\begin{align}
\boldsymbol{E}_z &= \hat{\boldsymbol{z}}E_z \tag{A.12} \\
\boldsymbol{E}_t &= (\hat{\boldsymbol{z}} \times \boldsymbol{E}) \times \hat{\boldsymbol{z}} \, . \tag{A.13}
\end{align}
$$

Similarly,

$$
\boldsymbol{B}(x,y,z,t) = \boldsymbol{B}_z(x,y,z,t) + \boldsymbol{B}_t(x,y,z,t) = \hat{\boldsymbol{z}}B_z + \boldsymbol{B}_t. \tag{A.14}
$$

Maxwell's equations (A.1)–(A.4) can be expressed in terms of E_z, $\boldsymbol{E}_t$, B_z, and $\boldsymbol{B}_t$. First, using

$$
\nabla = \left(\hat{\boldsymbol{x}}\frac{\partial}{\partial x} + \hat{\boldsymbol{y}}\frac{\partial}{\partial y} \right) + \hat{\boldsymbol{z}}\frac{\partial}{\partial z} = \nabla_t + \hat{\boldsymbol{z}}\frac{\partial}{\partial z} \tag{A.15}
$$

and Eq. (A.11), Eq. (A.1) becomes

$$
\left(\nabla_t + \hat{\boldsymbol{z}}\frac{\partial}{\partial z} \right) \cdot (\boldsymbol{E}_t + \hat{\boldsymbol{z}}E_z) = 0 \, ,
$$

leading to

$$
\nabla_t \cdot \boldsymbol{E}_t + \frac{\partial E_z}{\partial z} = 0 \, . \tag{A.16}
$$

Faraday's law Eq. (A.2) is combined with Eq. (A.8) to give

$$
\nabla \times \boldsymbol{E} = i\omega\boldsymbol{B}. \tag{A.17}
$$

With the help of Eqs. (A.11), (A.14), and (A.15), Eq. (A.17) leads to,

$$
\left(\nabla_t + \hat{\boldsymbol{z}}\frac{\partial}{\partial z} \right) \times (\boldsymbol{E}_t + \hat{\boldsymbol{z}}E_z) = i\omega \left(\boldsymbol{B}_t + \hat{\boldsymbol{z}}B_z \right) . \tag{A.18}
$$

The left-hand side of Eq. (A.18) is

$$\left(\nabla_t + \hat{\boldsymbol{z}}\frac{\partial}{\partial z}\right) \times (\boldsymbol{E}_t + \hat{\boldsymbol{z}}E_z)$$

$$= \nabla_t \times \boldsymbol{E}_t + \nabla_t \times (\hat{\boldsymbol{z}}E_z) + \left(\hat{\boldsymbol{z}}\frac{\partial}{\partial z}\right) \times \boldsymbol{E}_t + \left(\hat{\boldsymbol{z}}\frac{\partial}{\partial z}\right) \times (\hat{\boldsymbol{z}}E_z) \qquad \text{(A.19)}$$

$$= (z-\text{component}) + (t-\text{component}) + (t-\text{component}) + \boldsymbol{0}\,.$$

Making use of Eq. (A.19), and taking the inner product of Eq. (A.18) with $\hat{\boldsymbol{z}}$ gives

$$\hat{\boldsymbol{z}} \cdot (\nabla_t \times \boldsymbol{E}_t) = i\omega B_z \qquad \text{(A.20)}$$

whereas taking the cross product of Eq. (A.18) with $\hat{\boldsymbol{z}}$ yields

$$i\omega\hat{\boldsymbol{z}} \times \boldsymbol{B}_t$$

$$= \hat{\boldsymbol{z}} \times \{\nabla_t \times (\hat{\boldsymbol{z}}E_z)\} + \hat{\boldsymbol{z}} \times \left\{\left(\hat{\boldsymbol{z}}\frac{\partial}{\partial z}\right) \times \boldsymbol{E}_t\right\}$$

$$= \hat{\boldsymbol{z}} \times \{(\nabla_t E_z) \times \hat{\boldsymbol{z}}\} + \hat{\boldsymbol{z}} \times \left\{\hat{\boldsymbol{z}} \times \frac{\partial \boldsymbol{E}_t}{\partial z}\right\}$$

$$= \{(\nabla_t E_z) - [\hat{\boldsymbol{z}} \cdot (\nabla_t E_z)]\,\hat{\boldsymbol{z}}\} + \left\{\left(\hat{\boldsymbol{z}} \cdot \frac{\partial \boldsymbol{E}_t}{\partial z}\right)\hat{\boldsymbol{z}} - \frac{\partial \boldsymbol{E}_t}{\partial z}\right\}$$

$$= \nabla_t E_z - \frac{\partial \boldsymbol{E}_t}{\partial z}, \qquad \text{(A.21)}$$

where

$$\hat{\boldsymbol{z}} \cdot (\nabla_t E_z) = 0 \quad \text{and} \quad \hat{\boldsymbol{z}} \cdot \frac{\partial \boldsymbol{E}_t}{\partial z} = 0$$

have been used, since both $\nabla_t E_z$ and $\frac{\partial \boldsymbol{E}_t}{\partial z}$ are in the x-y plane. Equations (A.16), (A.20), and (A.21) are summarized as below:

$$\nabla_t \cdot \boldsymbol{E}_t = -\frac{\partial E_z}{\partial z}, \qquad \text{(A.22)}$$

$$\hat{\boldsymbol{z}} \cdot (\nabla_t \times \boldsymbol{E}_t) = i\omega B_z\,, \qquad \text{(A.23)}$$

$$\frac{\partial \boldsymbol{E}_t}{\partial z} + i\omega\hat{\boldsymbol{z}} \times \boldsymbol{B}_t = \nabla_t E_z\,. \qquad \text{(A.24)}$$

Formally, Eqs. (A.22)–(A.24) are derived from Eqs. (A.1) and (A.2):

$$\begin{cases} \nabla \cdot \boldsymbol{E} &= 0, \\ \nabla \times \boldsymbol{E} &= i\omega\boldsymbol{B}, \end{cases}$$

with assumptions Eqs. (A.7) and (A.8). Using the symmetry between $\boldsymbol{E}$ and $\boldsymbol{B}$, Eqs. (A.3), (A.4):

$$\begin{cases} \nabla \cdot \boldsymbol{B} &= 0 \\ \nabla \times \boldsymbol{B} &= -i\mu\epsilon\omega\boldsymbol{E} \end{cases}$$

and with assumptions Eqs. (A.7), (A.8)

$$\nabla_t \cdot \boldsymbol{B}_t = -\frac{\partial B_z}{\partial z}, \qquad \text{(A.25)}$$

$$\hat{\boldsymbol{z}} \cdot (\nabla_t \times \boldsymbol{B}_t) = -i\mu\epsilon\omega E_z\,, \qquad \text{(A.26)}$$

$$\frac{\partial \boldsymbol{B}_t}{\partial z} - i\mu\epsilon\omega\hat{\boldsymbol{z}} \times \boldsymbol{E}_t = \nabla_t B_z \qquad \text{(A.27)}$$

192

where replacements $\boldsymbol{E} \to \boldsymbol{B}$, $\boldsymbol{B} \to \boldsymbol{E}$, and $\omega \to -\mu\epsilon\omega$ were applied to Eqs. (A.22)–(A.24).

$\boldsymbol{E}_t$ and $\boldsymbol{B}_t$ can be expressed in terms of E_z and B_z. Using

$$\frac{\partial \boldsymbol{E}_t}{\partial z} = \frac{\partial}{\partial z} \left\{ [\hat{\boldsymbol{x}}E_x(x,y) + \hat{\boldsymbol{y}}E_y(x,y)] e^{[i(kz-\omega t)]} \right\} = ik\boldsymbol{E}_t \tag{A.28}$$

and

$$\frac{\partial \boldsymbol{B}_t}{\partial z} = ik\boldsymbol{B}_t\,, \tag{A.29}$$

Eqs. (A.24) and (A.27) give

$$ik\boldsymbol{E}_t + i\omega\left(\hat{\boldsymbol{z}} \times \boldsymbol{B}_t\right) = \nabla_t E_z, \tag{A.30}$$
$$ik\boldsymbol{B}_t - i\mu\epsilon\omega\left(\hat{\boldsymbol{z}} \times \boldsymbol{E}_t\right) = \nabla_t B_z. \tag{A.31}$$

Taking the cross product of (A.31) with $\hat{\boldsymbol{z}}$ yields

$$ik\left(\hat{\boldsymbol{z}} \times \boldsymbol{B}_t\right) + i\mu\epsilon\omega\boldsymbol{E}_t = \hat{\boldsymbol{z}} \times \left(\nabla_t B_z\right), \tag{A.32}$$

where

$$\hat{\boldsymbol{z}} \times \left(\hat{\boldsymbol{z}} \times \boldsymbol{E}_t\right) = \left(\hat{\boldsymbol{z}} \cdot \boldsymbol{E}_t\right)\hat{\boldsymbol{z}} - \left(\hat{\boldsymbol{z}} \cdot \hat{\boldsymbol{z}}\right)\boldsymbol{E}_t = -\boldsymbol{E}_t$$

was used. Calculating $[(A.30) \times k - (A.32) \times \omega]$ yields

$$i\left(k^2 - \mu\epsilon\omega^2\right)\boldsymbol{E}_t = k\nabla_t E_z - \omega\hat{\boldsymbol{z}} \times \left(\nabla_t B_z\right). \tag{A.33}$$

If either $E_z \neq 0$ or $B_z \neq 0$ and $k^2 - \mu\epsilon\omega^2 \neq 0$,

$$\boldsymbol{E}_t = \frac{i}{\mu\epsilon\omega^2 - k^2}\left[k\nabla_t E_z - \omega\hat{\boldsymbol{z}} \times \left(\nabla_t B_z\right)\right], \tag{A.34}$$

and similarly

$$\boldsymbol{B}_t = \frac{i}{\mu\epsilon\omega^2 - k^2}\left[k\nabla_t B_z + \mu\epsilon\omega\hat{\boldsymbol{z}} \times \left(\nabla_t E_z\right)\right]. \tag{A.35}$$

A.2   Transverse Electromagnetic (TEM) Wave

When both $E_z = 0$ and $B_z = 0$, the electromagnetic field in a waveguide has purely transverse components. Such a wave is called the transverse electromagnetic (TEM) wave. For both $E_z = 0$ and $B_z = 0$, and for non-zero $\boldsymbol{E}_t$, Eq. (A.33) gives

$$\mu\epsilon\omega^2 - k^2 = 0, \tag{A.36}$$

leading to

$$k = \pm\omega\sqrt{\mu\epsilon} \equiv \pm k_0. \tag{A.37}$$

Combining these wavenumbers with Eqs. (A.30) or (A.31), the relationship between $\boldsymbol{E}_t$ and $\boldsymbol{B}_t$ is given as

$$\boldsymbol{B}_t = \pm\sqrt{\mu\epsilon}\hat{\boldsymbol{z}} \times \boldsymbol{E}_t. \tag{A.38}$$

This relationship is the same as that for a plane wave propagating in an infinite space. Using both $E_z = 0$ and $B_z = 0$, Eqs. (A.22) and (A.23) give

$$\nabla_t \cdot \boldsymbol{E}_t = 0, \tag{A.39}$$
$$\nabla_t \times \boldsymbol{E}_t = \boldsymbol{0}, \tag{A.40}$$

meaning that $\boldsymbol{E}_t$ takes the same form as for the 2-dimensional electrostatic situation. These conditions impose a limitation on the environment in which the TEM wave can exist as described in Ref. [65].

If a volume is enclosed by a perfect conductor, the potential on its surface is equal under the electro-static situation and thus the electric field is zero inside the volume. Therefore, in a single cylindrical waveguide, for example, the TEM wave cannot exist. Conversely, if the volume is enclosed by multiple conductors, the potentials on the surfaces of different conductors can be different, providing a room for the electric field to exist. Therefore, the TEM wave can propagate inside a coaxial waveguide, which consists of two cylindrical conductors (the inner and outer conductors).

Appendix B

Signal Processing

B.1 Discrete Fourier Transform

In order to obtain the LHW wavenumber from probe signals, it is necessary to extract the phase and amplitude of the frequency component of interest. Since data are acquired discretely, a discrete Fourier transform is used [71].

A real function $x(t)$ which is periodic with period T can in principle be expressed in a linear combination of a constant, sine waves, and cosine waves as follows:

$$x(t) = \frac{a_0}{2} + \sum_{n=1}^{\infty} \left\{ a_n \cos(\omega_n t) + b_n \sin(\omega_n t) \right\}, \tag{B.1}$$

where n is a non-negative integer, $\{a_n\}$ and $\{b_n\}$ are real amplitudes, and ω_n is the angular frequency whose period T_n is included exactly n times in the time interval $\left[-\frac{T}{2}, \frac{T}{2} \right]$, i.e.,

$$n T_n = T, \tag{B.2}$$

$$\omega_n = \frac{2\pi}{T_n} = \frac{2\pi}{T} n. \tag{B.3}$$

Expression (B.1) is possible due to the completeness formed among a constant, sine waves, and cosine waves. Using the orthogonality:

$$\int_{-\frac{T}{2}}^{\frac{T}{2}} 1 \cdot \cos(\omega_n t) dt = 0, \qquad \int_{-\frac{T}{2}}^{\frac{T}{2}} 1 \cdot \sin(\omega_n t) dt = 0, \qquad \int_{-\frac{T}{2}}^{\frac{T}{2}} \cos(\omega_m t) \sin(\omega_n t) dt = 0, \qquad \text{and}$$

$$\int_{-\frac{T}{2}}^{\frac{T}{2}} \cos(\omega_m t) \cos(\omega_n t) dt = \int_{-\frac{T}{2}}^{\frac{T}{2}} \sin(\omega_m t) \sin(\omega_n t) dt = \frac{T}{2} \delta_{m,n},$$

where m is a non-negative integer and $\delta_{m,n}$ is the Kronecker delta. a_n and b_n are given as

$$a_n = \frac{2}{T} \int_{-\frac{T}{2}}^{\frac{T}{2}} x(t) \cos(\omega_n t) dt, \tag{B.4}$$

$$b_n = \frac{2}{T} \int_{-\frac{T}{2}}^{\frac{T}{2}} x(t) \sin(\omega_n t) dt. \tag{B.5}$$

$x(t)$ can be expressed with complex numbers by applying the relationships

$$\cos(\omega_n t) = \frac{e^{i\omega_n t} + e^{-i\omega_n t}}{2}, \qquad \sin(\omega_n t) = \frac{e^{i\omega_n t} - e^{-i\omega_n t}}{2i}$$

to Eq. (B.1) as

$$
\begin{aligned}
x(t) &= \frac{a_0}{2} + \sum_{n=1}^{\infty} \left(\frac{a_n - ib_n}{2} e^{i\omega_n t} + \frac{a_n + ib_n}{2} e^{-i\omega_n t} \right) \\
&= \frac{a_0}{2} + \sum_{n=1}^{\infty} \left(A_n e^{i\omega_n t} + B_n e^{-i\omega_n t} \right),
\end{aligned} \tag{B.6}
$$

where

$$
\begin{aligned}
A_n \equiv \frac{a_n - ib_n}{2} &= \frac{1}{2} \left\{ \frac{2}{T} \int_{-\frac{T}{2}}^{\frac{T}{2}} x(t) \cos(\omega_n t) dt - i \frac{2}{T} \int_{-\frac{T}{2}}^{\frac{T}{2}} x(t) \sin(\omega_n t) dt \right\} \\
&= \frac{1}{T} \int_{-\frac{T}{2}}^{\frac{T}{2}} x(t) \left\{ \cos(\omega_n t) - i \sin(\omega_n t) \right\} dt \\
&= \frac{1}{T} \int_{-\frac{T}{2}}^{\frac{T}{2}} x(t) e^{-i\omega_n t} dt
\end{aligned} \tag{B.7}
$$

and

$$
B_n \equiv \frac{a_n + ib_n}{2} = \frac{1}{T} \int_{-\frac{T}{2}}^{\frac{T}{2}} x(t) e^{i\omega_n t} dt. \tag{B.8}
$$

Since a_n and b_n are real, Eqs. (B.7) and (B.8) give

$$
B_n = \overline{A}_n, \tag{B.9}
$$

where $\overline{A}_n$ denotes the complex conjugate of A_n. Using

$$
A_0 = \frac{a_0 - ib_0}{2} = \frac{a_0}{2} \tag{B.10}
$$

and

$$
e^{-i\omega t} = \overline{e^{i\omega t}}, \tag{B.11}
$$

Eq. (B.6) becomes

$$
\begin{aligned}
x(t) &= A_0 + \sum_{n=1}^{\infty} \left(A_n e^{i\omega_n t} + \overline{A_n e^{i\omega_n t}} \right) \\
&= A_0 + \sum_{n=1}^{\infty} 2\text{Re} \left[A_n e^{i\omega_n t} \right] \\
&= A_0 + \sum_{n=1}^{\infty} 2\text{Re} \left[|A_n| e^{i(\omega_n t + \arg A_n)} \right] \\
&= A_0 + \sum_{n=1}^{\infty} 2|A_n| \cos (\omega_n t + \arg A_n).
\end{aligned} \tag{B.12}
$$

Since n represents a harmonic of the fundamental frequency $f_0 = \frac{1}{T}$, Eq. (B.12) states that $x(t)$ consists of various harmonic signals with amplitude $2|A_n|$ and phase $\arg A_n$. In practice, n is limited by the number of sampled data by the sampling theorem. This theorem requires the sampling frequency (or sampling rate) to be at least twice larger than that of the signal to be measured. For example, if the data sampling is conducted $N+1$ times with equal interval in the period T (i.e., the period T is equally divided into N intervals by $N+1$ sampling points including two end points), the sampling rate f_s for this case is

$$
f_s = \frac{T}{N} \tag{B.13}
$$

and the sampling theorem requires

$$f_s = \frac{N}{T} > 2 \times n f_0 = \frac{2n}{T},$$ (B.14)

restricting the value of n to

$$n < \frac{N}{2} \equiv m.$$ (B.15)

If N is an even number, m is a positive integer.

From now on, this case is considered. The summation in Eq. (B.12) is performed for n up to $\frac{N}{2} - 1 = m - 1$. Under this condition, Eq. (B.12) becomes

$$x(t) = A_0 + \sum_{n=1}^{m-1} 2|A_n| \cos(\omega_n t + \arg A_n).$$ (B.16)

It should be noted that, because of aliasing, contributions from higher frequency components with $n \geq m$ are included in the summation Eq. (B.16) as lower frequency components. Fortunately, in the plasma current drive experiments in TST-2 using the LHW at $200\,\mathrm{MHz}$, most of these unfavorable contributions are small enough or appear at frequencies different from that of interest.

Expression (B.16) is convenient for relating the Fourier component A_n to the real signal $x(t)$. Using the periodicity of $x(t)$ with time T, $x(t-T) = x(t)$, and the discrete integration, A_n can be computed from Eq. (B.7) as

$$
\begin{aligned}
A_n &= \frac{1}{T} \int_{-\frac{T}{2}}^{\frac{T}{2}} x(t) e^{-i\omega_n t} dt \\
&= \frac{1}{T} \left\{ \int_{-\frac{T}{2}}^{0} x(t) e^{-i\omega_n t} dt + \int_{0}^{\frac{T}{2}} x(t) e^{-i\omega_n t} dt \right\} \\
&= \frac{1}{T} \left\{ \int_{\frac{T}{2}}^{T} x(t-T) e^{-i\omega_n t} e^{i\omega_n T} dt + \int_{0}^{\frac{T}{2}} x(t) e^{-i\omega_n t} dt \right\} \\
&= \frac{1}{T} \left\{ \int_{\frac{T}{2}}^{T} x(t) e^{-i\omega_n t} dt + \int_{0}^{\frac{T}{2}} x(t) e^{-i\omega_n t} dt \right\} \\
&= \frac{1}{T} \int_{0}^{T} x(t) e^{-i\omega_n t} dt \\
&= \frac{1}{T} \sum_{k=0}^{N-1} x\left(k\frac{T}{N}\right) e^{-i\omega_n k \frac{T}{N}} \frac{T}{N} \\
&= \frac{1}{N} \sum_{k=0}^{N-1} x\left(k\frac{T}{N}\right) e^{-i\frac{2\pi n}{N} k},
\end{aligned}
$$ (B.17)

where $\omega_n = \frac{2\pi n}{T}$, $t = k\frac{T}{N}$ ($k = 0, 1, 2, \cdots, N-1$), and $dt = \frac{T}{N}$ were used. This is the discrete Fourier transform.

B.2 Cross-Spectrum

When considering the relationship between two time series data, say $x(t)$ and $y(t)$, the phase difference and the coherence between them are important. These two quantities stem from the cross-correlation function $C_{xy}(\tau)$, which is defined as a long time average of the product of $x(t)$ and $y(t+\tau)$ as

$$C_{xy}(\tau) = \langle x(t) y(t+\tau) \rangle = \lim_{T \to \infty} \frac{1}{T} \int_{-\frac{T}{2}}^{\frac{T}{2}} x(t) y(t+\tau) dt,$$ (B.18)

197

where "$<>$" means taking the average and τ is the time lag between the two signals. The cross-spectrum $S_{xy}(\omega)$ is defined as the Fourier transform of the cross-correlation function as

$$S_{xy}(\omega) = \frac{1}{2\pi} \int_{-\infty}^{\infty} C_{xy}(\tau) e^{-i\omega\tau} d\tau. \tag{B.19}$$

The cross-spectrum quantifies the "strength" of correlation between the two signals as a function of ω.

B.2.1 Expression of Cross-Spectrum in Terms of Fourier Transforms of $x(t)$ and $y(t)$

The purpose of this subsection is to express $S_{xy}(\omega)$ in terms of Fourier transforms of $x(t)$ and $y(t)$. The Fourier transform used here is a manipulation described as follows. Starting from Eq. (B.6), $x(t)$ can be expressed as

$$
\begin{aligned}
x(t) &= \frac{a_0}{2} + \sum_{n=1}^{\infty} \left(A_n e^{i\omega_n t} + B_n e^{-i\omega_n t} \right) \\
&= A_0 + \sum_{n=1}^{\infty} \left(A_n e^{i\omega_n t} + A_{-n} e^{i\omega_{-n} t} \right) \\
&= \sum_{n=-\infty}^{\infty} A_n e^{i\omega_n t},
\end{aligned}
\tag{B.20}
$$

where from Eq. (B.3),

$$-\omega_n = -\frac{2\pi n}{T} = \frac{2\pi(-n)}{T} \equiv \omega_{-n} \tag{B.21}$$

and from Eqs. (B.7), (B.8), and (B.21),

$$B_n = A_{-n} \tag{B.22}$$

are used. Substituting Eq. (B.7) into Eq. (B.20), $x(t)$ is expressed as

$$
\begin{aligned}
x(t) &= \sum_{n=-\infty}^{\infty} A_n e^{i\omega_n t} \\
&= \sum_{n=-\infty}^{\infty} \left\{ \left[\frac{1}{T} \int_{-\frac{T}{2}}^{\frac{T}{2}} x(t') e^{-i\omega_n t'} dt' \right] e^{i\omega_n t} \right\} \\
&= \sum_{n=-\infty}^{\infty} \left\{ \left[\int_{-\frac{T}{2}}^{\frac{T}{2}} x(t') e^{-i2\pi(n\Delta f)t'} dt' \right] e^{i2\pi(n\Delta f)t} \Delta f \right\},
\end{aligned}
\tag{B.23}
$$

where Δf was substituted for $\frac{1}{T}$ in the last row. Taking the limit $T \to \infty$ gives $\Delta f \to 0$, leading to

$$
\begin{aligned}
x(t) &\to \int_{-\infty}^{\infty} \left[\int_{-\infty}^{\infty} x(t') e^{-i2\pi f t'} dt' \right] e^{i2\pi f t} df \\
&= \int_{-\infty}^{\infty} [X(f)] e^{i2\pi f t} df,
\end{aligned}
\tag{B.24}
$$

where $n\Delta f$ is denoted by f and $X(f)$ takes the form

$$X(f) = \int_{-\infty}^{\infty} x(t) e^{-i2\pi f t} dt. \tag{B.25}$$

This is the Fourier transform. In practice, $\omega = 2\pi f$ is used instead of f and Eq. (B.24) gives

$$x(t) = \int_{-\infty}^{\infty} \frac{X(f)}{2\pi} e^{i\omega t} d\omega. \tag{B.26}$$

Denoting $\frac{X(f)}{2\pi}$ as $X(\omega)$, (B.25) and (B.26) give the forms of Fourier transform and the inverse transform as

$$X(\omega) = \frac{1}{2\pi} \int_{-\infty}^{\infty} x(t) e^{-i\omega t} dt, \tag{B.27}$$

$$x(t) = \int_{-\infty}^{\infty} X(\omega) e^{i\omega t} d\omega. \tag{B.28}$$

$C_{xy}(\tau)$ is expressed in terms of $S_{xy}(\omega)$ by inverse Fourier transform of Eq. (B.19) as

$$C_{xy}(\tau) = \int_{-\infty}^{\infty} S_{xy}(\omega) e^{i\omega\tau} d\omega. \tag{B.29}$$

From the definition of $C_{xy}(\tau)$ shown in Eq. (B.18) and using Eqs. (B.27) and (B.28), $C_{xy}(\tau)$ is expressed as

$$
\begin{aligned}
C_{xy}(\tau) &= \lim_{T\to\infty} \frac{1}{T} \int_{-\frac{T}{2}}^{\frac{T}{2}} x(t) y(t+\tau) dt \\
&= \lim_{T\to\infty} \frac{1}{T} \int_{-\frac{T}{2}}^{\frac{T}{2}} x(t) \left[\int_{-\infty}^{\infty} Y(\omega) e^{i\omega(t+\tau)} d\omega \right] dt \\
&= \int_{-\infty}^{\infty} \left\{ \left[\lim_{T\to\infty} \frac{1}{T} \int_{-\frac{T}{2}}^{\frac{T}{2}} x(t) e^{i\omega t} dt \right] Y(\omega) e^{i\omega\tau} d\omega \right\} \\
&= \int_{-\infty}^{\infty} \left\{ \left[\lim_{T\to\infty} \frac{2\pi}{T} \cdot \overline{\frac{1}{2\pi} \int_{-\frac{T}{2}}^{\frac{T}{2}} x(t) e^{-i\omega t} dt} \right] Y(\omega) e^{i\omega\tau} d\omega \right\}.
\end{aligned} \tag{B.30}
$$

If $x(t) = 0$ outside the time interval $[-\frac{T}{2}, \frac{T}{2}]$, which is reasonable in the large T limit,

$$\overline{\frac{1}{2\pi} \int_{-\frac{T}{2}}^{\frac{T}{2}} x(t) e^{-i\omega t} dt} \to \overline{\frac{1}{2\pi} \int_{-\infty}^{\infty} x(t) e^{-i\omega t} dt} = \overline{X(\omega)}$$

and Eq. (B.30) reduces to

$$C_{xy}(\tau) = \int_{-\infty}^{\infty} \left\{ \left[\left(\lim_{T\to\infty} \frac{2\pi}{T} \overline{X(\omega)} \right) Y(\omega) \right] e^{i\omega\tau} d\omega \right\}. \tag{B.31}$$

Comparing Eqs. (B.29) and (B.31), the cross-spectrum $S_{xy}(\omega)$ is given as

$$S_{xy}(\omega) = \lim_{T\to\infty} \left[\frac{2\pi}{T} \overline{X(\omega)} Y(\omega) \right]. \tag{B.32}$$

This equation gives the relationship between the cross-spectrum $S_{xy}(\omega)$ and the Fourier components $X(\omega)$ and $Y(\omega)$.

B.2.2 Phase Difference

Recalling from Eqs. (B.23)–(B.26) that $X(\omega) \left(= \frac{X(f)}{2\pi}\right)$ originates from A_n, and from Eq. (B.12), that $\arg A_n$ represents the phase of a real signal, $\theta_x(\omega)$ in the polar coordinate expression

$$X(\omega) = |X(\omega)|e^{i\theta_x(\omega)} \tag{B.33}$$

is regarded as the phase of a frequency component ω. Denoting $Y(\omega)$ as

$$Y(\omega) = |Y(\omega)|e^{i\theta_y(\omega)}, \tag{B.34}$$

the product $\overline{X(\omega)}Y(\omega)$ in $S_{xy}(\omega)$ is written as

$$\overline{X(\omega)}Y(\omega) = |X(\omega)||Y(\omega)|e^{i\{\theta_y(\omega)-\theta_x(\omega)\}}. \tag{B.35}$$

Since $\frac{2\pi}{T}$ in $S_{xy}(\omega)$ in Eq. (B.32) is real, Eqs. (B.32) and (B.35) give the phase difference $\Delta\theta_{yx}(\omega)$ of $y(t)$ with respect to $x(t)$ as a function of ω as

$$\Delta\theta_{yx}(\omega) \equiv \theta_y(\omega) - \theta_x(\omega) = \arg[S_{xy}(\omega)] = \arctan\left\{\frac{\mathrm{Im}[S_{xy}(\omega)]}{\mathrm{Re}[S_{xy}(\omega)]}\right\}. \tag{B.36}$$

Although $S_{xy}(\omega)$ is given in the limit $T \to \infty$, it is not practical to use data of infinite length. Fortunately, under the condition of ergodicity,

$$S_{xy}(\omega) = \lim_{T\to\infty}\left[\frac{2\pi}{T}\overline{X(\omega)}Y(\omega)\right] = \mathrm{E}\left[\frac{2\pi}{T}\overline{X(\omega)}Y(\omega)\right] \tag{B.37}$$

holds where "E[ ]" symbolizes taking an ensemble average. By virtue of ensemble averaging, the effect of random noise can be suppressed.

B.2.3 Coherence

By using $S_{xy}(\omega)$, the squared coherence $\mathrm{coh}^2(\omega)$ is defined as

$$\mathrm{coh}^2(\omega) \equiv \frac{|S_{xy}(\omega)|^2}{S_{xx}(\omega)S_{yy}(\omega)}, \tag{B.38}$$

which quantifies the linearity between the two signals $x(t)$ and $y(t)$.

Bibliography

[1] http://www.euronuclear.org/info/encyclopedia/bindingenergy.htm

[2] J. Freidberg, "Plasma Physics and Fusion Energy", Cambridge University Press, Mew York (2007).

[3] J. D. Lawson, *Proceedings of the Physical Society*, **B70**, 6 (1957).

[4] J. Wesson, "Tokamaks", Clarendon Press, Oxford (1997).

[5] R.J. Goldston and P.H. Rutherford, "Introduction to Plasma Physics", Institute of Physics Publishing, Bristol and Philadelphia (2003).

[6] R. Aymar, V.A. Chuyanov, M. Huguet, Y. Shimomura, ITER Joint Central Team, ITER Home Teams, *Nuclear Fusion*, **41**, 10 (2001).

[7] IAEA/ITER EDA/DS/22, "Summary of the ITER Final Design Report", IAEA, Vienna (2001).

[8] https://www.iter.org/proj/iterandbeyond

[9] F. Wagner, G. Becker, K. Behringer, D. Campbell, A. Eberhagen, W. Engelhardt, G. Fussmann, O. Gehre, J. Gernhardt, G.v, Gierke, G. Haas, M. Huang, F. Karger, M. Keilhacker, O. Klüber, M. Kornherr, K. Lackner, G. Lisitano, G.G. Lister, H.M. Mayer, D. Meisel, E.R. Müller, H. Murmann, H. Niedermeyer, W. Poschenrieder, H. Rapp, H. Röhr, F. Schneider, G. Siller, E. Speth, A. Stäbler, K.H. Steuer, G. Venus, O. Vollmer, Z. Yü, *Physical Review Letters*, **49**, 1408 (1982).

[10] F. Wagner, *Plasma Physics and Controlled Fusion*, **49**, B1 (2007).

[11] D.R. Sweetman, J.G. Cordey, T.S. Green, *Philosophical Transactions of the Royal Society of London*, A **300**, 589 (1981).

[12] M.G. Bell, *et.al.*, *Nuclear Fusion*, **35**, 1429 (1995).

[13] F. Romanelli, M. Laxaback on behalf of the JET EFDA Contributors, *Nuclear Fusion*, **51**, 094008 (2011).

[14] A. Isayama for the JT-60 Team, *Nuclear Fusion*, **51**, 094010 (2011).

[15] S. Ishida, P. Barabaschi, Y. Kamada, and the JT-60SA Team, *Nuclear Fusion*, **51**, 094018 (2011).

[16] Y. Kamada, P. Barabaschi, S. Ishida, the JT-60SA Team and JT-60SA Research Plan Contributors, *Nuclear Fusion*, **53**, 104010 (2013).

[17] Y-K.M. Peng and D.J. Strickler, *Nuclear Fusion*, **26**, 6 (1986).

[18] Y-K.M. Peng, *Physics of Plasmas*, **7**, 5 (2000).

[19] A. Sykes, M.F. Turner, S. Patel, *Plasma Physics and Controlled Fusion*, **VII-D**, 363 (1984) (*Proceedings of the 11th European Conference*, Aachen, 1983).

[20] F. Troyon, R. Gruber, H. Saurenmann, S. Semenzato, S. Succi, *Plasma Physics and Controlled Fusion*, **26**, 209 (1984).

[21] S. Nishio, K. Tobita, K. Tokimatsu, K. Shinya, I. Senda, T. Isono, Y. Nakamura, M. Sato, S. Sakurai, M. Yamauchi, T. Nishitani, K. Tani, S. Sengoku, Y. Kudo, Y. Song, S. Konishi, *Proceedings of the 20th International Conference on Fusion Energy* (Vilamoura, Portugal, 2004), CD-ROM file FT/P7-35, Vienna: IAEA (2004), and http://www-naweb.iaea.org/napc/physics/fec/fec2004/datasets/index.html

[22] K. Tobita, S. Nishio, M. Sato, S. Sakurai, T. Hayashi, Y.K. Shibama, T. Isono, M. Enoeda, H. Nakamura, S. Sato, K. Ezato, T. Hayashi, T. Hirose, S. Ide, T. Inoue, Y. Kamada, Y. Kawamura, H. Kawashima, N. Koizumi, G. Kurita, Y. Nakamura, K. Mouri, T. Nishitani, J. Ohmori, N. Oyama, K. Sakamoto, S. Suzuki, T. Suzuki, H. Tanigawa, K. Tsuchiya, D. Tsuru, *Nuclear Fusion*, **47**, 892 (2007).

[23] J.G. Gordey, *Plasma Physics and Controlled Fusion*, **26**, 1A (1984).

[24] N.J. Fisch, *Physical Review Letters*, **41**, 873 (1978).

[25] N.J. Fisch and C.F.F. Karney, *Physical Review Letters*, **54**, 897 (1985).

[26] N.J. Fisch, *Review of Modern Physics*, **59**, 175 (1987).

[27] S. Bernabei, C. Daughney, P. Efthimion, W. Hooke, J. Hosea, F. Jobes, A. Martin, E. Mazzucato, E. Meservey, R. Motley, J. Stevens, S. Von Goeler, R. Wilson, *Physical Review Letters*, **49**, 1255 (1982).

[28] F. Jobes, S. Bernabei, P. Efthimion, W. Hooke, J. Hosea, E. Mazzucato, E. Meservey, R. Motley, J. Stevens, S. von Goeler, *Physica Scripta*, **1982**, 418 (1982).

[29] Y. Takase, S. Ide, S. Itoh, O. Mitarai, O. Naito, T. Ozeki, Y. Sakamoto, S. Shiraiwa, T. Suzuki, S. Tanaka, T. Taniguchi, M. Aramasu, T. Fujita, T. Fukuda, X. Gao, M. Gryaznevich, K. Hanada, E. Jotaki, Y. Kamada, T. Maekawa, Y. Miura, K. Namamura, T. Nishi, H. Tanaka, K. Ushigusa, and the JT-60 Team, *Proceedings of the 19th IAEA Fusion Energy Conference* (Lyon) (2002), IAEA-CN94/PD/T-2 (IAEA, Vienna) (2003).

[30] Y. Takase, T. Fukuda, X. Gao, M. Gryaznevich, S. Ide, S. Itoh, Y. Kamada, T. Maekawa, O. Mitarai, Y. Miura, Y. Sakamoto, S. Shiraiwa, T. Suzuki, S. Tanaka, T. Taniguchi, K. Ushigusa, and the JT-60 Team, *Journal of Plasma and Fusion Research*, **78**, 719 (2002).

[31] S. Shiraiwa, S. Ide, S. Itoh, O. Mitarai, O. Naito, T. Ozeki, Y. Sakamoto, T. Suzuki, Y. Takase, S. Tanaka, T. Taniguchi, M. Aramasu, T. Fujita, T. Fukuda, X. Gao, M. Gryaznevich, K. Hanada, E. Jotaki, Y. Kamada, T. Maekawa, Y. Miura, K. Nakamura, T. Nishi, T. Tanaka, K. Ushigusa, and JT-60 Team, *Physical Review Letters*, **92**, 035001 (2004).

[32] R.J. Goldston, S.H. Batha, R.H. Bulmer, D.N. Hill, A.W. Hyatt, S.C. Jardin, F.M. Levinton, S.M. Kaye, C.E. Kessel, E.A. Lazarus, J. Manickam, G.H. Neilson, W.M. Nevins, L.J. Perkins, G. Rewoldt, K.I. Thomassen, M.C. Zarnstorff, *Plasma Physics and Controlled Fusion*, **36**, B213 (1994).

[33] T.S. Taylor, *Plasma Physics and Controlled Fusion*, **39**, B47 (1997).

[34] M.C. Zarnstorff, M.G. Bell, M. Bitter, R.J. Goldston, B. Grek, R.J. Hawryluk, K. Hill, D. Johnson, D. McCune, H. Park, A. Ramsey, G. Taylor, R. Wieland, *Physical Review Letters*, **60**, 1306 (1988).

[35] Y. Takase, A. Ejiri, H. Kakuda, T. Oosako, T. Shinya, T. Wakatsuki, T. Ambo, H. Furui, T. Hashimoto, J. Hiratsuka, H. Kasahara, K. Kato, R. Kumazawa, C.P. Moeller, T. Mutoh, A. Nakanishi, Y. Nagashima, K. Saito, T. Sakamoto, T. Seki, M. Sonehara, R. Shino, H. Togashi, O. Watanabe, T. Yamaguchi, *Nuclear Fusion*, **53**, 063006 (2013).

[36] T. Wakatsuki, A. Ejiri, T. Shinya, Y. Takase, H. Furui, J. Hiratsuka, K. Imamura, T. Inada, H. Kakuda, H. Kasahara, Y. Nagashima, K. Nakamura, A. Nakanishi, T. Oosako, K. Saito, T. Seki, M. Sonehara, H. Togashi, S. Tsuda, N. Tsujii, T. Yamaguchi, *Nuclear Fusion*, **54**, 093014 (2014).

[37] T. Ogawa, K. Hoshino, S. Kanazawa, M. Saigusa, T. Ido, H. Kawashima, N. Kasuya, Y. Takase, H. Kimura, Y. Miura, K. Takahashi, C.P. Moeller, R.I. Pinsker, C.C. Petty, D.A. Phelps, *Nuclear Fusion*, **41**, 1767 (2001).

[38] V.K. Gusev, S.E. Aleksandrov, V.Kh Alimov, I.I. Arkhipov, B.B. Ayushin, A.G. Barsukov, B.Ya Ber, F.V. Chernyshev, I.N. Chugunov, A.V. Dech, V.E. Golant, A.E. Gorodetsky, V.V. Dyachenko, M.M. Kochergin, G.S. Kurskiev, S.A. Khitrov, N.A. Khromov, V.M. Lebedev, V.M. Leonov, N.V. Litunovsky, I.V. Mazul, V.B. Minaev, A.B. Mineev, M.I. Mironov, I.V. Miroshnikov, E.E. Mukhin, Yu A. Nikolaev, A.N. Novokhatsky, A.A. Panasenkov, M.I. Patrov, M.P. Petrov, Yu V. Petrov, K.A. Podushnikova, V.A. Rozhansky, C.C. Rozhdestvensky, N.V. Sakharov, O.N. Shcherbinin, I. Yu Senichenkov, A.E. Shevelev, E.V. Suhov, I.N. Trapesnikova, E.I. Terukov, G.N. Tilinin, S. Yu Tolstyakov, V.I. Varfolomeev, A.V. Voronin, A.P. Zakharov, R.Kh Zalavutdinov, V.A. Yagnov, E.A. Kuznetsov, E.G. Zhilin, *Nuclear Fusion*, **49**, 104021 (2009).

[39] V.V. D'yachenko, V.K. Gusev, M.M. Larionov, A.D. Mel'nik, A.N. Novokhatskii, Yu.V. Petrov, V.V. Rozhdestvenskii, N.V. Sakharov, A.Yu. Stepanov, S.A. Khitrov, N.A. Khromov, F.V. Chernyshev, A.E. Shevelev, O.N. Shcherbinin, S.E. Bender, A.A. Kavin, K.M. Lobanov, *Plasma Physics Reports*, **39**, 189 (2013).

[40] T. Takahashi, S. Takamura, T. Okuda, *Journal of Applied Physics*, **53**, 6693 (1982).

[41] Y. Uesugi, S. Takamura, T. Okuda, *Plasma Physics*, **24**, 369 (1982).

[42] Y. Takase, M. Porkolab, J.J. Schuss, R.L. Watterson, C.L. Fiore, R.E. Slusher, C.M. Surko, *Physics of Fluids*, **28**, 983 (1985).

[43] M. Porkolab, *Physics of Fluids*, **17**, 1432 (1974).

[44] Y. Takase and M. Porkolab, *Physics of Fluids*, **26**, 2992 (1983).

[45] M. Porkolab, J.J. Schuss, B. Lloyd, Y. Takase, S. Texter, P. Bonoli, C. Fiore, R. Gandy, D. Gwinn, B. Lipschultz, E. Marmar, D. Pappas, R. Parker, P. Pribyl, *Physical Review Letters*, **53**, 450 (1984).

[46] M. Porkolab, B. Lloyd, Y. Takase, P. Bonoli, C. Fiore, R. Gandy, R. Granetz, D. Griffin, D. Gwinn, B. Lipschultz, E. Marmar, S. McCool, A. Pachtman, D. Pappas, R. Parker, P. Pribyl, J. Rice, J. Terry, S. Texter, R. Watterson, S. Wolfe, *Physical Review Letters*, **53**, 1229 (1984).

[47] R.E. Slusher and C.M. Surko, *Physics of Fluids*, **23**, 472 (1980).

[48] T. Shinya, A. Ejiri, Y. Takase, T. Wakatsuki, T. Oosako, N. Tsujii, H. Kakuda, H. Furui, J. Hiratsuka, T. Inada, K. Imamura, K. Nakamura, A. Nakanishi, M. Sonehara, H. Togashi, S. Tsuda, T. Yamaguchi, H. kasahara, K. Saito, T. Seki, F. Shimpo, Y. Nagashima, O. Watanabe, T. Yamada, *Plasma and Fusion Research*, **9**, 3402040 (2014).

[49] J.A. Schmidt, *Review of Scientific Instruments*, **39**, 1297 (1968).

[50] Y. Nagashima, S. Inagaki, K. Kamakaki, H. Arakawa, T. Yamada, S. Shinohara, Y. Kawai, M. Yagi, A. Fujisawa, S.-I. Itoh, I Itoh, Y. Takase, *Review of Scientific Instruments*, **82**, 033503 (2011).

[51] T.H. Stix, "Waves in Plasmas", AIP Press, New York (1992).

[52] T.J.M. Boyd and J.J. Sanderson, "The Physics of Plasmas", Cambridge University Press, New York (2003).

[53] J.D. Landau, *Journal of Physics USSR*, **10**, 25 (1946).

[54] F.F. Chen, "Introduction to Plasma Physics and Controlled Fusion", Plenum Press, New York (1984).

[55] J. Dawson, *Physics of Fluids*, **4**, 869 (1961).

[56] I. Langumur, *Physical Review*, **28**, 727 (1926).

[57] C. Hidalgo, R. Balbín, M.A. Pedrosa, I. García-Cortés, M.A. Ochando, *Physical Review Letters*, **69**, 1205 (1992).

[58] I.H. Hutchinson, "Principles of Plasma Diagnostics", Cambridge University Press, New York (2002).

[59] S. Shiraiwa, Y. Takase, A. Ejiri, K. Yamagishi, Y. Nagashima, N. Kasuya, *Proceedings of the 26th EPS Conference* (EPS, Maastricht) (1999), **23J**, 441 (EPS, Geneva).

[60] Y. Takase, A. Ejiri, N. Kasuya, T. Mashiko, S. Shiraiwa, L.M. Tozawa, T. Akiduki, H. Kasahara, Y. Nagashima, H. Nozato, H. Wada, H. Yamada, T. Yamada, K. Yamagishi, *Nuclear Fusion*, **41**, 1543 (2001).

[61] A. Ejiri, Y. Takase, T. Oosako, T. Yamaguchi, Y. Adachi, O. Watanabe, Y. Nagashima, B.I. An, H. Kobayashi, H. Kurashina, H. Hayashi, H. Matsuzawa, K. Yamada, H. Tojo, T. Masuda, M. Sasaki, R. Kumazawa, H. Kasahara, F. Shimpo, *Nuclear Fusion*, **49**, 065010 (2009).

[62] E. Abe, "Micro Waves", University of Tokyo Press, Tokyo (1992) [in Japanese].

[63] G. Chiodini, C. Riccardi, M. Fontanesi, *Review of Scientific Instruments*, **70**, 2681 (1999).

[64] C. Theiler, I. Furno, A. Kuenlin, Ph. Marmillod, A. Fasoli, *Review of Scientific Instruments*, **82**, 013504 (2011).

[65] J.D. Jackson, "Electrodynamics", Library of Congress Cataloging-in-Publication (1999).

[66] T.I. Cox, V.G.I. Deshmukh, D.A.O. Hope, A.J. Hydes, N.St.J. Braithwaite, N.M.P. Benjamin, *Journal of Physics D: Applied Physics*, **20**, 820 (1987).

[67] I.D. Sudit and F.F. Chen, *Plasma Sourses Science and Technology*, **3**, 162 (1994).

[68] T. Bonoli and E. Ott, *Physics of Fluids*, **25**, 359 (1982).

[69] T. Kobayashi, Y. Nagashima, S. Inagaki, H. Arakawa, M. Sasaki, T. Yamada, M. Yagi, N. Kasuya, A. Fujisawa, S.-I. Itoh, K. Itoh, *Plasma and Fusion Research*, **6**, 1401050 (2011).

[70] R.W. Harvey and M.G. McCoy, General Atomics Report GA-A20978, 1992 (1992).

[71] M. Hino, "Spectrum Analysis", Asakura Bookstore, Tokyo (2010) [in Japanese].